Laboratoire de Mécanique des Fluides de Lille
Kampé de Fériet

Université de Lille

Thèse de Doctorat de L'Université de Lille

Spécialité: Mécanique des milieux fluides

Simulation numérique directe et analyse des grandes échelles d'une couche limite turbulente

---

présentée et soutenue le 18 Juillet 2018 publiquement par

İlkay SOLAK

pour obtenir le grade de Docteur de l'Université de Lille

Soutenue le — devant le jury composé de:

Rapporteur	**Eric LAMBALLAIS**	Professeur, PPRIME, Université de Poitiers
Rapporteur	**Sébastien DECK**	Maître de Recherche, HDR, ONERA, Meudon
Examinateur	**Uwe EHRENSTEIN**	Professeur, M2P2, Aix-Marseille Université
Examinateur	**Ayşe Gül GÜNGÖR**	Associate Professor, Istanbul Technical University
Examinateur	**Jean-Marc FOUCAUT**	Professeur, LMFL, École Centrale de Lille
Directeur de thèse	**Jean-Philippe LAVAL**	Chargé de Recherche, HDR, CNRS, LMFL, Lille

Thèse préparée au Laboratoire de Mécanique des Fluides de Lille - Kampé de Fériet

Ecole Doctorale SPI 072 (LilleI, LilleIII, Artois, ULCO, UVHC, EC Lille)

Laboratoire de Mécanique des Fluides de Lille
Kampé de Fériet

Université de Lille

Ph.D. Thesis at University of Lille

Specialty: Fluid mechanics

Direct numerical simulation and large scale analysis of a turbulent boundary layer

---

publicly presented and defended on 18th July 2018 by

İlkay SOLAK

to obtain the doctorate of University of Lille

Defended on — in front the jury:

Reviewer	**Eric LAMBALLAIS**	Professor, PPRIME, Université de Poitiers
Reviewer	**Sébastien DECK**	Senior scientist, HDR, ONERA, Meudon
Examiner	**Uwe EHRENSTEIN**	Professor, M2P2, Aix-Marseille Université
Examiner	**Ayşe Gül GÜNGÖR**	Associate Professor, Istanbul Technical University
Examiner	**Jean-Marc FOUCAUT**	Professor, LMFL, École Centrale de Lille
Supervisor	**Jean-Philippe LAVAL**	Researcher, HDR, CNRS, LMFL, Lille

Ph.D. thesis prepared at Lille Laboratory of Fluid Mechanics - Kampé de Fériet

Doctoral School SPI 072 (LilleI, LilleIII, Artois, ULCO, UVHC, EC Lille)

This thesis has been prepared at

Laboratoire de Mécanique des Fluides de Lille - Kampé de Fériet (LMFL)
CNRS FRE2017
Blv Paul Langevin 59655 Villeneuve d'Ascq
FRANCE
lmfl@centralelille.fr

Abstract

This work lies at the intersection of two problems concerning turbulence (i) the description of coherent structures of turbulent boundary layer flow and (ii) the numerical methods for high-performance computing of these flows. The main objectives are to analyze coherent structures and to develop new numerical tools to be used in turbulence research with a special focus on the turbulent boundary layers. A new direct numerical simulation of a turbulent boundary layer flow over a flat plate is conducted with the code Incompact3d. A relationship between attached flow structures and the streamwise energy spectra in a turbulent boundary layer has been established similarly to an earlier experimental study. A novel application of the skeletonization method is proposed to obtain detailed statistics of coherent structures. Statistics of large-scale motions (LSM) and Reynolds Shear Stress quadrant structures are compared. In the second part, a new test-suite is implemented for the in-house incompressible Navier-Stokes solver. Performance of the code is analyzed. The stability problems at high Reynolds numbers are addressed and some solutions are proposed.

Keywords: turbulence, numerical method, direct numerical simulation, turbulent boundary layers, coherent structure

Résumé

Cette étude est à l'intersection de deux problématiques que sont (i) la description des structures cohérentes d'une couche limite turbulente et (ii) les méthodes numériques adaptées pour le calcul haute performance de ces écoulements. Les principaux objectifs sont de caractériser les grandes structures de la turbulence et de développer de nouveaux outils numériques pour la simulation de couches limites turbulentes. Une nouvelle simulation numérique directe de couche limite turbulente de plaque plane est réalisée avec le code Incompact3d. Une relation entre les structures cohérentes attachées à la paroi et le spectre d'énergie dans une couche limite turbulente est établie et comparée à une étude antérieure basée sur des résultats expérimentaux. Une application particulière de la méthode de squelettisation est proposée pour établir des statistiques plus précises des structures cohérentes de la turbulence. Les statistiques des structures grandes échelles de vitesse longitudinale (LSM) et les différents composantes des tensions de Reynolds turbulent instantanées (quadrants) sont comparées. Dans un second temps, un nouveau module de tests est implémenté dans le solveur Navier-Stokes incompressible développé en interne. La performance de ce nouveau code est analysée. Les problèmes de stabilité à nombre de Reynolds élevé sont abordés et certaines solutions sont proposées.

Mots clés : turbulence, méthode numérique, simulation numérique directe, couches limites turbulente, structure cohérente

Acknowledgments

First, I would like to express my sincere gratitude to my supervisor, Dr. Jean-Philippe Laval for giving me the opportunity to conduct this research with him. His guidance helped me enormously both during the research and writing of this thesis. I will always be indebted to him for sharing with me his knowledge of fluid mechanics, turbulence and his mentorship about life.

I would like to thank Prof. Eric Lamballais and Dr. Sébastien Deck for having accepted to review my thesis. I also thank Prof. Uwe Ehrenstein, Dr. Ayşe Gül Güngör and Prof. Jean-Marc Foucaut for having accepted to be part of the jury.

Life at building M6 was fascinating. I thank Prof. Emmanuel Leriche for his time that we spent discussing on numerical methods. I am fortunate to work with Dr. Christophe Cuvier who has always been ready for insightful discussions on wall-turbulence. Thanks to all my colleagues (Sri, Linh, Florian, Tai, Cedric, Raoul, ...) for providing an invaluable set of resources both inside and outside the lab. I am also grateful to Nathalie Labaeye and Anne-Marie Moudart for their unfailing support and assistance.

My friends Mei, Antoine, Perrine, Hubert, Naina, Erhan, Nick, Cansev, Oguzhan and many others: Your company has really made my time in Lille enjoyable and memorable. Finally, I would like to thank my family for their love and support over the course of my life and their patience over the last four years.

Without financial support and the computational resources, this study would not be possible. In that manner, I would like to thank the University of Lille for the financial support. Special thanks to GENCI and everyone working to make computer OCCIGEN running. I also like to express my gratitude to Dr. Sylvain Laizet for providing the code Incompact3d. I am thankful to every single person who put any effort into an open-source software project for their contribution not only in this study but on the world heritage.

This work was granted access to the HPC resources of IDRIS and CINES under the allocation 021741 made by GENCI (Grand Equipement National de Calcul Intensif).

Contents

List of Figures

List of Tables

Nomenclature

Abbreviations

2D	Two dimensional
3D	Three dimensional
APG	Adverse pressure gradient
BDF	Backward differentiation formula
CFD	Computational fluid dynamics
CFL	Courant-Fiedrichs-Lewy number
DNS	Direct numerical simulation
FPG	Favorable pressure gradient
LSM	Large-scale motions
PIV	Particle image velocimetry
PTV	Particle tracking velocimetry
TBL	Turbulent boundary layer
TKE	Turbulent kinetic energy
VLSM	Very large-scale motions
ZPG	Zero pressure gradient

Greek Symbols

β	Clauser's non-dimensional pressure gradient parameter
Δ	Laplace operator
δ	Boundary layer thickness, with $0.99u_\infty$ criteria, a.k.a. δ_{99}
δ^*	Displacement thickness

δ_ν	Viscous length scale in wall bounded flow, ν/u_τ
κ	Von Kármán constant
μ	Dynamic molecular viscosity of the fluid
$\nabla\cdot$	Divergence operator
∇	Gradient operator
ν	Kinematic molecular viscosity of the fluid, μ/ρ
ρ	Density of the fluid
θ	Momentum thickness

Others

$(\cdot)^+$	Variable in wall-units, normalized using u_τ and ν
$(\cdot)^\ominus$	Negative fluctuations of the variable
$(\cdot)^\oplus$	Positive fluctuations of the variable

Roman Symbols

c_f	Skin friction coefficient, $\tau_w = \frac{1}{2}\rho U_\infty^2 c_f$
L_x, L_y, L_z	Computational domain size in the streamwise, wall-normal, and spanwise directions
N_x, N_y, N_z	Number of computational mesh nodes in the streamwise, wall-normal, and spanwise directions
n_x, n_y, n_z	Number of computational mesh nodes in the streamwise, wall-normal, and spanwise directions for a sub-domain
Re	Reynolds number
Re_δ	Reynolds number based on the δ and u_∞
Re_τ	Reynolds number based δ and u_τ
Re_θ	Reynolds number based θ and u_∞
u, v, w	Velocity in the streamwise, wall-normal and spanwise direction
U_∞	Free stream velocity
u_τ	Wall friction velocity, $\sqrt{\tau_w/\rho}$
t	Time
x, y, z	Streamwise, Wall-normal and Spanwise direction

Part I

Introduction and Literature Review

1

Introduction

1.1 Background

For more than a century, understanding turbulence is one of the primary research interest in fluid mechanics. Laminar and turbulent states of the flow have been first formally recognized by Hagen[12]. Turbulent flows can be observed in the different scope of problems like the circulatory system of the living organism, atmospheric wind or, at much larger scale, dynamics of stellar systems. Turbulence was first characterized and parametrized in pipe flows by Reynolds[13]. Thus, comprehensive understanding of fundamentals of turbulence is helpful for aerodynamic optimization, noise reduction, and flow control methodologies of the industrial applications. For example a very early example from Eiffel[14] shows that turbulence reduces drag on a sphere. Following these works an enormous knowledge has been accumulated due to the strong motivation for turbulence research supported by the everyday existence of the turbulent flows in nature. A broad introduction on the theory of turbulence can be found in the books of Batchelor[15], Young[16] and Pope[17] among many others.

Different approaches to study turbulence problem from a wide research communities are available in the literature. Therefore, it is useful to classify the contribution in turbulence research to indicate the place of current study. First of all, the simplest classification is based on the methodology used in these studies. Chapman and Tobak[18] divided the research efforts into the three primary approaches namely statistical, structural and dynamical (deterministic). The present study builds up around various statistics and definitions of the specific types of coherent structures. Another classification which is particularly useful is given by Hinze[19] as free (absence of walls) and wall (generated and affected by the presence of walls) turbulence the latter being the subject of the present work with a particular focus on the three-dimensional large-scale coherent structures.

Turbulent boundary layer (TBL) is a specific region of a flow where mixing across several layers takes places (at different distances from a wall) and which contains multi-scale quasi-random fluid motion. There is a long history of research on TBL starting with the legacy mixing length theory of Prandtl[20; 21] and the law of the wall by Kármán *et al.*[22]. Turbulent boundary layer theory kept progressing following these studies. Interested readers can refer to the book of Schlichting and Gersten[23] for a complete review. For the sake of completeness of this document, a brief literature review of wall-bounded flow, focusing on TBL, is also given in Chapter 2.

The well known study of Hussain[24] is one of the earliest investigation of the variety of coherent structures in turbulent flows, including structures in free shear flows along with the wall-bounded flow results. Qualitative description of coherent structures is often straightforward, however quantitative matters (e.g., origin, lifespan, and other statistics) are subject to substantial discussions. Main reasons behind the long-lasting discussions around the coherent structures are the definition and extraction of the coherent motions which have always been the significant challenges in turbulence research. Today, it is apparent that 3D and time-resolved turbulent flow databases, especially for TBL flows, are essential to access and to study turbulent structures.

Fortunately, both experimental and numerical approaches are improving faster than ever thanks to the technological innovations. Experimental methods usually comes with a unavoidable trade-off between spatial or temporal resolution. Single point measurement methods such hot-wire and LDA can reach up to the high acquisition frequencies. On the other hand, PIV and Tomo-PIV provides multi-dimensional data however at much lower sampling rates. Recent developments in particle tracking velocimetry (PTV) methodology provides better accuracy than before (i.e., Shake The Box[25]). In parallel to the experimental methods, numerical techniques are also evolving fast with the modern computer technologies like the Intel's Xeon Phi gathering up to 72 Cores. In addition to the advanced multi-processor platforms, software technologies are developing as well such as CUDA, OpenCL to benefit from GPUs. Consequently, new opportunities are available for the numerical solutions of Navier-Stokes equations for both the commercial market and scientific research. Hybrid MPI-OpenMP is now routinely used since it potentially provides better granularity, load balancing, optimized communication and I/O. Thus, new parallelization strategies are becoming usable for the well-known challenging problems requiring linear and nonlinear solvers, while some of the distributed algorithms have better convergence for certain sequential iterative algorithms. The revival of interest towards the study of turbulent structures in recent years is strongly related to these new tools and more powerful computational resources which offer easier access to the 3D spatially resolved data with the desired time resolution.

Existence and smoothness of the Navier-Stokes in three-dimensions are still unanswered questions, but Leray[26] proved the existence of weak solutions of the equations which satisfy the equations in a mean sense. Despite the controversial discussions around the truthiness of the equations, numerical methods are implemented to solve Navier-Stokes equations based on the fact that weak solutions exist. Numerical solutions of Navier-Stokes often becomes a computationally exhaustive and costly task, especially DNS. Approaches like RANS and LES aimed to be cheaper, but they are not suitable for this study, as both of them are not able to provide fully resolved velocity fields in time and space which is counter-intuitive to the goal of this work. Although solving Navier-Stokes equations numerically is not an easy task, DNS provides a numerical solution of the Navier-Stokes equations without turbulence models to reach results at a resolution down to the Kolmogorov scales with a proper adjustment of flow/fluid parameters and simulation domain. Such features of DNS checks out the essentials for a robust study of coherent structures.

DNS becomes more accessible for turbulence research with every new powerful high-performance computational center which confirms the arguments about the effects of the technological progress in turbulence research. On the other hand, only handful flow cases like homogeneous isotropic turbulence[27] or channel flow[28] can be computed at significant Reynolds number, because of possible simplifications in computational approaches based on the physics of the flow. The two above references are examples of very large DNS performed at the largest possible Reynolds number accessible at that time among many other DNS of such flows. Summary of available ZPG and APG TBL simulations are listed in tables 1.1 and 1.2 to provide overall idea about the existing studies. However, it should not be considered as a complete list.

The first examples of wall bounded flow DNS were at relatively low Reynolds numbers such as the channel flow simulation of Kim *et al.*[29] and TBL simulation of Spalart[30]. Using the largest supercomputers a channel flow simulations up to $\mathrm{Re}_\tau = 5200$ can be performed[28]. Relatively large number of examples of channel flows[29;31;32;33] are present in literature. However, much fewer data are available for TBL over a flat plate. The simulations of Sillero *et al.*[34] and Schlatter and Örlü[6] are recent well-known examples of DNS of turbulent boundary layers.

Table 1.1 – Summary of some available TBL DNS with zero pressure gradient (ZPG). Streamwise and spanwise grid resolutions in wall units are Δx^+, Δz^+. $\delta^+ = u_\tau \delta/\nu$ is the Karman number at the highest Reynolds achieved within the computational domain, where u_τ is the friction velocity and δ is the boundary layer thickness.

Δx^+	Δ_z^+	Re_θ	δ^+	Year	Reference
20	6.7	1410	650	1988	Spalart[30]
6.1	4.1	1968	740	2009	Simens *et al.*[31]
17.9	9.6	2400	802	2009	Schlatter *et al.*[35]
9	4	4060	1270	2010	Schlatter *et al.*[7]
12.3	4.9	2500	735	2011	Lee and Sung[36]
6.5	3.78	6650	2025	2013	Sillero *et al.*[37]
8.2	3.9	2522	822	2018	Solak and Laval[38] (present case)

Available, TBL simulations with the presence of APG is even lesser than the ZPG simulations. Although various examples of periodic bumps and channel flow simulations with APG exists[39] in the literature, there is no example of a TBL DNS with a geometrical curvature which generates the desired effect. In the available examples, pressure gradient effect is generated using power-law free-stream distribution[40] or with a constant uniform suction at the top boundary of the simulation controlling the constant streamwise gradient[41].

Table 1.2 – Summary of some available TBL DNS with adverse pressure gradient (APG). The range or the maximum Reynolds number based on momentum thickness Re_θ within the computational domain is given. The non-dimensional pressure gradient parameter β, is defined as $\delta^*/\tau_w\,(dP/dx)$ where δ^* is the displacement thickness, τ_w is the wall-shear stress and dP/dx is the mean pressure gradient in the streamwise direction. Simulations with separated flows are not listed.

Re_θ	β	Year	Reference
1600	2	1993	Spalart and Watmuff[42]
430 – 690	0.65	1998	Skote *et al.*[43]
1200 – 1400	1.68	2008	Lee and Sung[40]
3500 – 4800	1	2016	Kitsios *et al.*[44]
10000 – 12300	39	2017	Kitsios *et al.*[45]
2840	9	2017	Lee[46]

Robinson[47] provides a broad review of the coherent structures in TBL and describes the computer-simulation era (1980–present) in the research of the turbulent boundary layer structures. As he expected, domination of the computer power continues to provide unique details. Now, the puzzles are how these somehow persistent motions can be used to represent turbulent boundary layer flow (i.e., how these structures can be related to theory) and how such a theory can be useful[48].

To conclude this section, it should be remarked that advanced tools have been developed to analyze the problem of turbulence, and many details were discovered the last few decades, but the global solution of the turbulence problem is not solved yet. Understanding canonical TBL flows with ZPG and APG have great value for the study of turbulence. Therefore, simple TBL flow cases with or without pressure gradient need to be simulated. Today, simulations at much higher Reynolds number are being conducted which provides unique databases while no experimental measurement can matched-up with the advantages of those. In short, research on LSM and APG is extremely worthy subjects and might result in a reduction of the negative environmental impact of industrial applications and transportation.

1.2 Objectives

The present work is part of the research project of the Laboratoire de Mécanique des Fluides de Lille - Kampé de Fériet. In our group, several researchers have completed individual projects on physics of TBL@. Earlier experimental works in the group have been focused on the organization of the LSM in TBL flow[49], and the modeling of wall attached structures[10]. Further investigations of the structures in ZPG TBL is one of the objective of this study. Generating DNS of an APG TBL over a curved wall is one of the long term objectives of the team. The in-house code MFLOPS3D-MD have been developed to serve this purpose. The development of the code was carried on and a test-suite was implemented within this study.

Following the ideas mentioned earlier, this research on TBL aims to answer the following questions:

1. Lozano-Durán and Jiménez[50] have investigated the vortex clusters and Reynolds shear stress components in channel flows. They also provided aspect ratios of these structures. Is it possible to get similar aspect ratios with a lower Reynolds number? How can models based on the 3D decomposition of the coherent structures in wall-bounded flows be improved?

2. Srinath *et al.*[10] proposes a simple model based on the strong events in streamwise fluctuations to show the connection with the footprint of the LSM in streamwise energy spectra (k^{-1} region) with the structures detected in physical space. Is it possible to get the similar results with DNS data? How the turbulent kinetic energy (TKE) decomposes in these streamwise fluctuation regions and the quadrants?

3. Mathis *et al.*[51] demonstrated that LSM has some effects down to the wall. Are these effects can be detected on a single structure? Is it possible to distinguish different classes of the LSM (regarding their features in various wall distances)?

4. Ganapathisubramani *et al.*[52] splits the streamwise fluctuation for large and small scales based on the energy spectra. What can be observed with such decomposition of the turbulent kinetic energy, by detecting the structures in physical space?

5. How much of the large-scale streamwise structures are also part of the strong quadrant structures such as $Q2$ and $Q4$?

The main objectives of the second part of the present study is to continue to develop the new code MFLOPS3D-MD which is a tool to simulate TBL flow with APG. Limits of the code will be tested and optimized parameters will be identified. Apart from the development of the code when necessary, following questions will be addressed with the extensive tests:

6. Hugues and Randriamampianina[53] propose a projection method with a pressure prediction step. Can this method implemented in MFLOPS3D-MD? Are there any potential improvements concerning projection method?
7. Is Helmholtz solver working properly? What are the sources of the stability problem?
8. How efficient is the influence matrix solver? Are there any unfavorable subdomain configuration?

1.3 Research strategy

This study includes numerical analyses of the turbulent boundary layer flows. Fundamental physics of turbulent boundary layer flows will be investigated alongside the development of the numerical tools.

Results related to the flat plate TBL obtained using the code Incompact3d[54] which is a high-order incompressible Navier-Stokes solver that scales with up to one million cores. Compact finite difference sixth-order schemes are used to discretize incompressible Navier-Stokes equations on a Cartesian mesh. Explicit and semi-implicit temporal schemes are available for time advancement. It uses fractional step method[55] in order decouple pressure from momentum equation. Pressure is solved completely in spectral space with the proper use of 3D Fast Fourier Transforms (FFTs), allowing all possible boundary conditions in any spatial direction. The spectral method is combined with a special stretching function which allows non-homogeneous grid spacing in one spatial direction only. The pressure field is staggered from the velocity field by half a mesh to avoid spurious oscillations. Tripping based on Schlatter and Örlü[6] is implemented to force the transition to turbulent flow. In addition to the features above, the code itself contains MPI I/O routines. However, in this study, parallel netCDF4 were implemented as most of the post-processing tools developed in the laboratory already written to use on this data format.

The code MFLOPSMD-3D, computes the solution of incompressible Navier-Stokes, on a Cartesian mesh using a mapping of coordinates. Mapping provides the ability to simulate geometries within the simulation domain without additional computational cost. For example, the effect of the adverse pressure gradient (over a geometrical bump) can be studied. In this solver, spatial discretization is achieved with compact finite difference schemes[56] up to 8th order. It uses fractional step method as most of the other incompressible flow solvers available for the simulation of TBL. Both pressure and velocity components are solved in physical space using a collocated grid. 3D domain decomposition grants the massively parallelized feature to the code. Therefore, complete simulation domain consists of sub-domains each of them handled by a single MPI process. Within each sub-domain, Helmholtz system is solved efficiently via 3D diagonalization to solve the momentum equations implicitly. Similarly, Poisson equation are solved in a sub-domain for pressure equation. Influence matrix method[57] is used to determine boundary conditions of each sub-domain. The linear system generated due to this method is solved with iterative methods based on Portable, Extensible Toolkit for Scientific Computation[58;59] (PETSc). Boundary conditions at the full-domain borders are also implemented inside Helmholtz solver when a sub-domain is on the edge of the solution domain. 2D mapping functions are derived and blended in the momentum equations as additional source terms, so curved walls can be defined without wasting grid points. Only a few additional derivatives are required for this purposes limiting the mapping in 2 dimensions. Therefore, it is cheaper and straightforward than curvilinear coordinates. Additionally, sharper geometries can be placed inside the simulation domain as well, by altering boundary conditions of the interfaces of the sub-domains properly and without additional computational cost. Details of the development being kept for the later part of this document, features of the code MFLOPS3D-MD is potentially more flexible than the other high performance, high order Navier-Stokes solvers.

The simulation of TBL over a flat plate will be considered as the baseline in the present work. Additionally, it provides the turbulent inflow for the potential future simulations. After, a detailed characterization of the large-scale structures in TBL over a flat plate, similar studies can be done for the TBL subjected to APG.

All the post-processing and reporting is accomplished with open-source tools during this projects. Most of them are developed in FORTRAN or Python.

This investigation is complemented by the experimental Ph.D. project of Sricharan Srinath, also associated with the same research group in LML. Although the background for the present project and experimental counterpart are similar, the main objectives differ substantially. The two research activities share some common analysis of boundary layer flows (e.g. wall attached LSM) and the continuous interaction between the investigators have been highly beneficial for the completion of the projects.

1.4 Organization of this document

The present document is organized into four parts, with a total of nine chapters. Four appendices complete the results and methods presented in the main document. Each chapter focuses on a single subject with its conclusions when necessary. While keeping the background section of the present chapter general enough for every readers, specific literature review with more technical details is written in the next chapter. The parts of the document have been organized in a convenient order so the reader can follow the motivations and findings of the study while reading along.

Part I is the introduction of this document. Chapter 1 reveals the motivation behind this study, discusses the objectives of the research project and presents numerical solvers shortly. Further details related to the numerical methods are given at the beginning of each part of the document for the associated code. Chapter 2 presents the related literature review of wall-bounded flows.

TBL simulation at moderate Reynolds number and study of LSM are reported in the context of part II. Chapter 3 reveals the details of the numerical solver and parameters of the simulation. Chapter 4 shows the statistical results and, the three-dimensional structure of TBL as sweeps, ejections and large structures based on strong streamwise fluctuations (negative and positive).

Part III consists of 2 chapters. Chapter 5 introduces the in-house code MFLOPSMD-3D. The numerical methods used in the code are given in this chapter. A simulation of the TBL as showcase along with comprehensive tests to identify the source of the stability problems are described in chapter 6.

Finally, the main conclusion is given in part IV. Potential applications and future work to continue this activity are also summarized. The list publications and communications derived from the present study are given at the end of the document.

2

Wall Turbulence

In the present work, we assume the flow to be incompressible isothermal such that the density and the dynamic viscosity are not affected by temperature. The Navier-Stokes equations (2.1) and (2.2) govern incompressible fluid flows. Equation (2.1) represents momentum conservation and eq. (2.2) is the continuity equation (incompressibility constraint).

$$\frac{\partial \mathbf{u}}{\partial t} + \mathbf{u} \cdot \nabla \mathbf{u} = -\frac{1}{\rho}\nabla p + \nu \nabla^2 \mathbf{u} + \mathbf{g} \tag{2.1}$$

$$\nabla \cdot \mathbf{u} = 0 \tag{2.2}$$

In these equations, t is the time, $\mathbf{u}$ is the velocity vector, p is the pressure, ρ is the fluid density and ν is the kinematic viscosity of the fluid. Body forces (such as gravity, magnetic forces) are given as $\mathbf{g}$.

Expression of the instantaneous flow quantities by the sum of their mean and fluctuating parts was introduced by Reynolds[60] as

$$u_i = \bar{u}_i + u'_i \quad and \quad p = \bar{p} + p' \tag{2.3}$$

where the mean and fluctuations are denoted by a bar and a prime respectively.

The Reynolds Averaged Navier-Stokes equations (RANS) (the result of the implementation of Reynolds decomposition[†] (2.3) into (2.1) and (2.2)) is

$$\begin{gathered} \frac{\partial \bar{u}_i}{\partial x_i} = 0 \\ \rho\left(\frac{\partial \bar{u}_i}{\partial t} + \bar{u}_j \frac{\partial \bar{u}_i}{\partial x_j}\right) = -\frac{\partial \bar{p}}{\partial x_i} + \mu \frac{\partial^2 \bar{u}_i}{\partial x_j^2} - \rho \frac{\partial \overline{u'_i u'_j}}{\partial x_j} \end{gathered} \tag{2.4}$$

where $\overline{u'_i u'_j}$ is the Reynolds stress tensor. Its trace is equal to twice the turbulent kinetic energy

$$k = \frac{1}{2}\overline{u'_i u'_i} \tag{2.5}$$

[†] Other decompositions are available in the literature[61] depending on the specific focus the studies (e.g., phase averaging). In this study only mean and fluctuating parts are considered, so definition in (2.3) is sufficient.

Reynolds shear stress transport (RSST) is obtained by subtracting (2.4) from (2.1) and multiplying the results with $u_j^{'}$

$$
\begin{aligned}
\underbrace{\rho\frac{\partial\overline{u_i^{'}u_j^{'}}}{\partial t}}_{1}+\underbrace{\rho\overline{u_k}\frac{\partial\overline{u_i^{'}u_j^{'}}}{\partial x_k}}_{2}=-\underbrace{\rho\overline{u_i^{'}u_k^{'}}\frac{\partial\bar{u}_j}{\partial x_k}-\rho\overline{u_j^{'}u_k^{'}}\frac{\partial\bar{u}_i}{\partial x_k}}_{3}+\underbrace{\frac{\partial\left(\overline{u_i^{'}\tau_{jk}}+\overline{u_j^{'}\tau_{ik}}\right)}{\partial x_k}}_{4}\\
-\underbrace{\frac{\partial\left(\overline{u_i^{'}p^{'}}\mathbb{d}_{jk}+\overline{u_j^{'}p^{'}}\mathbb{d}_{ik}\right)}{\partial x_k}}_{5}-\underbrace{\rho\frac{\partial\overline{u_i^{'}u_j^{'}u_k^{'}}}{\partial x_k}}_{6}\\
+\underbrace{\overline{p^{'}\frac{\partial u_i^{'}}{\partial x_j}}+\overline{p^{'}\frac{\partial u_j^{'}}{\partial x_i}}}_{7}-\underbrace{\overline{\tau_{jk}\frac{\partial u_i^{'}}{\partial x_k}}-\overline{\tau_{ik}\frac{\partial u_j^{'}}{\partial x_k}}}_{8}
\end{aligned}
\tag{2.6}
$$

where $\mathbb{d}$ is the Dirac function and $\tau_{ij}=\mu\left(\frac{\partial u_i^{'}}{\partial x_j}+\frac{\partial u_j^{'}}{\partial x_i}\right)$ is the Reynolds stress tensor.

Equation (2.6) can be used to investigate the dynamics of turbulent motions. Each term of the equation labeled from 1 to 8 has a distinct role in the overall Reynolds stress balance as described in the textbook of George[62]. Term (1) is the rate of change of kinetic energy per unit mass due to non-stationarity. Term (2) is the rate of change of kinetic energy per unit mass due to convection by the mean flow. Term (3) is the production term that takes kinetic energy from the mean flow to feed turbulence. Terms (4), (5) and (6) correspond to the viscous diffusion, diffusion by pressure fluctuations and diffusion by velocity fluctuations respectively. They transport the Reynolds stress from one place to another. Term (7) in the Reynolds shear stress equation is the pressure-strain rate term. It redistributes energy between normal stresses and makes them more isotropic. Term (8) is the rate of dissipation of turbulence kinetic energy due to viscous stresses.

2.1 Turbulent boundary layer flow

For simplicity Einstein notation will be left here and the equations will be written for 2D flow, so x_1, x_2, u_1, u_2 *will be* u, v, x, y.

In wall-bounded flows, a boundary layer forms in the vicinity of the limiting surface where the effect of viscosity is significant. Kinematic and no-slip boundary conditions on the wall drive this particular type of the flow. Kinematic boundary conditions are imposed by the fact that the wall does not let fluid to penetrate. No-slip boundary conditions mean that tangential components of the velocity have to match and it is

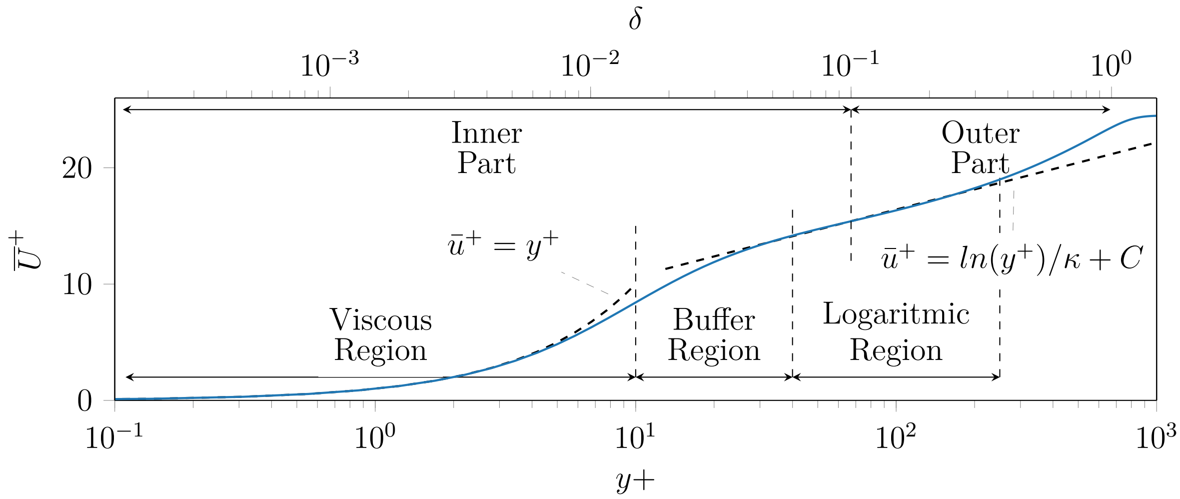

Figure 2.1 – An example of the velocity profile of the zero pressure gradient turbulent boundary layer at $Re_\theta = 2000$ showing the various regions. Note that ratio between δ and y^+ is Reynolds number dependent.

equal to zero when to wall is at rest. The theory of Prandtl[20;21] puts the no-slip conditions into the Navier-Stokes equation. More explicitly, his work shows that if the Reynolds number increases the flow will not behave more and more like an inviscid fluid which is the case for free shear flows. Consequently, inequalities listed in table 2.1 needs to be considered to resolve wall-bounded flows.

The use of a single turbulent length scale[63] is a satisfying approach for the turbulence closure problem but is not enough for wall-bounded flows (e.g., turbulent boundary layer). A second length scale is needed for Prandtl's boundary layer because boundary layer requires at least one viscous stress term in the equations to be maintained. As stated by George[62], "the necessary gradient in velocity is known as the boundary layer thickness".

Different layers can be identified in a turbulent boundary layer and scaled with boundary layer thickness or wall units. Typical limits for the regions are given in fig. 2.1 to provide a general picture of the TBL organization.

A boundary layer developing on a surface encounters first a laminar region which starts to destabilize in a transition zone before to become fully turbulent. The boundary layer thickness (δ) is defined as the wall normal distance where the velocity of the flow is equal to 99% of the free stream velocity. The displacement thickness δ^* (2.7) and the momentum thickness θ (2.8) are the vertical distances that the solid boundary must be displaced upward so that inviscid fluid at the free stream velocity U_e has the same mass flow rate and momentum as boundary layer with the original fluid.

$$\delta^* = \int_0^\delta \left(1 - \frac{\bar{u}(y)}{U_e}\right) dy \tag{2.7}$$

and

$$\theta = \int_0^\delta \frac{\bar{u}(y)}{U_e} \left(1 - \frac{\bar{u}(y)}{U_e}\right) dy \tag{2.8}$$

are the integral forms of the displacement thickness δ^* and the momentum thickness θ with U_e being the free stream (external) velocity.

The shape factor H is defined as the ratio between these two scales

$$H = \frac{\delta^*}{\theta} \tag{2.9}$$

Theoretical values of H are 2.59 and 1.25 for laminar (Blasius boundary layer) and turbulent (Prandtl approximation) flows. In canonical turbulent boundary layer flows[23;64] it is about 1.4.

Wall-bounded flows are often described with proper normalizations based on wall viscous length scale $\delta_\nu = \nu/u_\tau$ and wall friction velocity $u_\tau = \sqrt{\tau_w/\rho}$ where τ_w is the mean wall shear stress. The friction is better characterized by the friction coefficient

$$c_f = \frac{\tau_w}{\frac{1}{2}\rho U_e^2} \tag{2.10}$$

The turbulent boundary layer flows are usually characterized by the Reynolds number based on the friction velocity $Re_\tau = \frac{u_\tau \delta}{\nu}$ or the Reynolds number based on the momentum thickness $Re_\theta = \frac{U_\infty \theta}{\nu}$.

2.1.1 Boundary layer assumptions

Equation (2.4) can be reduced further based on the dimensional analysis of the equation for TBL. The two primary length-scales of the turbulent boundary layer are L (in streamwise direction), and δ (in wall-normal direction) considering a 2D flow ($w = 0$) over a wall at high Reynolds number. The length δ is much smaller than the longitudinal scale of the TBL ($\delta << L$).

To start the dimensional analyses the following scales are needed: (i) L_1, length scale along x, (ii) $L_2 \leq \delta(x)$, length scale along y, (iii) $V_1 \leq U_e$, velocity scale along x,

(iv) V_2, velocity scale along y and (v) v', velocity scale of turbulent fluctuations.

The scale V_2 can be related to the other scales with the help of the continuity equation.

$$\frac{V_1}{L_1} \sim \frac{V_2}{L_2} \Rightarrow V_2 \sim \frac{L_2}{L_1} V_1 \ll V_1$$

The relationship above is a natural result of the kinematic boundary condition mentioned earlier, and it also explains why entrainment rate is low in wall-bounded flows.

Dimensional analysis of the RANS equation (2.4) gives,

$$\frac{\partial \bar{u}}{\partial x} + \frac{\partial \bar{v}}{\partial y} = 0, \tag{2.11}$$

$$\bar{u}\frac{\partial \bar{u}}{\partial x} + \bar{v}\frac{\partial \bar{u}}{\partial y} = -\frac{1}{\rho}\frac{\partial \bar{p}}{\partial x} + \nu\frac{\partial^2 \bar{u}}{\partial y^2} - \frac{\partial \overline{u'v'}}{\partial y} \tag{2.12}$$

and

$$0 = -\frac{\partial \bar{p}}{\partial y} - \rho\frac{\partial \overline{v'v'}}{\partial y}. \tag{2.13}$$

The scales involved in (2.12) and (2.13) differs along the boundary layer, and further dimensional analyses can be done considering specific ranges of the boundary layer.

The region called “outer part” is the part of the TBL where wall-normal length scales is of the order of the boundary layer thickness δ and streamwise velocity scale is of the order of the external flow velocity.

As $L_2 \sim \delta$ and $L_1 \sim x$ and $V_1 \sim U_e$, viscous term became negligible leading to

$$\bar{u}\frac{\partial \bar{u}}{\partial x} + \bar{v}\frac{\partial \bar{u}}{\partial y} = -\frac{1}{\rho}\frac{\partial \bar{p}}{\partial x} - \frac{\partial \overline{u'v'}}{\partial y} \tag{2.14}$$

Close to the wall, streamwise velocity scale becomes smaller compared to the external velocity U_e. Scales in this region are $L_2 \sim \delta$, $L_1 \sim x$ and $V_1 \ll U_e$ (V_1 goes to 0 at the wall), therefore convection terms become negligible.

$$0 = -\frac{1}{\rho}\frac{\partial \bar{p}}{\partial x} + \nu\frac{\partial^2 \bar{u}}{\partial y^2} - \frac{\partial \overline{u'v'}}{\partial y} \tag{2.15}$$

Boundary layer flows can be classified in two categories, without pressure gradient ($\frac{\partial p}{\partial x} = 0$), and the with the pressure gradient. The pressure gradient can be “favorable”

($\frac{\partial p}{\partial x} > 0$) or “adverse” ($\frac{\partial p}{\partial x} < 0$) corresponding to accelerating or decelerating flows respectively.

2.1.2 Zero pressure gradient boundary layer

Equation (2.12) can be simplified further in the absence of the pressure gradient term.

Outer region: Above the inner region where $y > 0.1\delta$, neglecting pressure gradient term in (2.14), a velocity defect law can be defined:

$$\frac{U_e - \bar{u}}{u_\tau} = f\left(\frac{y}{\delta}\right) \tag{2.16}$$

George[65],[66] discussed defect law and proposed an alternative form based on a similarity solution of the RANS equations where u_τ is replaced by U_e in the scaling of the velocity deficit.

Inner region: George[62] demonstrates that inner equations needed to be below 0.1δ assuming convective terms are negligible ($\overline{u} << U_\infty$). For ZPG TBL (2.15) simplifies to:

$$\mu\frac{\partial^2 \bar{u}}{\partial y^2} - \rho\frac{\partial \overline{u'v'}}{\partial y} = 0 \tag{2.17}$$

Equation (2.17) can be integrated into wall normal direction and applying the boundary condition at the wall ($\tau = \tau_w$), it can be re-written as:

$$\tau = \mu\frac{\partial \bar{u}}{\partial y} - \rho\overline{u'v'} = \tau_{wall} = \rho u_\tau^2 \tag{2.18}$$

The inner part of TBL (eq. (2.18)) can be further divided into three parts called viscous, buffer and overlap (logarithmic) regions. The viscous region is also known as linear sub-layer. Effect of the viscosity gradually decreases, and the two terms of (2.18) became comparable in the buffer region. Later, the turbulent shear stress term dominates the flow and the overlap region emerges. Summary of these regions are given in table 2.1.

Table 2.1 – Regions of the inner part of the TBL

Region	Location	Characteristic	Equation
Viscous	$0 \leq y^+ \leq 5$	$\mu \frac{\partial \bar{u}}{\partial y} \gg \rho \overline{u'v'}$	$\bar{u}^+ = f(y^+)$
Buffer	$5 \leq y^+ \leq 30$	$\mu \frac{\partial \bar{u}}{\partial y} \sim \rho \overline{u'v'}$	Eq. (2.18)
Overlap	$y^+ \geq 30$ and $y \leq 0.1\delta$	$\mu \frac{\partial \bar{u}}{\partial y} \ll \rho \overline{u'v'}$	$\bar{u}^+ = ln(y^+)/\kappa + C$

At sufficiently large Reynolds numbers for which the log region exist, the overlap region can be defined between the inner and the outer regions. Note that logarithmic relation[67] is obtained by matching the equations of the inner and outer regions (eqs. (2.16) and (2.17)). George[65] also defines this region as a transition between the laminar similarity solution and infinite Reynolds number solution.

2.1.3 Turbulent boundary layers with pressure gradient

A non-dimensional pressure gradient parameter is defined by Clauser[68] as

$$\beta = \delta^* / \tau_w \frac{dP}{dx}. \tag{2.19}$$

β is a constant for boundary layers in equilibrium, and Clauser[68] expected these kind of boundary layers to be dynamically similar at all streamwise stations. $\beta = 0$ in ZPG case because $\frac{dP}{dx} = 0$, while larger values of β stands for strong APG cases.

Pressure gradient has a strong effect on the shape of the boundary layer mean velocity profiles and the characteristics of turbulence. The effect of a favorable pressure gradient in TBL has a tendency to reduce turbulence which can lead to relaminarization of the TBL at moderate Reynolds numbers affected by a strongly favorable pressure gradient. At the opposite, adverse pressure gradient generates an increase of turbulent kinetic energy which, in the case of strong adverse pressure gradient, is not enough to prevent the flow to separate. Another effect of the adverse pressure gradient is to increase the boundary layer thickness when decreasing the velocity derivative $\frac{\partial \bar{u}}{\partial y}$ at the wall. When the pressure gradient is strong enough, $\frac{\partial \bar{u}}{\partial y}$ becomes negative and leads to flow separation.

The inner part of the TBL with the pressure gradient can be described as:

$$\mu \frac{\partial^2 \bar{u}}{\partial y^2} - \rho \frac{\partial \overline{u'v'}}{\partial y} = \frac{\partial p}{\partial x} = \frac{\partial \tau}{\partial y} \tag{2.20}$$

Integrating in the wall-normal direction and applying the boundary condition ($\tau = \tau_w$) at the wall, (2.20) become:

$$\mu \frac{\partial \bar{u}}{\partial y} - \rho \overline{u'v'} = \frac{\partial p}{\partial x} y + \rho u_\tau^2 = \tau \tag{2.21}$$

Shear stress near the wall can be neglected similarly to the assumption made for ZPG case. Integrating one more time gives the equation for the viscous sub-layer with pressure gradient:

$$\bar{u}^+ = \frac{1}{2} \frac{\partial p^+}{\partial x} {y^+}^2 + y^+ \tag{2.22}$$

where

$$\frac{\partial p^+}{\partial x} = \frac{\nu}{\rho u_\tau^3} \frac{\partial p}{\partial x} \tag{2.23}$$

RANS models usually fail to predict accurately such flows. It is mostly because the near wall models rely on physics of the ZPG TBL as only little is known about APG cases. As shown in (2.22) effect of the pressure gradient affects the mean velocity profile very close to the wall. Equation $\overline{u}^+ = y^+$ (ZPG case) only holds for mild pressure gradients ($\frac{\partial p^+}{\partial x} {y^+}^2 \ll 1$). In case of strong pressure gradient this term cannot be neglected and should be considered in the models.

2.2 Coherent structures

Initially, Theodorsen[69] and Townsend[70] pointed out the significance of coherent structures in turbulent flows. Early studies questioned the contribution of the wall-attached structures to Reynolds stress[71]. Perry *et al.*[72] established a link between low wavenumbers spectra and streamwise motions. Hussain[73] defined a turbulent structure as "connected turbulent fluid mass with instantaneously phase-correlated vorticity over its spatial extent". Today, the existence of the coherent structures within the wall-bounded turbulent flows is widely accepted[47]. Nevertheless, it can also be evidenced by two-point correlations of two velocity components[74]. Recently, Lozano-Durán and Jiménez[75] followed the generation, lifespan, and disappearance of the structures related to the Reynolds shear stresses in detail via time-resolved DNS data which provides a complete mechanism of the turbulent structures.

This review is not explicitly categorizing the coherent structures as near-wall and outer structures because except the near-wall streaks there is not well distinguished wall-normal distance for the existence of the structures. However, the viscous and buffer regions have been subject to many studies and a recent review of the near-wall region was proposed by Stanislas[76]. Statistical organizations of the coherent structures in this region have been proposed in the literature[77;78;79]. Perry and Chong[80] proposed that Λ-shaped vortices fulfill the boundary layer. Similarly, a conceptual model of the organization of turbulence in the near-wall region based on the notion of "hairpin packets" was proposed by Adrian *et al.*[77]. del Álamo *et al.*[81] observed counter-rotating vortices around the wall-normal ejections in channel flow simulations. Dekou *et al.*[49] proposed another model based on counter-rotating vortices coupled with low and high speed momentum regions from the WALLTURB experimental results at $Re_\theta = 19660$. Their model consists of the low or high momentum regions accompanied with streamwise counter rotating vortices.

In the following, a brief literature review of coherent structures is presented in three parts. First vortices and near-wall streaks are presented briefly in section 2.2.1. This is followed by a review of the Reynolds shear stress structures (section 2.2.2) and large-scale motions of streamwise velocity fluctuations (section 2.2.3).

2.2.1 Vortices and near-wall streaks

Theodorsen[69]'s horseshoes vortex model for near-wall dynamics is one of the first efforts that use coherent structures to characterize wall-bounded turbulence. A vortex is a coherent structure that exhibits circular or spiral instantaneous streamlines in a plane normal to its core when viewed in a reference frame moving with the center of the vortex core. In addition to their theoretical value, vortices have been studied extensively also because of the strong experimental and numerical evidence of the important role of the vortices on streak instabilities[82].

Hunt *et al.*[83] identified vortices based on velocity gradient tensor but pressure minima can also be used to detect vortices as these structures correspond to low pressures zones. A more detailed review of the vortex identification methods can be found in Zhou *et al.*[84].

Vortices are involved in the redistribution term (pressure-strain correlation, the term (7) in eq. (2.6)). This is very important for RANS modeling as it is related to the mass and momentum transfer across the boundary layer. Additionally, Schoppa and Hussain[85] showed that reducing vortex generation can lead to drag reduction. Vortices have been investigated in details due to these interesting features. Consequently, detection and characterization of the different types of vortical structures appeared in literature such as horseshoes[86], canes, hairpins[77], streamwise vortices[87], transverse vortices, rings and others types of vortices represent a significant part of the literature on wall turbulence.

Shape and size of the hairpins depend on the Reynolds number[77;86], and they are thought to be tilted at about 45° from the plane parallel to the wall in the outer region[69;88]. Carlier and Stanislas[89] also emphasized that physical characteristics of vortices (size, intensity, convection velocity) in the logarithmic region scale in wall units. In a recent study from a DNS of channel flow at $Re_\tau = 1900$, del Álamo *et al.*[81] have identified two classes of clusters in the logarithmic region: detached small vortex packets and tall clusters which started from the near-wall region below $y^+ \approx 20$. They have shown the self-similarity of these attached tall clusters with a constant ratio $\lambda_x \approx 3\lambda_y$ and $\lambda_z \approx 1.5\lambda_y$ of their sizes in the three directions.

Streamwise fluctuations are the most accessible component experimentally. Historically, hot-wires are able to provide such data with high temporal resolution when classical PIV can also focus on the same component in 2D. Near wall streaks were first detected by Kline *et al.*[90] experimentally with a typical spanwise spacing around $100\nu/u_\tau$ at $y^+ \leq 10$. High-speed streaks found to be shorter (in the streamwise direction) and wider (in the spanwise direction) than the low-speed streaks[82]. Carlier and Stanislas[89] showed that spanwise spacing of streaks increases with both the distance to the wall and the Reynold number. The shape of the streaks are quite well defined in literature, they exhibit streamwise length of $500 < \lambda_x^+ < 2000$, spanwise width of $20 < \lambda_y^+ < 60$, and height of $\lambda_y^+ < 50$.

Lin *et al.*[79] showed that many of the streaks have a spanwise angle up to about 15° by identifying individual streaks in stereo PIV measurements of the viscous sub-layer of a turbulent boundary layer. Nolan and Zaki[91] investigated the role of the streaks in by-pass transition, and they determined that the strong-less frequent streaks become turbulent.

2.2.2 Quadrants

Corino and Brodkey[92] first observed experimentally the events of the flow directed from the wall and towards the wall experimentally which play a significant role in the turbulence production. Shortly later, Wallace *et al.*[93] introduced the quadrant analysis which consists in a decomposition of the Reynolds shear stress in four regions conditioned by the sign of u and v.

The relationship between high-pressure fluctuations in ejection and sweep cycle was found by Thomas and Bull[94]. The stronger contribution of the "ejection" ($Q2$) and "sweep" ($Q4$) to the production of turbulent kinetic energy has been identified by many authors[29;93;95;96]. Bernard and Handler[97] proposed that the existence of the weaker quadrants ($Q1$ and $Q3$) be related to the redirection of the $Q2$ and $Q4$ because of their relationship with the vortical structures in the near-wall region. Bernard *et al.*[98] showed that sweeps are dominated by Reynolds stress production close to the wall. Tilted vortex cores are thought to make regeneration system to advance by accelerating flow toward the wall and decelerating flow leaving the wall region. Lozano-Durán *et al.*[1] provide detailed analysis of $Q2$ and $Q4$ events from channel flows simulations including their overlap with vortex clusters[81] (see fig. 2.2). They found an optimal threshold factor of Reynolds Shear Stress, $H = 1.75$, based on the percolation analysis for detection of the quadrant structures. Using this threshold factor, they determined that attached quadrants are the most energetic ones even if they are smaller in volume. Additionally, they also grouped $Q2$ and $Q4$ as "gradient" events and $Q1$ and $Q3$ as "counter-gradient" and demonstrated a spatial similarity for the gradient events defined as $\lambda_x \approx 3\lambda_y$ and $\lambda_z \approx 1.0\lambda_y$ (del Álamo *et al.*[81] reported similar laws for the attached clusters, $\lambda_z \approx 1.5\lambda_y$ although slightly wider). The time evolution of quadrants has been investigated by Lozano-Durán and Jiménez[75] from DNS of channel flows for a range of Reynolds number of $Re_\tau = 930-4200$. They argue that if quadrant structures reach the large size, they are self-similar both geometrically and temporally, but most of these structures stay smalls and do not last for long times.

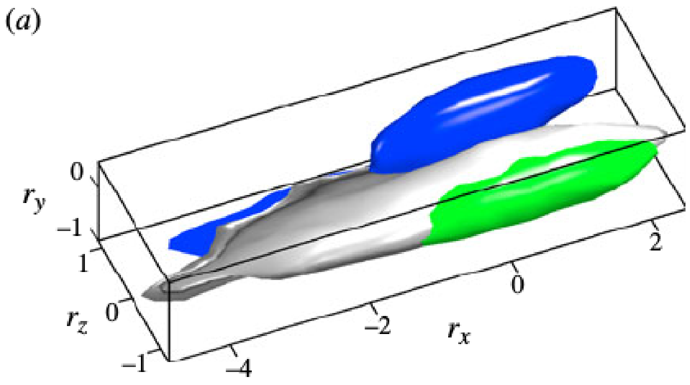

Figure 2.2 – Flow fields conditioned to attached $Q2$–$Q4$ pairs in the logarithmic layer. PDFs of the points belonging to the $Q2$ (green), $Q4$ (blue) and vortex clusters (gray). The isosurfaces plotted are 0.75 times the maximum value of the PDFs for the Qs and 0.85 for the vortex cluster. [*Reproduced from Lozano-Durán* et al.[1]]

In chapter 4 these structures are investigated for ZPG TBL and results are compared with the one of Lozano-Durán and Jiménez[75].

2.2.3 Large-scale motions

These structures are usually categorized into large-scale motion (LSM) and very larger-scale motion (VLSM) as the elongated regions of streamwise velocity fluctuations having a streamwise extent up to 3 boundary layer thickness (δ) for the former and longer for the latter[99;100;101]. They are located in the logarithmic and lower wake regions of a turbulent boundary layer[36;102;103]. Special focus has been laid on LSMs and VLSMs as they contribute to a significant amount of turbulent kinetic energy and Reynolds shear stress[104;105;106;107].

The literature on this subject is quite broad starting from the bulges of the turbulent boundary layer[108]. Other results also draw a picture for LSM as a group of hairpin packets[77]. For example, Ganapathisubramani *et al.*[104] reported hairpin packets extending up to 2δ. Srinath *et al.*[10]; Kim and Adrian[99]; Lee and Sung[109]; Marusic *et al.*[110]; Yoon *et al.*[111] called energetic streamwise structures as LSM (or VLSM) among many others.

Despite different definitions of LSM, their existence is supportable with simpler observations. It is clear that around $y^+ = 100$ a change occurs in the u_{rms} profiles such that a local minimum or flat region can be observed at sufficiently high Reynolds number[2;10;102]. The second (outer) energy peak[102] comes out as Reynolds number increases and this second peak is related to large-scale structures. Hultmark *et al.*[2] showed that the intensity of large-scale structures increases as the Reynolds number increases. However, the inner peak seems not affected similarly while the second peak gets stronger (see fig. 2.3).

Another method to show the large-scale structures is, the backbone for the modern statistical approach of turbulence, two-point velocity correlation[112]. In particular, it can be used to obtain the average statistics of the large-scale motions. Grant[113] observed the long streamwise extends of the streamwise velocity correlation. Christensen and Adrian[114] showed a statistical evidence for the hairpin packets using similar correlations. Tutkun *et al.*[115] demonstrated correlations for streamwise velocity using data from hot-wire rakes at a much higher Reynolds number ($Re_\theta = 19100$). Large-scale structures in channel flows have been investigated in detail by Sillero *et al.*[3] using two-point correlations as well. Their 3D representation of the correlation functions (fig. 2.4) illustrates the potential shape of the streamwise fluctuations structures.

Two-point correlation isocontours exhibit an ellipse shape with an average inclination function of the altitude of the fixed points suggesting an angle of the structures. Different results have been reported for an average angle of LSM ranging from 9° to 33°[92;113;114;116;117;118;119;120]. The broad range of values provided in literature is the

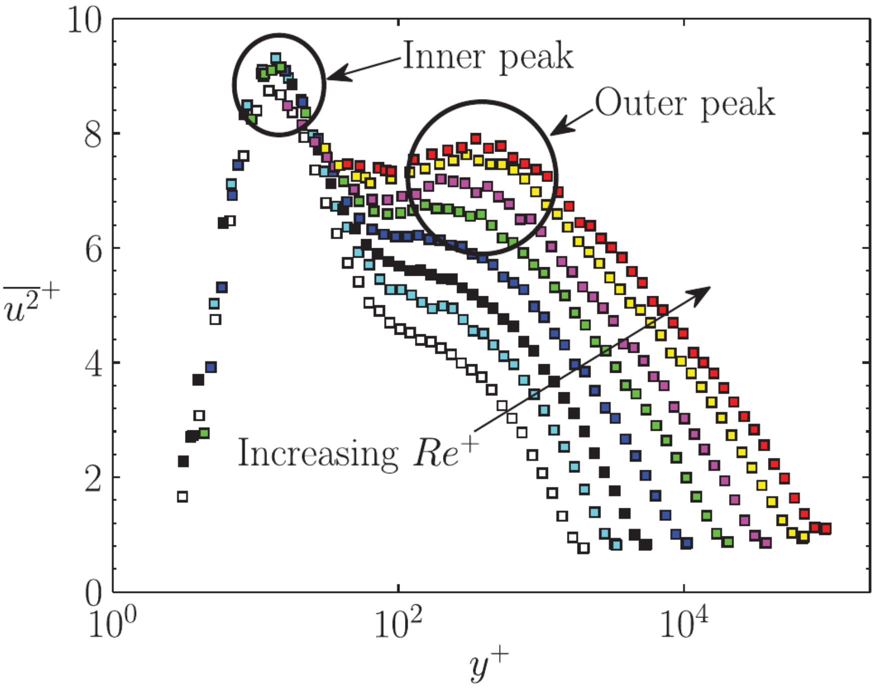

Figure 2.3 – Streamwise velocity fluctuation profiles from high Reynolds number experiments of pipe flow. [*Reproduced from Hultmark* et al. [2]]

result of the use of the simpler estimations such as pictures of the smoke visualizations and correlations of different quantities. For example, Falco [117] proposed an angle of 18° based on smoke visualizations of the turbulent boundary layer at $Re_\theta = 4000$. Christensen and Adrian [114] define the mean flow based series of swirling motion and found these motions are along a line at $12° - 13°$ in the outer region of turbulent channel flows. Christensen and Wu [120] models the average streamwise length based on two-point correlation of the streamwise velocity fluctuations for $y/h = 0.1$ and found an inclination of 11° using PIV data at $\mathrm{Re}_\tau = 2099$. Kähler [119] summarized all the possible angles in a streamwise wall-normal plane from stereo PIV data. He reported the inclination of the two-point correlation of the streamwise velocity as 8.88° at $Re_\theta \simeq 7800$ in the buffer region. Additionally, the inclination of the elliptical shape of isocontours varies with the wall distance. Results suggest that these structures move away from the wall with an increasing angle proportional to their distance to the wall.

In boundary layers, Hutchins and Marusic [102] used hot-wire rake measurements of an atmospheric surface layer and found very long meandering structures up to 20δ populating the log layer. On the other hand, when viewed from single point statistics, the meandering tendency masks the true length of these structures resulting in shorter length scales. Several DNS of wall-bounded flows at significant Reynolds numbers has already been performed to study LSM which provide a 3D view. Lee *et al.* [107]

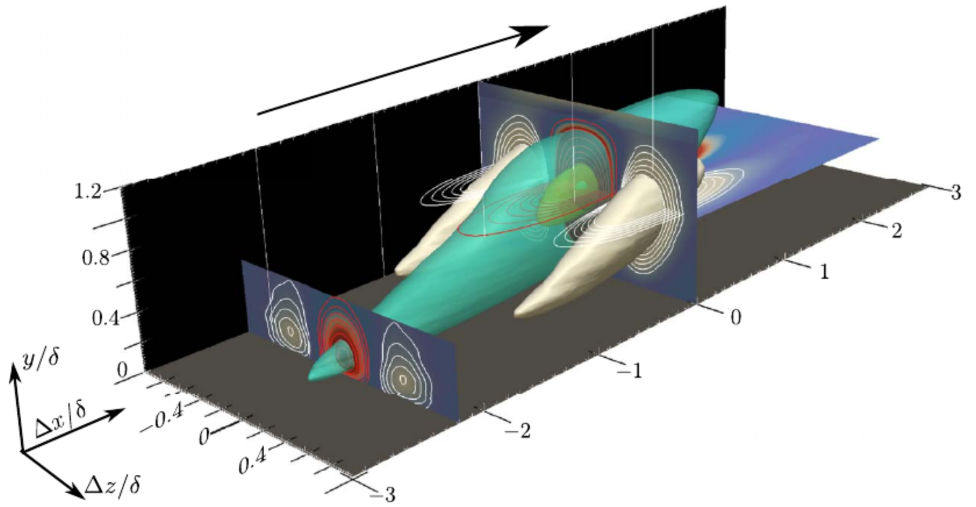

Figure 2.4 – Three-dimensional representation of the correlation of the streamwise velocity fluctuations for boundary layer at $Re_\tau = 1530$. [*Reproduced from* Sillero et al.[3]]

investigated the large-scale motions in channel flows with a detection method which consists of several operations on the velocity fluctuation fields. From temporal analyses, they related the merging of the LSM as a production mechanism for VLSM. These studies and many others reported very large-scale structures up to 15δ. LSM up to $20h$ long (h being the channel half-width) have also been observed in channel flows by del Álamo and Jiménez[121]; Del ÁLamo *et al.*[122]. Hwang *et al.*[123] investigated the inner-outer interactions of negative and positive large-scale structures in channel flow at moderate Reynolds number ($Re_\tau = 930$) using conditional correlation. DNS of flat channel flow are now available up to $Re_\tau = 5200$, but simulations of flat plate turbulent boundary layer are more challenging and therefore restricted to slightly lower Reynolds numbers. The behavior of very large scale structures is clearly dependent on the Reynolds number, and they are likely to become significant at extremely high Reynolds number. However, these Reynolds numbers are not accessible by DNS yet. Additionally, statistics of very large scales can be affected by the size of the computational domain or the forcing mechanism of the turbulent boundary layer simulations. Still, DNS is an essential tool to study space and time organization of these structures at moderate Reynolds numbers when conducted carefully. Several DNS of TBL has been performed at moderate Reynolds number with various boundary conditions and domain sizes[7;37;124]. Higher Reynolds numbers have been reached using wall resolved large eddy simulations (WRLES)[125;126] but the spatial resolution was not enough to investigate the coherent structures down to the buffer region.

The large-scale motions are also used for models of TBL like the vortices and streaks. Falco[117] proposed one of the very first structural model based on observations of the large-scale motions in TBL. The model is based on Reynolds number dependent "typical eddies", and Reynolds number independent large-scale motions both detectable from pictures of smoke. Brown and Thomas[118] found organized structures in the TBL flow at $Re_\theta = 10000$ with the length of 2δ based on wall shear velocity correlations. From PIV measurements in the streamwise wall-normal plane of the TBL flow up to $Re_\theta = 6845$, Adrian *et al.*[77] attributes the origin of LSM to the hairpin vortices packets aligned in streamwise direction by including low-speed regions in between the hairpin legs. Lin[78] built a model of the coherent structures organization in the inner region from spatial correlations analyses.

As mentioned above, Mathis *et al.*[51] have shown that these large-scale structures have an impact on the very near wall statistics starting from the streamwise Reynolds stress associated with the near wall streaks. Thus, LSMs and VLSMs have been interpreted to be responsible for the k_x^{-1} of the streamwise velocity spectrum[127] and thought to be the attached eddies discussed by Townsend[70]. Earlier, Perry *et al.*[72] related the forest of the hairpin vortices to this attached eddies. Baars *et al.*[128] identified universal attached eddies for relatively high Reynolds numbers flows from careful interpretation of coherence spectrogram while emphasizing the need for the unobstructed view of a k_x^{-1} range. Srinath *et al.*[10] proposed a new simple model of streamwise velocity large-scale structures and related this model to the k_x^q (with $q \simeq -1$) streamwise energy spectra in the low wavenumber range. This model relies on a length distribution of the large-scale structures of the fluctuating streamwise velocity with a -2 slope.

Particularly, recent findings on the influence of LSM in near-wall turbulence[129] and the observations of the sinusoidal mode instabilities of the streaks as an initiating mechanism of the LSM in a turbulent channel flow[130] makes the structural definition of the boundary layer more interesting than simple discussion around most energetic turbulent structures. Marusic *et al.*[110] wrote that high energy intensity of LSM suggests that comprehensive knowledge concerning the dynamics of these large energetic structures can help to model and control high Reynolds number wall-bounded flows. The energy transfer within the full boundary layer thickness is affected by the increasing intensity of these structures, Vassilicos *et al.*[131] proposed a modified Townsend-Perry model to obtain prediction varying with distance to the wall accounting for the interactions inside the boundary layer. Such connection between inner-layer turbulence and LSM in outer layer can be easily observed. An example is given in fig. 2.5 for a channel flow at $Re_\tau = 3000$ which shows how the low-speed regions of the flow are connected at different wall distances.

High Reynolds number experimental results of Srinath *et al.*[10] have been related the LSM with a statistical model. Chapter 4 includes the study of the same structures from DNS data at moderate Reynolds number where the k_x^{-1} region is shorter than

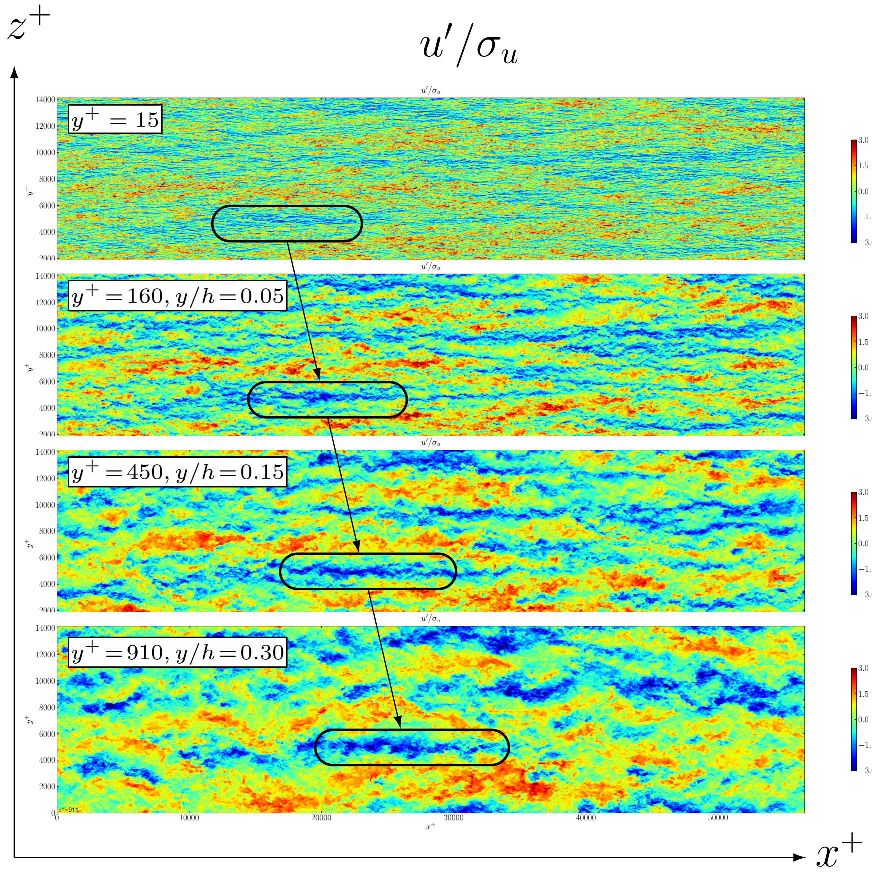

Figure 2.5 – Instantaneous streamwise velocity fluctuation fields at different wall distance from DNS of channel flow at $Re_\tau = 3000$ [*data from L. Thais*]

for the high Reynolds number experimental study. The effect of the lower Reynolds number, as well as the differences between 2D and 3D structure detection procedure, will be discussed. Relationship of these structures with quadrants in the same flow is also going to be investigated to provide a detailed view of spatial self-similarities of the structures in TBL.

2.2.4 Effect of pressure gradient

Studies of wall turbulence subjected to adverse pressure gradient are limited in literature as compared to the studies of wall-bounded flow over a flat plate. Recently, Gungor *et al.*[132] studied quadrants in a DNS of strongly decelerated large-velocity-defect TBL, and observed very large ejections, reaching the streamwise length of 5δ. For example emerging vortices under the effects adverse pressure are also observed by Laval *et al.*[4] in converging diverging channel flow (fig. 2.6). Their results show that presence of APG alters the TBL and the associated structures similar to the other examples in literature[133;134]. These results, like several others, show that the presence of APG significantly modifies the structures and the overall statistical properties of wall turbulence.

Lee and Sung[40] reported that the outer layer structures in APG TBL are more activated than for the ZPG case. The parametric studies were done by Monty *et al.*[135] with increasing β also emphasize that more energetic outer variables are observed with increasing pressure gradient. Laval *et al.*[4] performed a DNS of a turbulent channel flow with lower curved wall at a Reynolds number $Re_\tau \simeq 617$. They also found strong outer peaks in streamwise fluctuating velocity profiles at the adverse pressure gradient regions.

Recently, Lee[46] observed that strength of adverse pressure gradients alters the large-scale structures in log region. Larger structures are shown in mild adverse pressure gradients, however, under stronger pressure gradients, he observed shorter structures as the formation of hairpin packets is suppressed. Under strong adverse pressure gradient, the role of the wall attached structures as main contributors to the turbulence intensities diminishes progressively as well, and they become shorter in the streamwise direction according to Maciel *et al.*[136].

A turbulence regeneration process in the presence of adverse pressure gradient based on instability of low-speed streaks is proposed by Marquillie *et al.*[137] from DNS of converging-diverging turbulent channel flow at moderate Reynolds number. However, Maciel *et al.*[136] reported that in the presence of strong adverse pressure gradient this mechanism is infrequently observed in the TBL suggesting that there should be another mechanism involved under a strong pressure gradient.

In conclusion, there is a tremendous amount of new information gathered in a short period concerning APG TBL flow and it seems like different dynamics of turbulent motions can be expected with the presence of pressure gradient. In chapter 5 new numerical tools will be introduced with the objective to perform DNS of APG TBL with curved walls in order to investigate different configurations of APG flows. Different pressure gradient histories are likely to be another important parameter for the

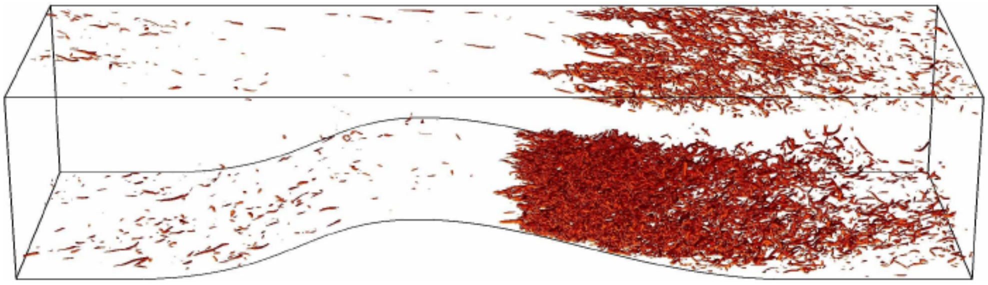

Figure 2.6 – Visualization of strong coherent vortices in the DNS of channel flow at $Re_\tau = 617$. [*Reproduced from* Laval et al.[4]]

turbulence.

Part II

Turbulent Boundary Layer over a Flat Plate

DNS of TBL

3

This chapter is devoted to the description of the DNS of TBL conducted during the current research project. Details of the numerical aspects such as the numerical solver, parameters of the simulation and the validation of the data are reported.

The DNS of TBL was performed with the code Incompact3d[†]. Only the numerical methods which are important for the current study are described in this chapter, but readers interested in the details of the code could refer to Laizet and Lamballais[54] and Laizet and Li[5]. Moreover, further extensions of the code with implicit LES[138] and implementation of immerse boundary method[139] are also available.

3.1 Numerical simulation procedure

Incompact3d is a massively parallelized code written in FORTRAN which solves the incompressible Navier-Stokes equations. Sixth order compact finite difference schemes are used for the spatial discretization and different time schemes are available for temporal discretization (3rd order Adams-Bashforth or 4th order Runge-Kutta). Inflow/outflow, periodic, free-slip or no-slip boundary conditions are implemented. Fractional step method ensures incompressibility condition which requires the solution of a Poisson equation for the pressure. The Poisson equation is solved in spectral space using Fast Fourier Transform routines. Combined with the concept of the modified wavenumbers, this direct technique allows the implementation of the divergence-free condition up to machine accuracy while also supporting the use of a stretched mesh in one direction. A partially staggered mesh is used where the pressure mesh is shifted by a half grid distance from the velocity mesh in each direction. This type of mesh organization leads to more physically realistic pressure fields with no spurious oscillations.

3.1.1 Performance and parallelization

The parallelization of the code is performed using the powerful 2DECOMP&FFT library[‡] based on a 2D domain decomposition strategy (see fig. 3.1) also known as pencil decomposition. This strategy commonly used in spectral codes allows users to efficiently run their simulations on massive supercomputers, despite the expensive

---

[†] https://www.incompact3d.com/
[‡] http://www.2decomp.org

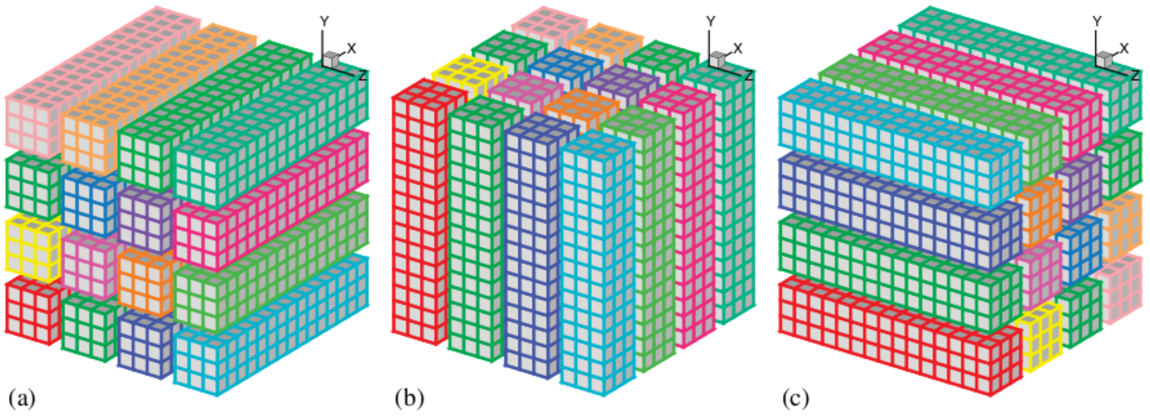

Figure 3.1 – 2D domain decomposition strategy used in Incompact3d. [*Reproduced from Laizet and Li*[5]]

cost of communications (as it requires many global transpose operations performed with the MPI command ALLTOALL to swap from the state a, b and c) as shown in fig. 3.1.

The performance of Incompact3D has been already evaluated on several super-computers including SuperMUC (147 146 cores, 3.185 PFlops) of the Leibniz Supercomputing Center. During previous projects (some of them from PRACE), extensive scalability tests for an extended range of flow configurations have been undertaken by the team developing the code at Imperial College London. The main performance results from Laizet and Li[5] are reproduced in fig. 3.2. Some tests were also conducted in the scope of this study on the French super-computer Occigen of CINES during the present DNS with almost one billion grid points on 2048 cores. In the configuration used in this study, the average performance of the code was estimated to approximately $8\mu s$ per iteration and per grid point on Occigen during the production to runs (including the saving of datasets on disk).

3.1.2 Parallel I/O via netCDF

Imperial College developed some tools that take advantage of the decomposition information available in the library kernel and uses MPI-IO to implement the most frequently used I/O functions for applications based on 3D Cartesian data structures. Despite, the existing parallel I/O routines, new I/O routines based on netCDF4 were also implemented within this project and tested on Occigen with up to 8192 cores.

The use of netCDF format allows the users to connect more easily with post-processing tools already available and developed within this project. Also, the new reading/writing based on netCDF4 uses the *netcdf-open-par* function which was found to be

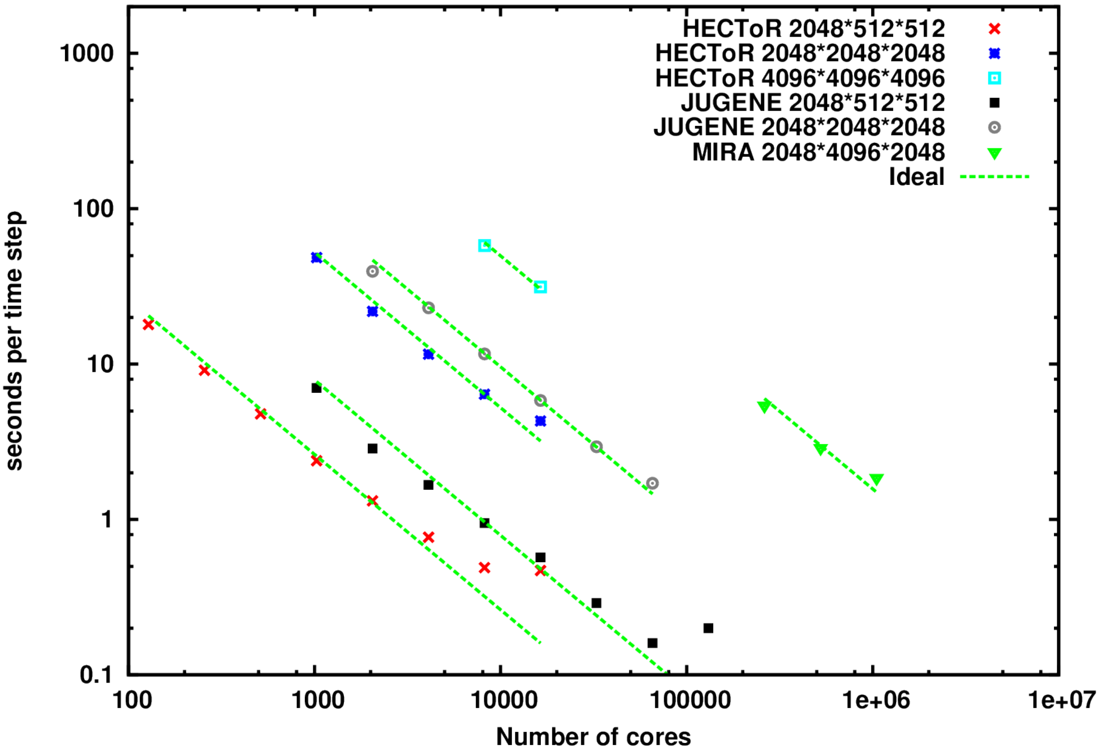

Figure 3.2 – Scalability results of Incompact3d up to 1 Million cores. [*Reproduced from Laizet and Li*[5]]

faster and more stable on OCCIGEN. The *netcdf-open-par* function opens a netCDF-4 dataset for parallel access and collective operations are become the default.

Collective netCDF-4 variables for velocity and pressure fields (all processors must participate) are set to be stored. These routines were used to save both complete 3D fields every few turnover times and 2D planes every 5-time steps. The 3D velocity fields are stored in a single netCDF file with an averaged data transfer of approximating 300Mb/s on Occigen for 3D variables (velocity component and pressure) of $\sim$ 21GB each. The data on the 2D planes were cached in a temporary variable in memory and recorded every 500 iterations only to optimize the performance as saving small variables every 5 time steps can reduce the overall performance of the code.

3.1.3 Tripping mechanism

Different techniques like recirculation[140;141] or volume forcing tripping mechanisms[6] are available to minimize the simulation of the turbulent boundary layer. Wu[142] completed a recent review which includes a comprehensive list of available methods. Additionally, he also investigated the effects of the different transition procedures, on the flow statistics.

One of these methods is to start DNS of TBL with laminar Blasius profiles of streamwise velocity. In this case, an additional mechanism is needed to force the transition to the turbulent state. Aforementioned is often achieved with a local injection of energy into the simulation to trigger the transition. Simulation domain includes the laminar part as well as the transition which contribute significantly to the total cost of the simulation. Transition must be achieved without sacrificing a long simulation domain as opposed to a boundary layer transitioning naturally. Thus, it is worth to focus on the forcing mechanism, not only because of its tied relation to the efficiency of the simulation but also forcing strategy may alter the natural development of the boundary layer undesirably.

In this study, a self-sustaining turbulent regime is initiated with a tripping mechanism as proposed by Schlatter and Örlü[6]. The process consists of tripping the wall-normal momentum equation with a random source term in a limited volume near the lower wall. The effect of this tripping is similar to a sandpaper strip used in experimental studies. The source term is a Gaussian attenuation centered at $x = x_0$ and $y = y_0$. It is active in a region of size l_x and l_y in the streamwise and wall-normal directions respectively while extending on the full span of the simulation domain. The tripping function of the wall-normal component is defined as:

$$\begin{aligned} F_2 &= g(z,t)e^{-[(x-x_0)/l_x]^2-[y-y_0/ly]^2} && (3.1)\\ g(z,t) &= A_f\left[(1-b(t))\,h^i(z)+b(t)\,h^{i+1}(z)\right] && (3.2)\end{aligned}$$

where $g(z,t)$ introduces the temporal and spatial fluctuations $b(t) = 3p^2 - 2p^3, p = t/t_s - i$ and i is the integer value of t/ts.

$h^i(z)$ is defined as Fourier series with random coefficients and phase:

$$h^i(z) = \frac{1}{\sqrt{N_f}}\sum_{j=1}^{N_f}\alpha_j cos\left(\frac{2\pi jz}{L_z}+\phi_j\right) \qquad (3.3)$$

where the N_f is the number of modes included in the signal, α_j is the random amplitude (Schlatter and Örlü[6] uses unit amplitude) and ϕ_j is a random phase shift.

Following the procedure above generates an example of tripping function given in fig. 3.3. Due to the third-order polynomial form of g, the energy spectrum of the tripping $G(f)$ reaches the cutoff length t_s followed by a sharp decrease of the energy.

Tripping is applied in a domain size $l_x = 1.4\delta_o$ and $l_y = 0.35\delta_o$ respectively. The Reynolds number at the tripping position is $Re_\theta \simeq 300$ and the temporal and spanwise cutoff scale of the tripping are set to $t_s = 1.4\delta_o/U_\infty$ and $z_s = 0.6\delta_o$ respectively leading

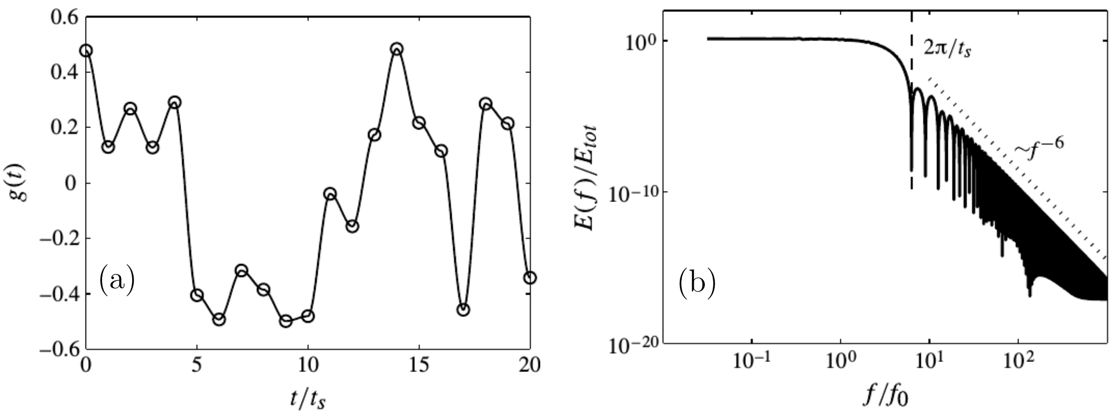

Figure 3.3 – (a) Sample evolution of tripping function g(t) defined by 3.1.3. Symbols indicate the change-over points at times $t = it_s$ for $A_f = 1$ (b) Normalized temporal power spectrum of the tripping amplitude. The cutoff time scale is denoted by $t_s = 1$. [*Reproduced from Schlatter and Örlü*[6]]

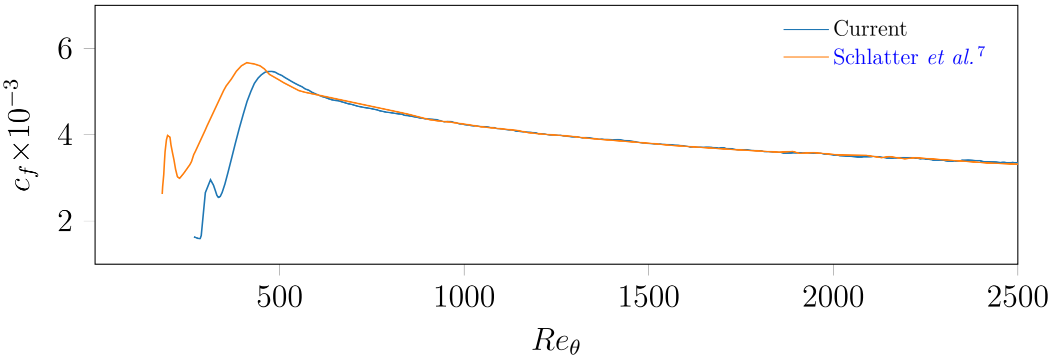

Figure 3.4 – Comparison of the friction coefficient c_f along the streamwise direction. The results are from current DNS and the DNS data of Schlatter *et al.*[7].

to $N_f = L_z/z_s = 33$ exited modes. Amplitude of the forcing is tuned to minimize the overshooting of the resulting friction coefficient c_f (See fig. 3.4) and set to a quarter of the temporal cutoff $A_f = 0.25/t_s \approx 0.178$. If the magnitude of the tripping is adapted to the Reynolds number of the simulation, the source term of the wall-normal velocity equation induces random fluctuations of the flow which lead to an unsteady three-dimensional turbulent regime downstream of the forced position.

3.2 Description of the simulation

The configuration file, controls the various options, used to run the simulation is given in appendix B.

3.2.1 Boundary conditions

The laminar boundary layer profile is used for inlet boundary conditions in streamwise and wall-normal directions. It is calculated by fitting a curve to the Blasius solution's profile at $Re_x = 2000$ with 9th order polynomial function.

$$u|_{x=0} = f_u(y),\ v|_{x=0} = f_v(y),\ w|_{x=0} = 0 \tag{3.4}$$

An advection condition

$$\frac{\partial u_i}{\partial t} + u_c \frac{\partial u_i}{\partial x} = 0 \tag{3.5}$$

is used at the outlet of the simulation domain for all velocity components using the local streamwise velocity $u_c = u(L_x, y, z, t)$ while backflow is avoided by the use of an additional condition to eliminate any possible negative convection velocity. It should be noted that such advection condition can result in a weak acceleration of the flow in the streamwise direction leading to a slightly modified boundary layer profile at the end of the domain.

No-slip and homogeneous Neumann boundary conditions are used for the bottom wall and the upper boundary respectively. However, Dirichlet wall-normal condition $V_\infty\,(Re_x)$ cannot be used for turbulent boundary layer as the value cannot be estimated accurately. Neumann boundary conditions are at least for v and w more appropriate. To summarize, the boundary conditions in the wall-normal direction are given by:

$$\begin{aligned} u|_{y=0} &= 0, & v|_{y=0} &= 0, & w|_{y=0} &= 0 \\ \left.\frac{\partial u}{\partial y}\right|_{y=y_{max}} &= 0, & \left.\frac{\partial v}{\partial y}\right|_{y=y_{max}} &= 0, & \left.\frac{\partial w}{\partial y}\right|_{y=y_{max}} &= 0 \end{aligned} \tag{3.6}$$

where y_{max} has to be sufficiently far from the bottom wall for the boundary condition on the top wall to become sufficiently accurate. The periodic boundary conditions used in the spanwise direction are implemented into the solver by the use of appropriate compact finite difference schemes.

3.2.2 Spatial and temporal discretizations

In the present study, the DNS of a turbulent boundary layer was performed with a domain of size $L_x = 600\delta_o$, $L_y = 40\delta_o$, $L_z = 20\delta_o$. For such large DNS of wall-bounded

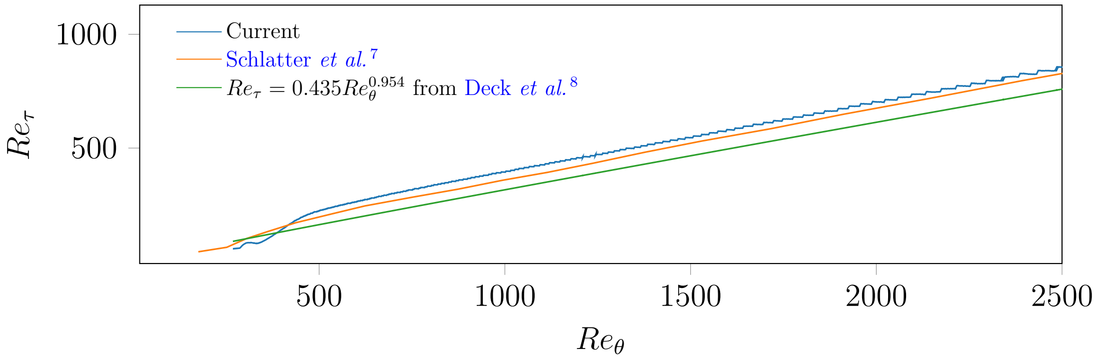

Figure 3.5 – Comparison of the Re_τ as function of Re_θ results from current DNS, the DNS data of Schlatter *et al.*[7] and ZDES data of Deck *et al.*[8].

flow, space and time discretization parameters must be estimated very accurately to obtain correct results with the minimum simulation cost.

The spatial resolution of a DNS of wall-bounded flows is usually estimated in wall units, but the friction velocity cannot be calculated a priory. However, existing experimental data can provide empirical relationships for canonical TBL flows. Particularly, the empirical relationship $Re_\tau = 0.435 Re_\theta^{0.954}$ given by Deck *et al.*[8] was found to be useful in this study to relate the targeted momentum thickness ($Re_\theta = 2500$ at outlet) to the necessary quantities in wall units. This relationship in comparison to the results of the current simulation and the DNS from Schlatter *et al.*[7] is plotted in fig. 3.5.

The second concern related to the spatial discretization is linked to the stability of the simulation. Implicit solvers and 6th order compact finite difference scheme are used in Incompact3d. Both are accurate yet not strongly dissipative. However, a correct DNS requires a very fine resolution at the level of Kolmogorov scale, so dissipative scales will be expected to be well resolved. The recent versions of Incompact3d provide semi-implicit solvers (explicit for streamwise and spanwise directions, implicit in wall-normal direction) different from the early explicit version of the code[54]. Among several available temporal discretization options, 3rd-order Adam-Bashforth is chosen for the current simulation.

Spatial resolution commonly used for DNS of TBL are within the ranges $\Delta x^+ \approx 10-20$, $\Delta y^+_{min} \le 1$, $\Delta z^+ \approx 3-10$[9;35;143]. Further readings like Choi and Moin[144] or Lozano-Durán and Jiménez[75] can be found in the literature for further discussions about the effects of the resolution and simulation size on the results. Laizet and Lamballais[54] proposed a method to use non-homogeneous grid spacing in one direction based on a single analytic stretching function to keep the benefit of the accurate solution of the spectral pressure treatment. This feature will be used in the wall-normal direction. Because of the growth of the boundary layer in the streamwise direction, the grid spacing could be adapted. However, as Incompact3D does not

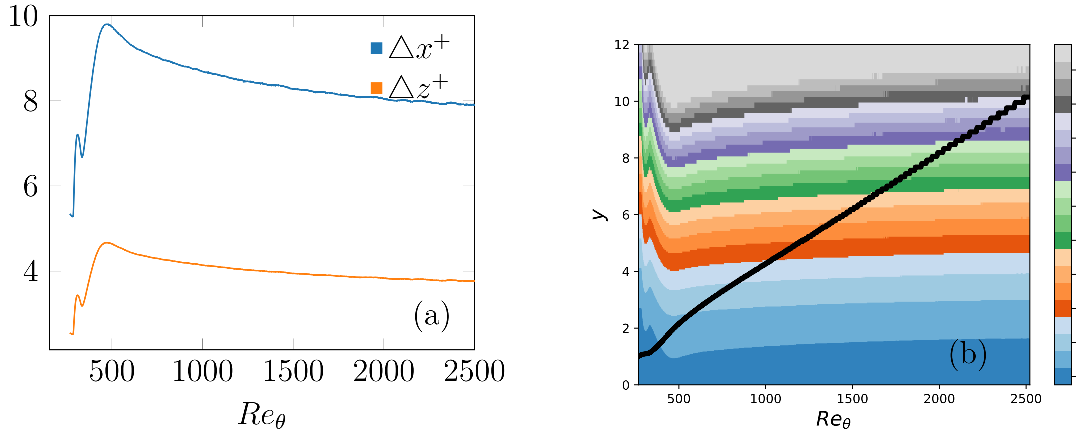

Figure 3.6 – Variation of spatial resolution in streamwise and spanwise directions (a). Variation of the spatial resolution in the wall-normal direction (b). The black line represents the boundary layer thickness δ.

allow such possibility, it is only possible to adapt the spatial resolution for a given streamwise location and therefore a given Reynolds number.

The stretching parameters were adapted to keep the resolution in the wall-normal direction below $y^+ = 15$ over most of the turbulent region up to $Re_\theta \simeq 2000$ which corresponds to the center of the investigated region in the following chapters (see fig. 3.6). The grid spacings in the two other directions are in agreement with the usual practices for the DNS of such flows ($\triangle x^+ \simeq 10$ and $\triangle z^+ \simeq 4.5$) for the most unfavorable position at $Re_\theta \simeq 500$ (at large Reynolds numbers $\triangle x^+ \simeq 8$ and $\triangle z \simeq 4$). The simulation parameters at $Re_\theta = 2068$ are summarized in table 3.1.

Table 3.1 – Parameters of the turbulent boundary layer at $Re_\theta = 2068$ for which the boundary layer thickness δ is equal to $8.46\delta_o$. L_x, L_y and L_z are the sizes of the simulation domain, N_x, N_y, and N_z the corresponding resolution. The reference momentum thickness θ and the friction velocity u_τ are also taken at the same streamwise position.

Re_θ	$(L_x,\, L_y,\, L_z)\,/\delta$	$\Delta x^+,\, \Delta y^+_{min},\, \Delta z^+$	$N_x \times N_y \times N_z$
$250 - 2500$	53.19, 4.72, 2.36	8.27, 1.0, 3.94	$6401 \times 321 \times 448$

A time step $\Delta t = 0.008$ corresponding to a CFL number of the order of 0.1 is set which preserves $t^+ \leq 0.5$ along the streamwise direction. As mentioned above, in Incompact3d, the grid can be only stretched in wall normal direction (constant along the streamwise direction), therefore this simulation has been designed to have a wall-normal resolution such that the first grid point is at $y^+ = 1$ at the streamwise position for which $Re_\theta = 2000$.

3.3 Databases

The simulation on slightly less than one billion grid points was performed on 2048 cores of Intel Xeon E5-2690v3 with multiple executions of 20 hours. In total, 1.3 million CPU hours were used from GENCI allocation on the OCCIGEN super-computer.

Two separate datasets were collected to compute converged statistics on large-scale structures. The first dataset consists of 3D velocity and pressure fields, collected every 500-time steps ($0.0168\,\delta/u_\tau$ based on outlet quantities) for the full simulation domain. For the second dataset, the same quantities were recorded at 4 spanwise-wall normal planes ($Re_\theta = 922$, 1522, 2068 and 2365) every 5-time steps corresponding to a streamwise displacement of half a grid spacing based on the free stream velocity. Details of the time-resolved databases are summarized in section 3.3. The time-resolved datasets will be used for the validation of the Taylor hypothesis and the comparison of spatial-temporal features of the investigated turbulent structures. Also, these last datasets can be used as turbulent inlet conditions for future simulations of the turbulent boundary layers (e.g., TBL with adverse pressure gradient) as the extent of the time-resolved data is enough to conduct new simulations over multiple characteristic times. This is the subject of a new Ph.D. project which started in 2017.

The DNS of turbulent boundary layer was integrated for more than 15 eddy turnover time, $\tau = Tu_\tau/\delta$, based on the boundary layer parameters at 75% of the domain length. However, the results are collected for the last $15Tu_\tau/\delta$ after convergence in order to reach a sufficient number of samples for the analysis of large-scale structures.

In fig. 3.7 development of the turbulent boundary layer along the streamwise direction is visualized by a snapshot of the fluctuating streamwise velocity in a streamwise-normal plane. The analysis of large-scale structures of streamwise velocity fluctuations will be conducted on a domain of 20 local boundary layer thickness centered at $Re_\theta = 2068$ ($0.6L_x < x < 0.9L_x$) extending up to $Re_\theta = 2407$ sufficiently remote from the

Table 3.2 – Parameters of the 2D (spanwise - wall-normal plane) time-resolved database. The boundary layer thickness δ and the friction velocity u_τ are evaluated at the streamwise location x given in fractions of the full domain size L_x. T is the total time over which datasets are collected.

x	Re_θ	Re_τ	δ/δ_o	Tu_τ/δ
$0.25L_x$	924	374	3.98	33.9
$0.50L_x$	1527	552	6.26	20.9
$0.75L_x$	2068	722	8.46	15.0
$0.90L_x$	2371	813	9.58	13.1

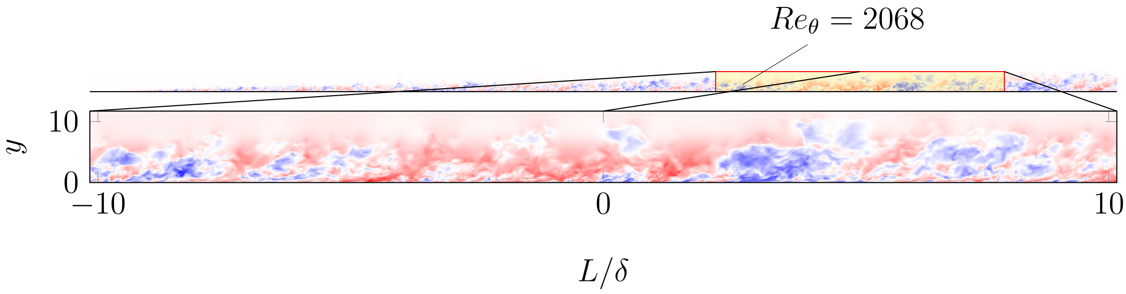

Figure 3.7 – A sample of instantaneous fluctuations of the streamwise velocity

outlet not to affect the statistics. The center of this region ($0.75L_x$) coincides with one of spanwise wall normal plan used to store time-resolved data that will be analyzed in the next chapter.

3.3.1 Validation of the simulation

Parameters concerning the resolution and forcing (see fig. 3.6 and fig. 3.4) of the simulation are designed to satisfy the criteria for high-quality DNS. In order to validate the results of the present simulation mean profiles of the streamwise velocity and the turbulent intensities are compared at 4 Reynolds numbers with the DNS of Jiménez *et al.*[9] and Schlatter *et al.*[7] (see fig. 3.8).

The comparisons are not always at the same Reynolds numbers as indicated in the caption of the related figure. However, slight differences might not be only attributed to the Reynolds number differences. Even for the profiles (green curves) at $Re_\theta \sim 2000$ where the present comparison is the closest among the 3 simulations the matching is not perfect. However, differences are of the same order overall. It suggests that the different spatial resolutions (especially in the outer part of the TBL) as well as different inlet conditions or forcing play a role in the deviation of these profiles.

3.3.2 Energy spectra

In the framework of the Townsend Eddy model, at sufficiently large Reynolds numbers the attached eddies are associated to a k_x^{-1} streamwise energy spectra close to the wall on a limited range of wall distances. Baars *et al.*[128] identified universal attached eddies for relatively high Reynolds numbers from careful interpretation of coherence spectrogram while emphasizing the need for the unobstructed view of a k_x^{-1}. As mentioned earlier, Srinath *et al.*[10] have shown that, even at moderate Reynolds number, a k_x^{-q} slope can be observed in the buffer and mesolayer with increasing value of q such as $q = 1$ is valid only at a specific wall distance between 100 and 200 wall units at

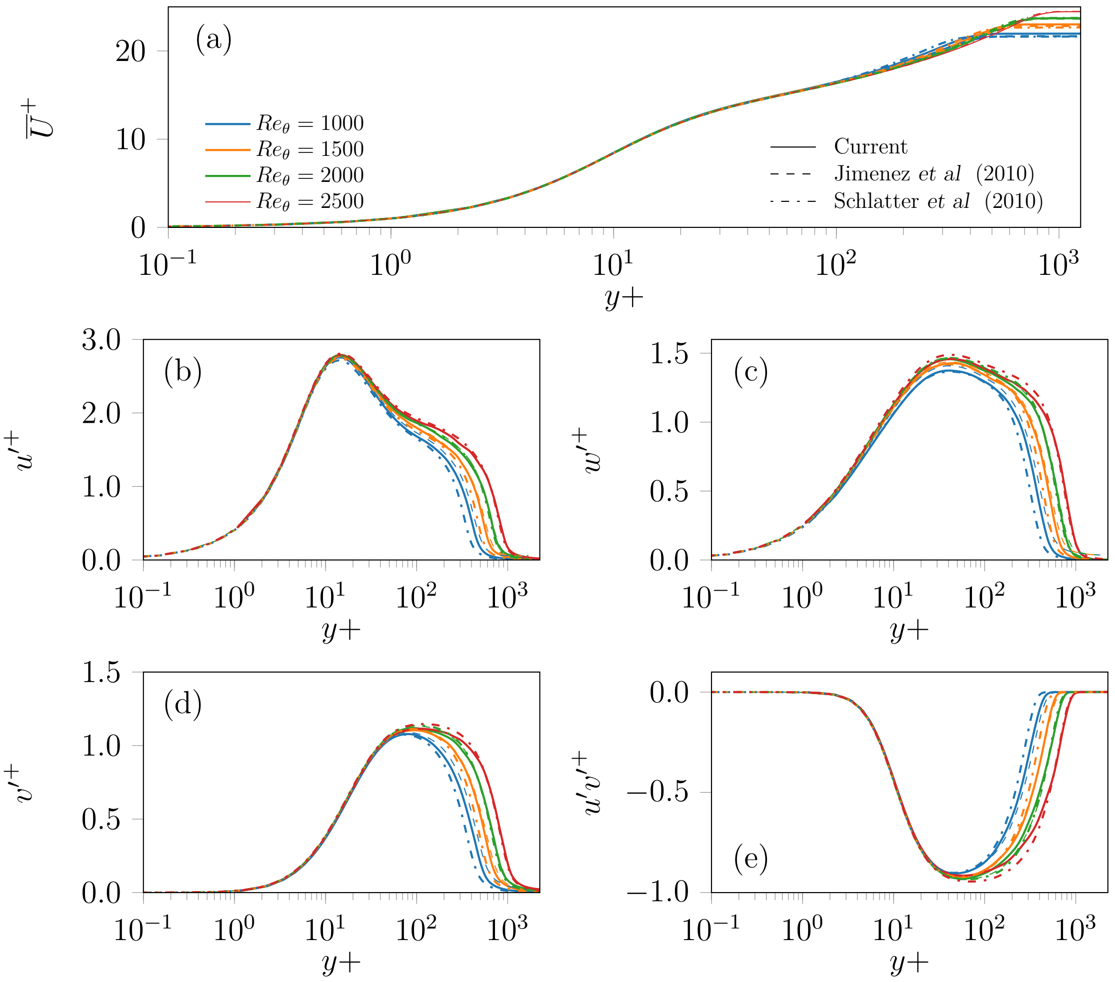

Figure 3.8 – The mean velocity and Reynolds stresses (continuous) profiles of the current study in comparison with profiles from (dashed) Jiménez *et al.*[9] (at $Re_\theta = 1100, 1551, 1968$) and (dash dot) Schlatter *et al.*[7] (at $Re_\theta =$ 1000, 1410, 2000, and 2540).

the investigated Reynolds numbers. The streamwise velocity fluctuations spectra of the present DNS at $Re_\theta = 2068$ are shown in Figure 3.9 for time-resolved and spatial databases. As the Reynolds number is not very high, the k_x^{-q} range is not clearly visible. Nevertheless, the streamwise energy spectrum near $y^+ = 100$ has the most compatible results with a k_x^{-1} scaling. The value of q increases when moving from the wall. However, as the local Reynolds number is $Re_\tau = 722$, the logarithmic region of the mean streamwise velocity profile is short, and $y^+ = 250$ is already located in the wake region.

As both time and space spectra are available at $Re_\theta = 2068$, the validity of the Taylor hypothesis can be evaluated very close to the wall as the two types of spectra are compared in fig. 3.9. They are almost identical above $y^+ = 30$ but start to depart from each other at $y^+ = 30$ indicating the limit of the Taylor hypothesis. Results at the other wall distances exhibit decent agreement for a wide range of wavenumbers (see fig. 3.9). Consequently, the use of Taylor hypothesis is not suitable for the detection of the structures down to the bottom of the buffer region.

It is well known that in the flow regions where shear is dominant (like the near wall region of TBL) Taylor's hypothesis does not hold anymore since local mean velocity is not equal to the convection velocity. Monty and Chong[145] proposed wavelength-dependent convection velocity as a correction to this problem. Extension of this concept was provided by Del Álamo and Jiménez[146] based on the local derivatives of the Fourier coefficients in time or space. They showed that error associated with the use of Taylor's hypothesis at the large scales serves to push energy to the larger scales, leading to an erroneously large-energy amplitude at LSM. Del Álamo and Jiménez[146] believe that it is the reason why Del ÁLamo *et al.*[122]; Morrison *et al.*[147] did not observe a k_x^{-1} region. On the other hand, a different approaches came from Srinath *et al.*[10] who proposed a model with demonstrating a relationship between the k_x^q region of streamwise energy spectra and average streamwise fluctuations of the LSM. The validity of the Taylor hypothesis is important as in the present study a similar analysis will be conducted by detecting LSM from spatial datasets.

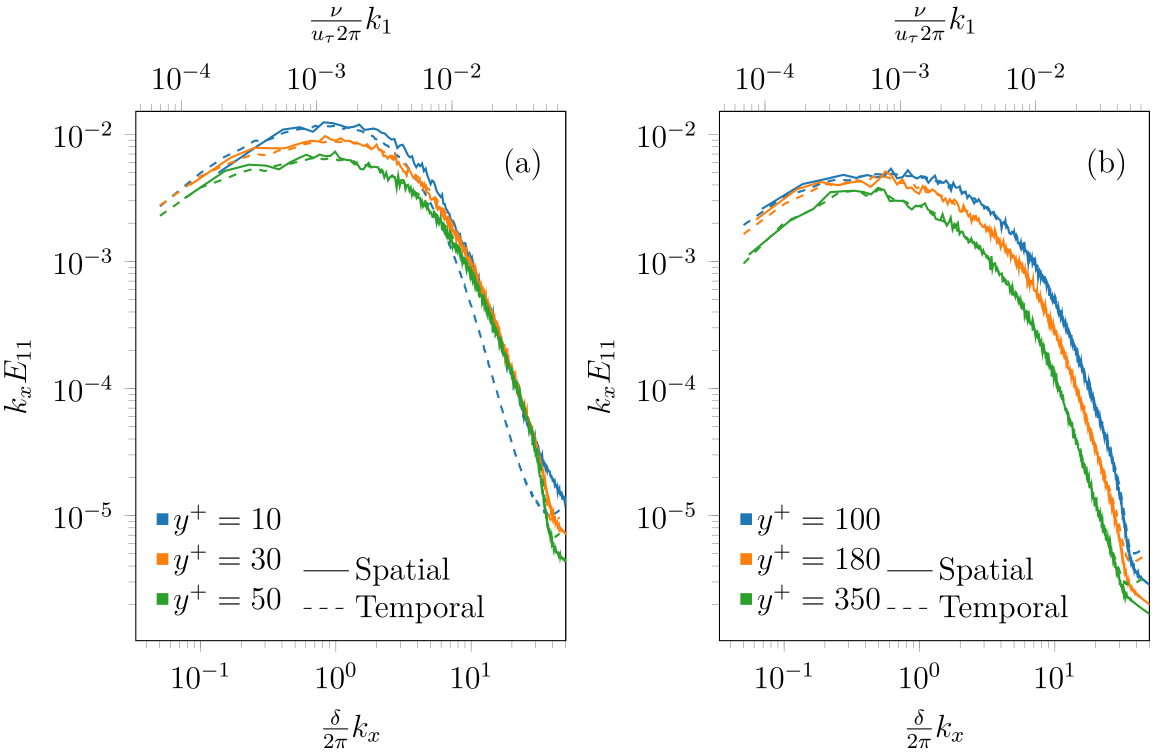

Figure 3.9 – Streamwise energy spectra using spatial (continuous) and temporal (dashed) data at different wall distances. The time spectra are computed at the streamwise position such that $Re_\theta = 2068$ using the Taylor hypothesis and the spatial one are computed in a domain corresponding to $1764 < Re_\theta < 2348$ which corresponds to approximately 20 local boundary layer thickness at $Re_\theta = 2068$.

4

Coherent structures of turbulent boundary layers

The different coherent structures of turbulent boundary layer identified in the literature have been described in the chapter 2. The present analyses will focus on two types of turbulent structures (i) LSM of low and high momentum regions based on the streamwise velocity fluctuations u', (ii) the fluctuating Reynolds shear stress component $u'v'$, decomposed into 4 quadrants, based on the sign of u' and v'. Their large contribution to the streamwise fluctuations in log region makes these energetic regions of the TBL interesting while quadrants are important for turbulent kinetic energy production. It should be noted that these two types of structures might be overlapping and their interaction can help to better understand underlying physics of TBL. This chapter describe the method used to identify these large scale structures and present the statistics of their size and shape.

The large-scale motions and quadrants will be characterized individually by taking the benefit of the 3D database. For both type of the structure considered in the present study, robust definitions are provided alongside their statistics. Different procedures can be used to extract the coherent motions of streamwise velocity fluctuations. For example, Zaki[148] proposed a detection method based on local maximum or minimum of the streamwise velocity fluctuations. However, such method is more adapted to regular streamwise structures. In the present study, we used another method based on simple thresholding of the velocity fluctuations which can be used to extract both LSM and quadrants. The same method was also used to study the time-resolved evolution of quadrants from a DNS of channel flow[50] or to characterize the near wall streaks from PIV databases[79]. Extraction procedure consists of two steps: (i) generation and (ii) labeling of the binary images or volumes. There is no other treatment on the data such as additional filtering or morphological operations except for specific treatments for which this will be indicated.

The analyses of the coherent structures is conducted on a domain of 20 local boundary layer thickness centered at $Re_\theta = 2068$ $(0.6L_x < x < 0.9L_x)$ with an extends up to $Re_\theta = 2407$, a sufficiently far from the outlet not to affect the statistics (See fig. 3.7).

4.1 Large-scale motions

The LSM have been described by several authors to originate from the hairpin packets at the same convective velocity[127]. In this study, the name, LSM only stands for relatively large coherent motions on streamwise fluctuations. It can be considered that the earlier definition is somewhat extended. Part of the LSM detected in this study can be included in hairpin packets, but such question will not be directly addressed. Other research teams have investigated large-scale motions in channel flows[107;149], but not necessarily with the exact same definitions. Relevant details of similar studies were given in section 2.2.3.

The average statistics of the large-scale motions can be evaluated from two-point correlations. Figure 4.1 shows the two-point correlation of the streamwise velocity fluctuations in the streamwise wall-normal plane at three wall distances. Correlation isocontours from 0.1 to 1 with a 0.1 increment are plotted as functions of $(x - x_o)/\delta$ and y/δ where x_o is the streamwise position for which $Re_\theta = 2068$. The spatial correlation extends over a distance of 4δ for all wall distances based on the 0.1 correlation isocontour. Tutkun *et al.*[115] demonstrated similar correlations using data obtained by hot-wire rakes at a much higher Reynolds number ($Re_\theta = 19100$). The correlation isocontours exhibit an ellipse shape with an average inclination function of the altitude of the fixed points from 10° to 20° at $y^+ = 100$ (see fig. 4.15). The overall streamwise extent of the correlation grows with the distance from the wall in the logarithmic region (and also broadens in the wall normal direction) but drops beyond that region in agreement with Ganapathisubramani *et al.*[150]. As stated before, such correlations reflect the averaged length, height and eventually width of streamwise structures if performed in 3D, like in Sillero *et al.*[3]. The extend of the low but significant values of the two-point correlations indicate the average size of the largest structures but nothing about their size distributions.

4.1.1 Detection and definition

As mentioned above, the goal is to study these large-scale structures by detecting them individually in space. In order to fulfill this objective, a methodology based on simple thresholding of the streamwise velocity fluctuations is used. Binary images $\mathbb{B}^{\ominus}$ and $\mathbb{B}^{\oplus}$ indicative of negative and positive streamwise fluctuations are obtained

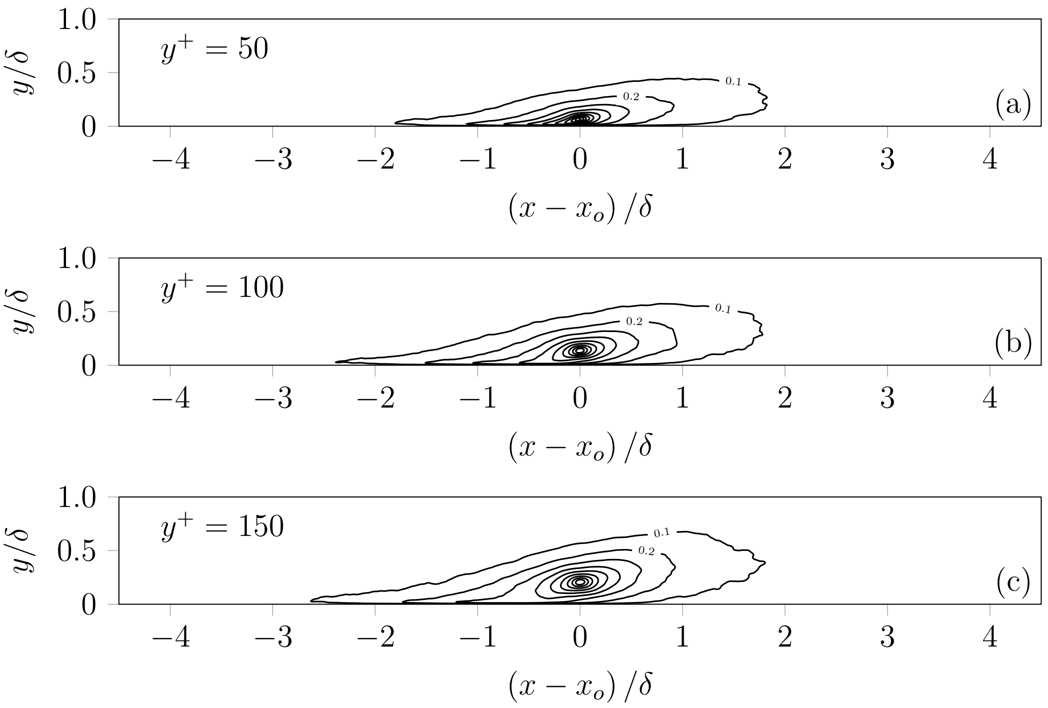

Figure 4.1 – Two-point spatial correlation functions of the streamwise velocity fluctuations $\langle u(x{-}x_o, y{-}y_o)u(x,y)\rangle$ at wall distances (a) $y_o = 50^+$, (b) $y_o = 100^+$ and (c) $y_o = 150^+$ where x_o is the streamwise position such that $Re_\theta = 2068$

respectively by,

$$\mathbb{B}^{\ominus} = \begin{cases} 1 & \text{if } u' < C_{thr}\,\sigma_u^{100^+} \\ 0 & \text{otherwise} \end{cases} \tag{4.1a}$$

$$\mathbb{B}^{\oplus} = \begin{cases} 1 & \text{if } u' > C_{thr}\,\sigma_u^{100^+} \\ 0 & \text{otherwise} \end{cases} \tag{4.1b}$$

where $\sigma_u^{100^+}$ is the standard deviation of the streamwise velocity at $y^+ = 100$, and C_{thr} is the threshold parameter. The second peak (or plateau) of u'^+ at very large Reynolds numbers is the results of the strengthening large-scale streamwise structures[151]. Even though there is no secondary peak at the moderate Reynolds number of the present simulation, $\sigma_u^{100^+}$ gives a good estimation of what would be the intensity of this plateau (or second peak) at much larger Reynolds numbers. Therefore this value can be taken as a reference intensity for the large-scale structures (See fig. 4.2).

An analysis is conducted with three different values of the threshold coefficient C_{thr} (0.5, 1.0 and 1.5) to demonstrate its effect on statistics. Figure 4.3 shows that such detection method retains a significant fraction of the streamwise turbulent kinetic energy while keeping only a small fraction of the total volume. Percentages of the

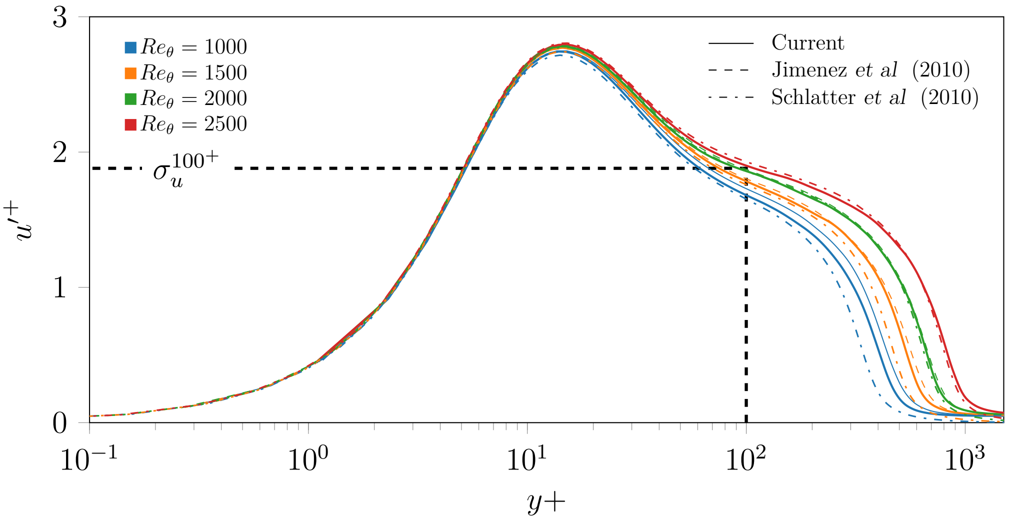

Figure 4.2 – Visualization of the thresholding value over streamwise turbulent fluctuations in wall units as a function y^+ for 4 different Re_θ (1000, 1500, 2000 and 2500)

retained energy, momentum and volume fractions with different thresholds are given in table 4.1.

Table 4.1 – Streamwise energy, momentum and volume fraction (in % of the total) after thresholding for low momentum regions (⊖) and high momentum regions (⊕) extracted using (4.1) and (4.2) as function of the threshold parameter C_{thr}.

	Energy			Momentum			Volume		
C_{thr}	⊖	⊕	⊖ ∪ ⊕	⊖	⊕	⊖ ∪ ⊕	⊖	⊕	⊖ ∪ ⊕
0.5	48%	49%	97%	43%	46%	89%	29%	34%	63%
1.0	39%	41%	80%	29%	32%	61%	15%	17%	32%
1.5	25%	25%	50%	15%	16%	31%	6%	7%	13%

In a second step, binary volumes ($\mathbb{B}^{\ominus}$ or $\mathbb{B}^{\oplus}$) are subjected to the labeling procedure one by one which assigns an index for each structure. Search for simple geometric connection in the orthogonal directions by one grid point is performed like Lozano-Durán and Jiménez[75]. However, the detection procedure generates a large number of small structures which are not the primary interest in this study. Therefore, structures with a total length (λ_x) of less than 0.2 local boundary layer thickness in the streamwise direction are discarded. This procedure is not necessary but reduces the total number of structures to be analyzed significantly without affecting the statistics of the larger ones. This study focuses on the attached structures but the detection procedure based on a threshold of the fluctuating streamwise velocity makes it impossible for a detected structure to touch the wall as fluctuations go to zero at the wall. Hence, all structures with a minimum wall distance larger than 50^+ are also discarded leading to the final definition

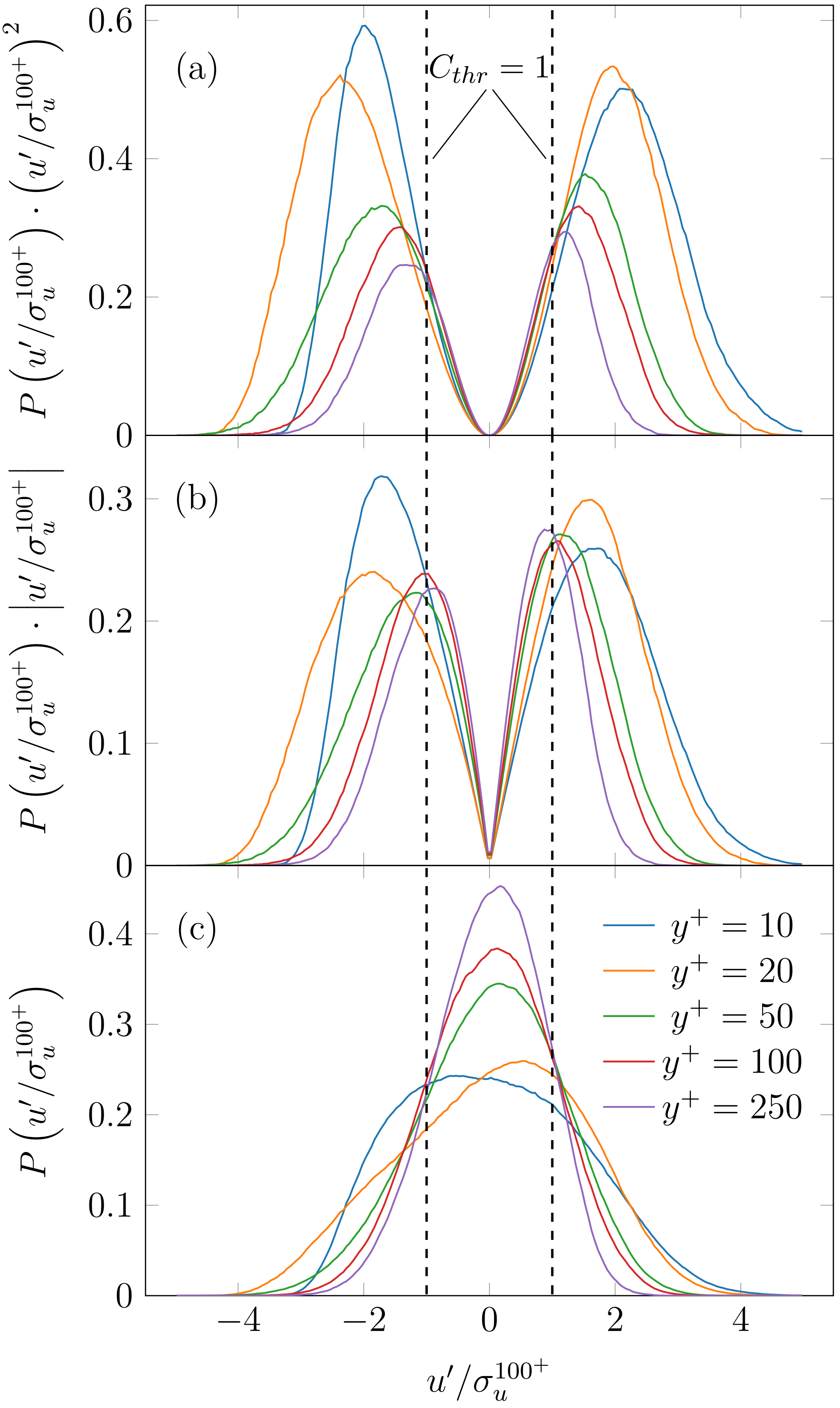

Figure 4.3 – Energy (a), momentum (b) and volume (c) distribution of the streamwise velocity fluctuations. Vertical dashed lines represent the unit threshold coefficient parameter ($C_{thr} = 1$) meaning that outer left and outer right regions will be kept for low and high momentum regions respectively.

$$\mathbb{L} = \begin{cases} 1, \ldots, N & \text{if } \lambda_x > 0.2\delta_{local} \quad \text{and} \quad y_{min} < 50^+ \\ 0 & \text{otherwise} \end{cases} \tag{4.2}$$

where $\mathbb{L}$ is the labeled image which consist of N structures with a unique index i. λ_x and y_{min} are the length and lower bound of the bounding box of the structure i.

Extracting a single scale for complex multi-branch structures is probably not meaningful enough. Therefore, to better characterize their complexity, the skeletons of the structures are also determined. This method simplifies the 3D binary volume of a single structure (individual objects extracted from $\mathbb{B}^{\ominus}$ and $\mathbb{B}^{\oplus}$) to a set of curves using a skeletonization algorithm. The advantage of this simplification is that quantitative statistics of each branch of the skeletons can be extracted. The simplest method, known as "thinning", is able to provide skeletons but the results are very sensitive to the surface smoothness of the volume analyzed. This method leads to very complex skeleton topology which needs to be simplified in order to gather useful statistics. The thinning has been applied successfully for instance by Marquillie *et al.*[137] for the detection of the near wall streaks which are more regular and therefore easier to characterize. The method which has been used in the present analyses is a more robust algorithm for computing continuous, sub-voxel accurate curves from volumetric objects. The basis of the method was developed by Hassouna and Farag[152] and has been adjusted for this work. It can represent a complex structure with a limited number of curves. Unlike other proposed methods to extract turbulent structures, the curves of the skeleton are not necessarily associated with the local maximum of the quantity to analyze (e.g., streamwise fluctuations). The skeletonization only represents the global shape and the geometric complexity of the volumetric structures. One parameter of the method controls the degree of refinement of the skeletons independently from the surface property of the associated volume. The method requires significant computational resources for the extraction of the well-resolved very large structures as several Eikonal equations have to be solved for each of the detected structure.

The skeletonization procedure has been applied to the same 20 local boundary layer thickness long 3D sub-domains centered at $Re_\theta = 2068$. Skeletons are extracted from structures in the binary volume $\mathbb{B}^{\ominus}$ or $\mathbb{B}^{\oplus}$ after the interpolation of the velocity field on a regular isotropic grid with a mesh size of 6.7^+ as the skeletonization procedure used in this study requires an isotropic discretization. Moreover, a weak cleaning procedure composed of opening and closing operations is applied to the binary objects before to apply the skeletonization. The cleaning steps are required to resolve better the small connections between selected regions originally determined by one or two pixels only. A minimum resolution of 3 to 5 pixels is needed to be able to extract a skeleton. When the soft cleaning procedure is not enough, the binary volume is interpolated

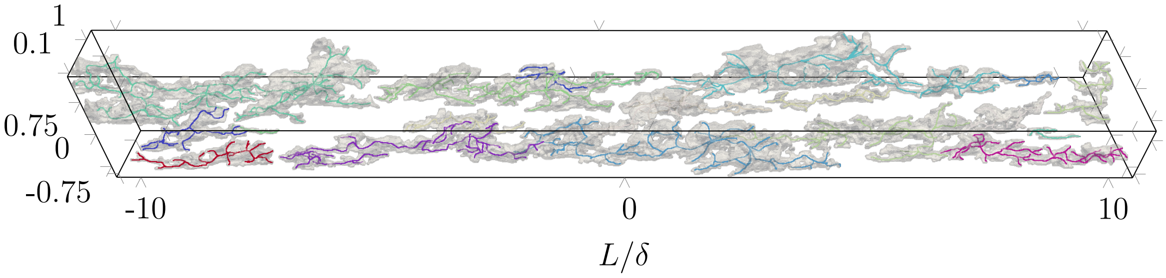

Figure 4.4 – Isovolume of the low speed streamwise fluctuating structures extracted using thresholding (eqs. (4.1) and (4.2)) with $C_{thr} = 1.0$ on a 20δ long sub-domain centered at the Reynolds number $Re_\theta = 2068$. The skeleton of each separated structure are represented with different colors.

on a finer grid to resolve the bottleneck regions adequately. The structures with a streamwise length smaller than 600 wall units or with a volume less than 15000 cubic wall units have been discarded as the aim is to concentrate on the largest structures.

The results of the skeletonization in a sub-domain is shown in Figure 4.4 with the isovolumes of the detected structures. The procedure reflects the complex multi-branch behavior of the detected binary volumes with 1D sub-pixel lines from which we can extract a topology. The same analysis is possible with the classical skeletonization algorithms as thinning which only provides pixelated information. The complex shape of the skeleton is presented in a single structure in Figure 4.5. The curves of the skeletons reveal the meandering nature of the structure in both the spanwise and the normal wall directions. Side view of the single structure with its skeleton shows the complexity of their shape and the difficulty of defining, for example, a single mean angle of a structure.

4.1.2 Two-dimensional and three-dimensional labeling

Once the structures have been detected, various analyses have been used to characterize them. At first, the edges of the smallest cuboid in the three directions (respectively $\lambda_x, \lambda_y, \lambda_z$) that contains a structure are measured. Additionally, the detection procedure was also performed in 2D for each streamwise-normal (XY) plane of the 3D fields to be able to compare the results with similar analysis conducted with PIV data[10]. The very first part of the detection methodology, a simple thresholding, is independent of the number of dimensions of the fields (4.1). On the other hand, the labeling procedure is sensitive to the connections on spanwise direction when applied in 3D. The labeling can be inquired ignoring the spanwise direction connections resulting to the 2D labeling. This type of detection is identical from what can be done with the

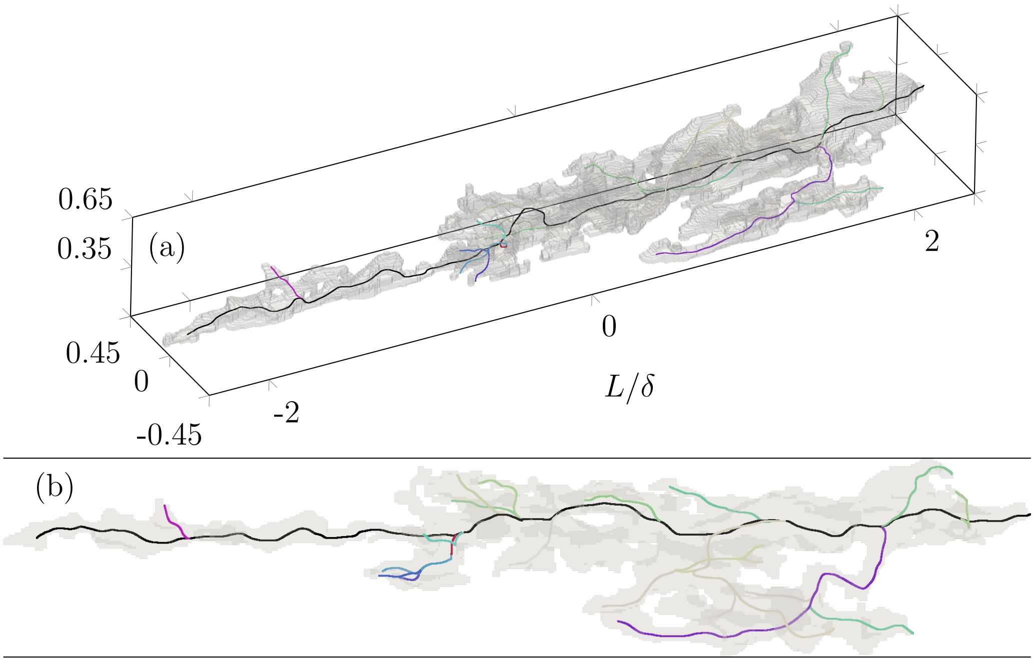

Top View

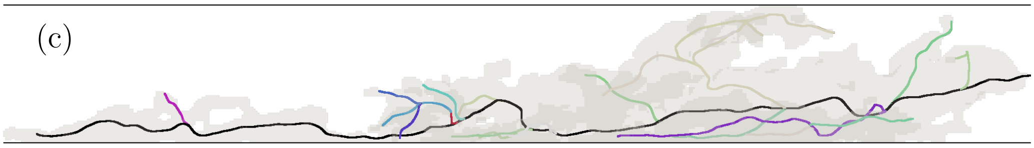

Side View

Figure 4.5 – The skeleton of a single structure. The black curve represents the longest curve (referred as the main curve), and colorful curves are the branches.(a) Isometric, (b) top and (c) side views of the geometry.

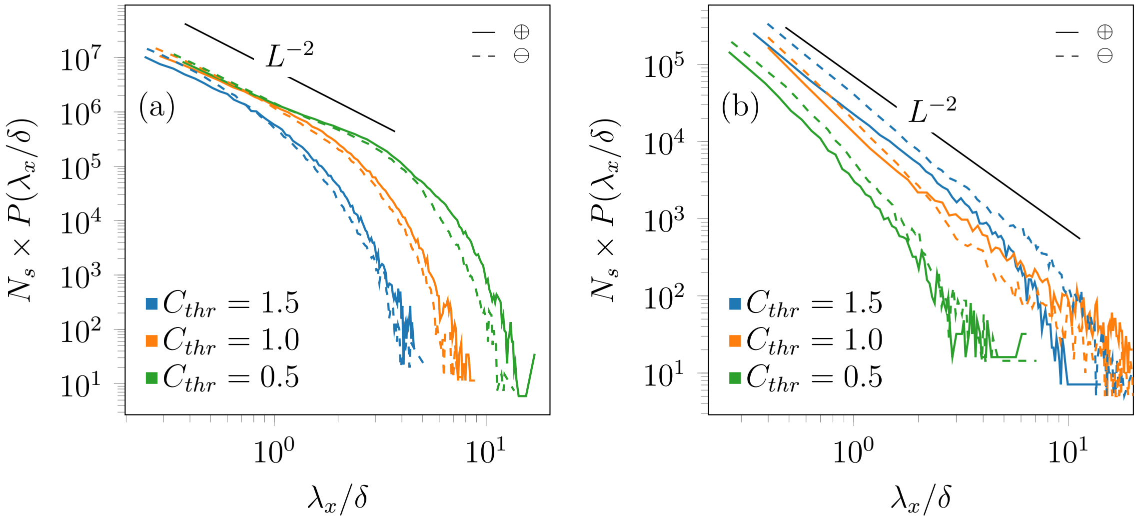

Figure 4.6 – PDF of the streamwise lengths of the detected structures from positive velocity fluctuations (continuous lines) and negative velocity fluctuations (dashed lines) for three different values of the detection threshold. Statistics are results of (a) 2D detection in XY planes and (b) 3D detection.

standard PIV data in the streamwise wall-normal plane. The 2D detection procedure does not allow to capture the complexity of the structure in the spanwise direction and the two methods could lead to some different statistics of the streamwise length as demonstrated by Soria *et al.*[153] for the quadrant analyses.

The probability density functions (PDFs) of the streamwise length premultiplied by the total number of detected structures N_s are shown in fig. 4.6 for the two different detection procedures and the three values of the threshold coefficient C_{thr} given in table 4.1. Multiplication of the PDF with the number of the detected structures is unusual but this way of plotting enlightens the effect of the spanwise connections on the total number of detected structures. The detection of the structures in XY-planes leads to a length distribution λ_x^{-2} for the three tested thresholds. This result is in agreement with the results of Srinath *et al.*[10] extracted from PIV at higher Reynolds numbers. Note that, for the 2D detection, the number of large structures decreases when increasing C_{thr}. Intuitively, increasing threshold results to shorter structures as observed for the structures detected in 2D. However, the results of 3D detection show the opposite. The main reason is that the largest structures are likely to be connected by the side (in the spanwise direction). As the connections in the spanwise direction are taken into account in 3D detection procedure, when the threshold is too low ($C_{thr} = 0.5$), the detection leads to one or few very large structures that cover most of the investigated volume. These structures are larger than the domain of investigation, so they are not taken into account in the statistics of length. This effect explains the smaller number of large structures for $C_{thr} = 0.5$ as compared to $C_{thr} = 1.0$ for which the largest structures start to be disconnected from each other.

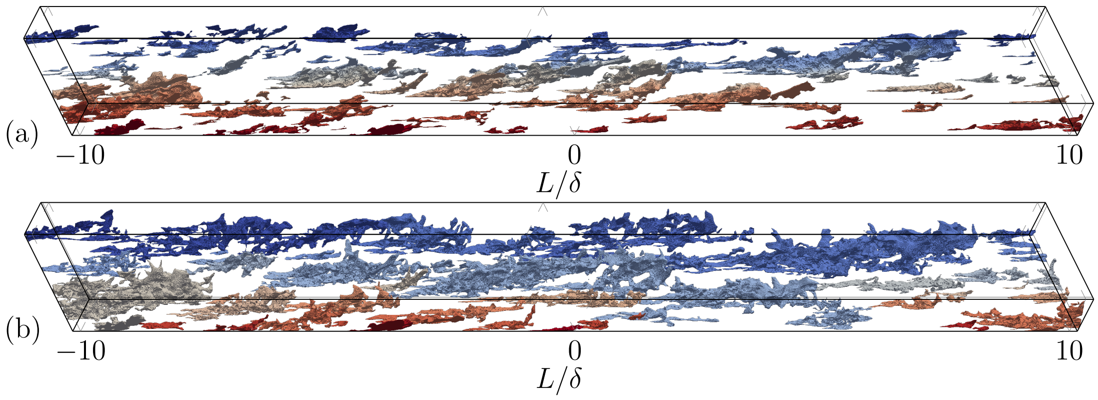

Figure 4.7 – Isovolume of the structures from $\mathbb{B}^{\ominus}$ labeled with 2D (a) and 3D (b) connections. Extraction conducted using thresholding (eqs. (4.1) and (4.2)) with $C_{thr} = 1.0$ on a 20δ long sub-domain centered at the Reynolds number $Re_\theta = 2068$. Each structure (either in 2D or 3D) is plotted with a different color.

The comparison of the 2D and 3D detections shows that considering the most intense structures, the two methods lead to a similar length distribution even if their topology is more complex than simple elongated structures. The detection in 3D fields can be considered as more realistic to measure the real size of the structures as it acknowledges spanwise motions of the structures. The -2 distribution of structure lengths for 3D detected structures is maintained for the larger range of streamwise lengths, even though the theory behind this slope[154] does not consider spanwise connections explicitly.

Spatial heterogeneity of the structures in spanwise direction is shown for a single field in figs. 4.7 and 4.8. These plots address the issues mentioned above and show clearly the effect of 2D observations. Like the results of the bounding boxes, 2D detection results to shorter structures. At first glance, it can be said that 2D labeling procedure leads to the detection of lesser large structures than the 3D one even though the total number of detected structures are much higher. This is result of the combined effect of the cleaning and labeling mechanism. 2D labeling leads to the detection of many small structures which are actually pieces of larger structures but they will be cleaned as they are too small, biasing the statistics for 2D detections. In other words 2D labeling will miss the long structures which have more chances to be connected in the spanwise direction. Therefore, distribution of the length of structures gets biased strongly for the structures with the length λ_x larger than few δ when they are detected in 2D because of the complexity of the structures. This effect is more obvious in fig. 4.8 which is the top-view of fig. 4.7 for a sub-domain. One can imagine the extensions of these structures in the spanwise direction which get cut when 2D labeling procedure is used.

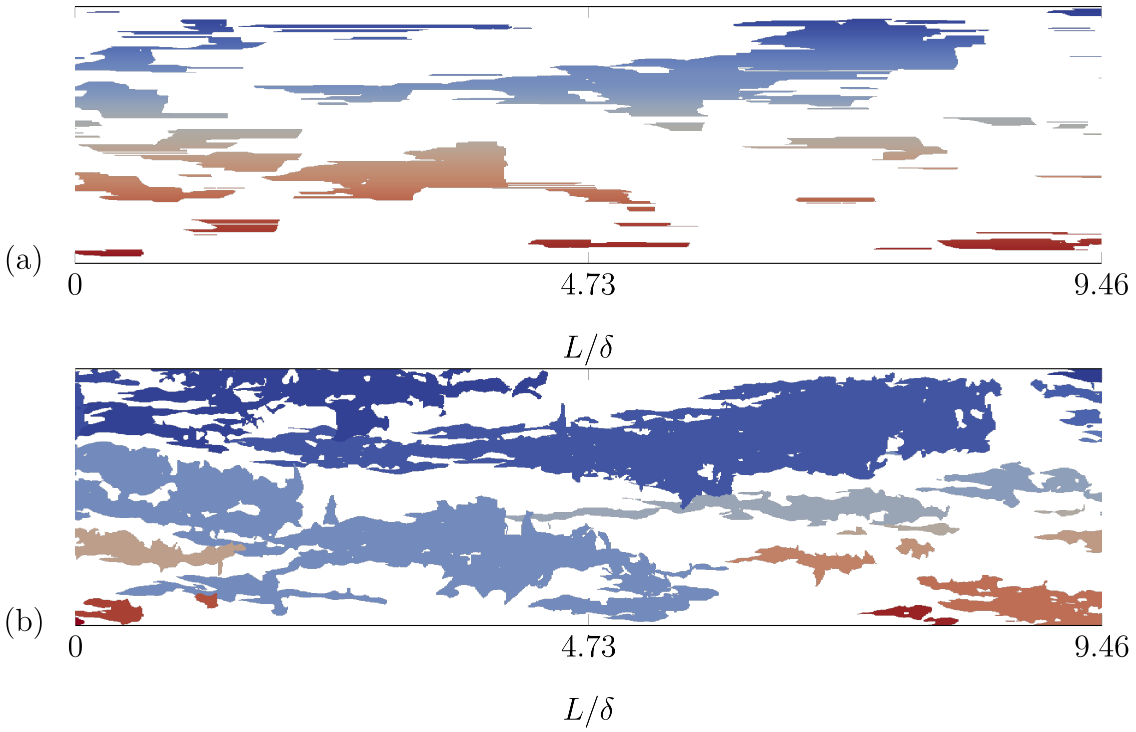

Figure 4.8 – Top-view of the structures from $\mathbb{B}^{\ominus}$ labeled with 2D (a) and 3D (b) connections. Extraction conducted using thresholding (eqs. (4.1) and (4.2)) with $C_{thr} = 1.0$ on a 20δ long sub-domain centered at the Reynolds number $Re_\theta = 2068$. Colors represent label of structures.

The sensitivity analysis of the detected lengths to the threshold coefficient parameter (C_{thr}) has been conducted only for the streamwise length statistics. Unless the results obtained with C_{thr} which are biased by the fact that a single long structure usually fills the domain, the probability of length for the different thresholds are qualitatively similar. Therefore, for the remaining analysis, results are given only for $C_{thr} = 1$.

The present analysis reveals that LSM in streamwise velocity fluctuations are more complex and have more branches than the near wall streaks. They are multi-branch structures somehow connected both from the bottom (via near-wall streaks) and by the sides. Their complex behavior make the 3D detection more suitable to extract useful information and will be investigated further with the help of the skeletons (See section 4.1.4).

The aspect ratios of the attached structures obtained by 3D detection are investigated via joint PDFs of their length $P(\lambda_x/\delta, \lambda_y/\delta)$ and $P(\lambda_x/\delta, \lambda_z/\delta)$ (Figure 4.9). The results show a clear trend for the shape of the detected structures with an average spanwise size around 20% of the streamwise length for both low and high momentum ones and an average height of 10% and 15% of the streamwise length for the low momentum and high momentum structures respectively. However, these trends can only be estimated on one decade of length due to the limited number of very

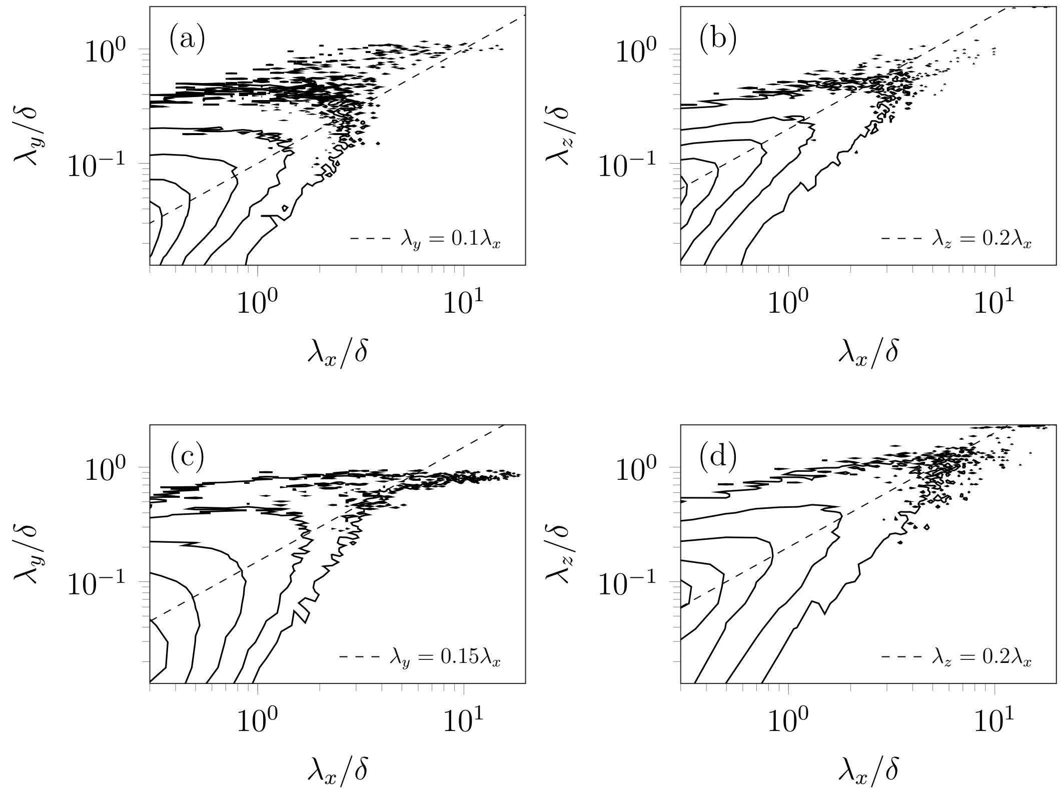

Figure 4.9 – Joint PDFs of streamwise wall-normal sizes $P(\lambda_x/\delta, \lambda_y/\delta)$ and streamwise spanwise size $P(\lambda_x/\delta, \lambda_z/\delta)$ of the detected structures. Areas inside the contour lines correspond to 99%, 90%, 75%, 50% and 25% of the detected structures. An indicative ratio between the two sizes of the joint PDFs are given with dashed lines. Figures (a) and (b) are based on the binary volume $\mathbb{B}^{\ominus}$ while (c) and (d) are based on $\mathbb{B}^{\oplus}$

large structures. The results also indicate that a larger fraction of high momentum structures reaches the top of the boundary layer (see fig. 4.9c).

The PDFs of the lower and upper bound of the LSM are given in fig. 4.10. A very large fraction of the large-scale structures starts very close to the wall as indicated with the strong peak around $y^+ = 50$. The highest starting position for a high speed structures is not more than 0.8δ while low speed structures can start up to $y = \delta$.

4.1.3 Energy contribution of the LSM

Spectral analyses show the energy contribution of the different turbulent scales, but the contribution of coherent structures to the terms of the (2.6) should be one of the first inquiry to understand the real impact of these structures.

The mean profiles of streamwise fluctuations inside the structures are compared to the same quantity for the whole domain to characterize the turbulence statistics of the

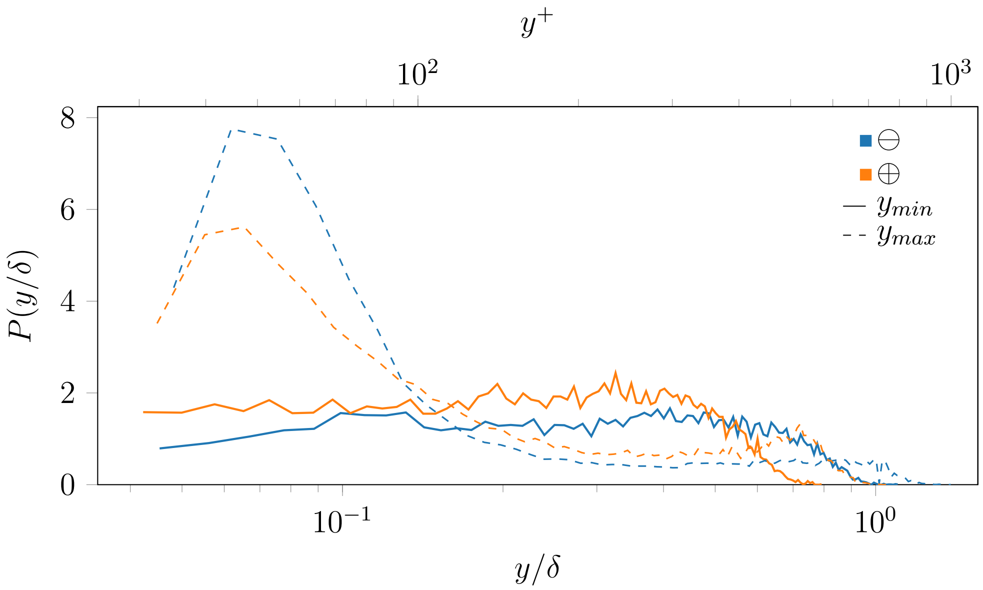

Figure 4.10 – PDF of the lower (y_{min}) and upper (y_{max}) bounds of streamwise fluctuations structures. In this figure statistics for the large-scale motion in streamwise fluctuations includes structures starting above $y^+ = 50$.

detected structures (fig. 4.11). A similar analysis of the content of detected streamwise velocity structures was proposed by Ganapathisubramani *et al.*[52]. However, in their study, the structures were classified by the energy spectrum. The mean profiles for both positive and negative velocity structures exhibit a similar shape than for the whole domain. The streamwise turbulent kinetic energy inside detected structures after cleaning the smallest structures represents approximately 72% of the same quantity for the whole domain suggesting that the contribution of the detached structures is small. Due to our definition of attached structures (with a minimum distance from the wall smaller than 50^+), the profiles including and excluding the detached structures are identical up to 50^+. However, it is shown that the detached structures do not contribute significantly even in the outer region. This result shows that the excluded part is essentially composed of weak fluctuations. It seems that low-speed structures contain more energy than the high-speed ones. Besides, strong positive fluctuations are not reaching the top of the boundary layer, unlike low-speed structures.

The Reynolds shear stress $\overline{u'v'}$ component of the streamwise velocity fluctuation structures is also significant ($\sim$ 72%) and dominated by the attached structures. A more detailed analysis of $u'v'$ will be conducted in section 4.2.

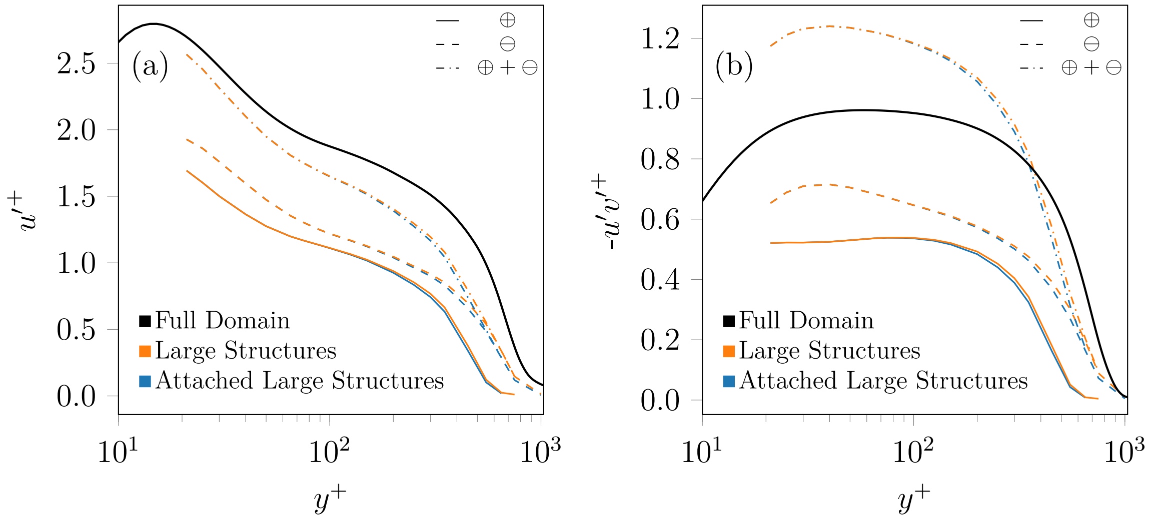

Figure 4.11 – Profiles of streamwise fluctuation (a) and Reynolds shear stress (b) computed from the detected structures with $C_{thr} = 1.0$. Note that, in this figure only, structures not completely included in the 20δ long investigated domain are kept. Statistics are given for $y^+ > 20$ which corresponds to the lower bound of the domain used to detect structures.

4.1.4 Statistics on skeletons

Volumetric detection of the 3D structures, as conducted in the previous subsection, is convenient for statistics based on bounding box and visualization. However, statistics based on the bounding box around these 3D shapes have some limitations, e.g., there is not an accurate way to access angle of these structures. A single line from start to end of the bounding box does not determine a meaningful angle as can be seen from the example in fig. 4.5.

Additional quantitative results of the structures can be extracted from their skeletons. The total length of a structure is computed differently, by extracting the main (longest) curve from its skeleton which is not necessarily aligned with the streamwise direction (unlike the size of the bounding box, λ_x). The PDF of the main curve lengths, $P(\lambda/\delta)$ computed from the skeletons is shown in fig. 4.12 (left). Structures up to $\mathcal{O}(10\delta)$ are detected in agreement with some previous results, and the distribution exhibits the same λ^{-2} slope which is comparable to the statistics computed from the streamwise size of the boxes circumscribing the 3D binary objects.

The complex shape of the long structures can be characterized by counting the number of branches having a significant length. This measure, only accessible from the skeletons, expresses the intricate 3D shape of the structures. The histogram of the number of branches with a length of at least 10% of their main curve for the longest

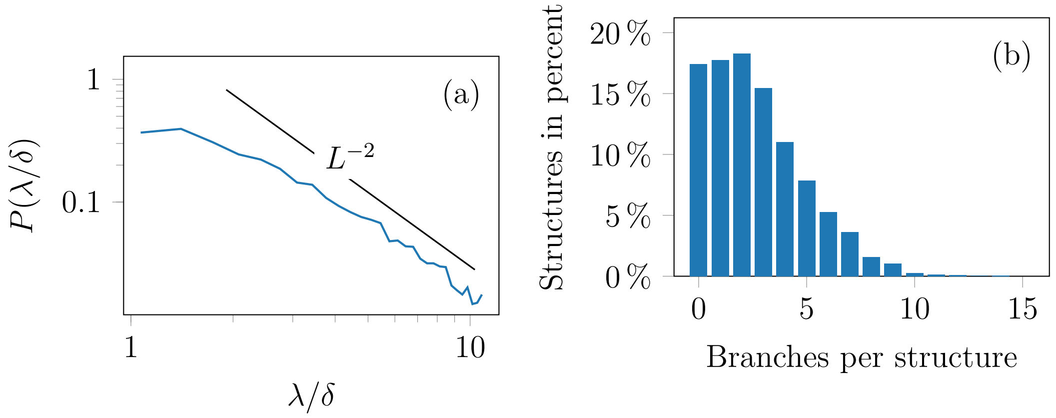

Figure 4.12 – PDF of the structure lengths computed from the main curve of the skeleton, $P(\lambda/\delta)$ (a) and the histogram of the number of branches having a length of at least 10% of its main curve for the structures longer than 4δ (b). The binary structures are extracted by (4.1) with $C_{thr} = 1.0$.

structures (longer than 4δ) is given fig. 4.12 (right). Most of the retained large-scale structures have at least one significant branch and more than 40% of them have even more than 3 significant branches. Such multi-branch structures are difficult to characterize with a single streamwise length and a mean angle with respect to the horizontal plane.

As discussed earlier, the mean angle of the large-scale structures can be estimated from two-point correlations (fig. 4.1). However, two-point correlations are computed with all possible fixed points meaning that they do not only represent the average of the most intense streamwise large-scale structures. Therefore, conditional two-point spatial correlations computed with the fix points inside the detected binary object ($\mathbb{B}^{\ominus}$ and $\mathbb{B}^{\oplus}$) are also provided (fig. 4.13). Longer iso-contours are observed which extend to 7δ using the same normalization $\langle u'u' \rangle (x_o, y_o)$ than the standard two-point correlations (fig. 4.1). These conditioned statistics are more representative of the average shape and size of the most energetic large-scale streamwise structures than the standard correlations.

Analyses based on the jPDFs can be taken one step further. Conditioned two-point correlations of low and high streamwise velocity fluctuations (fig. 4.14) shows differences in height and angle of low and high speed structures. In near-wall region low momentum LSM are shorter but their length become similar increasing the distance to the wall. Additionally, jPDFs of the positive fluctuations display larger upward angles than the structures of the low velocity fluctuations.

An advantage of the skeletons is that the angles along the curves can efficiently be computed for each structure as the curves are defined with sub-pixel accuracy. The skeleton angles are extracted only on the main curves (the black curve in fig. 4.5)

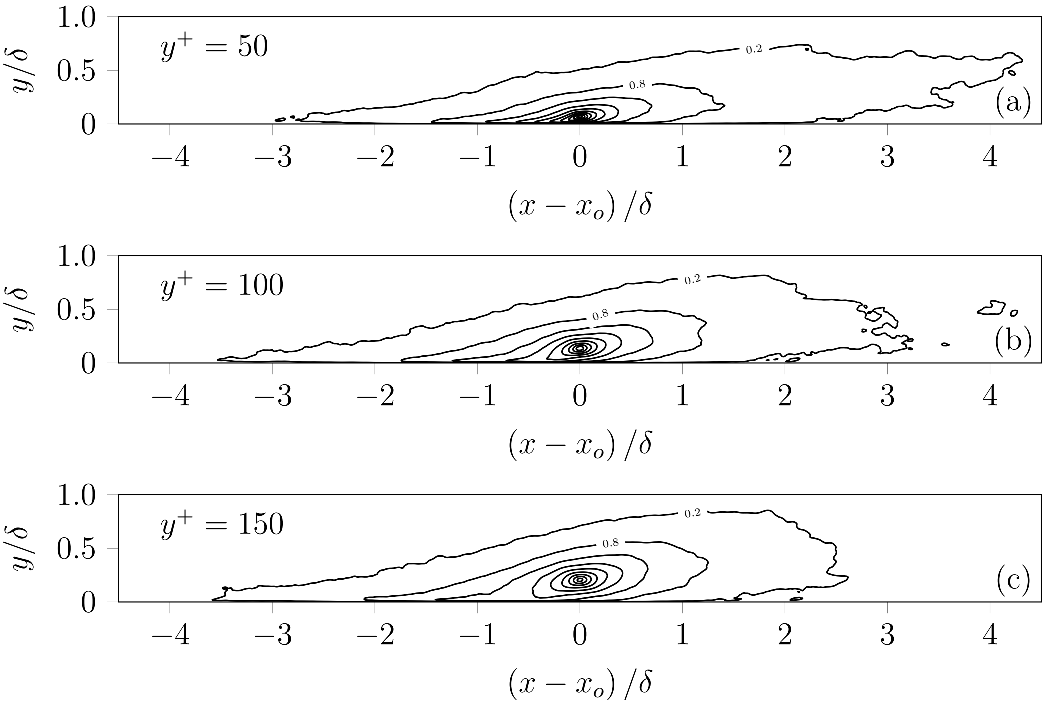

Figure 4.13 – Two-point spatial correlation functions of the streamwise velocity fluctuations $\langle u(x{-}x_o, y{-}y_o)u(x,y)\rangle$ conditioned by $|u(x_o,y_o)| > C_{thr}\sigma_u^{100^+}$ with $C_{thr} = 1$ at wall distances (a) $y_o = 50^+$, (b) $y_o = 100^+$ and (c) $y_o = 150^+$ where x_o is the streamwise position such that $Re_\theta = 2068$

to exclude the statistics of the branches which may have different statistics and a different meaning. The angles of the large structures (with the main curve longer than δ) are defined between the unit vector $\bar{\mathbf{x}}$ and the projections of the displacement vector of two consecutive points of a curve on the XZ-plane (pitch angle, α) and the XY-plane (yaw angle, β). The large tails of the PDF indicate that the main curves move up and down with a large distribution of angles as observed in fig. 4.5 for a single structure. The distribution of the pitch angle (α) is right-skewed, in agreement with the positive average angle seen in two-point spatial correlations. Both angles are widely distributed with no clear preferable values. The peak around very small angles and the short plateau around the small positive value of the distributions are the consequence of irregular oscillations of the skeletons.

The mean pitch angle (α) of the structures is evaluated from their main curves as a function of the wall distance and presented in comparison to the angle extracted from the isocontours of the standard (Figure 4.1) and conditioned (Figure 4.13) two-point correlations. The statistics from skeletons show that the detected large-scale structures of streamwise fluctuations move away from the wall with an average pitch angle of 5°, almost independently from the wall-normal distances (Figure 4.15). The conditional two-point correlations using only extreme streamwise fluctuations offer quite a reasonable estimation of the mean pitch angle (α) while standard two-point

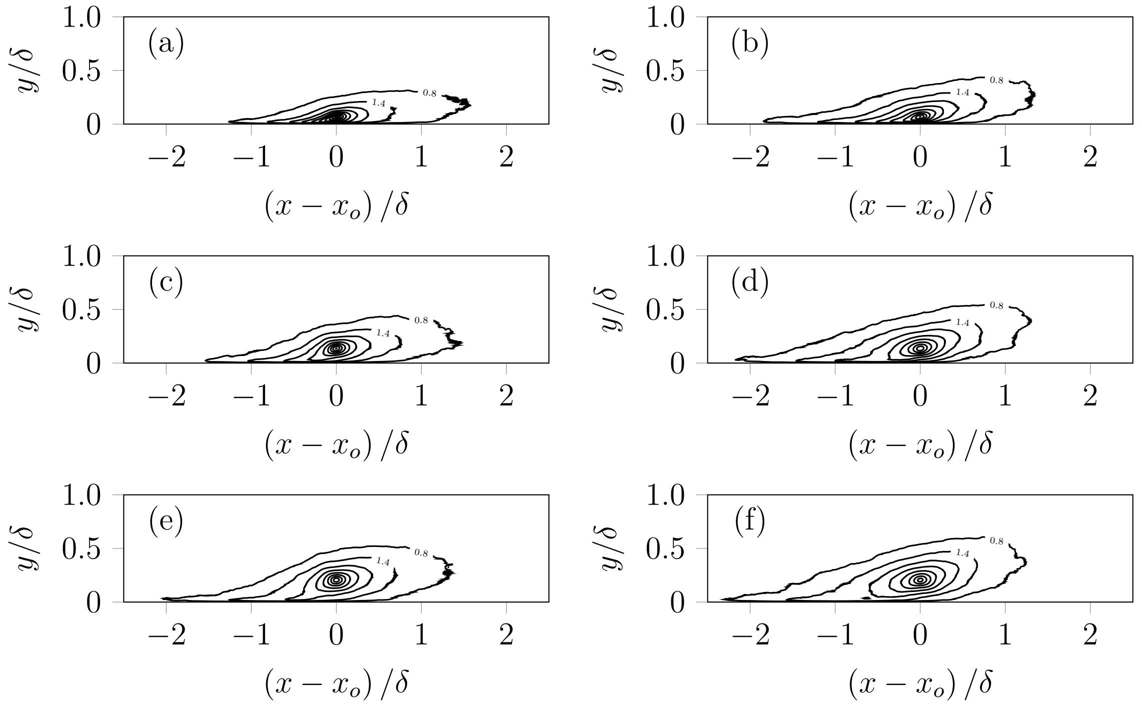

Figure 4.14 – Conditional two-point spatial correlation functions of the low streamwise velocity fluctuations $\langle u(x-x_o, y-y_o)u(x,y)\rangle$ if $u(x_o, y_o) < -C_{thr}\sigma_u^{100^+}$ with $C_{thr} = 1$ at wall distances $y_o = 50^+$ (a), $y_o = 100^+$ (c) and $y_o = 150^+$ (e) where x_o is fixed at $Re_\theta = 2068$. Same conditioned correlations for high streamwise velocity fluctuations, $\langle u(x-x_o, y-y_o)u(x,y)\rangle$ if $u(x_o, y_o) > C_{thr}\sigma_u^{100^+}$ with $C_{thr} = 1$ (b, d, f).

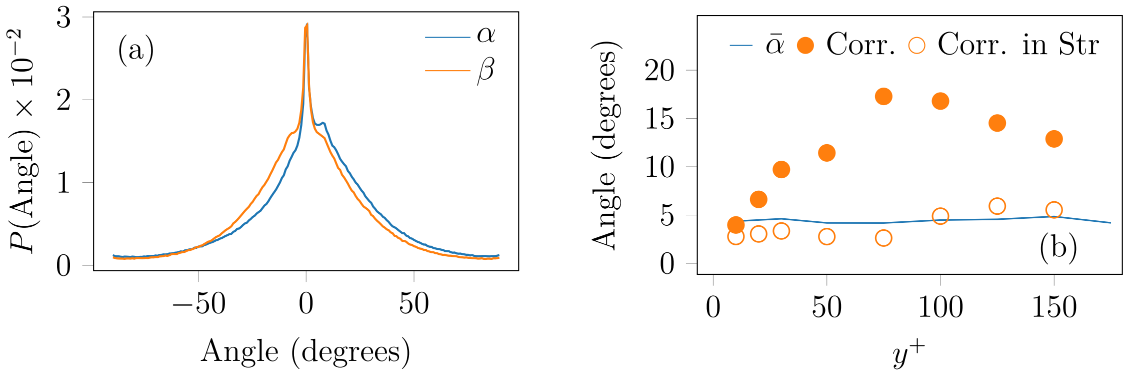

Figure 4.15 – (a) PDFs of the pitch (α) and yaw (β) angles from the main curve of the skeletons. (b) Mean pitch angle (α) as a function of wall distance extracted from skeleton in comparison with the mean angles detected from the two-point spatial correlations functions (Figures 4.1 and 4.13). The mean angle from two-point correlation function the slope of the longest line between the fixed point and the isocontour at the 80% of the fixed point.

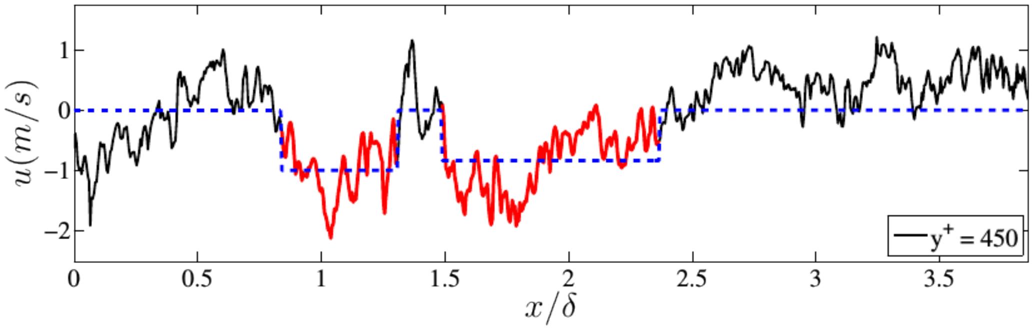

Figure 4.16 – Sketch for the simple on-off model in 1D, similar to the threshold mechanism used in this study. [*Reproduced from Srinath* et al.[10]]

spatial correlations lead to a higher average angle as it includes the information from structures with weak and strong detached fluctuations as well.

4.1.5 Validation of a simplified model for energy spectra

As discussed in the introduction, the LSMs near the wall have been interpreted as being responsible for the k_x^{-q} scaling range with $q \simeq 1$ of the turbulence spectrum. Srinath *et al.*[10] have demonstrated the relationship between the distribution of the structures detected in physical space and Townsend-Perry wavenumber range (also known as k^{-1} range) based on simple on-off model (fig. 4.16). This theoretical model is tested on the detected structures in this study.

Following the analysis of Srinath *et al*[10] on TBL experimental data, the turbulence intensity of the detected streamwise large-scale structures at a certain wall distance is evaluated. The length of the structure in the streamwise direction at a particular

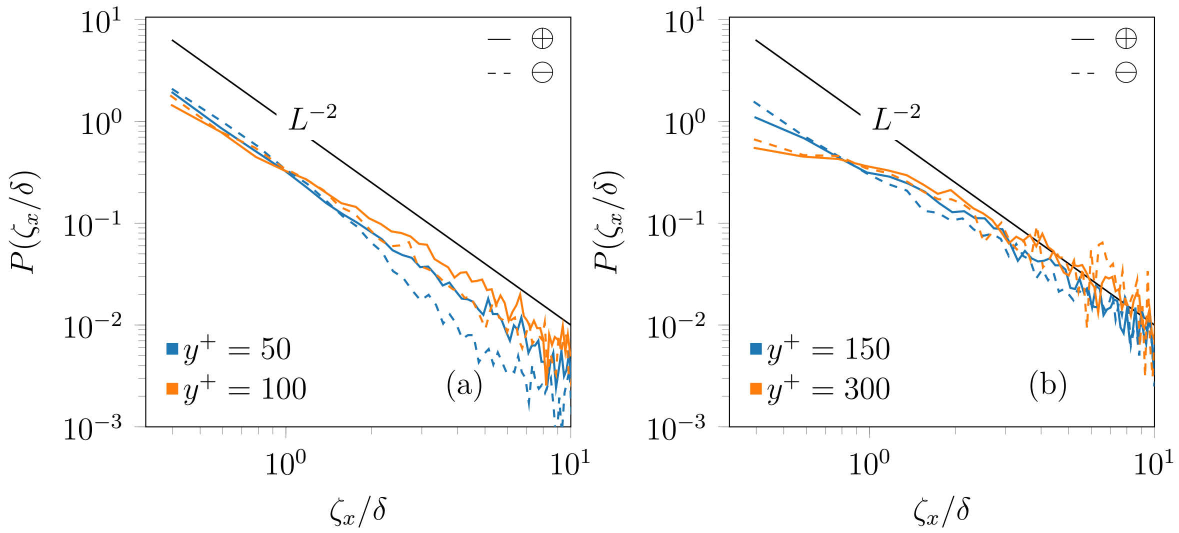

Figure 4.17 – PDF of the structure lengths at particular wall-distances using 3D detection from negative velocity fluctuations (dashed lines) and positive velocity fluctuations (continuous lines) at wall distances $y^+ = 50$, 100 (a) and $y^+ = 150$, 300 (b).

wall distance ζ_x is not necessarily equal to λ_x because structures have irregular shapes and may include holes due to a small region of streamwise fluctuating velocity lower than the selected threshold. Similar to the distribution of λ_x (Figure 4.6), ζ_x also demonstrates a fairly good -2 power law up to $y^+ = 150$ ($\simeq 0.2\delta$) as shown in Figure 4.17.

The fluctuating streamwise velocity averaged inside the detected structures is called $\overline{a^2}$. It has been computed per line of the detected structures in 2D as in the Srinath *et al* [10] while the results from 3D detected structures are also averaged in the spanwise direction. Therefore, the distributions of $\overline{a^2}(\zeta_x)$ at a particular distance from the wall (Figure 4.18) are not exactly the same for the 2D and 3D structures as the structures are not identical.

A ζ_x^p power law fit of $\overline{a^2}$ is evaluated on the same limited range of structure length as in Srinath *et al* [10] (from 0.5δ to 2.5δ) where the energy spectra exhibits a decent k_x^q region (with $q \simeq 1$) and where the distribution of structure lengths follows a -2 power law (Figure 4.17). Srinath *et al* [10] have shown that, for the experimental data at higher Reynolds number, power law exponents p and q are such that $p + q$ is very close to -1. They demonstrated such results for a range of distances from the wall ($y = 50^+$) up to 0.1δ with a special value of $p = 0$ near $y^+ = 150$ leading to an almost perfect k_x^{-1} slope for the streamwise energy spectra at this particular wall distance. In the present study, the q exponent of the streamwise energy spectra is decreasing when moving from the wall but the slope of $\overline{a^2}$ stays fairly constant in the present results as compare to the results of Srinath *et al.*[10]. This can be related to the moderate Reynolds number of the present study as $y^+ = 150$ corresponds to 0.2δ and the relationship $p + q = 1$ has been observed up to 0.1δ on the experimental data. However, the power law fits of both distributions of $\overline{a^2}$ on 2D and 3D detected structures have a small positive exponent $p \simeq 0.1$ at $y^+ = 50$ such as $p+q$ is close to -1. Despite the uncertainties of the fit due to the limited k_x^q range of E_{11} at lower Reynolds number, the present results support the findings of Srinath *et al.*[10].

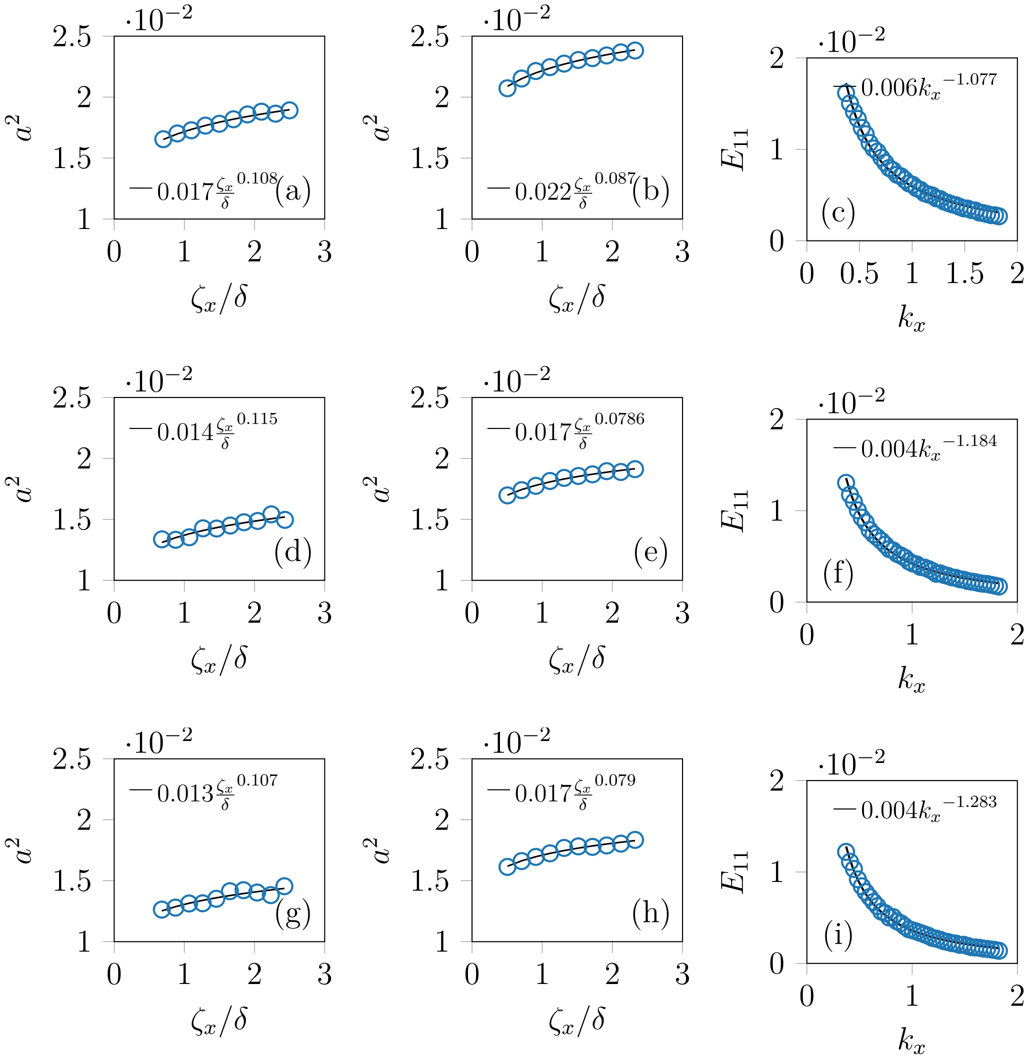

Figure 4.18 – Average mean squared streamwise velocity, $\overline{a^2}$ as function of structure length in 3D structures (a, d, g) and in 2D structures (b, e, h). Streamwise energy spectra (c, f, i) at three wall distances: $y^+ = 50$, 100, 150 (from top to bottom). All statistics are computed for $Re_\theta = 2068$.

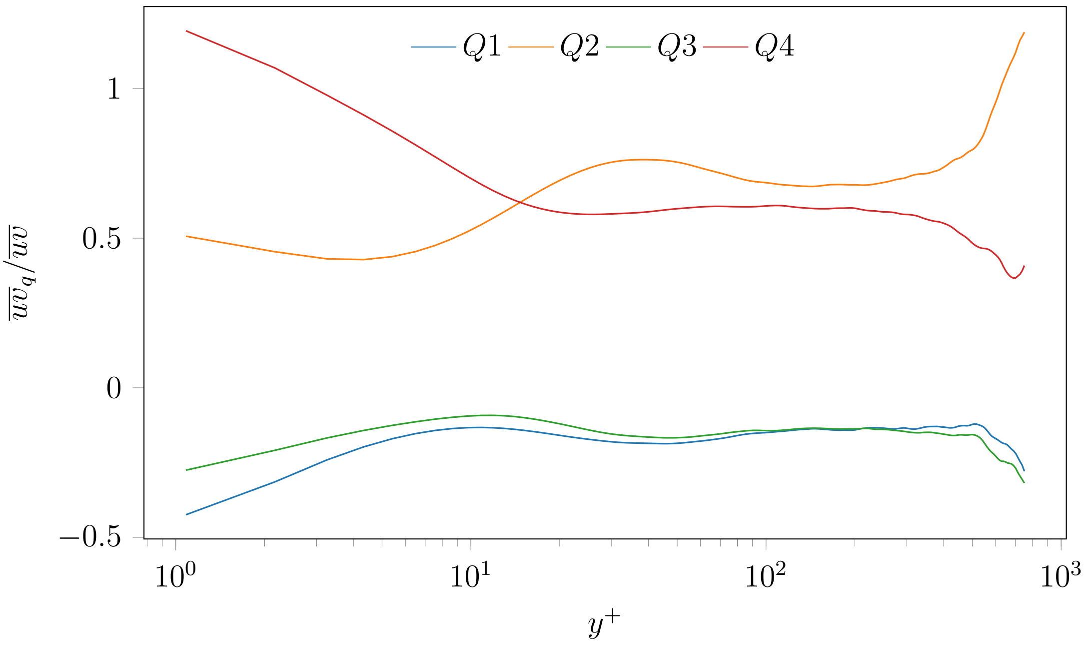

Figure 4.19 – Contribution of the quadrants to the Reynolds shear stress in a turbulent boundary layer at $Re_\theta = 2068$

4.2 Quadrants

Quadrants are also investigated inside the same 3D domains as LSM in the previous section. Quadrant structures have a special role in turbulence modeling because these coherent motions are the components of the Reynolds shear stress. Their contribution to the Reynolds shear stress in turbulent boundary layer are known to vary with the distance to the wall as shown in fig. 4.19 for the current DNS data. Similar results are shown in literature for wall-bounded flows (see i.e., Willmarth and Lu[95]; Wallace[155]). The contribution of $Q1$ and $Q3$ are weak in canonical wall-bounded flows except very close to the wall, while $Q2$ and $Q4$ dominates the RSS. The contribution of ejections ($Q2$) to the Reynolds shear stress exceeds the one of sweeps ($Q4$) at the limit of the viscous sublayer ($y^+ \sim 15$) and become maximum at the bottom of the logarithmic region.

4.2.1 Detection and definitions

In order to complement the statistics of coherent motions in turbulent boundary layers, the detection procedure used for streamwise LSM is applied to the quadrants using a simple threshold procedure. However, binary images $\mathbb{B}_{Q2}$ and $\mathbb{B}_{Q4}$ indicative of sweeps and ejections are obtained with the slightly different criteria.

$$\mathbb{B}_{Q2} = \begin{cases} 1 \text{ if } |uv| < H\, u'_{100+} v'_{100+} \text{ and } 0 < u' \text{ and } 0 > v' \\ 0 \text{ otherwise} \end{cases} \tag{4.3a}$$

$$\mathbb{B}_{Q4} = \begin{cases} 1 \text{ if } |uv| < H\, u'_{100+} v'_{100+} \text{ and } 0 > u' \text{ and } 0 < v' \\ 0 \text{ otherwise} \end{cases} \tag{4.3b}$$

where H is the hyperbolic hole size as defined by Willmarth and Lu[95]. A value of $H = 1.75$ is used in this study following the suggestion of Lozano-Durán *et al.*[1] based on a percolation analysis on a DNS of channel flows at $Re_\tau = 934$ and 2003 (Del ÁLamo *et al.*[122]; Hoyas and Jiménez[156]). Similarly to the detection of the LSM, binary images ($\mathbb{B}_{Q2}$ and $\mathbb{B}_{Q4}$) are obtained either in 2D or in 3D using appropriate labeling procedures.

The same criteria are used to select the quadrants to be retained base on their size and their connection to the wall.

$$\mathbb{L} = \begin{cases} 1, \ldots, N & \text{if } \lambda_x > 0.2\delta_{local} \\ 0 & \text{otherwise} \end{cases} \tag{4.4}$$

where $\mathbb{L}$ and λ_x have the same definition than for the streamwise large scale structures (see eq. (4.2)). There are no criteria for wall attachment in the quadrants' detection as shown in fig. 4.19. However, detailed statistics of the attached quadrant structures can be found in Lozano-Durán *et al.*[1]for turbulent channel flows.

4.2.2 Size and aspect ratio of quadrants

Following the detection procedure described in the previous section, the statistics related to the shape and size of the sweeps and ejections are investigated.

PDFs of the structure lengths are weighted with the number of detected structures to provide an analogy with the previous results of LSM. However, the quadrants statistics are collected for both attached and detached structures without distinctions. Using the definitions (4.3) and (4.4) a slightly larger number of ejections are detected than the sweeps. Similar to the LSM, statistics from 2D detection are biased as the large structures seem shorter. However, the present analysis shows that the structures extracted in 2D are in fact much shorter unlike what has been observed for the LSM. The reasons is that quadrants are not elongated in the streamwise direction, unlike

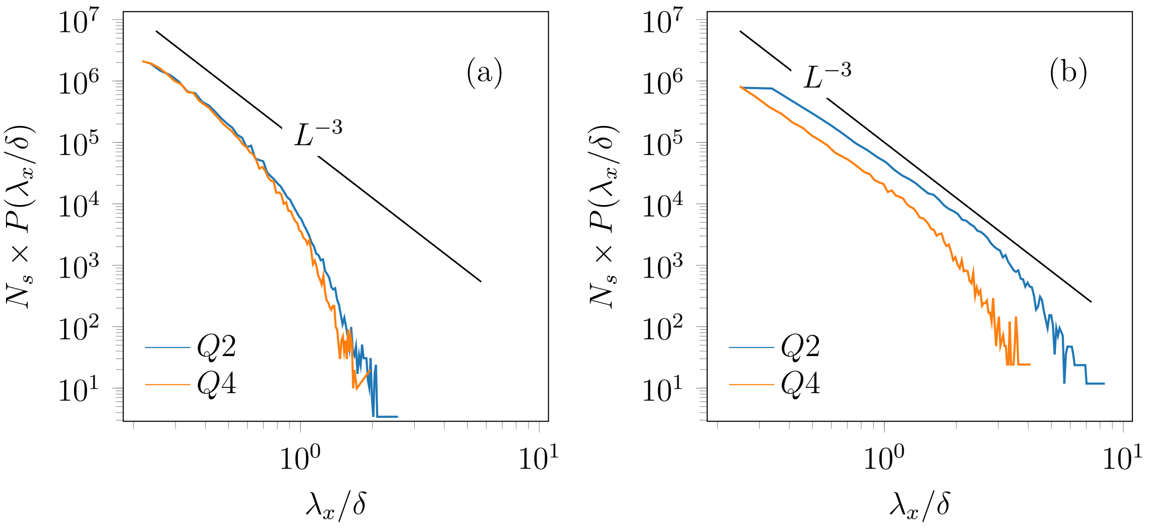

Figure 4.20 – PDF of quadrants length for the detection threshold $C_{thr} = 1.75$ defined in (4.3). Statistics from 2D detection in XY planes (a) and from 3D detection (b).

LSM. Therefore, spanwise connections are probably more important for the quadrant structures. Additionally, 3D detection reveals that there are longer $Q4$ events than the $Q2$ events but this effect is not visible on the 2D analysis. The distribution of the length of these structures is around -3 (fig. 4.20), but from the best author's knowledge there is no theory related to this slope.

In order to compare with LSM (fig. 4.17), quadrant lengths at different wall distance are plotted in fig. 4.21. A significant range of length with -2 power law is observed, especially for the short $Q4$ structures. Longer quadrants might be following a -4 slope, but the limited range of length as well as the level of convergence are too low to be affirmative.

After the analysis of their length, the aspect ratio of the the ejections and sweeps extracted in 3D are investigated. The structure sizes are defined as the one of the cuboid including the structures like for the study of LSM. Figure 4.22 shows the joint PDFs, $P(\lambda_x/\delta, \lambda_y/\delta)$ and $P(\lambda_x/\delta, \lambda_z/\delta)$ of the ejections and sweeps. The results show that ejections are shorter and thinner than the sweeps. The spanwise length of ejections is smaller per unit streamwise length than for sweeps, but sweeps do not get longer than 2δ whereas ejections can become slightly longer. Additionally, ejections can reach a wall-normal size up to δ while sweeps stop around 0.8δ. Similar results were found by Lozano-Durán *et al.*[1], in Figure 5 of their work, for attached quadrants in channel flows. The authors suggest very similar constant length ratio as $\lambda_x \approx 3\lambda_y$ and $\lambda_z \approx 1.5\lambda_y$ for unconditioned $Q2$ and $Q4$ events.

The PDF of the lower and upper bound of the quadrants is given in fig. 4.23 similarly

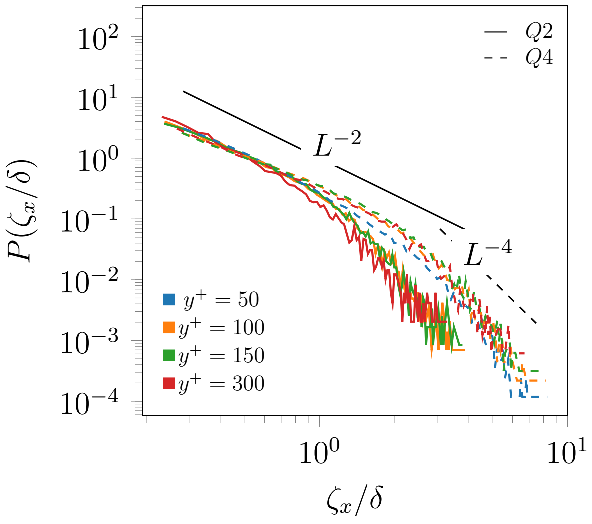

Figure 4.21 – PDF of quadrant structure lengths at different wall-distances for the structures extracted in 3D. Statistics for $Q2$ and $Q4$ are plotted with dashed and continuous lines respectively.

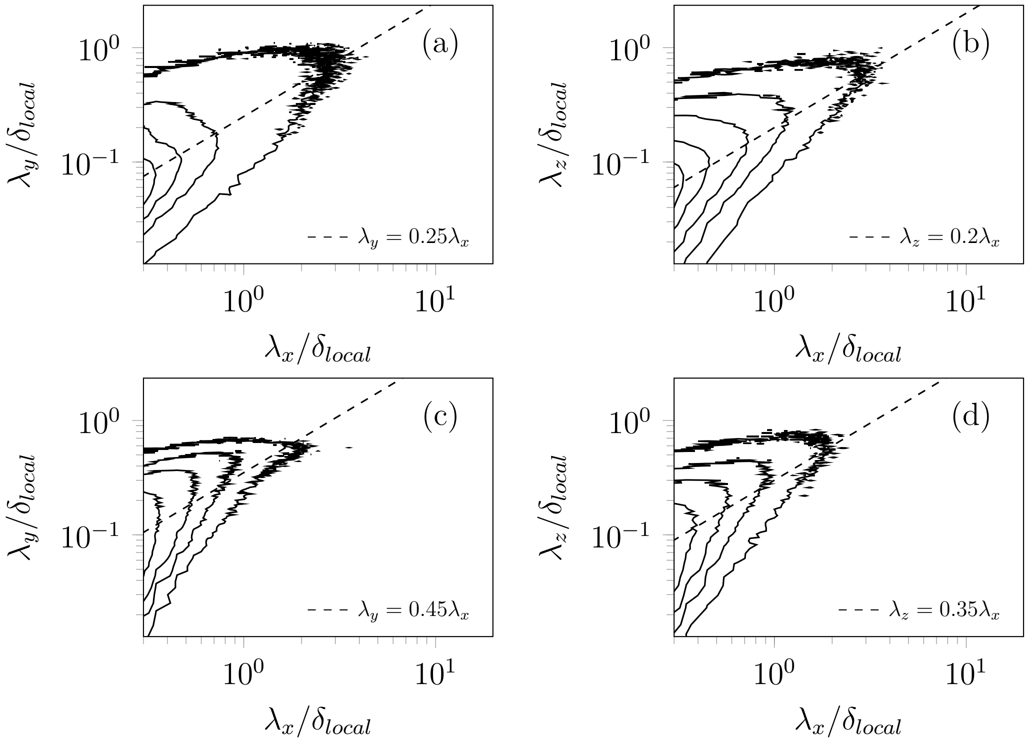

Figure 4.22 – Joint PDFs of streamwise-wall normal lengths (a, c) and streamwise-spanwise lengths (b, d) for ejections (a, b) and sweeps (c, d). Area inside the contour lines correspond to 99%, 90%, 75%, 50% and 25% of the detected structures. An indicative ratio between the two sizes is given with dashed lines.

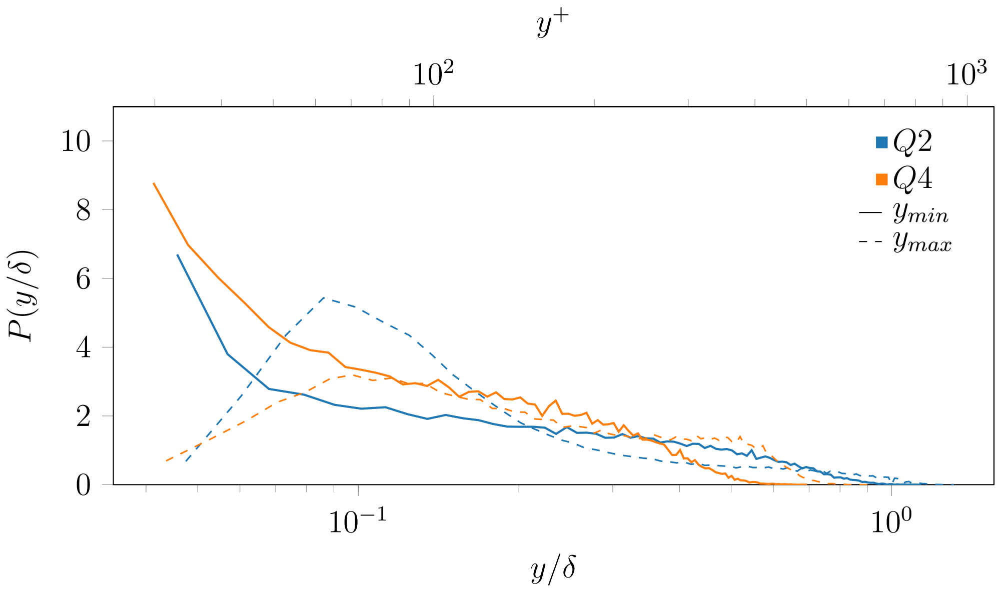

Figure 4.23 – PDF of the lower (y_{min}) and upper (y_{max}) bounds of quadrant structures. Statistics includes structures starting above $y^+ = 50$.

to the fig. 4.10 for the LSM. Quadrants structures starts much closer to the wall, and $Q2$ structures can start as high as δ. Even though the top of $Q2$ structures (ejection) can reach over δ, most of them only reach 0.1δ. Overall, $Q4$ structures remain shorter than the $Q2$ structures.

4.2.3 RSS contribution of the quadrants

As discussed in chapter 2, the quadrant statistics have been investigated by many authors. The aim of the present study is not only to provide a detailed description of these structures but also to quantify their contribution to the Reynolds shear stress and to relate them to the detected LSM of streamwise fluctuating velocity.

Thus, similar to the decomposition of the LSM, the contribution of the quadrants to the turbulence fluctuation profiles are given in fig. 4.24. This statistics can be related to the one presented in fig. 4.11. The difference between the two analyses is that the decomposition of the Reynolds shear stress as the results from LSM was signed sum, but the quadrants are already decomposed according to the sign of u'. The contribution from $Q1$ and $Q3$ are left out completely, and the sign of all 4 quadrants can be considered explicitly. For example, the sum of the integrals of $Q2$ and $Q4$ (119% of $\int_{y_{min}}^{y_{max}} \overline{uv}$) is larger than Reynolds stress profile as the contribution of the $Q1$ and $Q3$ will have opposite sign (see fig. 4.24 (a)). An example of isovolume of $Q4$ and $Q2$ structures detected in 3D is given in fig. 4.27. The very-large-scale structures seems qualitatively similar but medium scale $Q2$ structures are more numerous and more

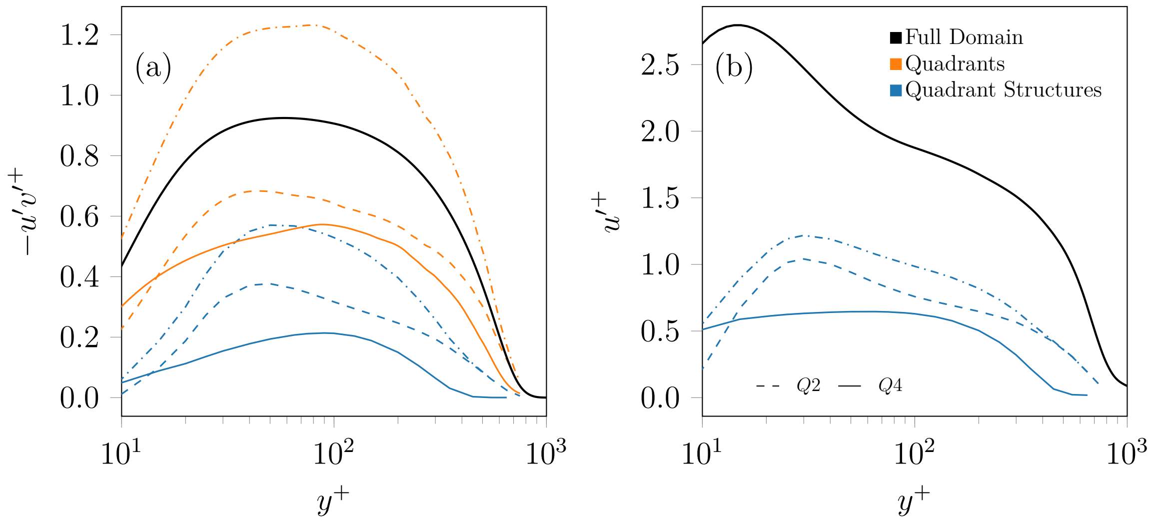

Figure 4.24 – Reynolds shear stress (a) and streamwise fluctuation profiles (b) computed from the detected quadrant structures with $H = 1.75$. Statistics are given for $y^+ > 20$ which corresponds to the lower bound of the detection domain.

elongated in streamwise direction than the $Q4$ ones confirming the findings shown in fig. 4.24 (b).

The streamwise turbulent kinetic energy contribution of ejection ($Q2$) and quadrant ($Q4$) structures exhibit couple of differences as function of wall distances (see fig. 4.24 (b)). $Q4$ structures contain an equally distributed amount of streamwise fluctuations. However, the profile for the $Q2$ structures resembles u'^+ profile with weakly pronounced inner peak. This peak at a wall distance slightly higher than the first peak of the streamwise velocity fluctuations meaning that the detected $Q2$ structures have the strongest streamwise component located just above the near wall low speed streaks.

The mean streamwise fluctuation inside the $Q2$ and $Q4$ quadrant structures are only 34% and 19% of the total u'^+ respectively. Note, that the fraction of the $\overline{uv}_q$ fluctuations inside the detected structures of $Q2$ and $Q4$ are 45% and 23% respectively (fig. 4.25). So, even though quadrants corresponds to the large part of the RSS, quadrant structures detected in represents only a part of it. Neither $Q2$ or $Q4$ structures seems to dominate the Reynolds shear stress in the near-wall region, but, they still have a significant correlation with the LSM (see fig. 4.24).

Conditional two-point correlations of LSM with an additional condition based on the quadrants $Q2$ or $Q4$ is given in fig. 4.26 to visualize this correlation in more detail. In other words, only the most energetic parts of the streamwise fluctuations which are also detected as strong quadrant motions are kept. It can be quickly spotted that $Q4$ spread inside the high-velocity structures more widely. These correlations are not as

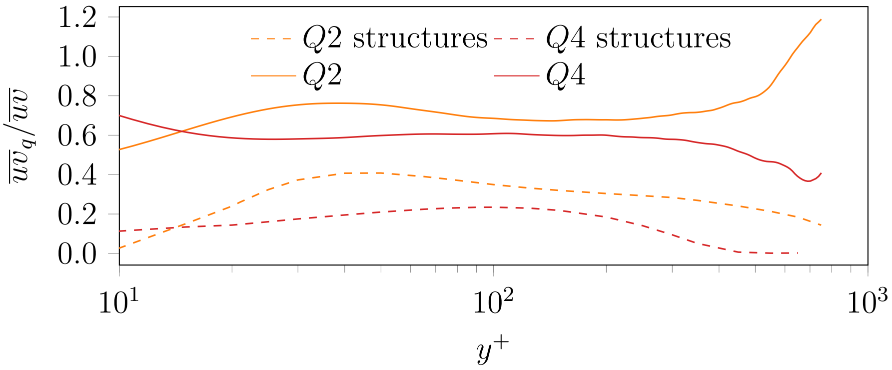

Figure 4.25 – Contribution of the $Q2$ and $Q4$ quadrants and detected quadrant structures (using (4.3) and (4.4)) to the Reynolds shear stress at $Re_\theta = 2068$.

large as the standard two-point correlations. However, they show that there are strong wall-normal events inside the LSM which can reach up to 4δ in length. The inclination of the standard two-point correlations is preserved, but $Q4$ structures in positive streamwise velocity fluctuations certainly have higher angles than the $Q2$ structures in negative streamwise velocity fluctuations. There is no significant difference (see fig. 4.14) with the correlations on the streamwise fluctuations alone.

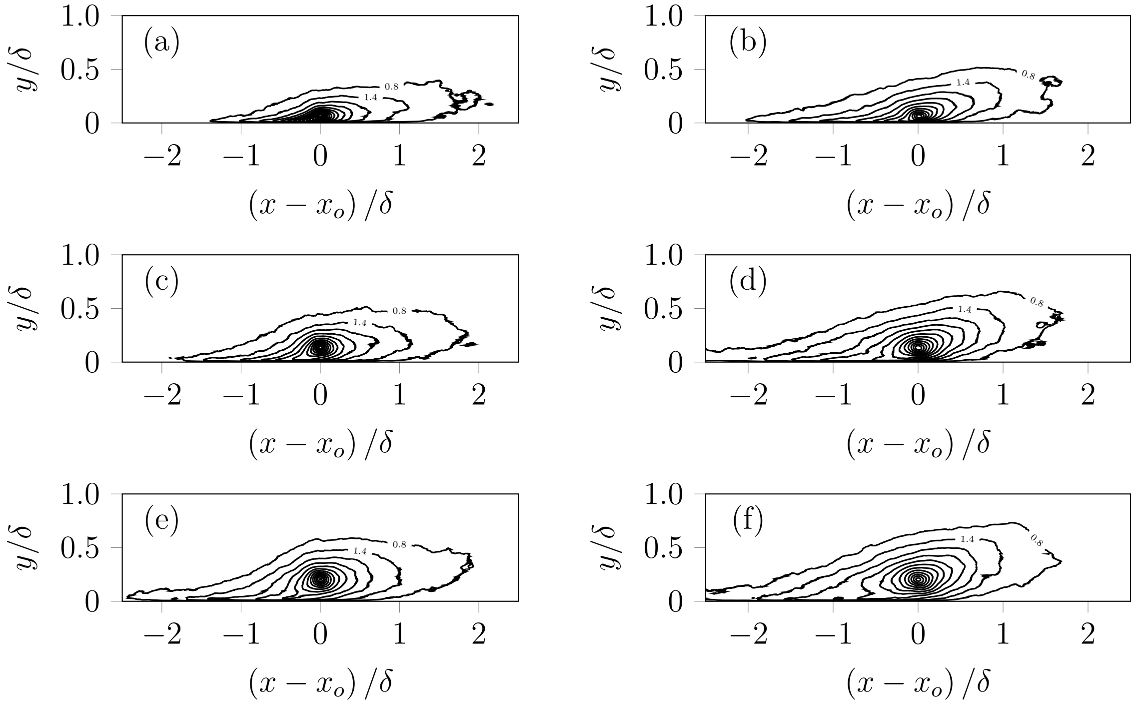

Figure 4.26 – Conditional two-point spatial correlation functions of the low streamwise velocity fluctuations $\langle u(x-x_o, y-y_o)u(x,y)\rangle$ if $u(x_o, y_o) < -C_{thr}\sigma_u^{100^+}$ with $C_{thr} = 1$ and $|uv| > Hu_{100^+}v_{100^+}$ with $H = 1.75$ at wall distances $y_o = 50^+$ (a), $y_o = 100^+$ (c) and $y_o = 150^+$ (e) where x_o is fixed at $Re_\theta = 2068$ and $C_{thr} = 1$. Same conditioned correlations for high streamwise velocity fluctuations, $\langle u(x-x_o, y-y_o)u(x,y)\rangle$ if $u(x_o, y_o) > C_{thr}\sigma_u^{100^+}$ with $C_{thr} = 1$ and $|uv| > H(u_{100^+}v_{100^+})$ with $H = 1.75$ (b, d, f). Note that for low streamwise velocity fluctuations and high streamwise velocity fluctuations $Q2$ and $Q4$ component of the quadrants are captured respectively.

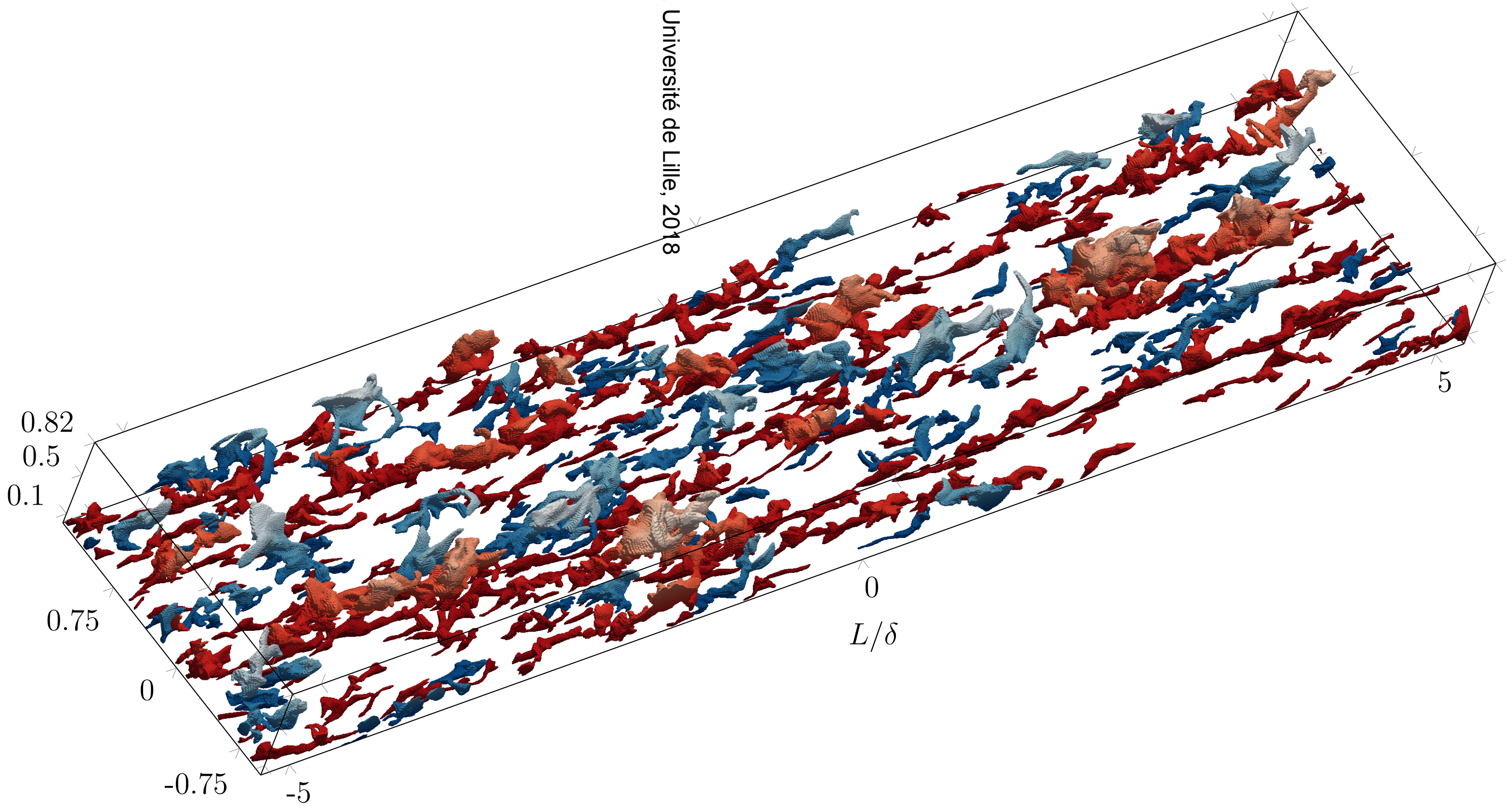

Figure 4.27 – Isovolume of $Q4$ (blues) and $Q2$ (reds) 3D structures with color intensity function of y^+. Structures are detected using the thresholding procedure defined in (4.3) and (4.4) with a threshold coefficient $H = 1.75$ on a 10δ long sub-domain centered at the Reynolds number $Re_\theta = 2068$.

4.3 Conclusion

A large database of 3D fields and 2D time-resolved data were collected from a new DNS for TBL flow at moderate Reynolds number. Spectral analysis shows that the streamwise energy spectrum is compatible with a k_x^{-q} scaling at large scales with $q \simeq 1$ near $y^+ = 100$ with increasing value of p when moving from the wall. Even though, the second peak (or plateau) of u'^+ is not clear at moderate Reynolds numbers, a reference value σ_u^{100+} at $y^+ = 100$ of the streamwise velocity fluctuation is used in the detection procedure of the large-scale structures.

LSM and quadrant structures are detected with a simple thresholding algorithms which results to a comparative study. The energy content of the LSM structures proves that they represent a substantial part of the streamwise velocity fluctuations and the thresholding does not alter the profile of the fluctuations inside the structures. As suggested by Marusic *et al.*[157], the pursuit of a novel decomposition is perhaps needed to enlighten the importance of the attached structures.

Aside from their energy level, the 3D shape of the structures has also been studied. Two different extractions of the structures were compared. The analyses of the 2D structures are comparable to the results given by Srinath *et al.*[10] on PIV data at higher Reynolds numbers. Moreover, a second method which benefits from having 3D numerical data is also applied, and the results are compared with the first method to make the connection with previous findings from experimental data. It is shown that 2D and 3D extractions may lead to different structure sizes due to the 3D nature of the structures. Information in the spanwise direction is meaningful as the longest structures also have a more complex topology. Representing the complex 3D shape of this structures with each length scale in each direction is not obvious. A specific skeletonization algorithm is used to simplify the 3D binary image of a single detected structure. Skeletons consist of a set of well-resolved lines which can be used to better characterize the whole structures regarding length, complexity, and angles. This simplification algorithm does not rely on lines of extrema which may be not representative of the full structure but rather defines curves based on its shape.

Distributions of the streamwise lengths of detected structures are investigated based on the results of both bounding boxes and skeletons. The results show that the distribution of streamwise lengths of the large-scale structures follows the same power law with a slope close to the -2 in agreement with the findings of Srinath *et al* [10]. Joint PDFs of their sizes in the 3 directions ($P(\lambda_x/\delta, \lambda_y/\delta)$ and $P(\lambda_x/\delta, \lambda_z/\delta)$) are given to provide 3D statistical descriptions of the detected structures. The results reveal some self-similarity between structures of different size but on a limited range due to the moderate Reynolds number of the DNS data.

The preferred angle of the detected structures is also investigated. Based on the main (longest) curve of the skeletons, a constant mean value of the angle is observed for all wall distances which is different from the results extracted from the standard two-point spatial correlations. A model of an elongated structure with a single positive angle with respect to the horizontal plane is not representative. However, measurements on the main curve of the skeletons suggest that large-scale wall attached structures follow an upward trend around 5° in average along the full boundary layer thickness.

Thresholding of the streamwise velocity fluctuations with a single parameter reveals the complex shapes of these streamwise structures and the skeletonization procedure is used to quantify their features. Their complexity was asserted by counting the number of significant branches of a structure. It is shown that most of the large structures ($> 4\delta$) have one or more significant branches.

Quadrant structures are also investigated with the same hyperbolic-hole size $H = 1.75$ as used by Lozano-Durán *et al.*[1]. It is shown that 2D and 3D extractions of the quadrants lead to larger differences in structure sizes than the LSM. This infers that spanwise connections are more important for quadrants. The distribution of the length of 3D quadrant structures follows a -3 slope. Spatial self-similarity of quadrant structures are demonstrated in accordance with previous results of Lozano-Durán *et al.*[1] on turbulent channel flow data.

Analysis of the fluctuating velocity inside quadrant structures exhibits the details of their composition. It is known that $Q2$ and $Q4$ gather a large fraction of the Reynolds shear stress $\overline{uv}$, but current results show that, with a simple threshold, only $\sim 50\%$ is the Reynolds shear stress is retained in the detected structures. Additionally, profiles of streamwise velocity fluctuations contained in quadrant structures have a similar shape than the profile to the Reynolds shear stress profile inside streamwise velocity LSM.

The analysis concerning the height of the structures are shown in figs. 4.10 and 4.23. Results are complementary because similar behaviors are observed for $Q2$ and low-speed structures (or $Q4$ and high-speed structures). These implies that valuable coupling between the discussions of LSM and quadrant structures.

Results shown in this study suggests that more detailed relations can be described between the large-scale motion and quadrants. In order to provide a preliminary result in this matter, correlations of the streamwise fluctuations conditioned with LSM and quadrants were computed (fig. 4.26). It is shown that $Q4$ structures exhibits longer and larger correlations inside the energetic parts of the streamwise fluctuations. Even though their size is smaller than other joint PDFs shown in this study there are still some significant quadrant events inside the LSM.

Part III

Turbulent Boundary Layer with Adverse Pressure Gradient

Navier-stokes solver MFLOPS3D-MD

5

This chapter introduces the incompressible Navier-Stokes solver MFLOPS3D-MD. The code is written and developed at LMFL and contains original approaches as compared to the existing Navier-Stokes solvers. A solver with geometrical flexibilities without damaging the scalability features of massively parallel code is the objective. The essential parts of the code which provides the central features and the numerical methods used to achieve these objectives are explained below.

5.1 Motivation behind the new code

It is quite common to develop Navier-Stokes solvers for a specific type of flow. So, the computationally expensive nature of the problem is dealt with applying a particular hypothesis or simplification based on the physics of the problem. This approach is beneficial and rapid in order to set up an effective solver but tuned for a specific type of problem. This often means that these high fidelity solvers are strongly tied to their original purposes which can be counterproductive due to their restricted versatility. For example spectral solution of Poisson equation for pressure is quite attractive due to convergence and performance properties. On the other hand, using Fourier space comes with particular limitations on the grid spacing (uniform grid or a special stretching function is needed). Moreover, any possible change requires tedious work if not absolutely impossible.

The MFLOPS3D-MD is designed with the objective to allow flexible use. It can be considered as a substantial upgrade to the earlier code MFLOPS3D (Marquillie[158] developed MFLOPS3D in the same research group). Even though naming suggests that the only difference is the multi-domain (MD) between these two codes, only a limited number of the features are common. A comparison between the features[†] of the MFLOPS3D and MFLOPS3D-MD are given in table 5.1. The details of the features are explained in section 5.2.

MFLOPS3D-MD uses non-homogeneous grids in the 3 directions to reach the resolution required by the physics of the problem. For homogeneous grids, both FFT and Multigrid based linear solvers scales very well. However, it is difficult to find simple

---

[†] Not all the features should be attributed to the author's work, it is a common effort of Dr. M. Marquille, Prof. U. Ehrenstein, Dr. J-P Laval, Dr. A. Poux

MFLOPS3D (previous solver)	MFLOPS3D-MD (new solver)
Spectral *(in 2 directions)*	Compact finite difference *(up-to 8th order)*
Implicit solver *(3d diagonalization)*	
MPI parallelization *(in 1 direction)*	MPI parallelization *(in 3 directions)*
Global mapping	Localized mapping (per domain)

Table 5.1 – Short list of the some features of MFLOPS3D and MFLOPS3D-MD

and scalable methods for non-homogeneous grids. The main feature of the new code is the domain decomposition based on influence matrix method[57] which provides a neat solution to this issue. In this approach, scalability is independent of spatial discretization, as sub-domains with any size can be solved and conceptually nothing changes concerning the use of this method when used with homogeneous or non-homogeneous grids.

Influence matrix method connects the sub-domains based on the continuity constraint. The best matching values of the interface points are found imposing the continuity constraint, simply by estimating a good value of an interface point from a linear system constructed based on the first order derivatives. This method does not require overlapping point between the sub-domains and interface points are solved only once per time step. No iterations are required inside a single time step as a single solution of the system is sufficient. Moreover, as each sub-domain is solved individually, they can have their unique boundary conditions including wall attached boundary conditions. This also means that the sub-domains can be efficiently solved with a direct solver thanks to their smaller size as in MFLOPS3D.

Mapping functions in 2-dimensions are implemented similarly to the Marquillie and Ehrenstein[159] but with mapping on the bottom and top walls. Aforementioned features the user to define a mapping function for each sub-domain independently. Coupling of these two features (influence matrix method and mapping) provides a solver which is capable of dealing with both smooth geometries and sharp corners (see fig. 5.1 i.e., rectangular geometries can be implemented inside the simulation domain using sub-domain with adapted BC while mapping delivers a method to define smooth curves.

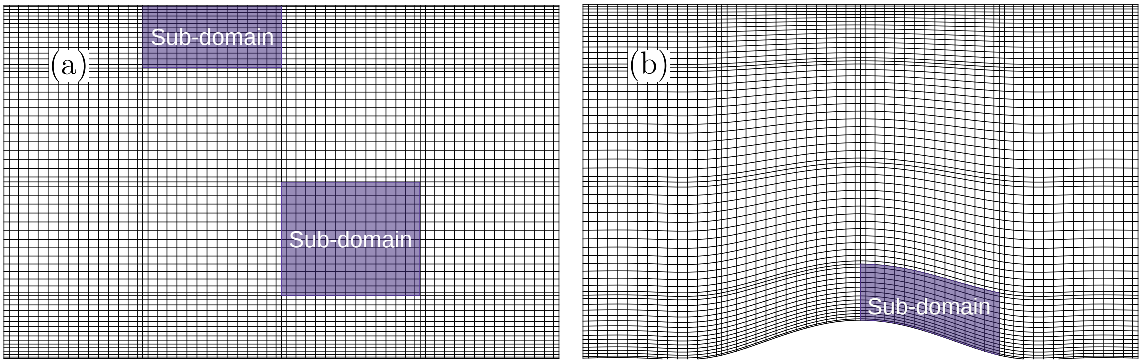

Figure 5.1 – The grid from MFLOPS3D-MD on XY-plane without (a) and with (b) mapping. Mapping custom function $y = f(x)$ is only applied on the lower wall in this example. Note that local stretching only applied in y-direction for this case, but it can be applied in 3 directions simultaneously.

Early examples using the code are available to demonstrate the flexibility of the code. Ehrenstein *et al.*[160] set an example of how the domain decomposition and mapping implemented in MFLOPS3D-MD can be used in DNS studies. Žnidarčič *et al.*[161] provided another extension algorithm for two-phase flows which works with the domain decomposition method used in MFLOPS3D-MD.

As mentioned, the code has been designed to be modular, and several different developments are being conducted based on MFLOPS3D-MD. For example, only pressure correction methods are available in the current version of the code, but A. Poux has also implemented the velocity correction methods as well as the WALE sub-grid scale models. The algorithm for cavitating flows has also been exercised in the Ph.D. of Znidarcic[162].

5.2 Numerical description of MFLOPS3D-MD

Different numerical methods are used to achieve a variety of tasks with a final goal which is to have an efficient solver for the incompressible Navier-Stokes equation while preserving the adaptability of the code. This section is listing the methods used while explaining the connections between the different methods and giving the necessary mathematical background. In other words, each subsection can be considered as building blocks of the MFLOPS3D-MD.

Solving the Navier-stokes equations for incompressible flows ((2.1) and (2.2)) require the definitions of boundary conditions of several types. The simplest BC for momentum equation is either the prescription of the velocity components (Dirichlet Type) or of the normal derivatives of velocity components (Neumann Type). Once the initial and boundary conditions are defined, the incompressible Navier-Stokes equations can be solved even though solving the velocity-pressure coupling (2.1) and (2.2) is not a simple task.

Technical procedures to solve of incompressible Navier-Stokes equations can be distinguished by the method used to deal with the pressure-velocity coupling. A powerful simplification to obtain solutions of the incompressible flows is based on the idea of decoupling pressure and velocity from each other what is known as operator splitting methods. Another approach is based on the assumption of weak compressibility which replaces the continuity constraint ($\nabla \cdot u = 0$) with an extra equation for pressure p. Weak compressibility assumption provides a scheme with two separate equations for $\mathbf{u}$ and p but it comes with a strict stability condition $\triangle t \sim 1/c$. On the other hand, applying forward Euler scheme to the system of governing equations results in a fully implicit method. Most of the implicit methods eventually become a saddle-point problem where Newton method can be used to handle non-linearity in this case. Details of the methods mentioned in this paragraph including derivation and comparison of the schemes can be found in the review of Langtangen *et al.*[163]. In this study, following the idea of operator splitting, projection methods based on pressure correction algorithms are used. Details of the methods available in the code with an application perspective will be given in section 5.2.1 following the notation of Guermond *et al.*[164].

The incompressible Navier-Stokes equations are

$$\frac{\partial \mathbf{u}}{\partial t} + \mathbf{u} \cdot \nabla \mathbf{u} = -\nabla p + \frac{1}{Re} \Delta \mathbf{u} \qquad \text{in } \Omega \times]0,t] \tag{5.1a}$$

$$\nabla \cdot \mathbf{u} = 0 \qquad \text{in } \Omega \times]0,t] \tag{5.1b}$$

where 3-dimensional flow field of an incompressible fluid flow is described by the velocity vector $\mathbf{u} = (u_1(\mathbf{x},t), u_2(\mathbf{x},t), u_3(\mathbf{x},t))^T \epsilon \, \mathbb{R}^3$, the pressure $p = (\mathbf{x},t) \, \epsilon \, \mathbb{R}$. Reynolds number ($Re = UL/\nu$) is the ratio of inertial forces to viscous forces. Δ is the Laplace operator and ∇ is the Divergence operator. These equations are the same as (2.1) and (2.2) except they are written with $\rho = 1$ which is used to simplify the description of the numerical schemes in this chapter.

5.2.1 Projection method

As emphasized above, the main difficulty for solving the incompressible Navier-Stokes equation is the necessity to solve the velocity and pressure solution simultaneously. Operator splitting is used to simplify PDEs into a set of equations. Projection methods† rely on the observation that left-hand side of (2.1) is a Hodge decomposition[167]. This method is thought to be inherently first-order. However, many contributions in the literature are proposing second-order accurate projection methods. Kim and Moin[55] have proposed a second order, time-discrete semi-implicit method for incompressible Navier-Stokes equations (5.2). Second order projection methods are also known as rotational forms (see Guermond *et al.*[164]). Brown *et al.*[167] have shown for a simulation of a periodic channel that rotational incremental pressure-correction schemes are second-order accurate.

$$\frac{\mathbf{u}^{n+1}-\mathbf{u}^{n}}{\triangle t}+[\mathbf{u}\cdot\nabla\mathbf{u}]^{n+1/2}=-\nabla p^{n+1/2}+\frac{1}{2Re}\Delta\left(\mathbf{u}^{n+1}+\mathbf{u}^{n}\right) \tag{5.2a}$$

$$\nabla\cdot\mathbf{u}^{n+1}=0 \tag{5.2b}$$

with boundary conditions

$$\mathbf{u}^{n+1}|_{\Gamma}=\mathbf{u}_b^{n+1} \tag{5.3}$$

Details of the explicit treatment of the $[\mathbf{u}\cdot\nabla\mathbf{u}]^{n+1/2}$ second order approximation of the convective term are given later. The discrete equation (5.2) can be reduced to a set of ODEs using velocity[168;169] or pressure[55] correction schemes. These schemes will be detailed later in this document.

Pressure corrections schemes are often preferred because pressure can be treated explicitly. In first sub-step, pressure is either ignored or treated explicitly. Then, a correction step (also called as projection step) is needed to satisfy the incompressibility constraint. Lastly, pressure update can be performed. It is especially important if the pressure is going to be used in the next time step for the estimation of the $\nabla p^{n+1/2}$.

In MFLOPS3D-MD, at each time step $t_n = n\triangle t$, an intermediate pressure and intermediate velocity are solved. The pressure correction scheme ensuring incompressibility followed with the pressure update in rotational form. A backward differentiation formula (BDF) approximation of the unsteady term at the qth order is applied instead of Crank-Nicolson time stepping used in the original scheme.

Unlike non-incremental pressure-correction scheme (simplest pressure correction scheme

---

† The term "projection method" often referred as "fractional step method" in literature while the original non-incremental pressure correction schemes from Témam[165;166] are called "méthode des pas fractionnaires" in French

originally introduced by Témam[165]; Chorin[170]) all the schemes used in MFLOPS3D-MD includes the pressure (or its effects) in the sub-step. Instead, strong setting incorporates tangential components of the pressure gradient into the boundary conditions of the intermediate velocity fields, and weak setting includes extrapolation of the pressure in the sub-step.

Generalized incremental pressure correction scheme equations are

$$\frac{1}{\triangle t}\left(\beta_q \mathbf{u}^{k+1}-\sum_{j=0}^{q-1}\beta_j \mathbf{u}^{k-j}\right)-\nu\nabla^2\mathbf{u}^{*}+\sum_{j=0}^{r-1}\gamma_j p^{k-j}=f\left(t^{k+1}\right),\quad \mathbf{u}^{k+1}|_{\varGamma}=0 \tag{5.4}$$

$$\begin{cases}\dfrac{\beta_q}{\triangle t}\left(\mathbf{u}^{k+1}-\mathbf{u}^{*}\right)+\nabla\phi^{k+1}=0\\ \nabla\cdot\mathbf{u}^{k+1}=0,\quad \mathbf{u}^{k+1}|_{\varGamma}=0\end{cases} \tag{5.5}$$

$$\phi^{k+1}=p^{k+1}-p^{\star,k+1}+\chi\nu\nabla\cdot\mathbf{u}^{*} \tag{5.6}$$

where $\frac{1}{\triangle t}\left(\beta_q \mathbf{u}^{k+1}-\sum_{j=0}^{q-1}\beta_j \mathbf{u}^{k-j}\right)$ is the qth-order backward difference formula (BDFq), $\mathbf{u}^{*}$ and $p^{\star,k+1}=\sum_{j=0}^{r-1}\gamma_j p^{k-j}$ being an intermediate velocity (estimation of $\mathbf{u}^{k+1}$) and an estimation of pressure while $q, r,$ and χ are the parameters to set appropriate form of the pressure correction scheme.

Equations (5.4) to (5.6) give a formal definition of the related schemes based on few parameters. Details of the derivation of this form can be found in the review paper of Guermond *et al.*[164] for projection methods. It includes discussions for both pressure and velocity correction schemes with details as well as complete equations for the different type of schemes.

BDFq for unsteady term will be given later (see eq. (5.22)) when discussing time discretization. The rth order extrapolation for pressure $p(\mathbf{x}, t^{k+1})$ is

$$\sum_{j=0}^{r-1}\gamma_j p^{k-j}=p^{\star,k+1}=\begin{cases}0 & if\ r=0\\ p^k & \text{if } r=1\\ 2p^k-p^{k-1} & \text{if } r=2\end{cases} \tag{5.7}$$

Finally, χ may be equal to 0 or 1. The choice $\chi=0$ yields to the standard forms of the algorithm, whereas $\chi=1$ yields to the rotational forms. In MFLOPS3D-MD only rotational versions of the projection algorithm is available. q is the order of the time stencil, parametrized as `to(1)`. r corresponding to the parameter `to(3)` defines the order of the extrapolation for the pressure estimation.

Boundary conditions of $\mathbf{u}^*$ has to be consistent with the projection step. Brown *et al.*[167] analyzed the 3 parameters of a projection method namely, the pressure approximation (5.7), the boundary condition $\mathbf{u}^*|_\Gamma$, and pressure update (5.6). They explain how second-order accurate projection method can be obtained from these decisions.

The 3 variations of the pressure correction scheme shown in (5.8), (5.13) and (5.16) are available in MFLOPS3D-MD. The motivation behind these methods as well as advantages/disadvantages are discussed below while important discussion concerning boundary conditions is given in section 5.2.3.1. The parameter `PT` (projection type) allows the users to choose between these three schemes. The intermediate velocity field $\mathbf{u}^*$ will be $\tilde{\mathbf{u}}^{k+1}, \hat{\mathbf{u}}^{k+1}$ and $\check{\mathbf{u}}^{k+1}$ for `PT=1`, `PT=2` and `PT=3` respectively.

Strong settings (`PT=1`)

The scheme is proposed by Kim and Moin[55] originally with a Crank-Nicolson time stepping but is given below using a BDFq approximation of the unsteady term.

$$\frac{1}{\triangle t}\left(\beta_q \hat{\mathbf{u}}^{k+1} - \sum_{j=0}^{q-1} \beta_j \mathbf{u}^{k-1}\right) - \nu \nabla^2 \hat{\mathbf{u}}^{k+1} \cancel{+ \nabla p^{\bigstar,k+1}} = f\left(t^{k+1}\right) \tag{5.8a}$$

$$\hat{\mathbf{u}}^{k+1}|_\Gamma = \frac{\triangle t}{\beta_q} \nabla \psi^{\bigstar,k+1}|_\Gamma \tag{5.8b}$$

$$\begin{cases} \dfrac{\beta_q}{\triangle t}\left(\mathbf{u}^{k+1} - \hat{\mathbf{u}}^{k+1}\right) + \nabla \psi^{k+1} = 0 \\ \qquad \nabla \cdot \mathbf{u}^{k+1} = 0, \quad \mathbf{u}^{k+1}|_\Gamma = 0 \end{cases} \tag{5.8c}$$

where $\nabla \psi^{\bigstar,k+1}$ is some approximation of $\nabla \psi\left(t^{k+1}\right)$, while $\psi(t)$ being a quantity related to the pressure via $p(t) = \psi(t) - \nu \frac{\Delta t}{\beta_q} \nabla^2 \psi(t)$.

Following choices can be used for the extrapolation;

$$\psi^{\bigstar,k+1} = \begin{cases} 0 & \text{if } r = 0 \\ \psi^k & \text{if } r = 1 \\ 2\psi^k - \psi^{k-1} & \text{if } r = 2 \end{cases} \tag{5.9}$$

where the r is chosen with the user parameter `TO(3)`.

This method has particular importance as it imposes a boundary condition on the tangential components of velocity at the sub-step $\hat{u}^{k+1}$ which satisfy the need of the consistent boundary condition emphasized above. Kim and Moin[55] demonstrated that tangential boundary conditions of the solution $\hat{\mathbf{u}}^{k+1}$ based on the lagged value of ψ or high order extrapolation is needed to ensure second-order accuracy. Notice that, $\hat{\mathbf{u}}^{k+1}$ satisfies an elliptic equation with continuous forcing and $\triangle t \nabla\phi = (I - P)\hat{\mathbf{u}}^{k+1}$ so $\nabla\phi$ is continuous in time[167]. So more accurate estimations of $\nabla\psi^{\star,k+1}|_{\Gamma}$ can be obtained by extrapolation in time.

Guermond *et al.*[164] reminded the difficulty to implement this method for finite element discretization and this is why successful examples using this method are using spectral or finite difference approximations. Moreover, we found that using this method for pressure driven flows combined with the semi-implicit method is more difficult keep it stable. Because, when strong pressure gradient needs to be captured with a solution of ϕ obtained using fully homogeneous Neumann boundary condition a sudden change around the boundaries needed to be captured in the direction of the pressure gradient which is not natural. This is exactly the situation for example for a channel flow simulation with an inlet and an outlet. For periodic channels this issue does not appear as a constant pressure gradient is added to the source terms. An advantage of this method is that $\Delta\phi^{k+1} = \nabla\tilde{\mathbf{u}}^{k+1}$ is solved only once to get the $\nabla\phi^{k+1}$ for the projection step, so it is computationally effective. Moreover, solution of ϕ^{k+1} is carried to the next time step only via the velocity, there is no direct link through pressure term. Potential errors (spurious waves) will be affected by the diffusion before the solution of ϕ reaches the next time step. This contributes indirectly to the stability of the numerical methods.

Weak settings (`PT=2`)

This form is a different option for the pressure correction. It includes different treatment of the boundary conditions. As shown by Guermond *et al.*[164], weak and strong setting are equivalent with appropriate change of variables.

Using change of variables

$$\tilde{\mathbf{u}}^{k+1} = \hat{\mathbf{u}}^{k+1} - \frac{\triangle t}{\beta_q}\nabla\psi^{\star,k+1} \tag{5.10}$$

$$p^{k+1} = \psi^{k+1} - \frac{\triangle t}{\beta_q}\nabla\psi^{k+1} \tag{5.11}$$

$$p^{\star,k+1} = \psi^{\star,k+1} - \frac{\triangle t}{\beta_q}\nabla\psi^{\star,k+1}, \tag{5.12}$$

eq. (5.8) becomes

$$\frac{1}{\triangle t}\left(\beta_q \tilde{\mathbf{u}}^{k+1} - \sum_{j=0}^{q-1}\beta_j \mathbf{u}^{k-1}\right) - \nu\nabla^2\tilde{\mathbf{u}}^{k+1} + \nabla p^{\bigstar,k+1} = f\left(t^{k+1}\right) \tag{5.13a}$$

$$\tilde{\mathbf{u}}^{k+1}|_{\Gamma} = \cancel{\frac{\triangle t}{\beta_q}\nabla\psi^{\bigstar,k+1}}|_{\Gamma} = 0 \tag{5.13b}$$

$$\begin{cases} \dfrac{\beta_q}{\triangle t}\left(\mathbf{u}^{k+1} - \tilde{\mathbf{u}}^{k+1}\right) + \nabla\phi^{k+1} = 0 \\ \nabla\cdot\mathbf{u}^{k+1} = 0, \quad \mathbf{u}^{k+1}|_{\Gamma} = 0. \end{cases} \tag{5.13c}$$

Subtracting (5.11) from (5.12),

$$p^{k+1} - p^{\bigstar,k+1} = \psi^{k+1} - \psi^{\bigstar,k+1} + \nu\frac{\triangle t}{\beta_q}\nabla^2\left(\psi^{k+1} - \psi^{\bigstar,k+1}\right) \tag{5.14}$$

Pressure can be estimated with (5.11) and (5.12) together with (5.9)

$$p^{\bigstar,k+1} = \begin{cases} 0 & if\; r = 0 \\ p^k & if\; r = 1 \\ 2p^k - p^{k-1} & if\; r = 2 \end{cases} \tag{5.15}$$

This form of the projection method includes the pressure gradient in the right-hand-side of the momentum equation. Therefore ϕ is a correction rather than a physical pressure gradient. Equations are similar to the ones given for weak setting, (5.13), but the numerical implementation is different. Also, extrapolation of the $p^{\bigstar,k+1}$, can accumulate the errors of pressure from the Poisson solver as the gradient of the potentially polluted $p^{\bigstar,k+1}$ will be placed into the solution of the $\tilde{u}^{k+1}$ in the next time step. This makes this method difficult to use in MFLOPS3D-MD as the solution of ϕ with a compact finite difference solver is not as accurate as with spectral methods.

Weak settings with pressure prediction (`PT=3`)

A better approach than the standard extrapolation of ϕ was proposed by Hugues and Randriamampianina[53]. In this method, the predictor step for pressure (5.16a) is solved before each time iteration to obtain preliminary pressure which replaces extrapolation of the pressure in (5.13). This method can be selected in MFLOPS3D-MD with the option `PT=3`.

In other projection type (`PT=1` and `PT=2`) the pressure is solved with $\Delta\phi^{k+1} = \nabla\tilde{u}^{k+1}$ which is obtained by taking the divergence of the equations (5.8c) or (5.13c). The pressure prediction step is established from the momentum equation which performs better than a simple extrapolation. The full scheme in that case becomes

$$\Delta p^{\blacklozenge,k+1} = -\nabla\cdot[\mathbf{u}\cdot\nabla\mathbf{u}]^{k+1} + \nabla\cdot f^{k+1} \tag{5.16a}$$

$$\left.\frac{\partial p^{\blacklozenge,k+1}}{\partial\mathbf{n}}\right|_{\Gamma} = \mathbf{n}\cdot\left.\left[-\partial\mathbf{u}_t - \mathbf{u}\cdot\nabla\mathbf{u} + \nu\nabla^2\mathbf{u}\right]^{k+1}\right|_{\mathit{\Gamma}} \tag{5.16b}$$

$$\frac{1}{\triangle t}\left(\beta_q\check{\mathbf{u}}^{k+1} - \sum_{j=0}^{q-1}\beta_j\mathbf{u}^{k-1}\right) - \nu\nabla^2\check{\mathbf{u}}^{k+1} + \nabla p^{\blacklozenge,k+1} = f\left(t^{k+1}\right) \tag{5.16c}$$

$$\check{\mathbf{u}}^{k+1}|_{\mathit{\Gamma}} = \cancel{\frac{\triangle t}{\beta_q}\nabla\psi^{\bigstar,k+1}}|_{\mathit{\Gamma}} = 0 \tag{5.16d}$$

$$\begin{cases} \dfrac{\beta_q}{\triangle t}\left(\mathbf{u}^{k+1} - \check{\mathbf{u}}^{k+1}\right) + \nabla\phi^{k+1} = 0 \\ \qquad \nabla\cdot\mathbf{u}^{k+1} = 0, \quad \mathbf{u}^{k+1}|_{\mathit{\Gamma}} = 0 \end{cases} \tag{5.16e}$$

Pressure update (relationship between p^{k+1}, $p^{\blacklozenge,k+1}$ and ϕ^{k+1}) is applied with the same equation (5.14).

The predicted pressure $p^{\blacklozenge,k+1}$ is quite accurate, if the accurate boundary condition (5.16b) can be obtained from extrapolation in time. Similar extrapolations are suggested by Karniadakis *et al.*[169] as well to approximate the pressure boundary conditions. Brown *et al.*[167] have shown that such extrapolations is necessary to achieve second-order accuracy. In the present implementation, this method was found to be more robust than the others.

Projection step

In addition to the categorization given above, projection methods can be classified as exact or approximated based on the way continuity condition is satisfied. Discrete continuity is satisfied up to machine precision with an exact projection method. However, approximate projection methods satisfy the continuity up to the order of the method[167].

Taking the divergence of (5.13c) or (5.16e) leads to

$$\nabla \cdot \nabla \phi = \frac{1}{c_k \triangle t} \nabla \cdot \mathbf{u}^* \tag{5.17}$$

where the c_k is coefficient depending on the temporal discretization (if (5.8c) is used ψ replaces the ϕ).

As mentioned by Reis *et al.*[171], the operator $\nabla \cdot \nabla$ is identical to the Laplacian Δ, but it is not always true in the discrete case. In MFLOPS3D-MD a Laplacian operator Δ is used, so the projection step is not exact.

Abide and Viazzo[172] give an example of an exact projection method with compact finite differences, but resulting stencil is not compact. A simpler method was proposed by Reis *et al.*[171] which does not require to build a stencil for the $\nabla \cdot \nabla$ but it requires larger number equations to be solved.

5.2.2 Temporal and spatial discretizations

The equations described in the previous section need to be discretized both in space and time. For direct numerical simulation high order schemes are more suited. The choice was made to use compact finite differences[56] in space and with BDFq schemes in time.

Compact finite difference discretization is a good compromise between accuracy and efficiency. The derivation of compact finite difference scheme with appropriate properties for non-homogeneous discretization is an extensive subject of research. A non-uniform collocated grid is used, meaning that pressure and velocity components are solved in the same grid points. The main properties of the scheme used in MFLOPS3D-MD are described in more detail in appendix C.1.

Simens *et al.*[31] reported that the pressure correction schemes with compact finite difference schemes could not be efficiently implemented. Accordingly, they chose to use 2nd order finite difference scheme for the pressure while keeping high-order compact schemes for the velocities. In the current study, the compact schemes are adopted for the Poisson solver. At first sight, it seems like there is no problem of efficiency as the direct solver performs similarly with different boundary conditions. However, other issues related to the stability of the simulation which is reported in the next chapter might be related to this choice or at least it gets combined with other potential problems and amplifies the problem. There might be more adapted compact schemes for the Poisson solver. For example, Chen *et al.*[173] introduced combined compact finite difference schemes to improve the issues related to the oscillations, but this idea was not tested in MFLOPS3D-MD.

In MFLOPS3D-MD, time integration relies on a semi-implicit second-order or third-order backward-Euler scheme, while Adams-Bashforth schemes are used for the estimation of the nonlinear terms. Additional time and space scheme are easy to implement due to the modularity of the code. Moreover, the modules such as the derivatives are also used for post-processing codes.

Spatial discretization

Higher order spatial discretization is required for reliable DNS high order compact finite difference schemes[56] provide spectral-like resolution without requiring large stencils. The MFLOPS3D-MD is using this type of schemes both for the derivatives and the linear solvers. For simplicity, derivatives and solvers are designed with the same stencils for a chosen order. Therefore second order derivatives and solvers are an order lower than the corresponding first derivatives, e.g., 8th order first derivatives are used alongside 7th order solver scheme.

Backward and forward schemes are used for the first point of the computational domain as well as for the interface points because domain decomposition method used in MFLOPS3D-MD does not require any ghost points. The 8th order scheme is the highest order compact finite difference implemented in the code, thus only first, and last 2 grid points in a given direction might need a special stencil depending on the order of the scheme.

The points requiring a backward/forwards treatment can be written with a lower order stencils than the order of the stencils for internal points to obtain similar level of errors. However, each scheme will be identified with the order of the central scheme, i.e., derivatives with 8th order accurate scheme mean that central schemes are 8th order, independently of the scheme order for the first and last two points. The stencils are summarized in table 5.2. Further details related to the stencils for each scheme can be found in appendix C.1.

A fully explicit scheme having the same order than the corresponding backward/forward scheme of the neighboring points is used for the extrapolation of the value at the first and last point when Neumann boundary conditions are used for the solver.

Implicit schemes require solving a discrete system to compute derivatives. For example in 1D, derivative in the x-direction is defined as:

$$A_i\left(\partial_x u\right) = B_i u \tag{5.18}$$

Table 5.2 – Summary of the stencil sizes for compact finite difference schemes (see details of the schemes in appendix C.1)

	8th order		6th order		4th order		2th order	
Points	Imp.	Exp.	Imp.	Exp.	Imp.	Exp.	Imp.	Exp.
$[1, n]$	3	8	1	6	1	4	0	3
$[2, n-1]$	1	5	1	5	1	5	0	3
$[3 : n-2]$	4	5	2	5	2	3	0	3

For each line i (corresponding to a point on the grid), the coefficients are solutions of the linear system (5.19):

$$C_{ij} D_{ij} \begin{pmatrix} A_i \\ B_i \end{pmatrix} = RHS \tag{5.19}$$

where every column j of C_i and D_i come from a truncated Taylor expansion

$$\begin{aligned} D_{ij} &= \left(0, 1, h_{i,,j}, \frac{h_{i,j}^2}{2}, \frac{h_{i,j}^3}{6}, \ldots\right) \\ C_{ij} &= \left(0, 1, h_{i,,j}, \frac{h_{i,j}^2}{2}, \ldots\right) \end{aligned} \tag{5.20}$$

$h_{i,j}$ is the distance between point i and j, and RHS is null except one value which is equal to one (the first for an interpolation, the second for a derivative, the third for a second derivative, ...). By changing the size of C_i and D_i (size of the stencil) one can change the spatial order of discretization. See (C.3) in appendix for an example of a linear system like (5.19).

Grid

The grid must be chosen to ensure integrability constraints. Incompressible Navier-Stokes solvers often use staggered grids, and they are required for a stable solver. This is convenient for most of the derivatives involved in the Navier-Stokes equations except an averagingAbdallah[174;175] of nonlinear term becomes required. Otherwise, stabilization techniques need to be used which consist of solving the perturbed continuity equation[163]. Luckily, certain splitting schemes provide stable solutions with a collocated grid as well. In addition, special high order schemes can be designed as proposed by Dormy[176] with proper damping effects. However, in the current study, non-homogeneous grids are used that makes such solutions much harder to implement. An other solution is to design compact scheme with additional dissipative properties at large frequency as in the implicit LES implementation of Lamballais *et al.*[138].

Grid generation is quite flexible with MFLOPS3D-MD, but must fulfill some requirements. First of all, stretching is not trivial as it can result in the linear system for the derivation of the compact scheme which is not invertible. Therefore it is not possible to use any stretching. This property is verified in the code by assessing the eigenvalues, which all need to be real positive. Second, there is an optimal ratio between the largest and smallest grid mesh which provides the same level of error for the derivatives at the points using both centered and non-centered stencils.

The stretching proposed in MFLOPS3D-MD is

$$x_i = x_0 + (x_N - x_0)\,\frac{\sin^{-1}\left(-\alpha \cos\left(\pi \frac{x_i - x_0}{x_N - x_0}\right)\right)}{2\left(\sin^{-1}(\alpha) + 1\right)} \tag{5.21}$$

with $h_{i,j} = (x_j - x_i)$. The ratio $\max(h_{i,j})/\min(h_{i,j}) \simeq 4$ was suggested by A. Poux to have good results based on derivative tests using splines. These predetermined $\max(h_{i,j})/\min(h_{i,j})$ ratios are coded into the code so optimum grid stretching parameter α can be deduced when number of grid points is changed.

The value of α, obtained by the optimization based spline derivatives, is falls within limits determined by Shukla and Zhong[177] as the same stretching function (5.21) have been used. All the tests are given in the chapter 6 conducted within the stable limits mentioned here.

In the current version of the code, grid points are stored/read in 1D vectors for each direction. Consequently, storing grids is extremely cheap even for the very large size of problems and 3D grids can be constructed easily if needed for post-processing purposes.

Grid coordinates need to be generated respecting the domain decomposition constrains. A local stretching applied to each sub-domain is combined with a global stretching which may be required to satisfy the physical constrains of the flow. Local stretching inside individual sub-domains is required to compensate the Runge phenomena of high order backward/forward schemes. The optimization of the stretching parameter α for the local stretching was explained above, if (5.21) is changed optimization parameter needs to be adjusted for the new stretching function.

Global stretching can be used to refine the mesh near walls in one or more directions. For example, boundary layer simulations over flat plate can benefit from stretching in wall normal direction, or the simulation over a physical bump can use the stretching in streamwise direction to better resolve the strong adverse pressure gradient region. However, the use of global stretching rises additional questions because the solver ends up being not having any truly centered scheme. In some cases, it might be preferable to scale the sub-domains individually instead of using a global stretching. Different forms of the stretching can be expected depending on the problem. Therefore, the proper place for such an enhancement is indicated in the source code. User can define the start and end coordinates in any direction from parameter file by setting desired values for `domain_len`. Stretching parameter α is also parametrized with `ratio_max`.

Temporal discretization

Second and third order BDFq schemes are implemented for the discretization of the unsteady term. Third order stencil (`TO(1)=3`)is found to be unstable as reported by Poux *et al.*[178] which is also emphasized in the dissertation of Znidarcic[162].

The qth-order backward difference (BDFq) that approximates $\partial_t \mathbf{u}\left(t^{k+1}\right)$ is

$$\partial_t \mathbf{u}^{k+1} = \beta_q \mathbf{u}^{k+1} - \sum_{j=0}^{q-1} \beta_j \mathbf{u}^{k-j} \tag{5.22}$$

In particular,

$$\partial_t \mathbf{u}^{k+1} = \begin{cases} \mathbf{u}^{k+1} - \mathbf{u}^{k} & if\ q = 1 \\ \dfrac{3}{2}\mathbf{u}^{k+1} - 2\mathbf{u}^{k} + \dfrac{1}{2}\mathbf{u}^{k-1} & if\ q = 2 \\ \dfrac{11}{6}\mathbf{u}^{k+1} - 3\mathbf{u}^{k} + \dfrac{3}{2}\mathbf{u}^{k-1} - \dfrac{1}{3}\mathbf{u}^{k-2} & if\ q = 3 \end{cases} \tag{5.23}$$

where q become the equivalent of the user parameter `TO(1)`. Following equations will be derived only for the second order BDF (`TO(1)=2`) for the sake of simplicity.

Discretization of the nonlinear term

Special attention needs to be dedicated to the discretization of the nonlinear term due to the importance of this term for the conservative properties of the discretized equations. In MFLOPS3D-MD, both convective (`NLT(2) = 1`) and skew-symmetric (`NLT(1) = 2`) form of the nonlinear terms are implemented. Nonlinear terms are estimated with one step extrapolation schemes while `NLT(2)` allows the user to choose between first, second and third order approximations. For example, a second-order approximation is:

$$(\mathbf{u}\nabla\mathbf{u})^{n,n-1} = 2\mathbf{u}^{n}\nabla\mathbf{u}^{n} - \mathbf{u}^{n-1}\nabla\mathbf{u}^{n-1} \tag{5.24}$$

Multi-step methods such as Runge-Kutta schemes were also tested. Runge-Kutta provides better results but requires additional solutions of the influence matrix for each intermediate step of the scheme.

The skew-symmetric form (eq. (5.25)) of the nonlinear term is preferable because of its conservative property as shown by Morinishi *et al.*[179].

$$\mathbf{u}\nabla\mathbf{u} = \left(\frac{1}{2}\nabla\mathbf{u}\mathbf{u} + \frac{1}{2}\mathbf{u}\nabla\mathbf{u}\right) \tag{5.25}$$

The skew-symmetric form needs to be correctly discretized in space in order to preserve conservation properties. According to Morinishi *et al.*[179], the skew-symmetric form of the nonlinear term on a collocated grid is conservative for kinetic energy without additional treatment when discretized with standard second and fourth order finite differences. For compressible flows, Morinishi[180] mentioned that compact finite difference schemes discrete nonlinear term is not a fully conservative form of the nonlinear term, but only a skew-symmetric form is stable. Use of non-uniform grids raises additional questions as well. Simple trade-off needs to be made between the accuracy of the discrete form and the modification of derivative coefficients for better conservation properties. MFLOPS3D-MD does not include special treatment for this problem, so the accuracy of the derivatives is preserved while kinetic energy conservation is not certain.

Complete discretized system

Fully discretized momentum equation in streamwise direction for the projection types `PT=1`, `PT=2` and `PT=3` with the non-linear term in skew symmetric form writes

$$\nabla^2\tilde{\mathbf{u}}^{n+1} - \frac{3Re}{2\triangle t}\tilde{\mathbf{u}}^{n+1} = Re\left[-\frac{4}{2\triangle t}\mathbf{u}^{n} + \frac{1}{2\triangle t}\mathbf{u}^{n-1} + [(\mathbf{u}\cdot\nabla)\mathbf{u}]^{n,n-1}\right] \tag{5.26}$$

$$\nabla^2\tilde{\mathbf{u}}^{n+1} - \frac{3Re}{2\triangle t}\tilde{\mathbf{u}}^{n+1} = Re\left[-\frac{4}{2\triangle t}\mathbf{u}^{n} + \frac{1}{2\triangle t}\mathbf{u}^{n-1} + \nabla p^{\bigstar,k+1} + [(\mathbf{u}\cdot\nabla)\mathbf{u}]^{n,n-1}\right] \tag{5.27}$$

$$\nabla^2\tilde{\mathbf{u}}^{n+1} - \frac{3Re}{2\triangle t}\tilde{\mathbf{u}}^{n+1} = Re\left[-\frac{4}{2\triangle t}\mathbf{u}^{n} + \frac{1}{2\triangle t}\mathbf{u}^{n-1} + \nabla p^{\blacklozenge,k+1} + [(\mathbf{u}\cdot\nabla)\mathbf{u}]^{n,n-1}\right] \tag{5.28}$$

Therefore Navier-Stokes equations using any of the projection types become a set of

Helmholtz problems which can be written as

$$\nabla^2 \tilde{\mathbf{u}}^{n+1} - \sigma \tilde{\mathbf{u}}^{n+1} = \mathbf{f} \tag{5.29}$$

with $\sigma = 3Re/(2 \triangle t)$ and $\mathbf{f}$ being the right-hand-side of (5.26) to (5.28) depending on the projection type.

5.2.3 Solver for the sub-domains

As mentioned above the choice of a semi-implicit second-order backward-Euler time integration combined with projection methods imply to solve several Helmholtz problems at each time step. For the projection methods corresponding to `PT=1` and `PT=2` the two variables $\mathbf{u}^*$ and ϕ need to be solved with appropriate boundary conditions. In the case of `PT=3`, a preliminary step is necessary to compute a prediction of pressure $p^\blacklozenge$. The Poisson equation for pressure is a particular case of (5.29) (with $\sigma = 0$ and $\mathbf{f} = \nabla \cdot \tilde{\mathbf{u}}^{n+1}$). Therefore, the same class of solver is required to solve the three unknown $\mathbf{u}^*$, ϕ^{k+1} and $p^\blacklozenge$.

Helmholtz equation needs to be solved with a linear solver with its boundary conditions, unlike explicit approach used in most of the original version of the projection methods. Helmholtz equation is solved efficiently using 3D diagonalization method. Discussions about the boundary conditions are given in the next subsection.

Solver coefficients are computed only once at the beginning of the simulation (see appendix C.2). During the initialization, LAPACK functions are used to obtain the eigenvalues of the system. After the diagonalization, the solution of the Helmholtz problem is obtained with tensor-matrix multiplications at every time step. The property of the system provides a sanity check about the quality of the compact finite difference coefficients at the initialization, as distribution and signs of the eigenvalues is easily assessed. A solution can be computed only for a system with negative and real eigenvalues. Pressure Poisson equation with homogeneous Neumann boundary conditions introduces zero eigenvalues (one for each direction with Neumann boundary conditions indicating the singularity). This decomposition using eigenvectors provides an effective way for the treatment of the singularity problem. Replacing the solution at the point where all three eigenvalues are zero (like a one-point Dirichlet) is sufficient to obtain the solution up-to a constant. There is no need for other treatments such as null-space-removal in this case. However, singularity problem is transferred into the influence matrix in the multi-domain cases requiring treatments which have to be implemented differently (see section 5.2.4).

3D diagonalization algorithm is efficient because it is based on matrix multiplications, but algorithm complexity remains $\mathcal{O}(n^4)$. It is a very fast method for moderate domain sizes like in the case of MFLOPS3D-MD which uses influence matrix method to scale-up by multiplying the number of sub-domains. Another approach to increase the performance of the solver for larger problems is to parallelized the diagonalization. Abide *et al.*[181] proposed a possible parallelization relying on 2DECOMP&FFT[182] used in Incompact3d.

Solution of the Helmholtz equations are difficult to obtain at high wavenumbers $k = w/c = \sqrt{\sigma}$ where w is the frequency of the wave propagation and c is the speed of sound. This is directly related to the Reynolds number of the simulation in the way Helmholtz is written. Different solutions are proposed to solve this problem such as special 6th order compact finite difference scheme[183] or the use of exact finite difference schemes[184]. Unfortunately, none of these are currently implemented in MFLOPS3D-MD, but issues thought to be related to this phenomenon are investigated further in section 6.3.2.

5.2.3.1 Boundary conditions

The solution of the Helmholtz system requires proper treatment of the boundary conditions. Up to 5 boundary conditions (3 for $\mathbf{u}$, ϕ and $p^{\blacklozenge}$ in case pressure prediction) should be identified on the 6 surfaces of every sub-domain. As it can be seen in appendix C.1 only the stencils of the first and last two points uses the boundary condition values which appear in right-hand-side of the solver and needs to be updated every time step. If Neumann conditions are used, an extrapolation step is required at the end of the solver, to obtain to the value of the boundary conditions from its derivative. This extrapolation is performed using an explicit scheme with the same order than the solver.

Some of the projection methods[185] does not strictly follow compatible boundary conditions for pressure. These methods remain first order accurate for pressure while second-order accuracy is satisfied for the velocity. This problem is usually solved by using the rotational form of the pressure update (see Eq. (13) in Brown *et al.*[167]). The methods without pressure updates[55] does not suffer from this problem if the tangential components of dynamic equation is handled correctly like in (5.8). Hugues and Randriamampianina[53] tried to solve the problem of the inconsistent boundary conditions caused by the pressure update solving a Poisson problem for the provisional pressure gradient $p^{\blacklozenge}$ which appear in momentum equation like in the weak settings (5.16). Brown *et al.*[167] mentioned that the method of Hugues and Randriamampianina[53] could be further improved by using similar pressure update with the rotational term. This last options were tested but no difference was observed.

Different boundary conditions implemented in the solver are listed below for the sake of completeness, even though some of the boundary conditions simply set as homogeneous Neumann boundary condition just because there is no better guess.

Boundary conditions for $\mathbf{u}$ are probably the simplest, as $\mathbf{u}$ is discrete in time any Dirichlet or Neumann boundary condition can be easily implemented. Note that this boundary condition needs to be satisfied by adapting the boundary condition of the prediction step if boundary conditions of ψ are different from homogeneous Neumann boundary conditions considering the projection step.

Boundary condition of $\mathbf{u}^*$ [†] is more complicated, especially because this variable is function of the type of the projection method and because it is not a physical variable with well defined boundary conditions. However, the boundary condition of $\mathbf{u}$ can be considered as a sufficiently good guess for `PT=2` and `PT=3` but not for `PT=1` where the pressure gradient is set to zero in that case. This is why a tangential boundary conditions appears in the equation of $\hat{u}$.

Boundary condition of ψ is also difficult to determine because physical boundary conditions for pressure are usually unknown. Homogeneous Neumann boundary conditions are the primary choice in such cases, but it results in a singular Poisson equation for incompressible flow solvers requiring special treatment.

Boundary condition of $p^\blacklozenge$ is defined as Hugues and Randriamampianina[53] when it is used. An estimation of the pressure gradient at the boundaries is obtained by an extrapolation in time of the remaining terms of the momentum equation (see (5.16b))

Boundary condition of ϕ needs to be set in accordance with the boundary conditions of $\mathbf{u}$ and $\mathbf{u}^*$ as, at the projection step, $\mathbf{u}^*$ will be added to $\nabla\phi$ including at the boundaries. It is a correction step for `PT=2` and `PT=3` so homogeneous Neumann conditions are used in that cases. Using same boundary condition with `PT=1` is causing a strong change in $\nabla\phi$ thus extrapolation of the boundary condition in time is preferred especially in case of strong pressure gradient.

In MFLOPS3D-MD, Dirichlet, Neumann or periodic boundary condition types are available for all of the different boundaries listed above. Specific Dirichlet boundary conditions tailored for the wall bounded flow simulation such as an outlet boundary condition with standard advection and inlet boundary based on the interpolation of the Blasius profile are implemented. Periodic boundary conditions are only possible if there are multiple sub-domains in the direction of the periodicity. Even though

---

[†] Here $\mathbf{u}^*$ can be $\tilde{\mathbf{u}}$, $\hat{\mathbf{u}}$ or $\check{\mathbf{u}}$

periodic boundary condition can be implemented into the Helmholtz solver in the current version of the code this feature is build into the influence matrix but not in the Helmholtz solver. Thus periodic simulations has to be conducted with at least two sub-domains in the periodic direction.

5.2.4 Influence matrix method

In the current study, non-overlapping exact domain-decomposition (DD) method is used to achieve massive parallelization. In particular, influence matrix method approach (also known as Schur complement matrix[186] and continuity influence matrix[172]) is implemented in order to connect solutions of each sub-domain to the neighboring ones and obtain the boundary conditions of each sub-domain at once. As stated by Daube[187], "Influence matrix method makes use of the superposition principle for linear problems". This method provides a smaller linear system than the one which would be required to solve the equations on the full domain.

Convergence rate of overlapping domain decomposition (DD) method is $\mathcal{O}(H/h)$ where H is the width of the overlap, and h is the mesh size. Using really small overlap results to cheaper computation by sub-domain and by iteration, but the method would not converge fast. By contrast, having a large overlap leads to more computation per sub-domain, but the whole method converges faster. Using influence matrix method avoids this trade-off and influence matrix is better conditioned than the original system itself. On the other hand, the influence matrix method requires to form, to store and to solve a large system. The creation of the influence matrices is required only once as all the time steps use the same influence matrices. Even though the matrix is large, storing the matrix for the production runs is a better choice. Due to the large size of the system to solve direct methods practically impossible, therefore, it is solved iteratively using PETSc toolkit.

In practice, solving the multi-domain problem with influence matrix method lead to 3 main steps: (i) creating the influence matrix, (ii) obtaining the true interface values, and (iii) solve each sub-domain using true interface values. An adapted copy of the simple example given by Danabasoglu *et al.*[57] is reproduced in appendix C.3 to explain these steps in detail.

The algorithm describing the generation of the influence matrix can be found in algorithm 1 and the steps of the algorithm are detailed in appendix C.3.1. The step 2 requires solving the Helmholtz solver mentioned in the previous subsection. Influence matrix method has to be used with the same solver and boundary conditions types that he ones used to generate the matrix. It has to be used with the same solver coefficients as it is generated, meaning that the matrix is dependent on time step and Reynolds number as well as spatial discretization. In MFLOPS3D-MD, the matrix is generated using the same solver subroutines than the ones used during the solution of Helmholtz equations.

Algorithm 1 How to create an influence matrix

```
while Each point on the interfaces of each sub-domain do
    Nullify both the right-hand-side and boundary conditions
    Add a Dirac on the current interface point
    Solve with the Helmholtz or Laplace solver (has to be the one going to be used
  in time marching)
    Determine the place of this solution in the influence matrix (part of a row)
    Place the residual vectors, $R_i$ , to their corresponding place
    Repeat for all the other interface points
end while
```

The procedure explained in the appendix can be generalized for 3-dimensional problems with any number of sub-domains k. The computational domain $\Omega = \cup \Omega_k$ is partitioned into sub-domains with interfaces $\mathit{\Gamma}_{ij} = \Omega_i \bigcap \Omega_j$ therefore Helmholtz problems in each sub-domain become

$$\nabla^2 \phi_k - \sigma \phi_k = f_k \quad \text{in} \quad \Omega_k \quad \text{and} \quad \phi_k = g \quad \text{on} \quad \partial\Omega_k \cap \partial\Omega \tag{5.30}$$

where g is physical boundary condition on the exterior of the whole computational domain (or inside for specific problems). The interface conditions are obtained from the influence matrix solution by solving once the Helmholtz equation with zeros either Dirichlet or Neumann boundary conditions at the interface of each sub-domain. These interface conditions are used in the second solution of the Helmholtz problems. Steps of solving a Helmholtz or Laplace equation for multi-domain problems are summarized in fig. 5.2.

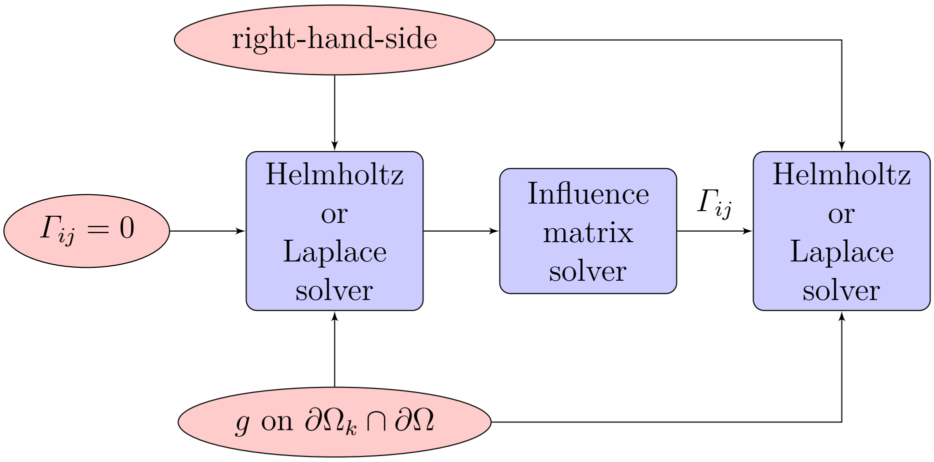

Figure 5.2 – Graphical presentation of the work-flow of the MFLOPS3D-MD to solve Helmholtz or Laplace equation for multi-domain problems with influence matrix method

An influence matrix should be defined for each unknown in the problem. However, this is not always necessary. If the unknowns have the same boundary condition types (regardless having the same boundary conditions) a single influence matrix is enough. For example, in the Navier-Stokes tests presented in the next chapter (section 6.4) only two influence matrices are used to solve the 3D problem instead of 4 (3 for velocities and 1 for pressure) which reduces the memory requirements and the time to generate the matrices. The current version of the MFLOPS3D-MD provides a single influence matrix for the all 3 velocity components and the second matrix for pressure. This choice is consistent with the fact that only single boundary condition types are accepted from the parameter file for velocity fields.

Size of the influence matrix

As mentioned by Abide and Viazzo[172] the cost of using an influence matrix can become a real issue especially for 3D cases. The size of the matrix can be estimated easily, but the important parameter is the memory usage as the number of non-zeros defines real memory cost. The system gets sparser when increasing the number of sub-domains. If N is the number of points on the one edge of a cubic full domain and M is the number of points on one edge of each sub-domain, the domain is decomposed on C^3 sub-domains of equal size. Size of the influence matrix is $\sim (6M^2C^3)^2$, but the sparsity of the matrix goes like $\sim 1/C^3$. Measurements of the size of the influence matrix for $2 \times 2 \times 2$ domain decomposition which leads to a full matrix as each sub-domain are connected is given fig. 5.3.

The scalable linear equations solvers (KSP) library of PETSc toolkit is used to solve the system associated with the influence matrix. It provides an easy-to-use interface

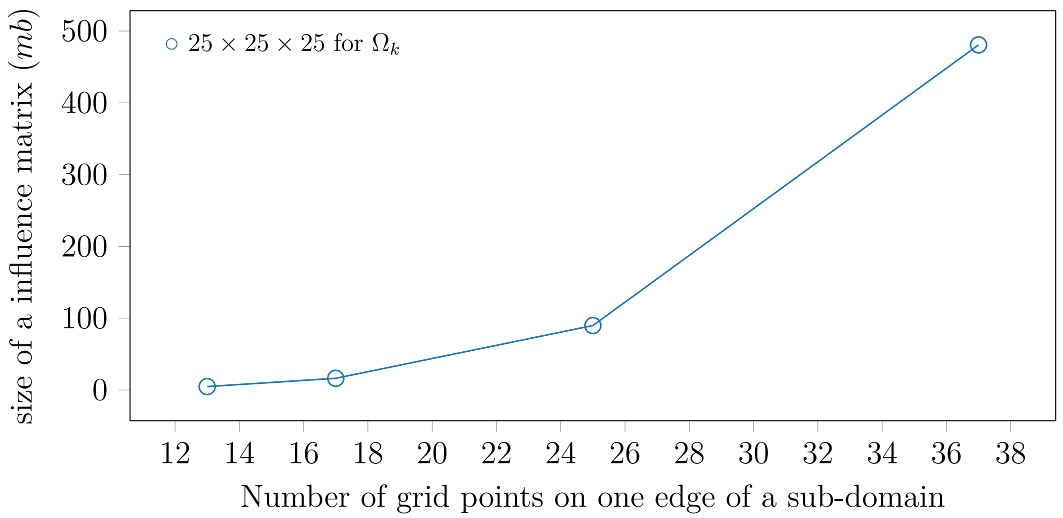

Figure 5.3 – Size of the influence matrix as function of the number of grid points of the full domain for 2 × 2 × 2 formation of the sub-domains.

to the combination of a Krylov subspace iterative method and a preconditioner or a sequential direct solver. In standard executions block Jacobi preconditioner are used with error limits for the iterative solvers `ksp_rtol` equal to 10^{-8} and 10^{-5} for $\tilde{\mathbf{u}}^{n+1}$ and ϕ (or $p^{\blacklozenge}$) respectively. These choices of parameters are selected like in the following commands prior to the execution.

```
export petscu='-u_ksp_rtol 1.e-8 -u_ksp_type lgmres -u_pc_type bjacobi -u_ksp_sub_pc_type ilu -u_sub_ksp_type gmres -u_sub_ksp_max_it 6 -u_sub_pc_type bjacobi -u_sub_sub_pc_type ilu -u_ksp_initial_guess_nonzero'
export petscp='-p_ksp_rtol 1.e-5 -p_ksp_type lgmres -p_pc_type bjacobi -p_ksp_sub_pc_type ilu -p_sub_ksp_type gmres -p_sub_ksp_max_it 6 -p_sub_pc_type bjacobi -p_sub_sub_pc_type ilu -p_ksp_initial_guess_nonzero  -p_ksp_constant_null_space'
mpirun -n 36 ./testnav $petscu $petscp
```

The solutions of the interface points for the components of $\tilde{\mathbf{u}}^{n+1}$ are typically obtained in few iterations. However, a solution of the interface points for ϕ or $p^{\blacklozenge}$ takes $10 - 30$ iterations in average for 2 × 2 × 2 domain configuration. It can reach up-to the maximum iteration limits (1000 in this case) suggesting that GMRES iterations are not converging when the larger domain configuration is used.

Treatment of the singular Poisson equation

The main difficulty with this solver is in the case of Poisson equations with homogeneous Neumann boundary conditions where the singular nature of the problem is transferred to the influence matrix system as observed by Abide and Viazzo[172]. Therefore, the solution of ϕ and $p^{\blacklozenge}$ requires special treatments of the singularity as singular linear systems are only solvable if and only if its right-hand side is orthogonal to the null space of the singular matrix.

The two well known methods are available in MFLOPS3D-MD namely removal of the null space[188] and one point Dirichlet. Implementation of these methods is slightly different for influence matrix than it would be to solve the Poisson equation but the same fundamentals are shared as discussed in the literature.

Generally, it is difficult to find efficient and accurate methods to solve a singular problem with infinite condition number. Specialized fast solvers exist for singular Poisson equations like cyclic reduction with a complexity of $\mathcal{O}(n^2 \log n)$, but they work on square grids with matrices $n \times n$. The method proposed by Golub *et al.*[189] allows to use non-uniform meshes, but the complexity of their algorithm is $\mathcal{O}(n^3)$. These methods cannot be utilized to solve our influence matrix which is quite large and can only be solved with iterative solvers. This is the reason why for practical reasons, GMRES methods provided by PETSc is kept.

Null singular vector removal

This method relies on the implementation of the PETSc toolkit to remove the null-space, and the use of the command line option `-ksp_constant_null_space` takes of the null space removal. There is no guaranteed treatment here. The method does not necessarily convergence to the good solution because of the ill-posed problems like our detection of the null space cannot be achieved in all the cases. The success of the creation of the null-space can be assessed, but even for the small simulations, it is an expensive operation.

Dirichlet boundary condition at a single point

Another widely used method consists of imposing a Dirichlet condition at one point along the physical boundaries of the domain. This results in a matrix which is no longer singular. Implementation of this treatment into the influence matrix is slightly different than for Poisson equation. Changing a single point on the boundaries of the physical domain means that a row of the influence matrix and a point on the vector at right-hand-side of the equation must be replaced. Nevertheless, for the cases where a Dirichlet pressure boundary condition along an entire boundary of the computational domain might be dictated by the physics of the flow, e.g., for an outflow boundary of the cavitating flow, the use of a Dirichlet pressure boundary condition is very suitable.

The problem with this technique is that it may produces a spike in the solution around the fixed Dirichlet point which eventually pollutes the entire domain.

5.2.5 Mapping

Dealing with complex geometries on structured meshes is a difficult task. Mapping offers an interesting trade-off when curvilinear coordinates are not truly needed to keep benefits from the simplicity of finite differences method instead of finite elements or finite volumes methods more adaptable to unstructured meshes.

The principle of mapping is to change the geometry of interest into a rectangular geometry in which standard Cartesian coordinate system can be used for discrete derivatives and solvers. The method leads to additional terms into the Navier-Stokes equations. It can be used only with smooth geometries but the benefit of a resolution with multi-domains is that sharp corners of the geometries can be implemented with sub-domain interfaces.

Two sets of coordinates can be defined: one to represent physical (mapped) coordinates denoted with the barred variables (e.g., $\bar{x}$) and another one for the Cartesian mesh without bars (e.g., x). Using this notation, the mapping is defined by

$$t = \bar{t} \tag{5.31a}$$

$$x = \bar{x} \tag{5.31b}$$

$$y = \frac{\bar{y}\,(y_b - y_a) + \eta_2(\bar{x},\bar{z},\bar{t})y_a - \eta_1(\bar{x},\bar{z},\bar{t})y_b}{\eta_2(\bar{x},\bar{z},\bar{t}) - \eta_1(\bar{x},\bar{z},\bar{t})} \tag{5.31c}$$

$$z = \bar{z} \tag{5.31d}$$

with $y_a \leq y \leq y_b$ and $y_a + \eta_1(\bar{x},\bar{t}) \leq \bar{y} \leq y_b + \eta_2(\bar{x},\bar{t})$.

An example of a geometry created with the mapping functions (5.31) is given fig. 5.4 to illustrate the Cartesian and physical coordinates.

In the current version of the MFLOPS3D-MD, only the y coordinate system is transformed to $\bar{y}$ and mapping functions can be defined as in (5.31) with curvatures on both the bottom and top walls. These mapping functions can be used to study flows around smooth 2D geometries but for more complicated geometries additional terms should be added. Similar mapping derivatives was introduced by Marquillie *et al.*[190]

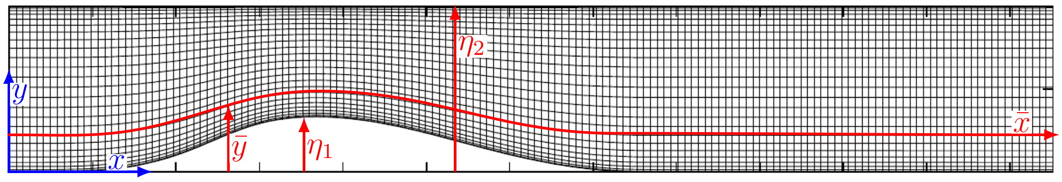

Figure 5.4 – Cartesian (blue) and mapped (blue) coordinates. Mapping custom function $y = f(x)$ on 2D grid.

for the case with only one mapped wall. The mapping can be function of time like for the problem of flapping plate studied by Ehrenstein *et al.*[160] or more general flows around moving (oscillating) geometries.

It is relatively easy to implement new derivatives on explicit terms. Derivatives in physical coordinates can be written in terms of derivatives in Cartesian coordinates as shown in appendix C.4 Therefore, existing derivatives in Cartesian coordinates can be used and complemented with additional one coming from the mapping. When these derivatives are used the results are on the physical coordinates, so no transformation is needed. Practically, the impact of the mapping on the derivative is seamless to the users as the wrappers of the derivatives on Cartesian coordinates are replaced with the new ones on the physical coordinates if the mapping is applied.

Transformed divergence and Laplacian operators can be separated in two contributions :

$$\bar{\nabla} = \nabla + \mathbf{G}_\eta, \quad \bar{\Delta} = \Delta + L_\eta \tag{5.32}$$

with

$$\begin{aligned} \mathbf{G}_\eta &= \left(\frac{\partial}{\partial y}\frac{\partial y}{\partial \bar{x}}, \frac{\partial}{\partial y}\left(\frac{\partial y}{\partial \bar{y}} - 1\right), 0 \right), \\ L_\eta &= \frac{\partial^2}{\partial y^2}\left(\frac{\partial y}{\partial \bar{x}}\right)^2 + 2\frac{\partial x}{\partial \bar{x}}\frac{\partial y}{\partial \bar{x}}\frac{\partial^2}{\partial x \partial y} + \frac{\partial^2}{\partial y^2}\left(\left(\frac{\partial y}{\partial \bar{y}}\right)^2 - 1\right) \end{aligned} \tag{5.33}$$

Consequently, the physical domain can be transformed into a Cartesian one which can be computed on variables (x, y, z).

$$\frac{\partial \mathbf{u}}{\partial t} + \mathbf{u}\cdot\nabla\mathbf{u} + \mathbf{u}\cdot\mathbf{G}_\eta\mathbf{u} = -\bar{\nabla}p - \mathbf{G}_\eta p + \frac{1}{Re}\Delta\mathbf{u} + \frac{1}{Re}L_\eta\mathbf{u} \tag{5.34a}$$

$$\nabla\cdot\mathbf{u} = -\mathbf{G}_\eta\cdot\mathbf{u} \tag{5.34b}$$

Equation (5.34) are the mapped version of the Equation (5.1). Projection methods can be applied on (5.34) following the same methods then the ones discussed before for the standard Navier-Stokes equations without mapping. For instance, for the projection method `PT=3` given in section 5.2.1 (`TO(1)=2`) the intermediate velocity are calculated with:

$$\left(\Delta - \frac{3Re}{2\triangle t}\right)\check{\mathbf{u}} = \left(\frac{-4\mathbf{u}^n + \mathbf{u}^{n-1}}{2\triangle t} + \nabla p^{\blacklozenge} + \mathbf{G}_\eta p^{\blacklozenge} + [\mathbf{u}\cdot\nabla\mathbf{u}]^{n,n-1} + [\mathbf{u}\cdot\mathbf{G}_\eta\mathbf{u}]^{n,n-1}\right)Re \\ - [L_\eta \mathbf{u}]^{n,n-1} \tag{5.35}$$

where the terms with $\mathbf{G}_\eta$ and L_η are solved explicitly for velocity components so existing linear solvers can be used without modification.

Following Marquillie *et al.*[190], physical gradient operator $\bar{\nabla}$ is used for the sake of stability when Poisson equation needs to be solved for the pressure related terms. Therefore pressure correction $\phi = p^{n+1} - p^*$ is obtained with an equation similar to (5.16e) with the physical gradient operator $\bar{\nabla}$.

$$\bar{\nabla}\phi^{k+1} = -\frac{3}{2\triangle t}\left(\mathbf{u}^{n+1} - \check{\mathbf{u}}\right), \qquad \bar{\nabla}\mathbf{u}^{n+1} = 0 \tag{5.36}$$

The Poisson equation for the pressure is obtained by applying the divergence operator to these equations combined with incompressibility condition, but the result is slightly different. As used in Marquillie *et al.*[190], iteration sequence is written in (5.37) with homogeneous Neumann boundary conditions.

$$\Delta\phi^{k+1} = \frac{3}{2\triangle t}\left(\nabla\cdot\check{\mathbf{u}} - \mathbf{G}_\eta\cdot\check{\mathbf{u}}\right) - L_\eta\phi^k \tag{5.37a}$$

$$\nabla\phi^{k+1}\cdot\mathbf{n} = -\mathbf{G}_\eta\phi^k\cdot\mathbf{n} - \mathbf{G}_\eta\phi^k\cdot\mathbf{n}_\eta - \nabla\phi^k\cdot\mathbf{n}_\eta \tag{5.37b}$$

where normal vector around the geometry is

$$\bar{\mathbf{n}} = \frac{1}{\sqrt{1+\left(\frac{\partial\eta}{\partial x}\right)^2}}\left(\mathbf{n} + \mathbf{n}_\eta\right) \quad \text{with} \quad \mathbf{n} = (0,1,0) \quad \text{and} \quad \mathbf{n}_\eta = \left(-\frac{\partial\eta}{\partial x}, 0, 0\right) \tag{5.38}$$

Finally, divergence-free velocity field and new pressure are obtained with:

$$\mathbf{u}^{k+1} = \mathbf{u}^* - \frac{2\triangle t}{3}\left(\nabla\phi + \mathbf{G}_\eta\phi\right) \quad \text{and} \quad p^{k+1} = p^{\blacklozenge} + \phi \tag{5.39}$$

where $\check{\mathbf{u}}$ can be $\hat{\mathbf{u}}$ or $\tilde{\mathbf{u}}$ and $p^{\blacklozenge}$ can be 0 or one of the extrapolation formula (5.15) depending on the projection type being used.

The use of a mapping and a strong stretching of the grid can lead to complex eigenvalues which is not suitable to obtain a clean solution for each sub-domain.

5.3 Other features of the code

Tripping function from Schlatter and Örlü[6] as explained in section 3.1.3 for Incompact3d is also implemented for MFLOPS3D-MD. Also to simulate pressure driven simulation another forcing to maintain required pressure gradient was implemented.

Parallel I/O relying on netCDF4 similar to the one explained in section 3.1.2 for Incompact3d is also available in MFLOPS3D-MD. However, in the current version, *netcdf-open-par* is based on a different library than the one used in Incompact3d which is known to perform better with a large number of MPI processes (> 100).

In the early stage of development, MFLOPS3D-MD did not follow test-driven development requirements, but included simple tests. During the current study, a built-in test suite was developed, including earlier tests and many additional ones, as it was found to be the reliable way to progress efficiently in the development of the code. At this moment, built-in tests are probing more than 150 functionality of the code. The details of these tests will be presented in chapter 6 when analyzing some properties of the solver.

5.4 Performance Analysis

Performance analyses of the code are conducted on the CINES machine OCCIGEN. The HPC monitoring tools Scalasca and TotalView are used along with direct measurements. As expected, solving influence matrix takes more time than to solve Helmholtz equation (2 order of magnitudes more in the worse cases). Another computationally expensive part is the generation of the influence matrix, but this has to be done only once at the beginning of the simulation. So the cost of matrix generation will be neglected in the following discussions. There is no other particular bottleneck detected, means that parallelization strategy works as planned.

The first configuration is designed to observe strong scaling characteristics by using a periodic cube with the physical size $[2\pi, 2\pi, 2\pi]$. It is resolved with 145^3 grid points. The code was executed with different sub-domain sizes to solve the same domain. The results of strong scaling are satisfactory as shown in fig. 5.5. The results suggest that MFLOPS3D-MD scales better than the ideal case (100% efficiency). However, this effect is due to the fact that the number of non-zeros of the influence matrix (which is

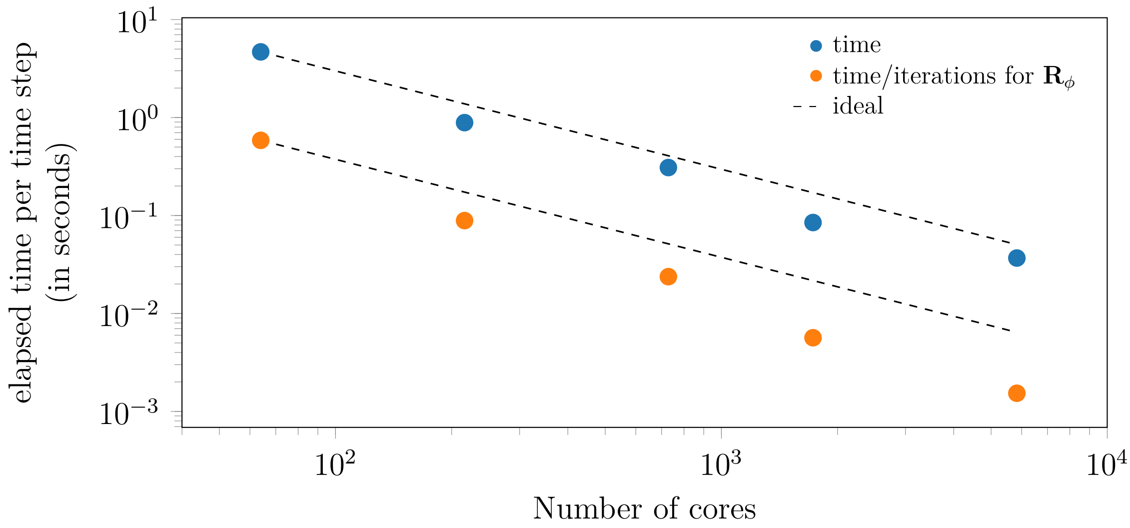

Figure 5.5 – Strong scaling of the MFLOPS3D-MD with the global domain Ω discretized with $145 \times 145 \times 145$ points. The elapsed time per time per time step (blue) is compared to the same quantity rescaled by the number of iterations to solve the influence matrix for ϕ ($\mathbf{R}_\phi$) (orange).

decreasing per MPI process) is getting smaller, so the computationally most expensive part becomes easier to handle.

The second group of tests was performed to analyze the weak scaling properties of the code. In these tests, a sub-domain of fix size (25^3) is duplicated with the number of MPI processes. The results in fig. 5.6 reveals the bad weak scaling performances. Such results usually happen due to communication cost of MPI, but the similar problem should be observed similarly on strong scaling as well. Also, it is confirmed that the memory cost of an influence matrix is not increasing more than few *megabits* per MPI process. On the other hand, the number of iterations required for the KSP solver of the influence matrix for pressure is increasing dramatically to solve the influence matrix and explains the poor week scaling. Once the computational time normalized with the number of iteration, correct weak scaling properties are recovered.

These tests suggest that, an optimum configuration to run simulations with MFLOPS3D-MD is with sub-domains containing $\sim 20 - 30$ grid points per direction. At this size, the cost of solving influence matrix is $10 - 100$ times more expensive than solving the Helmholtz equation but this ratio increases rapidly with the size of sub-domains. Sub-domain size smaller than $\sim 20-30$ grid points might be faster to solve but lead to a very large number of MPI process for large problems. Moreover, high order compact finite differences require a sufficient number of grid points which can be treated with central scheme.

Simulations with MFLOPS3D-MD are running at $100\mu s$ per grid point per iteration if

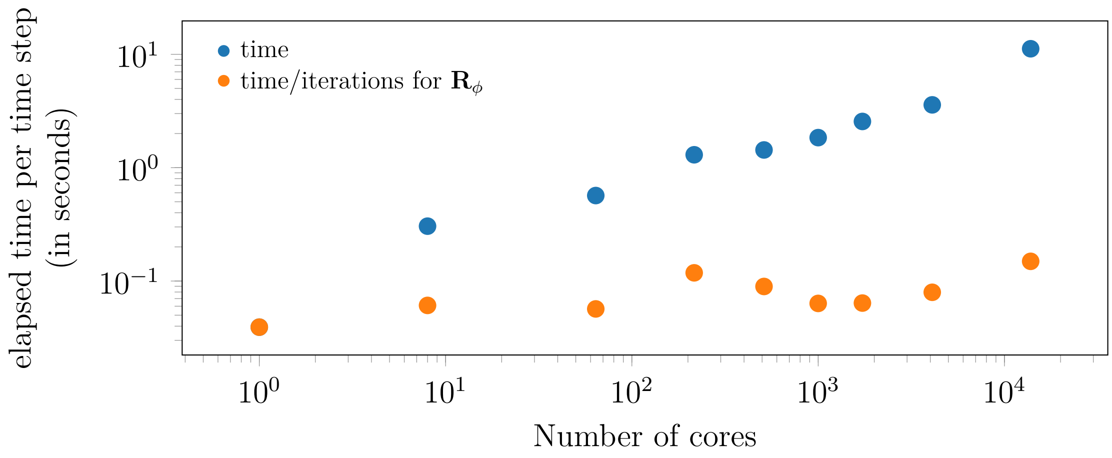

Figure 5.6 – Weak scaling of the MFLOPS3D-MD with sub-domains Ω_k of size $25 \times 25 \times 25$ (same notations as in fig. 5.5.)

the number of iteration for the pressure solver stays constant. The problem mentioned above does not exist for the solution of the influence matrices for velocity components as they often get solved within $3-5$ iterations independently from the number of domains. The reason behind the increasing number of iterations for the pressure solver which seems proportional to the number of sub-domains is not investigated directly in the current study. However, discussions about the stability of the code in the chapter 6 are related to this observation as the singularity of the system appears to be one of the main reason.

Validation of MFLOPS3D-MD

6

This chapter is dedicated to the validation and the investigation of the stability problems faced by MFLOPS3D-MD. A built-in test environment of MFLOPS3D-MD was developed to accomplish this task. The objective is to identify the numerical problems that need to be solved in the future development of the code. Two different ideas for the stabilization of the solver are proposed. In addition to these tests within the code, a simpler Python script is written to solve Burgers equation with the same compact finite discretization and direct solver used in the code in order to evaluate the algorithms in a simpler 1D problem.

6.1 TBL simulation at $Re = 200$

Before a complete investigation of the code at high Reynolds number, a simulation of a laminar boundary layer at $Re = 200$ was conducted on multi-domain. A total of 384 CPU are used in sub-domain configuration $32\times4\times3$ with each domain containing $21\times21\times21$ grid points. 8th order compact finite difference as given in appendix C.1 used both for the derivatives and solvers. Results are obtained with the projection method `PT=3` (with the first step of pressure estimation) following the method introduced by Hugues and Randriamampianina[53]. Skew-symmetric form of the nonlinear term is used with forward difference scheme `NLT = (2,1)`. Implicit Euler time step for the unsteady term and the nonlinear term estimation based on the previous time step is used without any extrapolation for pressure (`TO=(1,0,1)`). Pressure prediction $p^{\blacklozenge}$ and correction ϕ are both calculated with Neumann boundary conditions. All of the boundary conditions for velocity components are Dirichlet, unlike the large TBL simulations described in chapter 3. No-slip and moving wall with the $\mathbf{u}_{y_{max}} = (u_\infty, 0, 0)$ boundary conditions are used for the bottom wall and the upper boundary respectively. Inlet and outlet boundary conditions are the same as (3.4) and (3.5).

As an example of the effect of the influence matrix, streamwise intermediate velocity fields are shown in fig. 6.1 for the two internals step of the momentum equation solution. Results demonstrate that influence matrix is able to satisfy continuity.

The number of iterations for the influence matrix for momentum equations and pressure solvers are very different similarly to the results of the performance tests given in the previous chapter. Additionally, it is observed that iterative solver performs

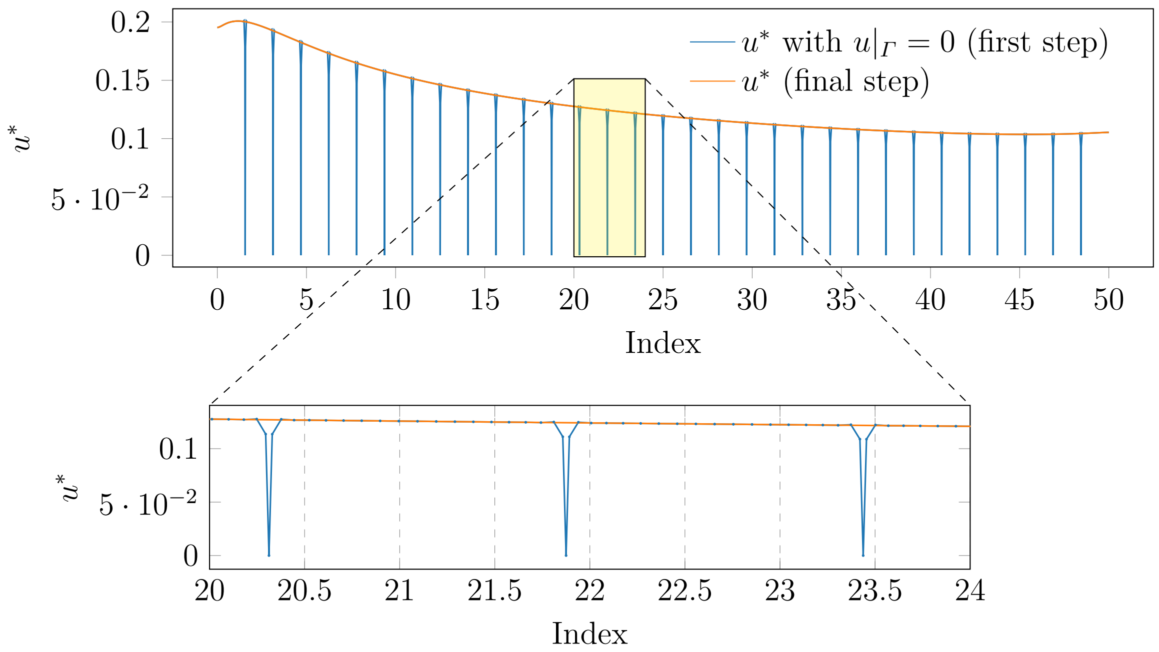

Figure 6.1 – Streamwise intermediate velocity with the zero and calculated interface values over a line in the streamwise direction. The interface values are computed with solving influence matrix **R**. The details of the work-flow are given in fig. 5.2.

relatively better after few time steps. Once the solution starts to converge, influence matrix for pressure requires around $\sim 200 - 300$ iterations while velocity components it is usually less than 5 iterations for a maximum error of iterative linear solver of 10^{-8} for the velocity and 10^{-5} for the pressure. A large number of iteration for the pressure is linked to the singularity of the problem Poisson problem due to Neumann boundary conditions. Some other preconditioners for the linear system solvers than the block Jacobi were also tested (e.g., Conjugate gradient) and better results are obtained in terms of the number of iterations. However, these preconditioners used in those tests are slower, so there is no satisfactory solution yet to this problem.

The advantages of the spatial discretization of MFLOPS3D-MD were mentioned in the previous chapter. To generated a stretched grid suitable for boundary layer simulation, the height of each domain is weighted with coefficients given by the following formula

$$\sum_{i=1}^{N_y} (\beta + 2(i-1)(1-\beta)/(N_y - 1)) \tag{6.1}$$

where the coefficient $\beta = 0.25$ is the stretching strength, and N_y is the number of domains in the y-direction.

In this way, a global stretching is applied by changing the size of each sub-domain without stretching each sub-domain. Meanwhile, a local symmetrical stretching is

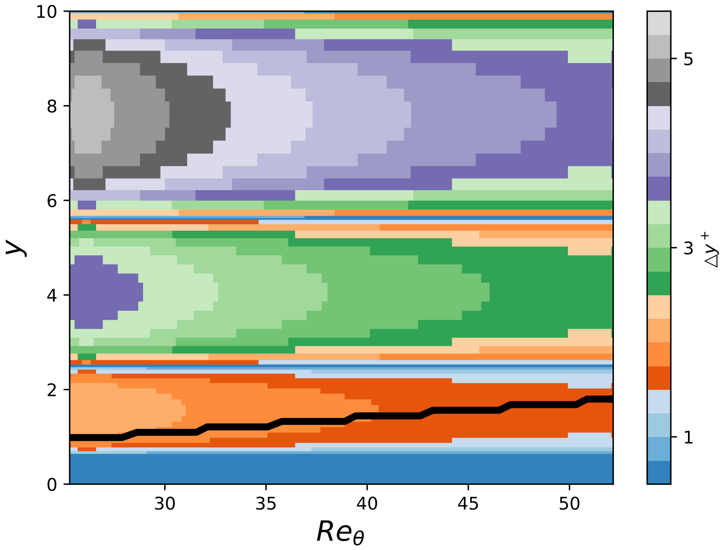

Figure 6.2 – Variation of the spatial resolution in the wall-normal direction is in streamwise and wall-normal directions used in the TBL simulation with $Re = 200$. The black line represents boundary layer thickness δ.

applied to refine the mesh at the edges of each sub-domain to avoid aliasing effect due to high order finite difference schemes. An example of such stretched grid used in this TBL simulation is given in fig. 6.2.

The above settings allowed to integrate the equations over an extended period (2 flow through times based on U_∞). One way to quantify the success of the projection step is to compare divergence of the fields before and after the projection steps. In fig. 6.3 average (for internal nodes) and maximum values of the divergence are plotted as a function of the number of iterations. Average value of the divergence inside the domain systematically decreasing and converging to a constant because this is a laminar flow case. It is striking that maximum divergence value is not decreasing but increasing even though overall divergence is being corrected in average. However, these maximum values are not necessary at the same points meaning that the projection may have a negative effect somewhere in the flow. Additionally, after 2000 iterations, strange oscillations of maximum divergence have occurred. The regularity of the velocity fields (fig. 6.4) does not point out any anomaly before these oscillations are damped again.

This problem of projection is quite sensitive to the parameters of the simulations. Slightly different stretching or the number of grid points lead to instability even after few thousand time steps. The high Reynolds number simulations show a constant slope systematically in the values presented in fig. 6.3 leading to a diverged simulation. It usually takes few hundred iterations for this effects to surpasses the level of the divergence due to the accuracy of the projection method. In that case, waves appear close to the boundaries/interfaces (often at the corners of the sub-domains).

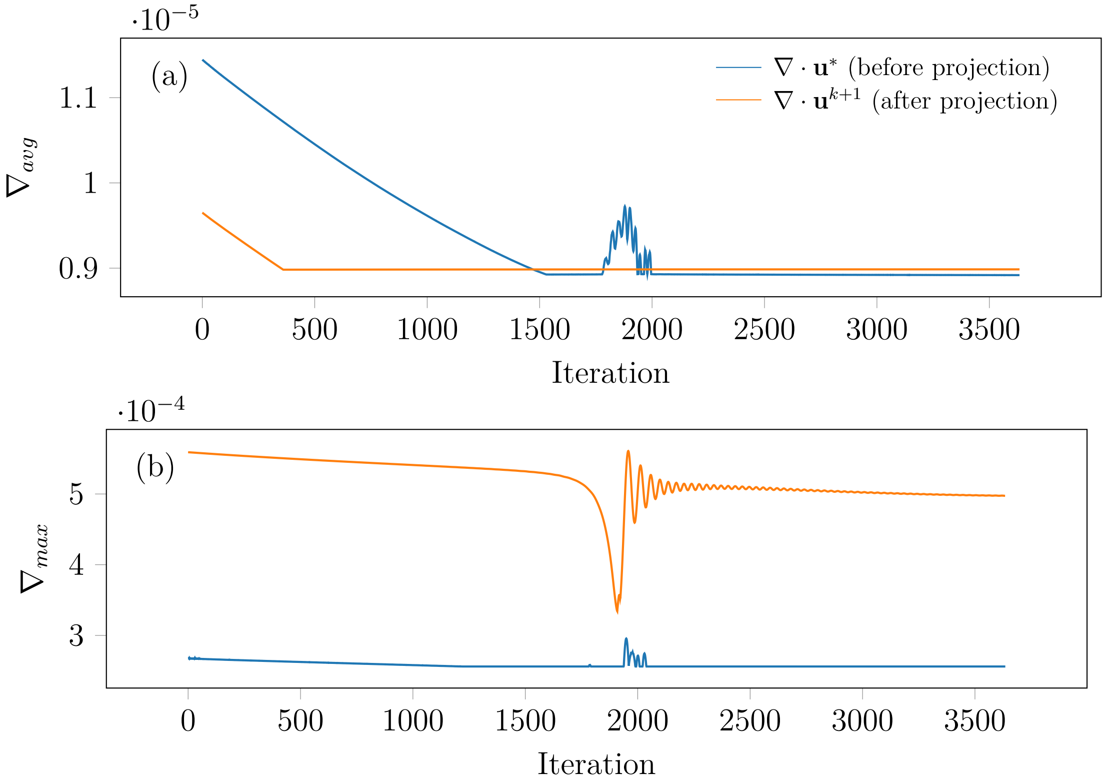

Figure 6.3 – Average of internal nodes values (a) and maximum values (b) of divergence during the simulation of TBL at $Re = 200$ to observe the effect of projection method.

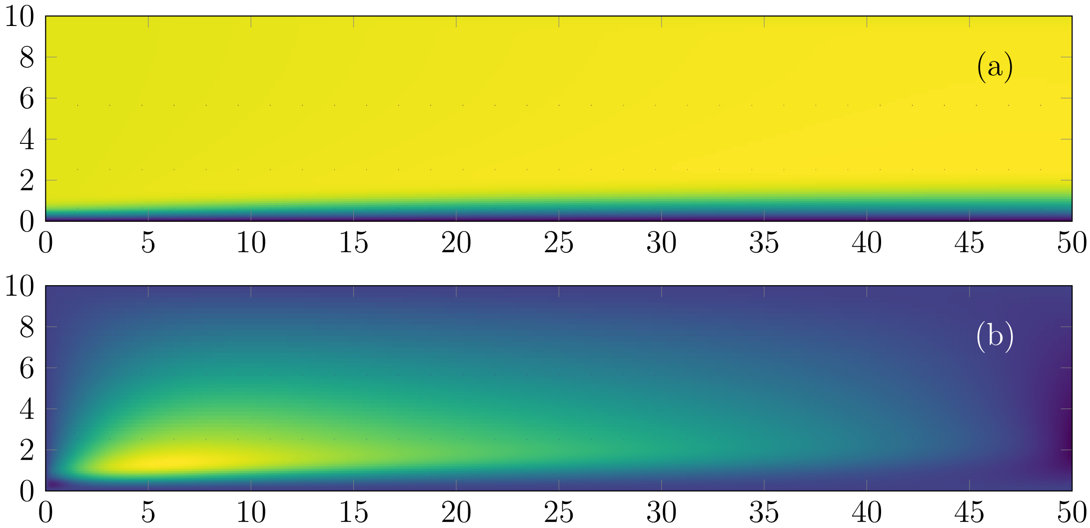

Figure 6.4 – Streamwise (a) and wall normal (b) velocity components for the sample TBL simulation. Small dots in the fields are the points of the edges in spanwise direction colliding to the plane plotted in this figure which never get computed.

6.2 Tests with Burger equation solver

Investigation of the stability problems will be examined further in this section solving a 1D problem. In order to demonstrate the problem on a simple problem, Burger equation is solved with the same spatial and temporal discretization used in MFLOPS3D-MD. This part of the study was conducted with a separate code written in Python and does not include all of the features of MFLOPS3D-MD, especially the multi-domain solver.

Burger equation was chosen because it is a simple case to compute transport of the initial waves. The effect of Reynolds number can be observed easily and the solution can be compared with the exact one. Two different direct solvers were tested including the eigenvalue decomposition as in MFLOPS3D-MD and the LU decomposition which requires more computations in 3D but which is very fast in 1D.

The 1D Burger equation is

$$\frac{\partial u}{\partial t} + u\frac{\partial u}{\partial x} = \nu\frac{\partial^2 u}{\partial x^2} \tag{6.2}$$

where $u = u(x,t)$.

Solutions in this section will be obtained with an implicit solver,

$$D_x^{(2)}u_i^{n+1} - \sigma u_i^{n+1} = \left(uD_x^{(1)}u\right)^{n,n-1} Re \tag{6.3}$$

where $D_x^{(2)}$ and $D_x^{(1)}$ are the discrete first and second order derivative operators in matrix form generated with compact finite difference schemes (see appendix C.1). $\left(uD_x^{(1)}u\right)^{n,n-1}$ is a second-order approximation as defined in (5.24) with the terms calculated in skew-symmetric form as in (5.25) where σ with approite coefficient of the temporal discretization and Reynolds number Re are defined as before.

This discretization leads to a 1D Helmholtz problem to solve like the ones solved in MFLOPS3D-MD. Linear system is solved with direct solvers similarly. Eigenvalue decomposition method gives the same results than the LU decomposition.

Current results will be given only for 4th and 8th order schemes. They are exactly like in the DNS code meaning that the stencil for central points is as given in Lele[56] but for the backward/forward stencils are different (see table C.1).

Instability problems can be related to the CFL and diffusion condition. Formally[191] these conditions are,

$$\frac{|U_{max}|\triangle t}{\triangle x_{min}} \leq \frac{\sigma_i}{k'_{max}} \tag{6.4}$$

and

$$\frac{\nu \triangle t}{\triangle x^2_{min}} \leq \frac{\sigma_r}{k''_{max}} \tag{6.5}$$

where U_{max} is the maximum velocity magnitude, $\triangle x_{min}$ is the minimum grid spacing, σ_i and σ_r are the bounds of the stability region of the time discretization schemes. Maximum modified wavenumbers for the second derivatives k'' is defined in (C.5). A similar equation can be derived for k' as well following the given steps. Reference values for standard stencils on homogeneous grids are available in Lele[56].

The initial conditions for the Burger equation were chosen as[†]:

$$u(t=0) = -2\frac{\nu}{\phi_o}\frac{\partial \phi_o}{\partial x} + 4 \tag{6.6}$$

with $\phi_o = e^{-(x)^2/(4\nu)} + e^{-(x-2\pi)^2/(4\nu)}$.

The analytic solution is

$$u(x,t) = -2\frac{\nu}{\phi}\frac{\partial \phi}{\partial x} + 4 \tag{6.7}$$

with $\phi = e^{-(x-4t)^2/(4\nu(t+1))} + e^{-(x-4t-2\pi)^2/(4\nu(t+1))}$.

A periodic boundary conditions will be used ($u(0) = u(2\pi)$).

Results using 4th and 8th order compact finite difference schemes for two difference CFL numbers are compared in fig. 6.5. An instability due to the CFL condition appears in the solution when the 8th order compact scheme is used with $CFL = 0.5$. As expected higher order compact finite difference discretization required lower CFL as the maximum modified wavenumber k'_{max} increases with the order of the scheme (see Lele[56] fig. 1). One can notice that problem initiates for large values of u close to U_{max}. These cases allow us to determine a safe CFL number and to show how the stability problem due to such instability appears in the solutions.

The main problem encountered in MFLOPS3D-MD is not a CFL problem, and it normally appears close to the boundaries with the high Reynolds numbers. It was decided to start the simulation with a constant convection velocity and perturbing the inlet velocity in time with sinus waves because of the strong gradient at the initial condition of the exact solution of the Burger equation (6.7). So, the base flow with a given magnitude should convect and dissipate the sinus wave. Initial field is a constant

---

[†] Same as given in CFD Python: 12 steps to Navier-Stokes :: Lorena A. Barba Group

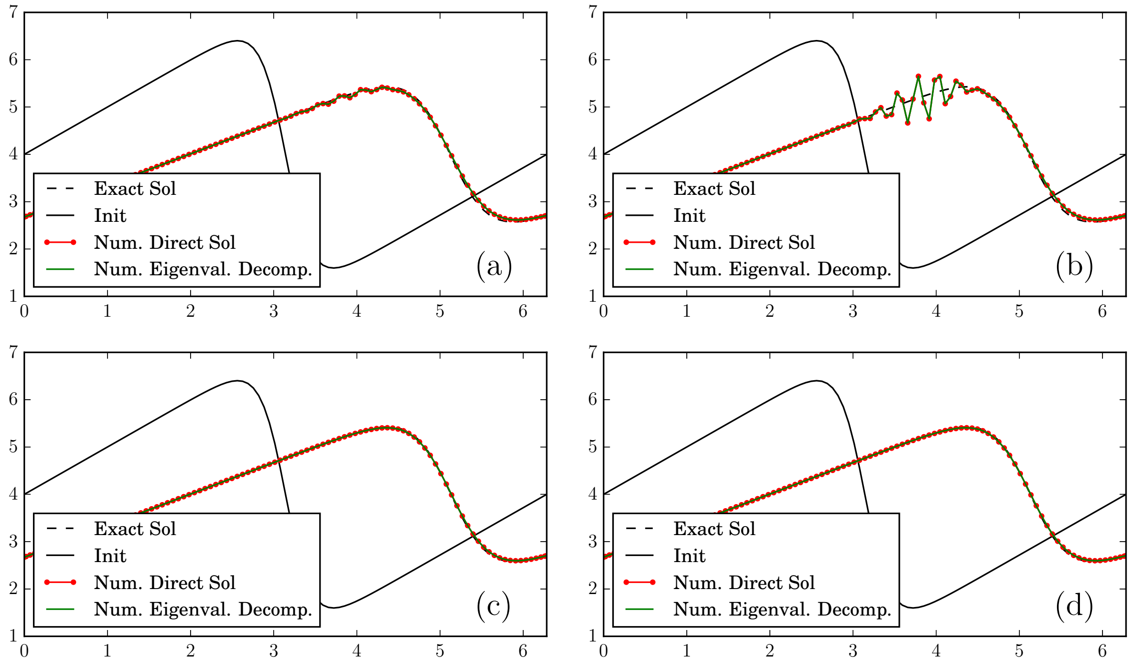

Figure 6.5 – Solution of the Burger equation after 100 time steps initialized using (6.7). The results are obtained with 4th (a, c) and 8th (b, d) order compact finite difference schemes for $CFL = 0.5$ ($\triangle t = 0.005$) (a, b) and for $CFL = 0.25$ ($\triangle t = 0.0025$) (c, d). σ is 400 ($\nu = 0.5$) for all the results.

velocity, with the magnitude of 1. Inlet boundary condition is $u_0 = 1 + 0.1 sin(i\pi\triangle t)$ where i is the time step. Homogeneous Neumann boundary condition is used for outlet condition. Low frequency forcing waves are used to identify better high-frequency fluctuations like the ones observed in the MFLOPS3D-MD Navier-Stokes solver. As previous results have shown that $CFL = 0.25$ satisfies the stability of the scheme, $CFL = 0.15$ was chosen to stay on the safe side.

The expected solution for this test is given in fig. 6.6 (a) in which sinus waves dissipate and convects without spurious oscillations due to instabilities. Figure 6.6 (b) demonstrates the problem observed in Navier-Stokes solver. The solution destabilized by changing viscosity from $\nu = 0.015$ to $\nu = 0.014$. This small increase of σ demonstrates how the Helmholtz equation solver is sensitive to viscosity (wavenumber). Velocity is increased artificially almost up to 50% of the convection velocity even though the forcing is only 10% of it at maximum. Only the results for 4th order solver are shown. However, results with the 8th order scheme behave similarly. The results described above were obtained with a regular grid. In order to test the effect of the grid, some tests were conducted with stretched grids.

The stretching used in these examples are such that the ratio between the minimum and the maximum grid spacing is around 4 (which is the optimum for 8th order

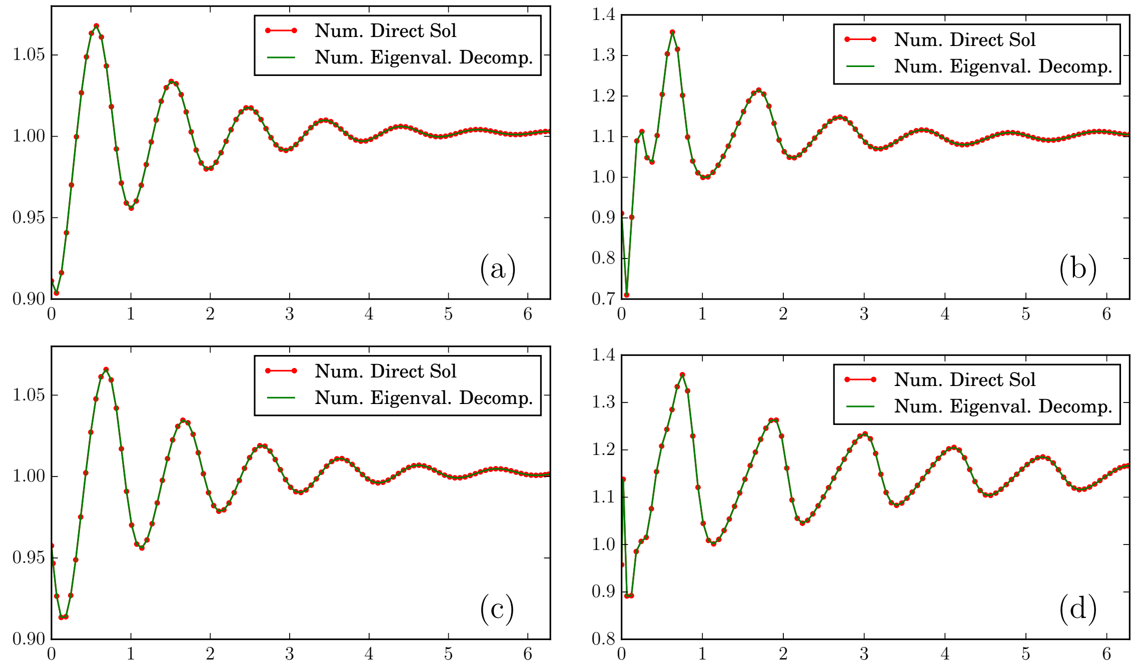

Figure 6.6 – Solution of the Burger equation after 6000 time steps using 4th order compact finite difference schemes with $CFL = 0.15$ ($\Delta t = 0.001$). The results are for $\nu = 0.015$ ($\sigma = 1300$) (a, b), $\nu = 0.014$ ($\sigma = 1400$) (c) and $\nu = 0.0076$ ($\sigma = 2600$) (d) on a regular grid (a & b) and stretched grid (c, d)

scheme, based on the distribution of the accuracy of the derivatives). The equivalent results of fig. 6.6 (b) are shown in fig. 6.6 (c) for the stretched grid. Note that high-frequency oscillations have disappeared. However increasing σ ($\nu = 0.0076$) leads to the same instability again.

For the accurate solution of the Helmholtz problem, $\sqrt{\sigma}\triangle x$ has to be small. However, even if $\sqrt{\sigma}\triangle x$ is constant, when k increased numerical accuracy is lost rapidly. Solving Helmholtz equation with the high wavenumbers $\sqrt{\sigma}$ can lead to such problems, known as "pollution effect"[192]. This problem can be solved for 1D entirely[193] but not for the 2D and 3D problems. Attempts to fix this problem in 3D is discussed in section 6.3.3.

6.3 Test suite

Before going deeper in the analyses of the stability problem of the Helmholtz solver, a description of the testing methodology is first given. In order to ensure the benefit of the following tests to provide effective guidance for the future development of the code, an advanced test suite was built. The test suit uses a small FORTRAN test framework known as "FORTRAN Unit Test Framework" (FRUIT). FRUIT is written in FORTRAN 95 and has features such as assertion, fixture, setup, tear-down, report,

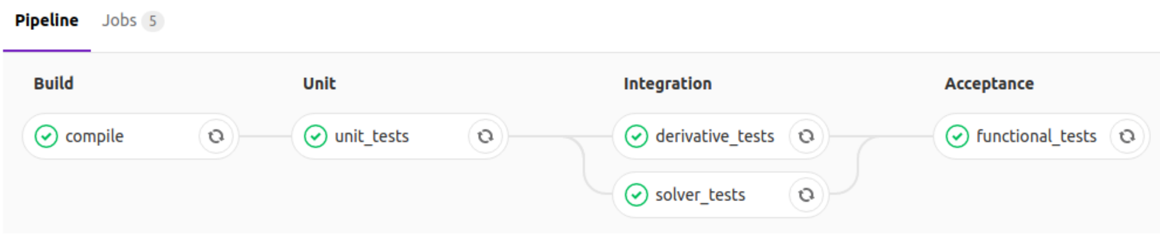

Figure 6.7 – A screen-shot of the pipelines on Gitlab CI

spec, driver generation. Originally, "Rake" is used as build tool which requires using language Ruby. The core of the testing part is in FORTRAN and can be used independently of the Ruby codes. Using Ruby was found to be counter-productive and against the strategy the research group. So instead of using Ruby, build is carried out with cmake which is already used for MFLOPS3D-MD. Integration to Git-lab CI is also maintained during this work (fig. 6.7).

Tests are in four main segments: build, unit, integration, and acceptance. Build only includes the compilation of the code and test is done for a single system so far. This particular build also provides the executables for the following tests. Unit tests are the simplest possible tests for an individual unit of source code as used in software development practices. Derivatives and solvers require integration of the important parts of the code, so they are added to the pipeline as the third step. The last step consists of functional tests which are full Navier-Stokes solutions based on the Ethier and Steinman[194]. In conclusion, all these assertions included in the code at this moment provides a great deal of help to developers and quick access to simple test cases. All the tests shown below are part of this test suit.

Many parameters alter the tests made for the investigation of the stability problems emphasized in section 6.1. Therefore, only 3 types of grids are allowed to be used with tests, as it is thought to be helpful to define various spatial discretization. The tests also ensure that acceptable grid is used as some stretchings are impossible[195]. Grid stretching with $\alpha = 0.9$ and $\alpha = 0.8$ (5.21) are safe up to 8th order schemes which are the highest order of accuracy used in this study (fig. 6.8).

6.3.1 Derivative tests

As shown in the appendix C.1, depending on the position inside the domain, different compact finite difference schemes are used. Therefore convergence tests are represented for these 3 different types of grid points separately, (i) internal points (ii) points on the edges and (iii) points next to the edges. The derivatives are computed on a domain Ω using different grid spacing h and L_2 error is shown for these

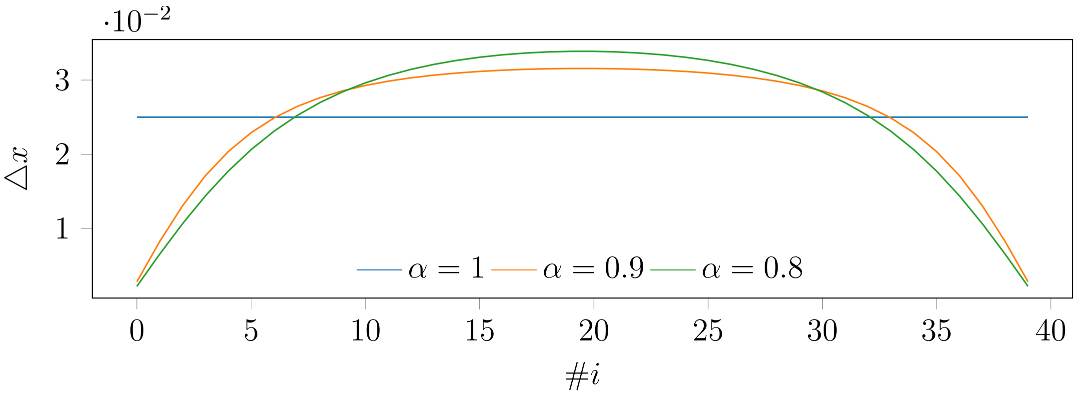

Figure 6.8 – Grids used in the following tests for single domain cases, generated with eq. (5.21)

different grid sizes (see fig. 6.9). The parameters `SO(1)` and `SO(2)` are used to define the order of derivatives and solver respectively. A fixed stencil size is not used for all points but the order based on the order of accuracy of the central points (see appendix C.1). Schemes of the first order derivatives are always one order higher than the second order derivatives as same stencils are used for both derivatives.

In addition to the convergence tests, the effect of the stretching needs to be assessed on the actual error of the derivatives for a given function. The error of derivatives of the simple trigonometric function

$$f(x, y, z) = sin(2\pi x) + sin(2\pi y) + sin(2\pi z)$$

is given in fig. 6.10 to demonstrate that stretching can be adjusted to diminish error on the backward/forward points. For all cases, the error of the derivatives in the middle of the domain is a few orders of magnitudes smaller than for the borders. As stretching is getting stronger the errors of the derivatives are decreasing. In the last row, α is 0.8, and the error is not decreasing any further.

The results show that stretching provides the desired effects, but extreme stretching is not necessarily giving better results as for a fixed number of points this naturally means coarser mesh for the middle points. Results are not given for multi-domain cases as the derivatives are only calculated inside a sub-domain.

6.3.2 Solver tests

Before testing the solver on Navier-Stokes equations, it is first evaluated on pure diffusion problems with the stretched grid ($\alpha = 0.9$) which is also used to test the derivatives (fig. 6.8).

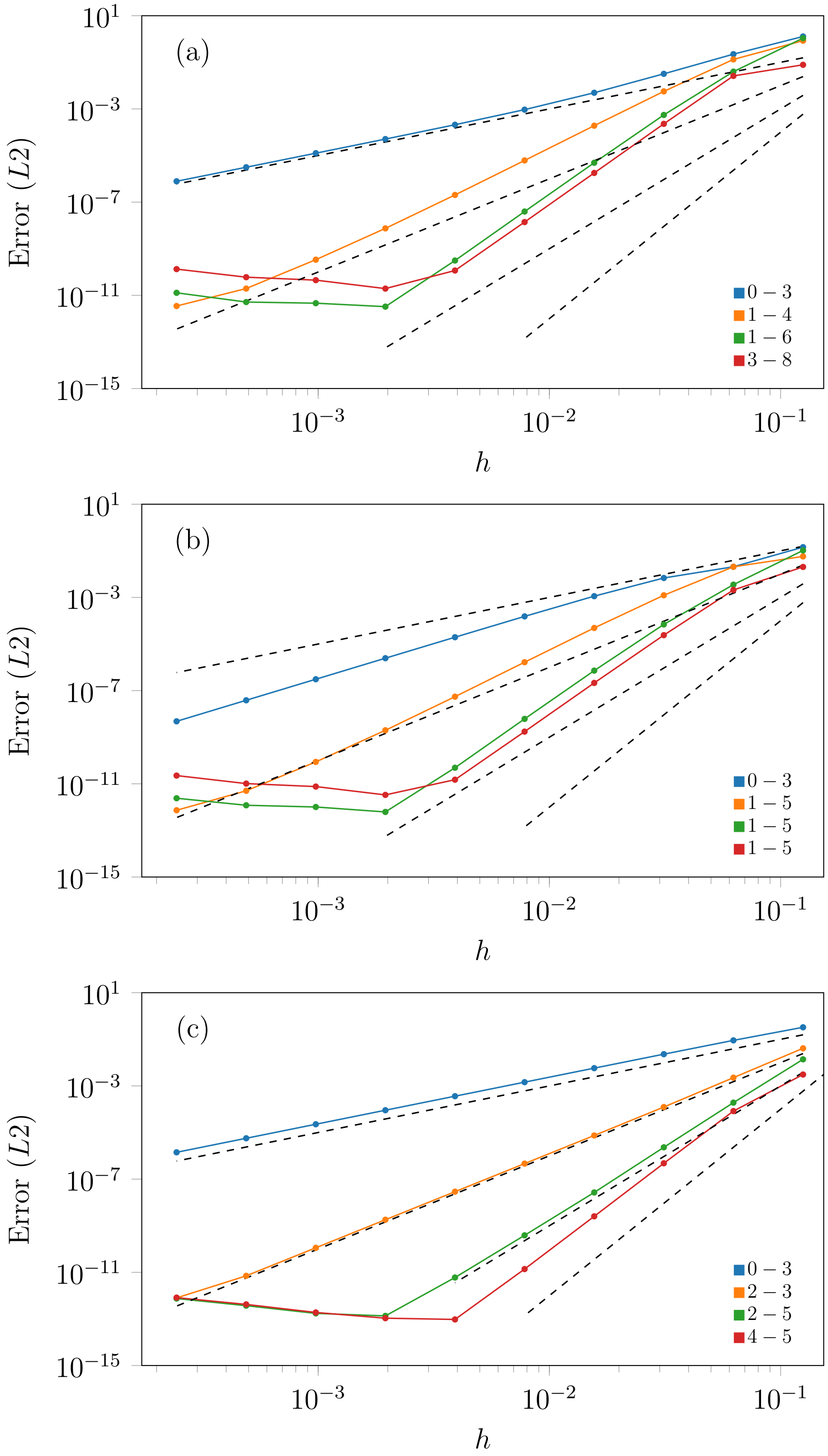

Figure 6.9 – L_2 error of first order derivatives of the function $f(x, y, z) = sin(2\pi x) + sin(2\pi y) + sin(2\pi z)$ for different order of schemes for points on the edges (a), points next to the edges (b) and internal points (c). Stencils are described in table C.1. Each color is for a given stencil indicated in the legend of each plot.

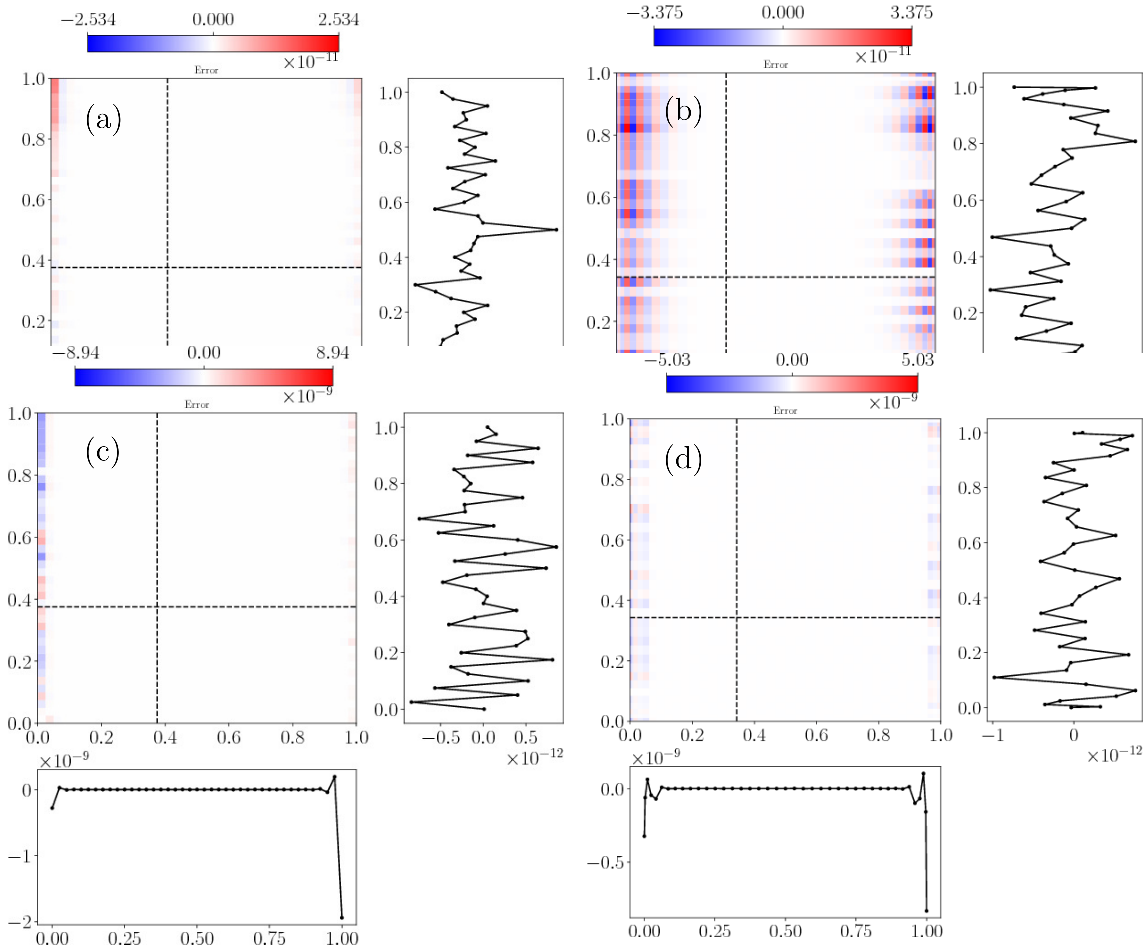

Figure 6.10 – Error on the first (a, b) and second (c, d) derivatives of the function $f(x, y, z) = sin(2\pi x) + sin(2\pi y) + sin(2\pi z)$ using 8th order compact finite difference schemes unstretched grid with $\alpha = 1$ (a, c) and stretched grid with alpha=0.9 (b, d)

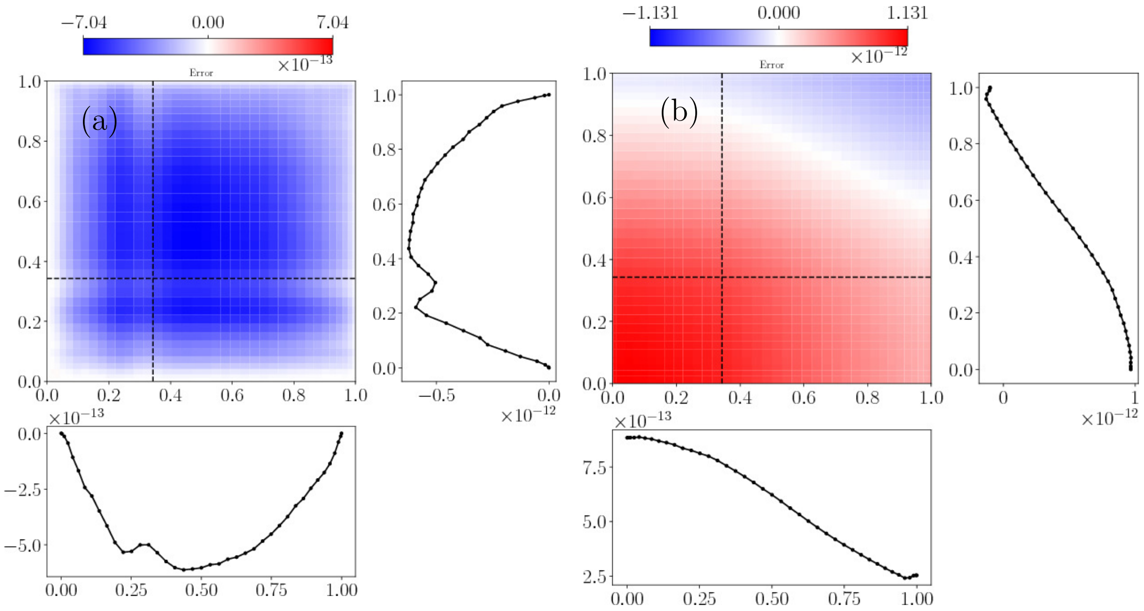

Figure 6.11 – Errors of the 8th order solver on a single domain with full Dirichlet (a) and full Neumann (b) boundary conditions with the second grid described in fig. 6.8 with $\alpha = 0.9$. Exact solution of the system is $f(x, y, z) = e^{\sqrt{2}xyz}$

Figure 6.11 (a) shows the expected behavior of the Laplace solver with Dirichlet boundary conditions. The error is very low at the boundaries and grows slightly in the center of the domain. Laplace solver with Neumann boundary conditions is also working as expected where the Neumann condition seems to be satisfied (fig. 6.11 (b)).

The similar results on multi-domain (see fig. 6.12) field are given in fig. 6.12. These results are obtained using influence matrix method. The interface points have a higher error with a maximum close to the junctions of the interfaces as this area has the most difficult conditions to satisfy. The overall error is at the level of the convergence limits set for the iterative solver suggesting that solver converged as expected.

In conclusion, these tests show that the linear solver is working correctly with different boundary conditions in both mono-domain or multi-domains. Influence matrix method is able to provide interface values within the accuracy of the iterative solver. Results above demonstrates that the spatial discretization works correctly. Derivatives and solver (with second-order derivative coefficients) are reliable. Below, the discussion is going to focus on the Helmholtz solver to improve the performance and stability of the code for high Reynolds number simulations.

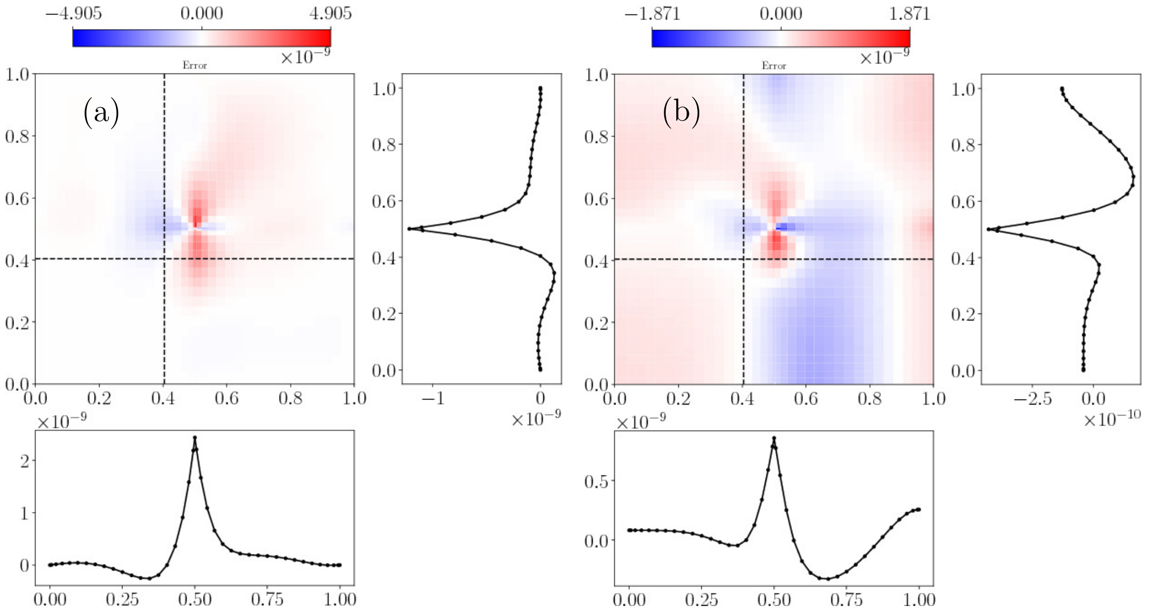

Figure 6.12 – Errors of the 8th order solver on a multi-domain (2,2,2) with full Dirichlet (a) and full Neumann (b) boundary conditions with the second grid is described in fig. 6.8 with $\alpha = 0.9$. Exact solution of the system is $f(x,y,z) = e^{\sqrt{2}xyz}$

6.3.3 Helmholtz solver tests

Figure 6.13 shows how the wave number $\sqrt{\sigma}$ fundamentally influences the solution of the Helmholtz equation. Homogeneous Dirichlet conditions were set on all boundaries, except on the left, where the Robin condition $\partial_n u - \sigma u = 0$ was imposed and used as a point source in the corner. In the case of Laplace's equation ($\sqrt{\sigma} = 0$) the solution is large only near the point source in the corner, whereas for $\sqrt{\sigma} = 25$, the solution is large throughout the domain.

Solver of MFLOPS3D-MD probably suffers from the similar problem for high *Re*

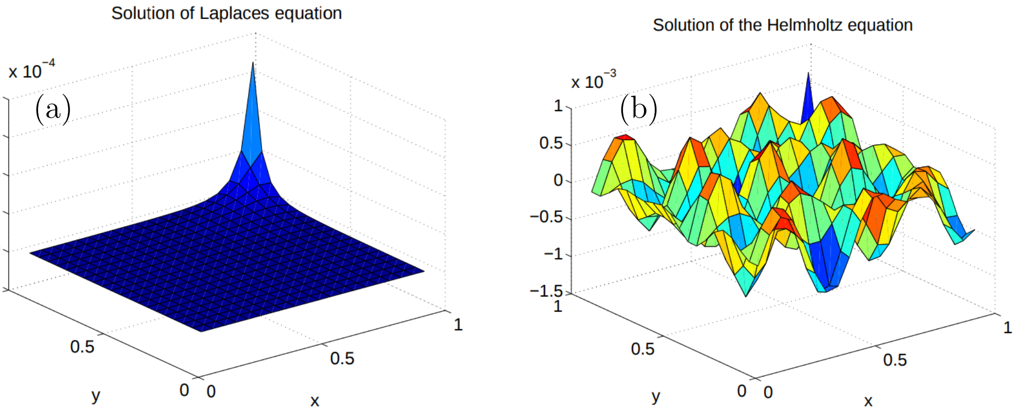

Figure 6.13 – Solution of Laplace's equation (a), with a point source on the boundary, and on the solution of the Helmholtz equation (b), with the same boundary conditions. [*Reproduced from Ernst and Gander*[11]]

number cases (large σ). Careful tests are conducted using exact 3-dimensional Navier-Stokes solutions proposed by Ethier and Steinman[194]. The exact solution provides each component namely pressure term, non-linear term, and the time derivative at any given points as following:

$$u_1(x,y,z,t) = -a\left(e^{ax}\sin\left(ay+dz\right) + e^{az}\cos\left(ax+dy\right)\right)e^{-\nu d^2 t} \tag{6.8a}$$

$$u_2(x,y,z,t) = -a\left(e^{ax}\cos\left(ay+dz\right) + e^{ay}\sin\left(az+dx\right)\right)e^{-\nu d^2 t} \tag{6.8b}$$

$$u_3(x,y,z,t) = -a\left(e^{ay}\cos\left(az+dx\right) + e^{az}\sin\left(ax+dy\right)\right)e^{-\nu d^2 t} \tag{6.8c}$$

$$\begin{aligned} p(x,y,z,t) = -0.5a^2 \Big[& e^{2ax} + e^{2ay} + e^{2az} \\ & + 2.0e^{a(x+y)}\sin\left(az+dx\right)\cos\left(ay+dz\right) \\ & + 2.0e^{a(x+z)}\sin\left(ay+dz\right)\cos\left(ax+dy\right) \\ & + 2.0e^{a(y+z)}\sin\left(ax+dy\right)\cos\left(az+dx\right)\Big] e^{-2\nu d^2 t} \end{aligned} \tag{6.8d}$$

where ν is the viscosity and the coefficients are set to $a = 0.5$ and $d = 3$ for the following tests.

Using the velocity and pressure functions (6.8), it is possible to generate initial conditions of these variables and all terms in the right-hand-side of the Helmholtz solver individually. In the current study, 3 tests will be conducted in order to evaluate the Laplace and Helmholtz solvers. The first two are to test the Laplace solver and the third one is a Helmholtz problem. These problems will be solved with various estimation of the right-hand-side. Summary of the tests designed to demonstrate the effects of the different terms and source of errors is given in table 6.1.

Table 6.1 – Summary of the 3D solver tests for the development of the stabilization methods.

	Solver Type	∇P	$\mathbf{u}\cdot\nabla\mathbf{u}$	$\partial u/\partial t$
Case 1	Laplace	Exact	Exact	Exact
Case 2	Laplace	Exact	Exact	Discrete
Case 3a	Helmholtz	Exact	Exact	Discrete
Case 3b, 3c	Helmholtz	-	Exact	Discrete

Case 1: This test is repeating the previous test of Laplace solver in order to have a reference with the new initial and boundary conditions. All the terms on the right-hand-side are calculated from exact solution, and $\sigma = 0$ (as there is no implicit part of the time derivative.

$$\nu\nabla^2\mathbf{u}^{n+1} = \left[\frac{\partial\mathbf{u}}{\partial t}\right]^{n+1} + \nabla p^{n+1} + [\mathbf{u}\cdot\nabla\mathbf{u}]^{n,n-1} \tag{6.9}$$

The result shown in fig. 6.14 (a) are satisfactory like the previous Laplace solver tests. It can be noticed that the error goes smoothly to zero at the boundaries.

Case 2: In this case, only the non-linear term and the pressure gradient are calculated from the exact solution (6.8), and the time derivative is obtained with second-order BDF. However, all the terms of the unsteady terms are moved to the right-hand-side, so that this is still a test of the Laplace solver. This case was designed to see the error from the Backward-Finite-Difference which is a function of the time step $\triangle t$.

$$\nu\nabla^2\mathbf{u}^{n+1} = \frac{1}{2\triangle t}\left(3\mathbf{u}^{n+1} - 4\mathbf{u}^{n} + \mathbf{u}^{n-1}\right) + \nabla p^{n+1} + [\mathbf{u}\cdot\nabla\mathbf{u}]^{n+1} \tag{6.10}$$

Insignificant difference in the error is observed in comparison to the Case 1 (fig. 6.14 (b)). The discrete $\triangle t$ with the BDF time scheme has only introduced errors due to the extrapolation scheme.

Case 3a: For this last case, the Helmholtz problem will be tested for 3 different configurations. First, only the non-linear term and the pressure gradient are calculated from the exact solution and the time derivative obtained with the same scheme as in (6.10). However, the implicit part of the time derivative is kept in the left-hand-side which leads to a Helmholtz problem to solve ($\sigma \neq 0$).

$$\nabla^2\mathbf{u}^{n+1} + \sigma\mathbf{u}^{n+1} = Re\left(\frac{1}{2\triangle t}\left(-4\mathbf{u}^{n} + \mathbf{u}^{n-1}\right) + \nabla p^{n+1} + [\mathbf{u}\cdot\nabla\mathbf{u}]^{n+1}\right) \tag{6.11}$$

For the Helmholtz test, the shape of the error is changed noticeably as compared to the error based on the Laplacian solutions. It can be seen in fig. 6.14 (b), that the implicit solver provides a much accurate result than the previous tests with Laplace equation. The smooth behavior of the error close to the border of the domain is preserved as right-hand-side stays compatible to the left-hand-side of the equation. Ideally, Helmholtz problems should be solved with such configuration, but it is not possible in real situations of simulations. Unlike this synthetic case, exact values of u^{k+1} are not accessible when the Navier-Stokes equations are being solved with the estimation of the right-hand-side including other errors. However, in practice, right-hand-side of the momentum equation and the implicit part of the unsteady term will not be perfectly matching. The situation is even worse when projection method is used, for example, if `PT=1`, right-hand-side will be wrong as ∇p is set to zero.

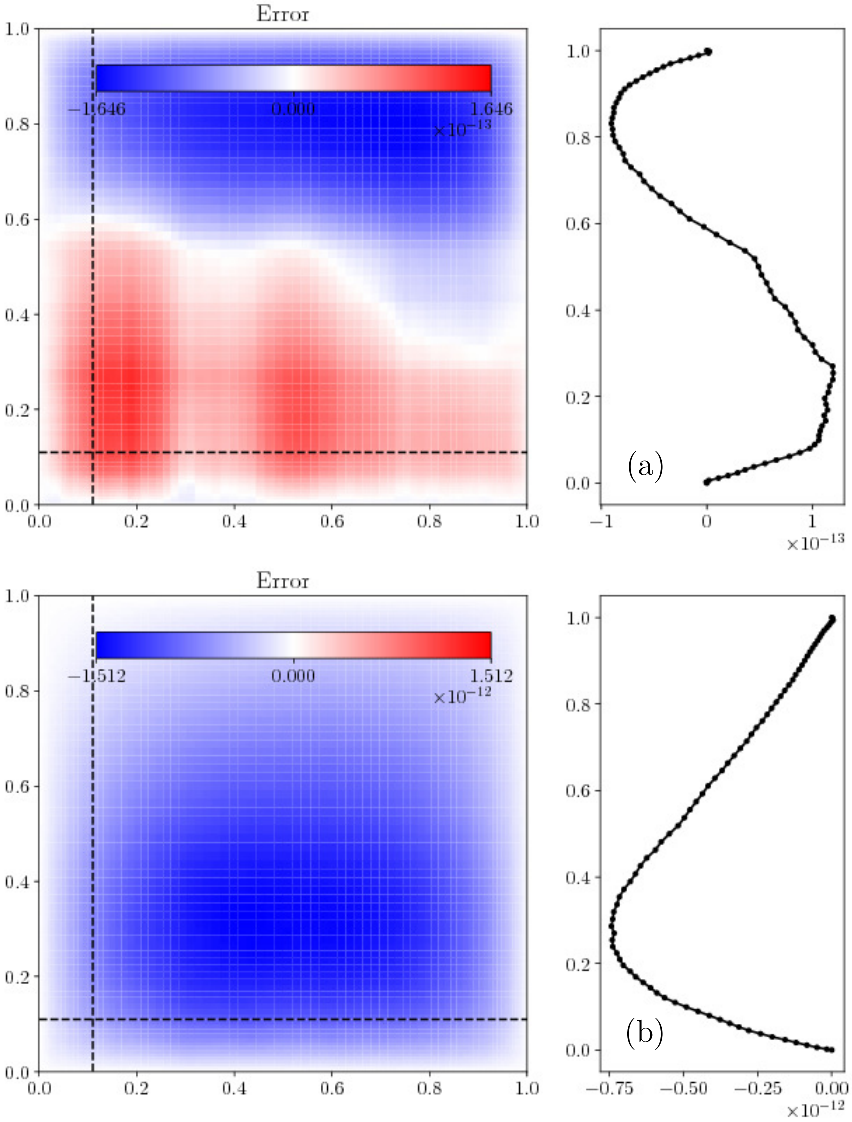

Figure 6.14 – Results of **Cases 1** and **2**. **Case 1** (a), all the terms on the right-hand-side are computed from the exact derivatives of (6.8). **Case 2** (b), a discrete $\frac{\partial u}{\partial t}$ with second order BDF is used instead of the exact time derivatives from (6.8). Both results represent a Laplace solver as $\sigma = 0$.

Case 3b: In this test, only the non-linear term is calculated from the exact solution, and the time derivative is discretized with the same scheme (6.11) but the pressure gradient is set to zero.

The corresponding equation is

$$\nabla^2 \mathbf{u}^{n+1} + \sigma \mathbf{u}^{n+1} = Re\left(\frac{1}{2\triangle t}\left(-4\mathbf{u}^n + \mathbf{u}^{n-1}\right) + \cancel{\nabla p^{n+1}} + \left[\mathbf{u}\cdot\nabla\mathbf{u}\right]^{n+1}\right) \tag{6.12}$$

This test is closer to the real situation during a simulation using MFLOPS3D-MD because momentum equations are solved with $\sigma \neq 0$ and eliminating pressure is like the projection method `PT=1`.

Removing the pressure gradient introduces a relatively large error on the right-hand-side. As a result, the error of the solution is much higher than the previous tests of Laplace or Helmholtz solver. The error is exactly zero at the boundaries, meaning that the Dirichlet conditions are implemented correctly. However, the error does not grow smoothly from the borders as seen in the solution of the Laplace solution but is discontinuous near the boundaries of the domain. This effect is related to the nature of the implicit solver with large σ, as the crude approximation of the right-hand-side without pressure gradient is not compatible with the boundary conditions imposed by the solver. This effect will lead to high-frequency oscillations as such jumps will introduce significant errors in the compact derivatives.

Case 3c: In order to enlighten the effect of σ, the last test is performed. The test is the same as the **Case 3b** but with a time step 200 times bigger. This leads to a smaller σ which can also be interpreted as a low Reynolds number case. The result demonstrates that, as already explained, σ plays a significant role in this jump of the solution at the boundaries. As shown in fig. 6.15 (c) errors gets smoother because the dissipative term becomes dominant with respect to σ.

Discussions for better Helmholtz solver

The **Case 1** was designed to evaluate the error due to the spatial discretization for a pure Laplace equation. Then a time discretization scheme was introduced by keeping the explicit property of the equation. This leads to a small increase in the error as expected.

For the third case, the implicit time scheme is kept leading to a test of the Helmholtz solver. However, at the first test (6.15 (a)) were performed with a right-hand-side close to the exact solution. The right-hand-side was adapted to the exact boundary conditions and it is shown that implicit solver is more accurate than the Laplace

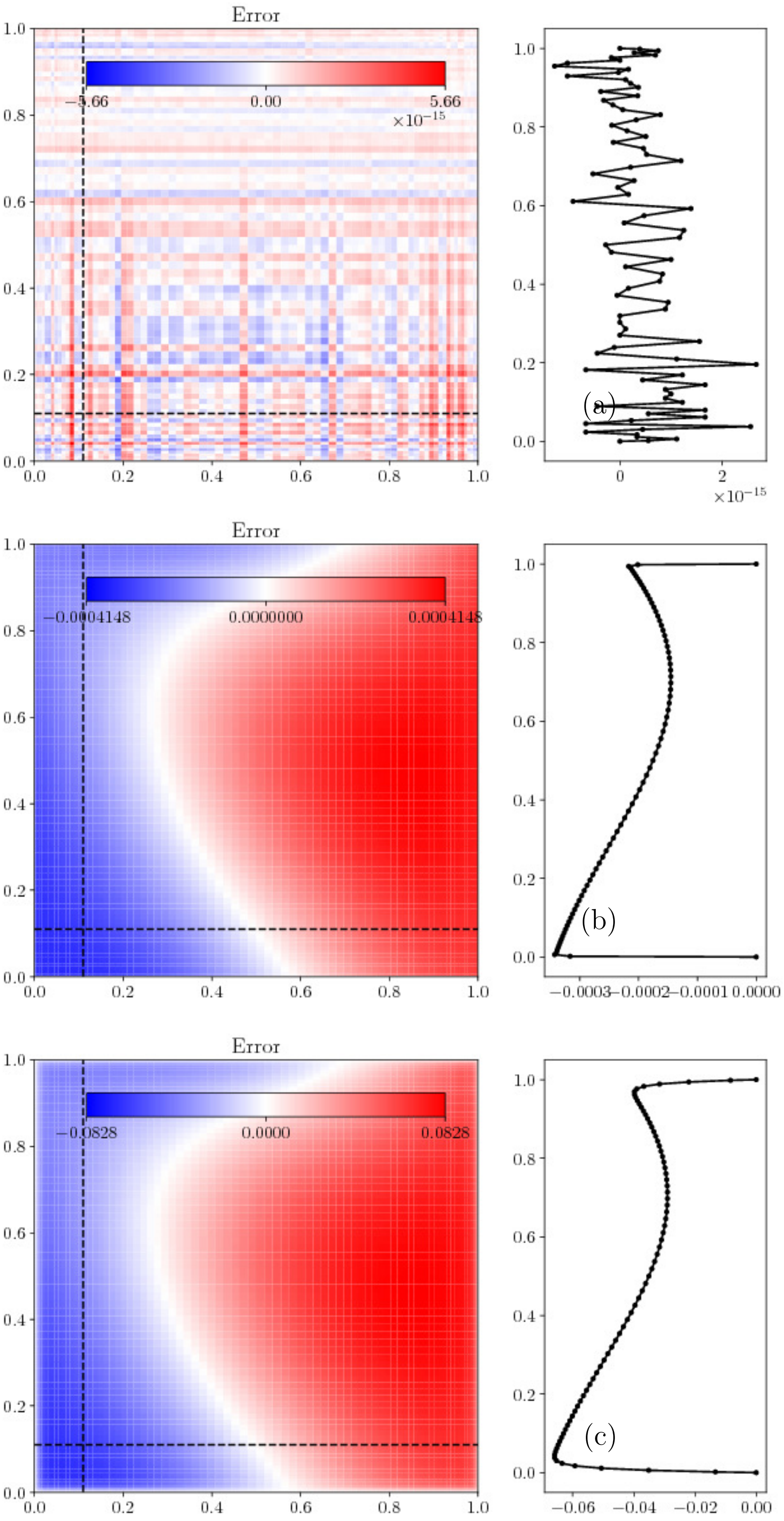

Figure 6.15 – Results of **Cases 3a, 3b** and **3c**. **Case 3a** (a) $\frac{\partial u}{\partial t}$ is calculated using a second-order BDF time scheme and the remaining terms on the right-hand-side are computed from the exact derivatives of (6.8) and solved implicitly. **Case 3b** (b) same as (a) except that the pressure gradient is dropped to mimic the conditions of the intermediate step in the projection method. **Case 3c** (c) same as (b) but with $\triangle t$ which is 200 times higher than (b). They are all results of Helmholtz problems ($\sigma \neq 0$)

solver cases. A more realistic situation is going to contain a more significant error on the right-hand-side, due to errors introduced by the time scheme and the inaccurate estimation of the pressure gradient. Therefore, an example without pressure gradient is generated (**Case 3b**). It possibly demonstrates the source of the stability problem of MFLOPS3D-MD. Even if the error is small, the main problem is that the present solution has discontinuities near the boundary conditions. The derivation of this solution with high order compact scheme will generate oscillations on the first points. In order to show that this jumps come from the nature of the Helmholtz equation, another test under the conditions of the previous one was conducted with a time step ($\triangle t$) which is 200 times higher. Bigger time step will introduce a higher error on the BDF scheme used for $\partial u/\partial t$. As demonstrated with the **Case 3c**, the solution is smoother when a smaller σ is used similarly to the at low Reynolds number case. In this case, the discontinuities still exist, but they are much smoother.

It has been shown that the problem appears because the right-hand-side is not adapted to the boundary conditions which are connected to the solution by the Laplacian operator. Two different approaches are proposed below to overcome this issue.

First approach: High Reynolds number assumption

The Helmholtz equation that needs to be solved for the first component of $\mathbf{u}$ is

$$(\triangle - \sigma I)u = f \tag{6.13}$$

In high Reynolds number case, the second term $\sigma I u$ on the left-hand-side is much greater than the Laplacian operator. In this case, one can estimate the value of the expected jump with

$$(\cancel{\triangle} - \sigma I)u = f \tag{6.14}$$

The estimation of the jump can be subtracted from the right-hand-side of the equation. This process can be used iteratively to minimize the jump.

It is found that this method does not work well because estimation of the jump is not accurate enough as this method completely ignores the diffusion. Another method is developed which does not suffer from this problem.

Second approach: Modified right-hand-side

This approach looks like the stabilization techniques used to obtain stable solutions of the Navier-Stokes equations on the collocated grids. A regularization function ϵ is added to the right-hand-side to adapt it to boundary conditions with the motivation to obtain a right-hand-side compatible with boundary conditions.

The different steps of the method are described below for the first component of $\mathbf{u}$

1. Compute u^* with the original Helmholtz without correction

$$(\triangle - \sigma I)u = f \tag{6.15}$$

2. Extrapolate u^* at the extreme points using an extrapolation scheme like for a Dirichlet boundary condition;

$$u_0 = \left(u_0^{(6)} - bu_1 - cu_2 - \cdots\right)/a \tag{6.16}$$

   or for a Neumann boundary condition;

$$u_0^{(1)} = \left(u_0^{(6)} - bu_1 - cu_2 - \cdots\right)/a \tag{6.17}$$

   where a, b, c, ... are coefficients for the high order finite difference (explicit) scheme. This extrapolation forces 6th order derivative of the field u^{k+1} at the boundary to be zero. A similar procedure is used close to each boundary.

3. Compute the difference, $\epsilon|_\Gamma$, between the extrapolated values of the boundary and the exact boundary

$$\epsilon|_\Gamma = u_0 - u_{0,BC} \tag{6.18}$$

   This difference will be the boundary conditions of the next step.

4. Compute a smooth solution using the Poisson equation and the boundary condition $\epsilon|_\Gamma$

$$\triangle\epsilon = 0 \tag{6.19}$$

   The solution ϵ of the equation above is then added to the right-hand-side of the original Helmholtz system.

5. Compute the Helmholtz equation once again with an updated right-hand-side,

$$(\triangle - \sigma I)\, u = f - \epsilon\sigma \tag{6.20}$$

New results for **Case 3b** using this correction are given in fig. 6.16. Global error is always lower after this correction. The original jump of the solution is reduced. However, the benefit of this correction is linked to the property of the solution without correction. The extrapolation step is more effective when the original solution has a very sharp jump meaning that the resolution is coarse with respect to the diffusion term. However, the local stretching of the grid will help to resolve the original jump of the solution better but will reduce the benefit of the correction due to the difficulty to extrapolate the solution to obtain an adapted correction ϵ.

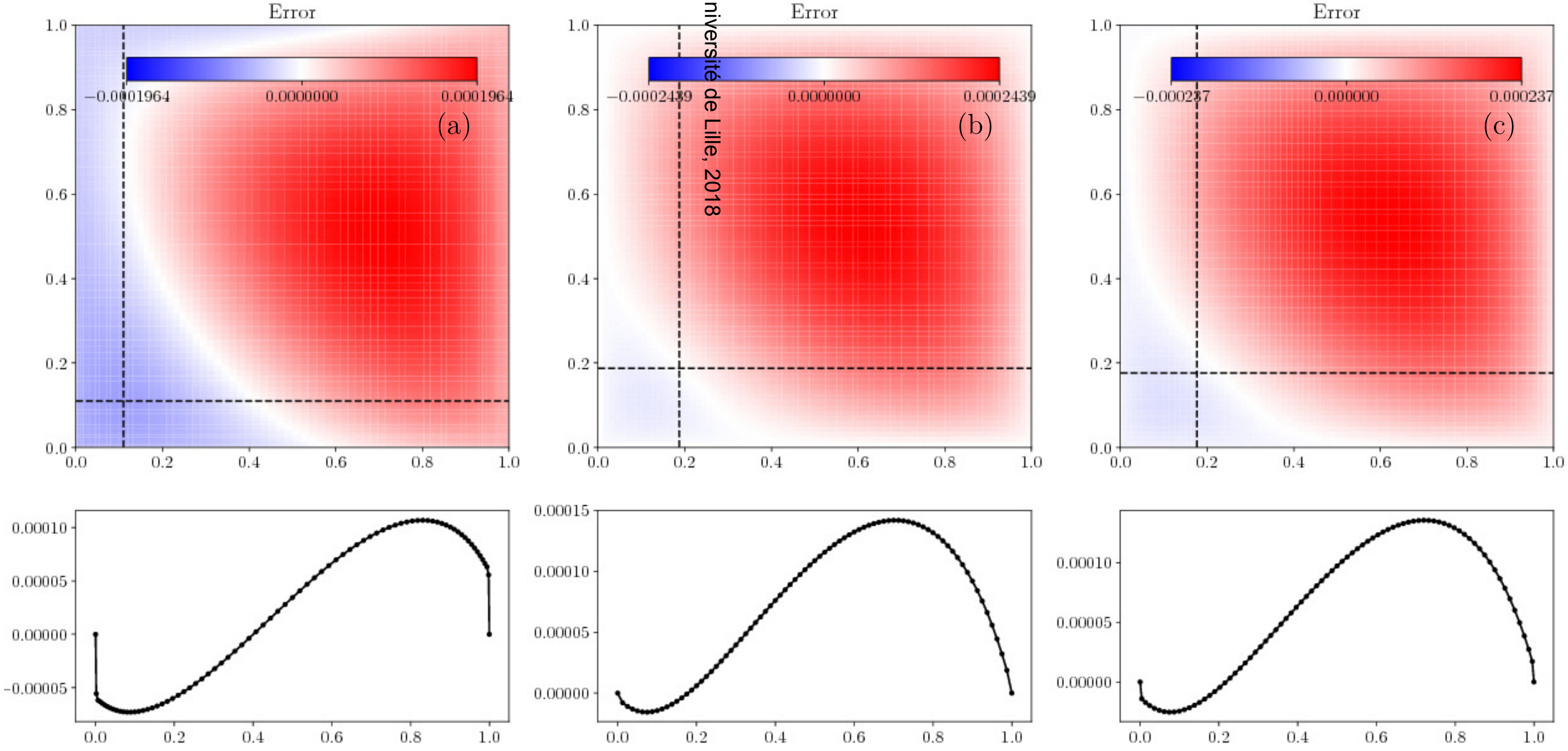

Figure 6.16 – New results of **Case 3b** (fig. 6.15 (b)) with correction steps (6.15) to (6.20). (a) with the same stretching ($\alpha = 0.8$), (b) with moderate stretching ($\alpha = 0.9$) and (c) without stretching.

6.4 Navier-Stokes solver tests

Some improvements are proposed in the previous section. However, no stable solutions could be obtained at high Reynolds numbers. The following results demonstrate the evolution of the error on the velocity component u_1 when Navier-Stokes equations are solved with the $Re = 1000$. Two different cases are compared to observe the effect of the estimations of the terms on the right-hand-side. The same exact solution (6.8) is used for initial and boundary conditions of these tests.

In the first case (fig. 6.17) all the terms on the right-hand-side of the momentum equations are computed from the exact solution (6.8) except the discrete unsteady term. The solution of the pressure correction ϕ and projection u^{k+1} steps are calculated in usual ways. Therefore, the components of $\mathbf{u}^{k+1}$ exposed to the potential errors at the end of each time step. Any pollution in the $\mathbf{u}^{k+1}$ appears in the next time step when it became $\mathbf{u}^k$ and used in the discretization of the unsteady term. At the very first iteration (fig. 6.17 (a)) the jump observed in the some of the previous Helmholtz solver tests is not present (situation here is similar to the results given in fig. 6.15 (a)). However, after 200 time steps (fig. 6.17 (b)) jump in the error become noticeable. Even if the error level is low, some instabilities start to grow. High-frequency waves can be detected in both directions. Notice that the reason why the jump around edges is more pronounced in the x-direction is that high-frequency waves in that directions have smaller amplitudes.

The second case corresponds to the standard Navier-Stokes solver where all the terms are calculated as they are supposed to be in a simulation. Projection method `PT=3` is used meaning that pressure is estimated prior to the solution of the momentum equation at every time step. Even if this preliminary step is expected to give a good estimation of the right-hand-side, the solution is not fully compatible with the boundary conditions at the initial time step and there is a sudden change in the error around edge points. This was similar in the results given in fig. 6.15 (b). Some oscillations start to appear after few iterations with an amplitude that seems higher than the case with exact right-hand-side after the same number of iteration.

As can be seen in fig. 6.17 (a) the solution for the first iteration seems accurate, thanks to the very accurate estimation of the right-hand-side. However, in few iterations (fig. 6.17 (b)) the error in the estimation of right-hand-side is becoming large enough and is leading to a wavy solution. When the right-hand-side includes errors due to estimations of the various terms, the sudden jump on the solution appears even at the first iteration as in previous results, but wavy behavior appears at the similar time like when the perfect right-hand-side is imposed in the momentum equations. So, the first issue is related to the incompatible left and right-hand-side of the equation. Unlike Laplace equation, the solution of the Helmholtz solver is not smooth and the jump becomes significant in time. Such a problem combined with the weakly dissipative compact finite difference schemes perhaps the reason of the high-frequency oscillations.

6.5 Conclusion

A laminar BL simulation on a flat plate is at $Re = 200$ is conducted with MFLOPS3D-MD. Careful adjustment of the spatial resolution allowed to run the code for a long simulation time. However, stability problems have been observed at high Reynolds number simulations. Thus, a test suite integrated into MFLOPS3D-MD was developed and used to test the different parts of the code. The test suite also helps to ensure future development easier and safer.

The first tests were applied to derivatives which happened to behave as expected. Error on the derivatives increases around boundary points due to smaller stencils sizes used for backward/forward stencils. Tests showed that an optimum stretching factor α is beneficial. This optimization based on the error of the derivatives at different points in the discretization is made based on controlled trials. The ratio between maximum and minimum grid distance equal to 4 was found to be satisfying which is also compatible with the results given by Shukla *et al.*[195].

Laplacian solver works properly as well. However, problems are noticed with Helmholtz solver at high Reynolds numbers. Solver based on 3D diagonalization performs well but leads to discontinuities at the second point from the edge. Error on those points has a direct impact on the projection step because right-hand-side of Poisson equation solver is set with the divergence of fields with such erroneous points. In addition to that, the right-hand-side of influence matrix solver is set by the derivatives calculated using those points, so the solution of the interface points are also affected in multi-domain cases.

It is known that Helmholtz solver is a difficult numerical problem to solve with the high wavenumbers $\sqrt{\sigma}$. A large part of the current study is dedicated to understanding the source of this problem.

A Burger equation solver was created for this purposes. This tool was able to test the effect of different parameters on the stability of the solution. Different stencils for the derivatives and the solver were tested on the Burger equation, but a more stable combination of implicit and explicit points could not be found, so those tests are not reported. However, the results helped to identify the problem. It is shown that with a slight change of Reynolds number solver can become unstable.

Based on the learnings from the Burger equations, tests were carried out in the MFLOPS3D-MD. In this regard, two different stabilization techniques are proposed without changing compact finite difference schemes. Both of them provides satisfying results for 1D problems but not for 3D problems. Additionally, in some settings, promising corrections are observed in a single time step, they also do not provide a big improvement after a few iterations. The oscillations in the solutions are stronger close to the corners of each sub-domain where the corrections cannot be applied efficiently as the extrapolation step of the correction method is in 1D. Therefore the corner points cannot be fixed accurately with the proposed method. Besides, results show that correction methods are sensitive to the grid stretching. The correction based on the extrapolation performs better if the jump is restricted within a single grid point thanks to the successful estimation of the jump.

The situation is more complicated than the solver tests when Navier-Stokes equations are solved. It is difficult to decouple the problem between velocity fields and pressure to find a solution. Various tests and calculations apart from the ones shown in this chapter have been performed on 3D problems using MFLOPS3D-MD, but completely satisfactory results are not obtained.

It is also noted that the solution of the Poisson equation with Neumann boundary conditions can require large computational efforts. It is problematic for the very large simulations as the number of iterations for the influence matrix solver increases rapidly depending on the size of the problem in the current version of the code. No efficient preconditioner could have been identified.

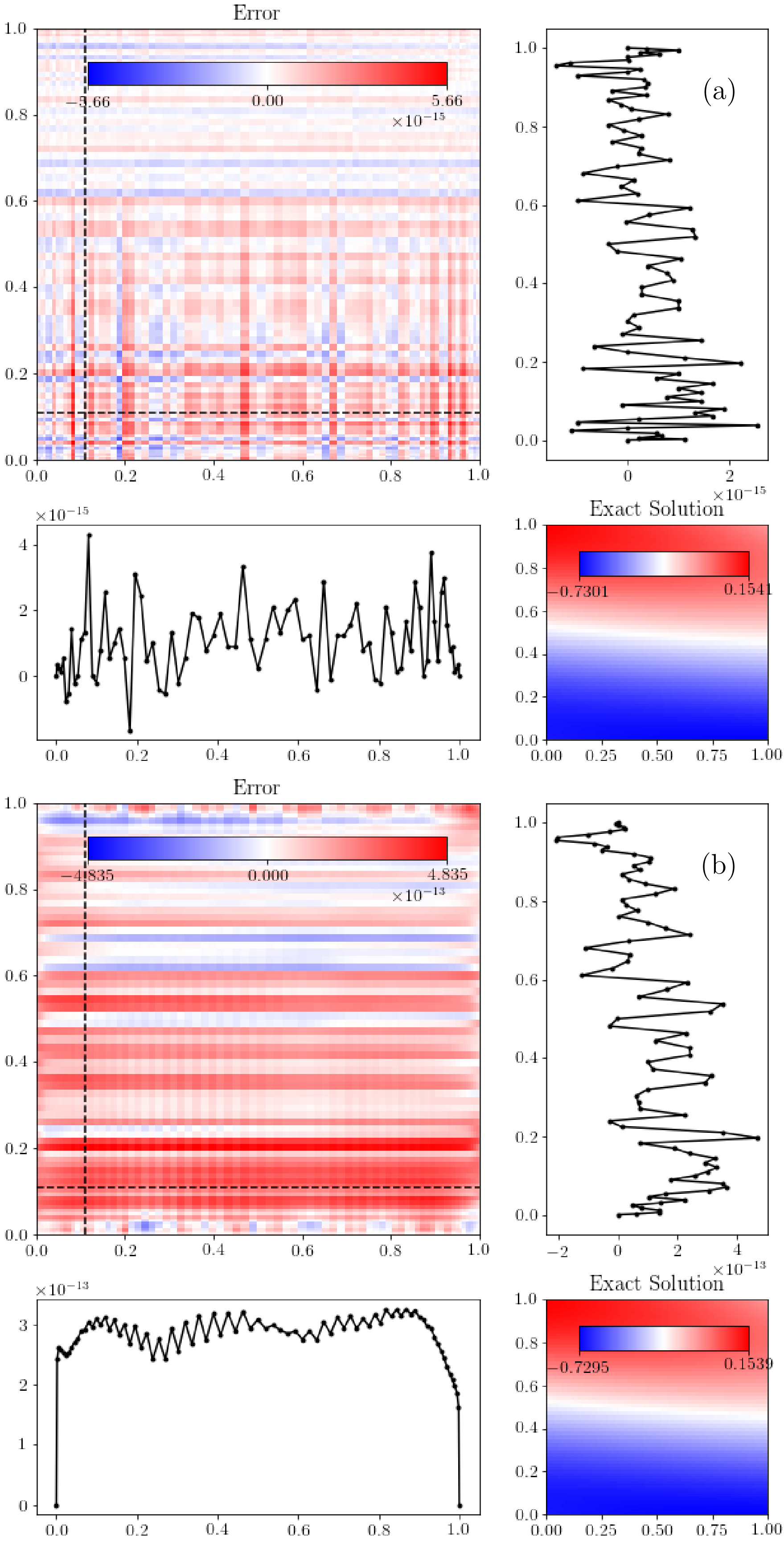

Figure 6.17 – Error on the solution of the Navier-Stokes equation (with `PT=3`) using 8th order compact finite difference schemes for derivatives and linear solver on a single domain with exact values of terms on the right-hand-side computed from the exact derivatives of (6.8) except for the time derivative at time $t = 0.0005$ (a), 0.1 (b) where $\triangle t = 0.0005$.

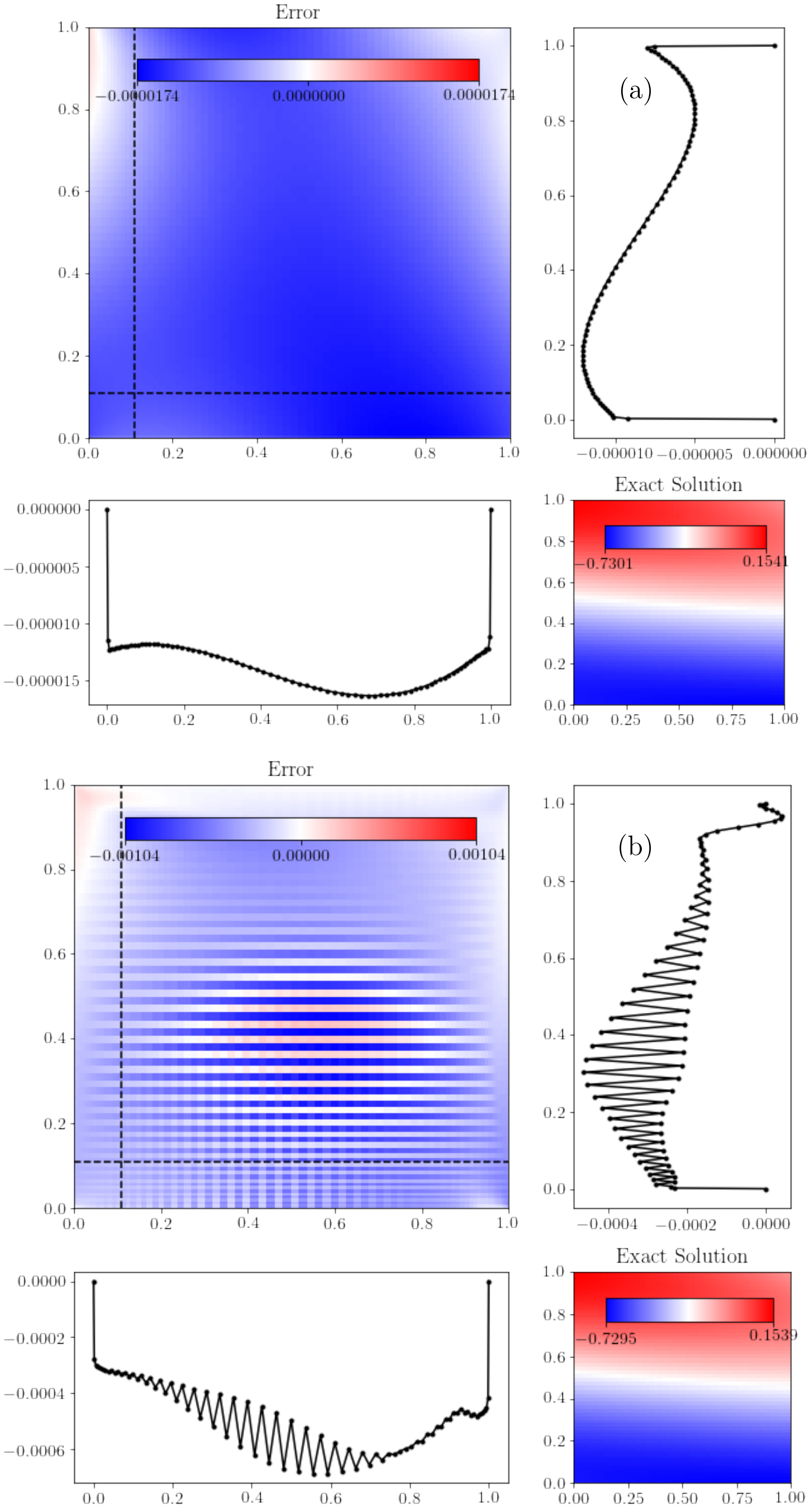

Figure 6.18 – Error on the solution of the Navier-Stokes equation (with `PT=3`) using 8th order compact finite difference schemes for derivatives and linear solver on a single domain with standard right-hand-side (exact solutions are only used as the initial conditions) at time $t = 0.0005$ (a), 0.1 (b) where $\triangle t = 0.0005$.

Part IV

Conclusion

Conclusions and Perspective

The main motivation of this work is to understand the physics of the LSM in TBL on a flat plate and with the adverse pressure gradient. Such knowledge is important for the theory of turbulent flows and turbulence modeling. The two main parts of the manuscript are devoted to a DNS of TBL conducted using Incompact3D up to $Re_\theta = 2500$ and the development of the existing laboratory code MFLOPS3D-MD.

In part II a DNS of ZPG TBL is presented. The aim of this study is to provide some reference statistics of coherent structures with rigorous definitions. A new database of 3D fields and 2D time-resolved planes is generated, large-scale motions and quadrants are investigated.

The interest of the having a TBL simulation over a curved wall is a strategy of the LMFL team which will eventually allow us to study similar geometries than the ones studied in LMFL wind-tunnel. Development of the in-house code MFLOPS3D-MD (part III) was carried out to fulfill this needs. The MFLOPS3D-MD is one of the few examples of the implementation of the influence matrix method in 3D. It is based on an efficient direct solver for the Helmholtz equations and 2D mapping functions to generate smooth geometries in the simulation domain. An alternative methodology was considered, to perform a DNS on such smooth geometry using immersed boundary methods implemented in Incompact3D. However, this would not be computationally efficient as it requires a fine mesh over a large simulation domain. A low Reynolds number TBL simulation is conducted with MFLOPS3D-MD to show the capabilities of the code. However, the large part of the efforts on the development of the code is focused on the stability problem at high Reynolds. Partial improvements are proposed, but substantial changes are probably required for MFLOPS3D-MD to cope with high Reynolds numbers.

Summary of findings

The present work allows us to draw several conclusions on the physics of the turbulent boundary layer flows on the one hand and on an original numerical tool to solve the Navier-Stokes equations with multi-domain on the other hand. The main findings are listed below.

A new database of ZPG TBL

The mean velocity and Reynolds stress profiles of the current study successfully compare with the results from Jiménez *et al.*[9] and Schlatter *et al.*[7]. The benefit of this database is that the 3D and 2D time-resolved data can be used to compare time and space statistics. Even if the Reynolds number is moderate, these data provide useful information about large-scale structures.

Townsend-Perry model for wall attached structures

Spectral analysis shows that the streamwise energy spectrum is compatible with a k_x^{-q} scaling of the streamwise energy spectra at large scales with $q \simeq 1$ near $y^+ = 100$ with increasing value of q when moving from the wall. The relation $p+q = -1$ is satisfied in agreement with the model proposed by Srinath *et al.*[10] over the range of scales where the streamwise lengths of streamwise velocity structures follow a $(\lambda_x/\delta)^{-2}$ distribution. Results are valid for a limited range of the wall-normal distances as compared to the experimental study, but this result can be explained as the logarithmic region is much shorter than the high Reynolds number case obtained with PIV. Nevertheless, the model is confirmed with low Reynolds number DNS data.

Characterization of coherent structures using skeletonization

A novel application of the skeletonization technique is demonstrated in order to obtained detailed statistics of coherent turbulent structures like LSM. Skeletons of these structures are formed by tangled curves. The complexity of the structures is revealed and even quantified. Consequently, accurate curve definition allowed to obtain an average angle of the structures with respect to the horizontal plane which is around 5°.

Quadrants statistics

It is showed that quadrants lengths are also distributed with a specific power law, $(\lambda_x/\delta)^{-3}$. Average aspect ratio of the structures ($\lambda_x \approx 3\lambda_y$ and $\lambda_z \approx 1.5\lambda_y$) were identified based on joint PDF similarly to what was observed in channel flows[1].

Multi-domain Navier-Stokes solver

Even though the potentially discouraging computational cost of using influence matrix in 3D is emphasized by several authors[57;172], the current study provides an example of working state-of-art example for such an algorithm. The technological improvements towards larger multi-cores systems justify the choice of this algorithm. However, this choice leads to several difficulties. Singularity problem of the Poisson equation with homogeneous Neumann boundaries conditions is transferred to the influence matrix even though none of the individual sub-domains suffers from this problem. The traditional methods to correct this problem at the level of the influence matrix are used. Both one point Dirichlet and null space removal found to be problematic when implied to the influence matrix.

Perspectives

Organization of the structures

The model proposed by Srinath *et al.*[10] provides a new interpretation of the Townsend-Perry attached eddy model by establishing a connection between streamwise structures and the slope of energy spectra. The large-scale streamwise structures, as defined in this work, contribute to a large part of the turbulent kinetic energy ($\sim 70\%$). Therefore the characterization of these structures provide useful information about the scaling and can help to have an exhaustive knowledge of the turbulent boundary layers. This detailed description even at moderate Reynolds is a necessary step to improve turbulence models[196] and to derive low order models of the near-wall turbulence.

Besides, it is shown that LSM and quadrants have common parts throughout the boundary layer thickness. In the present study, the overlap of RSS and LSM is investigated. The fact that these structures co-exist inside the TBL makes the statistics of common regions an interesting point to investigate (figs. 4.11 and 4.24). The RSS contribution of the positive u' fluctuations (fig. 4.11) remains quite constant over the logarithmic region while the same can not be said for negative u' fluctuations. These study can be expanded to better understand the relationship between the turbulence production and Reynolds shear stress.

Future of the MFLOPS3D-MD

It is realized that some parts of the code can be replaced with more conventional methods without sacrificing extensible features of the code. For example, using exact projection[171;172] method instead of an approximation projection is one of them. Another important aspect is to improve the performance of the Helmholtz solver. Perhaps, exact compact finite difference schemes for solving Helmholtz equation (the numerical scheme is exact) like the one designed by Wong and Li[184] can be tested next which at least provides better control of the overall error as spatial discretization can be considered error-free. Recently, Wang and Wong[197] provided accurate results with for 2D Helmholtz equations in Cartesian coordinates with $\sqrt{\sigma}h \sim 0.7$ which is around the limit to make simulations with $1/\nu = 2000$ ($\sqrt{\sigma}h \sim 0.64$ is estimated for such a simulation).

The fact that the singularity problem is transferred into the influence matrix is an important issue for the performance. There is no dedicated method to treat this problem, but the idea of solving the problem at the sub-domain level is appealing because replacing the value of the point with the zero eigenvalues in all directions works effectively.

Database and tools

Different post-processing tools and a database are the products of this study. They are also valuable for further studies. For example,

- Skeletonization can also be used to study other coherent structures like quadrant and vortices in 3D possibly on time-resolved data to follow the structures in time. A general picture of coherent structures in turbulence can be drawn.
- Statistics of coherent structures should be compared with the same structures in APG. Similar analyses could be done on experimental data at much higher Reynolds number (for instance with large-scale tomo-PIV) using the post-processing tools developed in this study.
- The database of time-resolved data in a plane of ZPG TBL can be used as inlet condition for other DNS of the boundary layer with or without pressure gradient at much higher Reynolds numbers. Incompact3D was designed to work in massively parallel and can handle much more grid points than used in the present DNS. The confirmation of the present results on ZPG TBL at a Reynolds number comparable to the experimental study of Srinath would be a valuable result.

Publications and communications

Conference participation

[1] *Massively Parallelized DNS Code for Turbulent Boundary Layer Studies* (CISIT, Valenciennes, May 20, 2016, 2016).

[2] *The three-dimensional structure of large scale motions in a turbulent boundary layer* (The 16th European Turbulence Conference, Stockholm, Sweden, August 21-24, 2017, 2017).

[3] *The three-dimensional structure of large scale motions in a turbulent boundary layer* (Congrès Français de Mécanique, Lille, August 28 - September 1, 2017, 2017).

[4] *Direct Numerical Simulation of a Turbulent Boundary Layer* (ELSAT2020 Workshop, Lille, ONERA, September 13, 2017, 2017).

[5] *Direct Numerical Simulation of Turbulent Boundary Layer using Incompact3d* ((In)Compact3d User Group Meeting, 2018).

Journal Articles

[1] Solak, I. and Laval, J.-P. (2018). Large-scale motions from a direct numerical simulation of a turbulent boundary layer. *Accepted to Phys. Rev. E.*

Professional courses followed

- École de physique des Houches, New Challenges in Turbulence Research IV, Les Houches, March 20-25, 2016
- L'IDRIS, Initiation à la programmation hybride MPI/OpenMP, Orsay, September 8-9, 2016

Teaching

Teaching 2017/2018 (ATER) I taught FORTRAN in Master Turbulence and was assistant for several other courses including Fluid Mechanics and Numerical Methods practices.

Teaching 2016/2017 I taught FORTRAN and was the assistant of Prof. Jean-Marc Foucaut for the Fluid Mechanics practices in Master Turbulence.

Teaching 2015/2016 I taught FORTRAN and was the assistant of Prof. Jean-Marc Foucaut for the Fluid Mechanics practices in Master Turbulence.

Other related activities

IMP-Turbulence Master Alumni Day I initiated the idea of an alumni day for the graduates of the program to present their current work to the M1 students in Lille. The event was held on the 17th of March 2017 with the participation of 5 graduates of the master program from various years, including myself as speakers.

ASPID (Ph.D. Association) I worked in the administration of the ASPID as treasurer from June 2016 for one year.

ADSL (Ph.D. Association) I am a member of the administrative office of the new association for graduate students of SPI and SMRE, born from the fusion of the ASPID and TILDA.

Part V

Appendices

Skeletonization

A

The curve extraction framework proposed by Hassouna Hassouna and Farag[152] along with structure detection steps is abstracted in fig. A.1.

The main steps of the method can be summarized as follows:

1. Compute the first distance field D from boundaries solving an Eikonal equation,
2. Compute the gradient vector flow (GVF) based medial function $\lambda(x)$ that points out toward the source point of the object,
3. Detect the source point P_s defined as $P_s = argmax(\lambda D)$
4. Propagate a β-front from P_s and solve a new Eikonal equation to get a new distance field D_1;
5. Discretize D_1 (clusterize) and construct level-set-graph, which represent the connection between adjacent clusters,
6. Detect extreme and merge points for appropriate clusters,
7. Propagate a α-front from P_s and solve a new Eikonal equation to get a new distance field D_2,
8. Extract curves by backtracking from extreme points following the negative gradient of D_2 (stops at P_s or on a previously extracted part of the skeleton).

Two optional procedures (opening-closing and interpolation) can be applied after the extraction of the 3D structure if the structure exhibit some regions which are not sufficiently resolved (a minimum resolution of $5 \times 5 \times 5$ is necessary for the healthy progress of Runge-Kutta stepping to extract a curve).

For a simple domain with C shape, some of the steps above are visual-

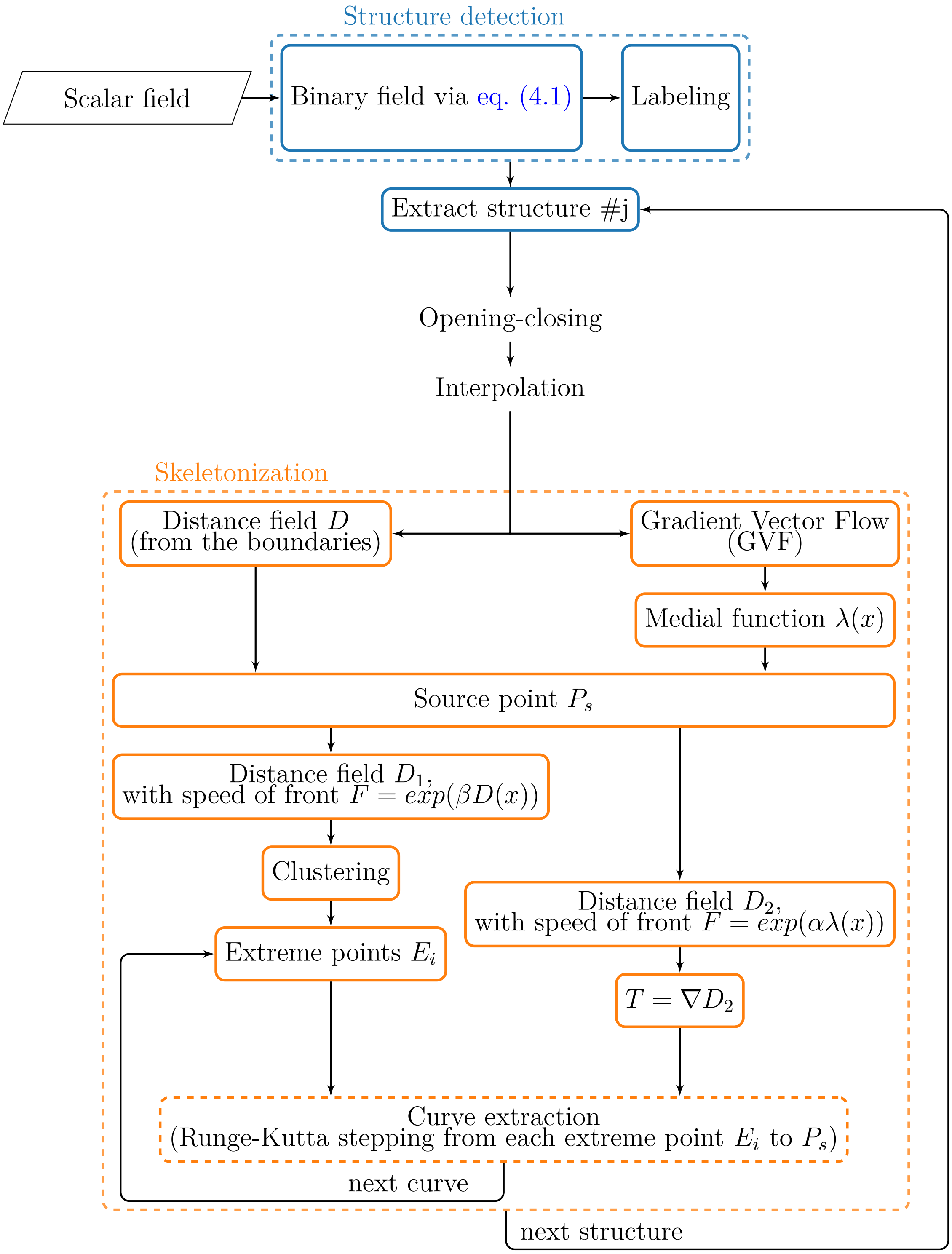

Figure A.1 – Graphical presentation of the work-flow to extract the skeleton's curves for a single 3D spatially resolved data. The red steps correspond to the structure detection method used priorly to the bounding box statistics.

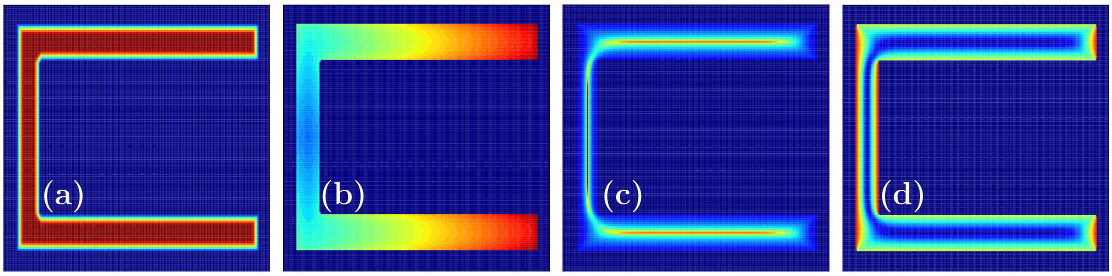

Figure A.2 – Visualization of some of the steps of the curve extraction procedure: (a) D, (b) clusters, (c) medial function, (d) GVF.

ized in fig. A.2. The procedure aims to get sharper but homogeneous distance fields so that extracted curves are more accurate and do not get affected by corners of the shape.

The procedure includes several parameters. Even though extraction can work with a range of values of these parameters, computational cost and completeness of the skeletons can be largely affected. A careful parametric study was carried out to find the optimum set of parameter for our purpose. Another difficulty is that the thin parts of the turbulent structures make the extraction of the skeletons difficult. Distance fields are able to create proper gradients if the section of the structures is thicker enough as mentioned before. As the method works on homogeneous grids, interpolations have to be done in all 3 directions which might generate a large volume of data to be analyzed. Moreover, the computationally most expensive part of the overall process is the solution of the Eikonal equation as this part was not parallelized.

Extraction of curves is a computationally expensive process for this specific application on turbulent coherent structures as additional local interpolations are often required to increase the resolution of the binary images. Several distance fields (D, D_1, D_2) are computed by solving the Eikonal equation using multi-stencils fast marching method (MSFM). The complexity of MSFM is $\mathcal{O}(n\text{log}n)$ where n is the total number of pixels. $\mathcal{O}(kn)$ is the cost of the computing gradient vector field (GVF), where k is the number of iterations. So the total complexity is $\mathcal{O}(n\text{log}n + kn)$.

B

Parameters for Incompact3d

```
#
# INCOMPACT 3D Flow parameters
#
600.    #xlx  # Lx (Size of the box in x-direction)
40.     #yly  # Ly (Size of the box in y-direction)
20.     #zlz  # Lz (Size of the box in z-direction)
2000.   #re   # Reynolds number
1.      #sc   # Schmidt number (if passive scalar)
1.      #u1   # u1 (max velocity) (for inflow condition)
1.      #u2   # u2 (min velocity) (for inflow condition)
0.0     #noise# Turbulence intensity (1=100%) !! Initial condition
0.0     #noise1# Turbulence intensity (1=100%) !! Inflow condition
0.008   #dt   # Time step
#
# INCOMPACT3D Flow configuration
#
2       #nclx   # nclx (BC)
2       #ncly   # ncly (BC)
0       #nclz   # nclz (BC)
8       #itype  # Type of flow
1       #iin    # Inflow condition (1: classic, 2: turbinit)
430001      #ifirst # First iteration, attention add +1
450000      #ilast  # Last iteration
4       #nscheme# Temporal scheme (1:AB2, 2: RK3, 3:RK4, 4:AB3)
3       #istret # y mesh refinement (0:no, 1:center, 2:both sides, 3:bottom)
1.3     #beta   # Refinement parameter (beta)
1       #iskew  # (0:urotu, 1:skew, for the convective terms)
0       #iscalar# (0: no scalar, 1:scalar)
#
# INCOMPACT 3D File parameters
#
1       #ilit     # Read initial flow field ?
5000    #isave    # Frequency for writing backup file
500     #imodulo  # Frequency for visualization for VISU_INSTA
#
# INCOMPACT 2D File parameters, all perpendicular to the x-dir
#
1       #isaveinlet    # Save 2D planes ?
4       #inbplanes     # How many planes to save ?
5       #iinletfreq    #Frequency for collecting data through time
1600 3200 4800 5760    #iposplanes  # Positions of the planes
#
# INCOMPACT 3D Body  old school
#
0      #ivirt# IBM? (1: old school, 2: Lagrangian Poly)
5.     #cex  # X-centre position of the solid body
5.     #cey  # Y-centre position of the solid body
0.     #cez  # Z-centre position of the solid body
0.5    #re   # Radius of the solid body
#
```

Details of MFLOPS3D-MD

C

C.1 Compact finite difference schemes

Coefficients for Compact Finite Difference Scheme are obtained from a solution of linear system that is built to force the desired order of the error with columns consist of Taylor expansions at the points used in the stencil. Notice that this linear system gives the coefficient for a given point. Linear systems similar to the example (C.2) and (C.3) should be solved for each grid point sequentially. Results of these systems will be eventually used to construct a larger linear system to solve the problems.

C.1.1 Example approximation for a first derivative

The compact finite difference scheme with a $5-7$ stencil (5 for implicit and 7 for explicit) can be defined as in Lele[56]

$$\beta f^{(1)}_{i-2} + \alpha f^{(1)}_{i-1} + f^{(1)}_{i} + \alpha f^{(1)}_{i+1} + \beta f^{(1)}_{i+2} = c\frac{f_{i+3}-f_{i-3}}{6h} + b\frac{f_{i+2}-f_{i-2}}{4h} + a\frac{f_{i+1}-f_{i-1}}{2h} \quad \text{(C.1)}$$

where $f^{(p)}_i$ is the pth derivative at point i.

Columns of the following linear system (C.2) consist of corresponding Taylor expansions (C.1). Linear systems are constructed by keeping the derivative of the point alone on the one side of the equation.

Second derivative stencils can be used similarly to generate matrix systems. Linear solvers are written following the idea represented here except that boundary conditions are introduced into the linear system appropriately.

$$\begin{bmatrix} 0 & 0 & 0 & 0 & f_i & f_i & f_i & f_i & f_i & f_i \\ -f_i^{(1)} & -f_i^{(1)} & -f_i^{(1)} & -f_i^{(1)} & (-3h)f_i^{(1)} & (-2h)f_i^{(1)} & (-h)f_i^{(1)} & (h)f_i^{(1)} & (2h)f_i^{(1)} & (3h)f_i^{(1)} \\ -(-2h)f_i^{(2)} & -(-h)f_i^{(2)} & -hf_i^{(2)} & -(2h)f_i^{(2)} & \frac{(-3h)^2}{2!}f_i^{(2)} & \frac{(-2h)^2}{2!}f_i^{(2)} & \frac{(-h)^2}{2!}f_i^{(2)} & \frac{(h)^2}{2!}f_i^{(2)} & \frac{(2h)^2}{2!}f_i^{(2)} & \frac{(3h)^2}{2!}f_i^{(2)} \\ -\frac{(-2h)^2}{2!}f_i^{(3)} & -\frac{(-h)^2}{2!}f_i^{(3)} & -\frac{h^2}{2!}f_i^{(3)} & -\frac{(2h)^2}{2!}f_i^{(3)} & \frac{(-3h)^3}{3!}f_i^{(3)} & \frac{(-2h)^3}{3!}f_i^{(3)} & \frac{(-h)^3}{3!}f_i^{(3)} & \frac{(h)^3}{3!}f_i^{(3)} & \frac{(2h)^3}{3!}f_i^{(3)} & \frac{(3h)^3}{3!}f_i^{(3)} \\ -\frac{(-2h)^3}{3!}f_i^{(4)} & -\frac{(-h)^3}{3!}f_i^{(4)} & -\frac{h^3}{3!}f_i^{(4)} & -\frac{(2h)^3}{3!}f_i^{(4)} & \frac{(-3h)^4}{4!}f_i^{(4)} & \frac{(-2h)^4}{4!}f_i^{(4)} & \frac{(-h)^4}{4!}f_i^{(4)} & \frac{(h)^4}{4!}f_i^{(4)} & \frac{(2h)^4}{4!}f_i^{(4)} & \frac{(3h)^4}{4!}f_i^{(4)} \\ -\frac{(-2h)^4}{4!}f_i^{(5)} & -\frac{(-h)^4}{4!}f_i^{(5)} & -\frac{h^4}{4!}f_i^{(5)} & -\frac{(2h)^4}{4!}f_i^{(5)} & \frac{(-3h)^5}{5!}f_i^{(5)} & \frac{(-2h)^5}{5!}f_i^{(5)} & \frac{(-h)^5}{5!}f_i^{(5)} & \frac{(h)^5}{5!}f_i^{(5)} & \frac{(2h)^5}{5!}f_i^{(5)} & \frac{(3h)^5}{5!}f_i^{(5)} \\ -\frac{(-2h)^5}{5!}f_i^{(6)} & -\frac{(-h)^5}{5!}f_i^{(6)} & -\frac{h^5}{5!}f_i^{(6)} & -\frac{(2h)^5}{5!}f_i^{(6)} & \frac{(-3h)^6}{6!}f_i^{(6)} & \frac{(-2h)^6}{6!}f_i^{(6)} & \frac{(-h)^6}{6!}f_i^{(6)} & \frac{(h)^6}{6!}f_i^{(6)} & \frac{(2h)^6}{6!}f_i^{(6)} & \frac{(3h)^6}{6!}f_i^{(6)} \\ -\frac{(-2h)^6}{6!}f_i^{(7)} & -\frac{(-h)^6}{6!}f_i^{(7)} & -\frac{h^6}{6!}f_i^{(7)} & -\frac{(2h)^6}{6!}f_i^{(7)} & \frac{(-3h)^7}{7!}f_i^{(7)} & \frac{(-2h)^7}{7!}f_i^{(7)} & \frac{(-h)^7}{7!}f_i^{(7)} & \frac{(h)^7}{7!}f_i^{(7)} & \frac{(2h)^7}{7!}f_i^{(7)} & \frac{(3h)^7}{7!}f_i^{(7)} \end{bmatrix} \begin{bmatrix} \beta \\ \alpha \\ \alpha \\ \beta \\ c \\ b \\ a \\ a \\ b \\ c \end{bmatrix} = \begin{bmatrix} 0 \\ f_i^{(1)} \\ 0 \\ 0 \\ 0 \\ 0 \\ 0 \\ 0 \\ 0 \\ 0 \end{bmatrix} \tag{C.2}$$

$$\begin{bmatrix} 0 & 0 & 0 & 0 & 1 & 1 & 1 & 1 & 1 & 1 \\ -1 & -1 & -1 & -1 & (-3h) & (-2h) & (-h) & (h) & (2h) & (3h) \\ -(-2h) & -(-h) & -h & -(2h) & \frac{(-3h)^2}{2!} & \frac{(-2h)^2}{2!} & \frac{(-h)^2}{2!} & \frac{(h)^2}{2!} & \frac{(2h)^2}{2!} & \frac{(3h)^2}{2!} \\ -\frac{(-2h)^2}{2!} & -\frac{(-h)^2}{2!} & -\frac{h^2}{2!} & -\frac{(2h)^2}{2!} & \frac{(-3h)^3}{3!} & \frac{(-2h)^3}{3!} & \frac{(-h)^3}{3!} & \frac{(h)^3}{3!} & \frac{(2h)^3}{3!} & \frac{(3h)^3}{3!} \\ -\frac{(-2h)^3}{3!} & -\frac{(-h)^3}{3!} & -\frac{h^3}{3!} & -\frac{(2h)^3}{3!} & \frac{(-3h)^4}{4!} & \frac{(-2h)^4}{4!} & \frac{(-h)^4}{4!} & \frac{(h)^4}{4!} & \frac{(2h)^4}{4!} & \frac{(3h)^4}{4!} \\ -\frac{(-2h)^4}{4!} & -\frac{(-h)^4}{4!} & -\frac{h^4}{4!} & -\frac{(2h)^4}{4!} & \frac{(-3h)^5}{5!} & \frac{(-2h)^5}{5!} & \frac{(-h)^5}{5!} & \frac{(h)^5}{5!} & \frac{(2h)^5}{5!} & \frac{(3h)^5}{5!} \\ -\frac{(-2h)^5}{5!} & -\frac{(-h)^5}{5!} & -\frac{h^5}{5!} & -\frac{(2h)^5}{5!} & \frac{(-3h)^6}{6!} & \frac{(-2h)^6}{6!} & \frac{(-h)^6}{6!} & \frac{(h)^6}{6!} & \frac{(2h)^6}{6!} & \frac{(3h)^6}{6!} \\ -\frac{(-2h)^6}{6!} & -\frac{(-h)^6}{6!} & -\frac{h^6}{6!} & -\frac{(2h)^6}{6!} & \frac{(-3h)^7}{7!} & \frac{(-2h)^7}{7!} & \frac{(-h)^7}{7!} & \frac{(h)^7}{7!} & \frac{(2h)^7}{7!} & \frac{(3h)^7}{7!} \end{bmatrix} \begin{bmatrix} \beta \\ \alpha \\ \alpha \\ \beta \\ c \\ b \\ a \\ a \\ b \\ c \end{bmatrix} = \begin{bmatrix} 0 \\ 1 \\ 0 \\ 0 \\ 0 \\ 0 \\ 0 \\ 0 \\ 0 \\ 0 \\ 0 \end{bmatrix} \tag{C.3}$$

C.1.2 List of Schemes used in the code

Stencils discussed in Lele[56]'s paper are the generic stencils for homogeneous grid. Stencils used in the code are given in table C.1. They are the result of the optimization based on grid stretching as different stencils are found to give better results. The most important difference from the standard stencils is that lower order stencils for the second point of the discretization matches with the high order stencils for the central points.

Stencils are given in table C.1 for both the solver (second order derivatives) and the first order derivatives as they are using the same points in their stencils.

Table C.1 – Details of the stencils used in the MFLOPS3D-MD. χ is equal to 1 or 2 depending on the order of derivative as the same stencils are used for both the first and second derivatives. Only difference is in the construction of the matrix, boundary points are excluded for the solver and the right-hand-side is modified accordingly. For the derivatives such treatment is not necessary. If Neumann boundary conditions are used, one of $\aleph_1$, $\aleph_2$, $\aleph_3$ or $\aleph_4$ is equal to 1 (the point on the boundary) instead of 0 representing first derivative of the term on explicit side, this is how the Neumann boundary conditions are implemented. Stencils for the point $n-1$ and n are not given as their stencil is the symmetry of ones for the point 2 and 1.

		Implicit Points							Explicit Points								
Parameter	Points	$f_{i+3}^{(\chi)}$	$f_{i+2}^{(\chi)}$	$f_{i+1}^{(\chi)}$	$f_{i}^{(\chi)}$	$f_{i-1}^{(\chi)}$	$f_{i-2}^{(\chi)}$	$f_{i-3}^{(\chi)}$	f_{i+4}	f_{i+3}	$f_{i+2}^{(\aleph_1)}$	$f_{i+1}^{(\aleph_2)}$	f_i	$f_{i-1}^{(\aleph_3)}$	$f_{i-2}^{(\aleph_4)}$	f_{i-3}	f_{i-4}
`so==4`	[1]				1	α						a	b	c	d		
`so==4`	[2]			α	1						a	b	c	d	e		
`so==4`	$[3:n-2]$			α	1	β						a	b	c			
`so==6`	[1]				1	α						a	b	c	d	e	f
`so==6`	[2]			α	1						a	b	c	d	e		
`so==6`	$[3:n-2]$			α	1	β					a	b	c	d	e		
`so==8`	[1]				1	α	β	γ				a	b	c	d	e	f
`so==8`	[2]			α	1						a	b	c	d	e		
`so==8`	$[3:n-2]$		α	β	1	γ	δ				a	b	c	d	e		

C.1.3 Discretization error

The spectral methods are very useful to analyze differently the truncation error. A small example is given below for the completeness of the study. Example in literature often plots the modified wavenumber for homogeneous grids, therefore following derivation is essential for the current study.

Let's define the function, $\Phi(x) = \mathrm{e}^{ikx}$ so $\partial\Phi/\partial x = ik\mathrm{e}^{ikx}$, and $\partial^2\Phi/\partial x^2 = -k^2\mathrm{e}^{ikx}$

The compact finite difference scheme for a second derivative is defined as,

$$\begin{aligned} & f_i^{(2)} + \alpha f_{i-1}^{(2)} + \beta f_{i-2}^{(2)} + \gamma f_{i-3}^{(2)} \\ & \qquad = a f_{i+1} + b f_i + c f_{i-1} + d f_{i-2} + e f_{i-3} + g f_{i-4} \end{aligned} \tag{C.4}$$

Replacing the function and its derivative at each points for the function Φ the equation becomes

$$\begin{aligned} & \left(ik''\right)^2 \left(\mathrm{e}^{ikx} + \alpha \mathrm{e}^{ik(x+\triangle x_{-1})} + \beta \mathrm{e}^{ik(x+\triangle x_{-2})} + \gamma \mathrm{e}^{ik(x+\triangle x_{-3})}\right) \\ & \qquad = a\mathrm{e}^{ik(x+\triangle x_{+1})} + b\mathrm{e}^{ikx} + c\mathrm{e}^{ik(x+\triangle x_{-1})} \\ & \qquad\qquad + d\mathrm{e}^{ik(x+\triangle x_{-2})} + e\mathrm{e}^{ik(x+\triangle x_{-3})} + g\mathrm{e}^{ik(x+\triangle x_{-4})} \end{aligned}$$

By extracting k'' from this equation, modified wavenumbers for the second derivative is

$$k''(k) = \sqrt{-\frac{a\mathrm{e}^{ik\triangle x_{+1}} + b + c\mathrm{e}^{ik\triangle x_{-1}} + d\mathrm{e}^{ik\triangle x_{-2}} + e\mathrm{e}^{ik\triangle x_{-3}} + g\mathrm{e}^{ik\triangle x_{-4}}}{1 + \alpha\mathrm{e}^{ik\triangle x_{-1}} + \beta\mathrm{e}^{ik\triangle x_{-2}} + \gamma\mathrm{e}^{ik\triangle x_{-3}}}} \tag{C.5}$$

The real part of (C.5) is associated with the dispersion error and the imaginary is associated the dissipation error (for second order derivative).

C.2 Diagonalization

Ehrenstein and Peyret[198] shows an implementation of the Helmholtz solver for a 2D problem based on a diagonalization technique. A 3D implication of similar diagonalization is straightforward but requires meticulous matrix multiplications[181].

The Helmholtz equation to be solved in MFLOPS3D-MD for each subdomain is:

$$\nabla^2\Phi - \sigma\Phi = f \ in \ \Omega \qquad with \qquad \Phi = g \ on \ \Gamma \tag{C.6}$$

where $\sigma = const \geq 0$, Γ is the boundaries of the domain Φ, and f, g are given functions.

Let $\Phi_{N,M,P}$ be the polynomial approximation of the solution of (C.6). (x_n, y_m, z_p) are the discretization points for $0 \leq n \leq N$, $0 \leq m \leq M$ and $0 \leq p \leq P$.

The compact scheme discretization of the Helmholtz equation in general form[181;198] can be written

$$\left(D_x^{(2)} \otimes I_y \otimes I_z + I_x \otimes D_y^{(2)} \otimes U + I_z \otimes I_y \otimes D_z^{(2)}\right)\Phi - \sigma\Phi = \mathcal{F} \tag{C.7}$$

where $D_x^{(2)}$, $D_y^{(2)}$ are $D_z^{(2)}$ the square matrices with the size equal to the number of inner nodes n, m and p in each direction.

$$D_x^{(2)} = \left[f_x^{(2)}(n,n)\right],\ 1 \leq n \leq N-1$$
$$D_y^{(2)} = \left[f_y^{(2)}(m,m)\right],\ 1 \leq m \leq M-1$$
$$D_z^{(2)} = \left[f_z^{(2)}(p,p)\right],\ 1 \leq p \leq P-1$$

with $f_N^{(2)}$, $f_M^{(2)}$ and $f_P^{(2)}$ are the coefficients computed from the compact finite scheme. They contain both an explicit and an implicit part, $f_x^{(2)} = A^{-1}Bf$ with A and B being the matrix of implicit and explicit coefficients respectively. See appendix C.1 for their derivation.

Finally, $\mathcal{F}$ is the rank-3 tensor defined as,

$$\mathcal{F} = \left[F\left(x_n, y_m, z_p\right)\right]$$

with

$$\begin{aligned}F\left(x_n, y_m, z_p\right) = {} & f\left(x_n, y_m, z_p\right) \\ & - f_N^{(2)}(n,0)g_1(x_n) - f_M^{(2)}(m,0)g_2(y_m) - f_P^{(2)}(p,0)g_1(z_p) \\ & - f_N^{(2)}(n,n)g_4(x_n) - f_M^{(2)}(m,m)g_5(y_m) - f_P^{(2)}(p,p)g_6(z_p)\end{aligned}$$

where g_i are the boundary conditions on each face of the domain ($g_i = g\ |_{\Gamma_i}$). The boundary conditions affect all the points due to implicit schemes. Dirichlet boundary conditions are simply going to be placed in the solution once the internal points are solved. In the case of the Neumann boundary conditions, the value of the boundary nodes (or interface in multi-domain case) will be calculated from the boundary conditions once the solution is obtained, like it is done in Abide and Viazzo[172].

Assume the eigenvalues of each of the matrices $D_x^{(2)}$, $D_y^{(2)}$ and $D_z^{(2)}$ are real, distinct and negative[†], these matrices are diagonalized as

$$D_x^{(2)}S_x = S_x\Lambda_x, \quad D_y^{(2)}S_y = S_y\Lambda_y, \quad D_z^{(2)}S_z = S_z\Lambda_z \tag{C.8}$$

where S_x, S_y and S_z are matrices of the right eigenvectors of $D_x^{(2)}$, $D_y^{(2)}$

[†] It is suppose to be checked for each grid as it is not always true. It is very easy to validate this property when diagonalization method is in use as most of the libraries used to obtain eigenvalues provides both real and complex pairs. One must, verify that the complex part is zero and the real part is negative. Additionally, performance of the method strongly depends on the distribution of the eigenvalues which is not discussed in this study.

and $D_z^{(2)}$. The diagonal matrices Λ_x, Λ_y and Λ_z are formed with eigenvalues of the associated matrices.

Applying diagonalization on the linear system (C.7) leads to

$$\Lambda\tilde{\Phi} - \sigma\Phi = \tilde{\mathcal{F}} \tag{C.9}$$

where the diagonal matrix Λ is

$$\Lambda = \Lambda_x \otimes I_y \otimes I_x + I_x \otimes \Lambda_y \otimes I_z + I_x \otimes I_y \otimes \Lambda_z - \sigma\Phi \tag{C.10}$$

and the modified fields are

$$\tilde{\Phi} = \left(S_x^{-1} \otimes S_y^{-1} \otimes S_z^{-1}\right)\Phi, \quad \tilde{\mathcal{F}} = \left(S_x^{-1} \otimes S_y^{-1} \otimes S_z^{-1}\right)F \tag{C.11}$$

Finally point-wise relations to obtain the solution the modified linear system are,

$$\left(\lambda_{x,n} + \lambda_{y,m} + \lambda_{z,p} - \sigma\right)\tilde{\phi}_{n,m,p} = \tilde{f}_{n,m,p} \tag{C.12}$$

In practice, the multiplication $S_x^{-1}U_{N,M,P}\left(S_y^{-1}\right)^T\left(S_z^{-1}\right)^T$ is used. Such writing benefits from the continuous chunks of the rank-3 tensor in the memory during the multiplication. For example, LAPACK's DGEMM routine can deal with this more efficiently.

C.3 Influence matrix method

This appendix is the reproduction of the example given by Danabasoglu *et al.*[57] for two domains. The three main part creating an influence matrix, obtaining true interface values and using these true interface values are described below.

Consider Laplace equation,

$$\mathcal{L}P = \text{r.h.s.} \tag{C.13}$$

where P is the matrix of unknowns. The Laplace operator $\mathcal{L}$ discretized in a Cartesian domain is defined as

$$\begin{aligned} x &\in [a,b], \, b > a \\ y &\in [d,e], \, d < e \end{aligned} \tag{C.14}$$

And the boundary conditions are

$$\begin{aligned} P(a,y) =& f_a(y), \quad P(x,d) = f_d(y), \\ P(b,y) =& f_b(y), \quad P(x,e) = f_e(y) \end{aligned} \tag{C.15}$$

where $f_a(y),\ f_b(y),\ f_d(y),$ and $f_e(y)$ are arbitrary functions representing boundary conditions.

The domain is split in two sub-domains on direction-y at $y = c$ constructed as Domain I: $[d,c]$ and Domain II: $[c,e]$.

So sub-domains are discretized in Cartesian domains defined as

$$\begin{aligned} x \in [a,b], \, y \in [d,c], \, d < c \\ x \in [a,b], \, y \in [c,e], \, c > e \end{aligned}$$

C.3.1 Creating an influence matrix

The influence of the unit interface disturbances needs to be computed to form an influence matrix. First, the same equation needs to be solved on each sub-domain:

$$\mathcal{L}P_m^I = 0 \quad and \quad \mathcal{L}P_m^{II} = 0 \tag{C.16}$$

with the following boundary conditions;

$$\begin{aligned} &P^I(a,y)=0 && P^I(b,y)=0 \\ &P^I(x,d)=0 && P^I(x,c)=\delta(\tau_m) \\ &P^{II}(a,y)=0 && P^{II}(b,y)=0 \\ &P^{II}(x,c)=\delta(\tau_m) && P^{II}(x,e)=0 \end{aligned}$$

where superscripts I and II are for the two sub-domains. Simply there is only a single point on the interface with the unit disturbance $\delta(\tau_m)$.

The equations (C.16) are solved for each interface point (subscript m) for which the residual vectors are;

$$R_m = \left(\frac{\partial P_m^I}{\partial y} - \frac{\partial P_m^{II}}{\partial y} \right)$$

And finally residual vectors are arranged to compose the influence matrix **R**.

$$\mathbf{R} = [R_1,\ R_2,\ \cdots\ ,\ R_{N_\Gamma}]$$

The steps above are required only once at the beginning of a simulation. Once the influence matrix is generated, the same matrix is used for all the time steps.

C.3.2 Obtaining true interface values

To obtain the true interface values, sub-domains are solved with their correct right-hand-side and correct boundary conditions but with zeros at the interface points;

$$\begin{aligned}
&P^I(a,y) = f_a(y) && P^I(b,y) = f_b(y)\\
&P^I(x,d) = f_d(x) && P^I(x,c) = 0\\
&P^{II}(a,y) = f_a(y) && P^{II}(b,y) = f_b(y)\\
&P^{II}(x,c) = 0 && P^{II}(x,e) = f_e(x)
\end{aligned}$$

It is known that the boundary conditions $P^I(x,c) = 0$ and $P^{II}(x,c) = 0$ are not correct. So,

$$R_r = \left(\frac{\partial P^I}{\partial y} - \frac{\partial P^{II}}{\partial y}\right)$$

is not zero.

True interface values are defined such that the interface residuals are zero. They can be obtained by solving:

$$R_t = \mathbf{R}^{-1} R_r$$

In MFLOPS3D-MD this linear system is solved iteratively using linear solvers provided by PETSc.

C.3.3 Using true interface values

Sub-domains needs to be solved a second time to obtain the final solutions using correct boundary conditions at the interface points.

$$\begin{aligned}
&P^I(a,y) = f_a(y) && P^I(b,y) = f_b(y)\\
&P^I(x,d) = f_d(x) && P^I(x,c) = R_t\\
&P^{II}(a,y) = f_a(y) && P^{II}(b,y) = f_b(y)\\
&P^{II}(x,c) = R_t && P^{II}(x,e) = f_e(x)
\end{aligned}$$

The steps mentioned in appendices C.3.2 and C.3.3 are repeated every time step and for every unknown.

C.4 Mapping

Let's redefine the physical and Cartesian coordinate system first. Using the chain rule for composition of derivative, first derivatives can be defined as

$$\frac{\partial}{\partial \bar{x}} = \frac{\partial x}{\partial \bar{x}}\frac{\partial}{\partial x} + \frac{\partial y}{\partial \bar{x}}\frac{\partial}{\partial y} \tag{C.17}$$

$$\frac{\partial}{\partial \bar{y}} = \frac{\partial x}{\partial \bar{y}}\frac{\partial}{\partial x} + \frac{\partial y}{\partial \bar{y}}\frac{\partial}{\partial y} \tag{C.18}$$

Similarly second derivatives are

$$\begin{split}\frac{\partial^2}{\partial \bar{x}^2} = \left(\frac{\partial x}{\partial \bar{x}}\right)^2 \frac{\partial^2}{\partial x^2} + \frac{\partial^2 x}{\partial \bar{x}^2}\frac{\partial}{\partial x} \\ + 2\frac{\partial y}{\partial \bar{x}}\frac{\partial x}{\partial \bar{x}}\frac{\partial}{\partial x \partial y} + \left(\frac{\partial y}{\partial \bar{x}}\right)^2 \frac{\partial^2}{\partial y^2} + \frac{\partial^2 y}{\partial \bar{x}^2}\frac{\partial}{\partial y}\end{split} \tag{C.19}$$

$$\begin{split}\frac{\partial^2}{\partial \bar{y}^2} = \left(\frac{\partial x}{\partial \bar{y}}\right)^2 \frac{\partial^2}{\partial x^2} + \frac{\partial^2 x}{\partial \bar{y}^2}\frac{\partial}{\partial x} \\ + 2\frac{\partial y}{\partial \bar{y}}\frac{\partial x}{\partial \bar{y}}\frac{\partial}{\partial x \partial y} + \left(\frac{\partial y}{\partial \bar{y}}\right)^2 \frac{\partial^2}{\partial y^2} + \frac{\partial^2 y}{\partial \bar{y}^2}\frac{\partial}{\partial y}\end{split} \tag{C.20}$$

Mapping functions are simplified as compared to the (5.31).

$$x = \bar{x} \tag{C.21}$$

$$y = \frac{y_a \eta_b(\bar{x}) - y_b \eta_a(\bar{x}) + \bar{y}\left(-y_a + y_b\right)}{-\eta_a(\bar{x}) + \eta_b(\bar{x})} \tag{C.22}$$

with $y_a \leq y \leq y_b$ and $y_a + \eta_a(\bar{x}) \leq \bar{y} \leq y_b + \eta_b(\bar{x})$

Derivatives in physical coordinates as function of the derivatives in Cartesian coordinates are obtained by applying mapping functions to the derivatives defined in (C.17) to (C.20).

$$\frac{\partial x}{\partial \bar{x}} = 1 \tag{C.23}$$

$$\begin{aligned}\frac{\partial y}{\partial \bar{x}} = \frac{1}{\left(\eta_a(\bar{x}) - \eta_b(\bar{x})\right)^2} \Bigg[&\left(-y_a \frac{d}{d\bar{x}}\eta_b(\bar{x}) + y_b \frac{d}{d\bar{x}}\eta_a(\bar{x})\right)\left(\eta_a(\bar{x}) - \eta_b(\bar{x})\right) \\ &- \left(\frac{d}{d\bar{x}}\eta_a(\bar{x}) - \frac{d}{d\bar{x}}\eta_b(\bar{x})\right)\left(-y_a\eta_b(\bar{x}) + y_b\eta_a(\bar{x}) + \bar{y}\left(y_a - y_b\right)\right)\Bigg]\end{aligned} \tag{C.24}$$

$$\frac{\partial x}{\partial \bar{y}} = 0 \tag{C.25}$$

$$\frac{\partial y}{\partial \bar{y}} = \frac{y_a - y_b}{\eta_a(\bar{x}) - \eta_b(\bar{x})} \tag{C.26}$$

$$\frac{\partial^2 x}{\partial \bar{x}^2} = 0 \tag{C.27}$$

$$\begin{aligned}\frac{\partial^2 y}{\partial \bar{x}^2} = \frac{1}{\eta_a(\bar{x}) - \eta_b(\bar{x})} \Bigg[&-y_a \frac{d^2}{d\bar{x}^2}\eta_b(\bar{x}) + y_b \frac{d^2}{d\bar{x}^2}\eta_a(\bar{x}) \\ &+ \frac{2}{\eta_a(\bar{x}) - \eta_b(\bar{x})}\left(y_a \frac{d}{d\bar{x}}\eta_b(\bar{x}) - y_b \frac{d}{d\bar{x}}\eta_a(\bar{x})\right)\left(\frac{d}{d\bar{x}}\eta_a(\bar{x}) - \frac{d}{d\bar{x}}\eta_b(\bar{x})\right) \\ &- \frac{1}{\eta_a(\bar{x}) - \eta_b(\bar{x})}\left(\frac{d^2}{d\bar{x}^2}\eta_a(\bar{x}) - \frac{d^2}{d\bar{x}^2}\eta_b(\bar{x})\right)\left(-y_a\eta_b(\bar{x}) + y_b\eta_a(\bar{x}) + \bar{y}\left(y_a - y_b\right)\right) \\ &+ \frac{2\left(\frac{d}{d\bar{x}}\eta_a(\bar{x}) - \frac{d}{d\bar{x}}\eta_b(\bar{x})\right)^2}{\left(\eta_a(\bar{x}) - \eta_b(\bar{x})\right)^2}\left(-y_a\eta_b(\bar{x}) + y_b\eta_a(\bar{x}) + \bar{y}\left(y_a - y_b\right)\right)\Bigg]\end{aligned} \tag{C.28}$$

$$\frac{\partial^2 x}{\partial \bar{y}^2} = 0 \tag{C.29}$$

$$\frac{\partial^2 y}{\partial \bar{y}^2} = 0 \tag{C.30}$$

The other terms involved in the Laplacian are defined as:

$$\left(\frac{\partial y}{\partial \bar{x}}\right)^2 = \frac{1}{\left(\eta_a(\bar{x}) - \eta_b(\bar{x})\right)^4}\left[\left(y_a \frac{d}{d\bar{x}}\eta_b(\bar{x}) - y_b \frac{d}{d\bar{x}}\eta_a(\bar{x})\right)\left(\eta_a(\bar{x}) - \eta_b(\bar{x})\right) - \left(\frac{d}{d\bar{x}}\eta_a(\bar{x}) - \frac{d}{d\bar{x}}\eta_b(\bar{x})\right)\left(y_a\eta_b(\bar{x}) - y_b\eta_a(\bar{x}) - \bar{y}\left(y_a - y_b\right)\right)\right]^2 \tag{C.31}$$

$$\left(\frac{\partial y}{\partial \bar{y}}\right)^2 = \frac{\left(y_a - y_b\right)^2}{\left(\eta_a(\bar{x}) - \eta_b(\bar{x})\right)^2} \tag{C.32}$$

C.5 Parameters for MFLOPS3D-MD

The MFLOPS3D-MD parameter file to run the tests at $Re = 100$ with 6th order compact finite difference schemes is given below.

```
#####
# Flow Paramaters
#####
100.0         #reynolds (reynolds number)
 0.5          #inletu  (Define inlet velocity, only works if ifinlet==0)
 0.7          #outu    (Define advection velocity for outlet)
#####
# Simulation Configuration
#####
0             #simtype (Simulation type >> 0:test, exact, 1:channel, 2:TBL, 4:Decay)
21 21 21      #nx ny nz (monodomain dimensions)
2 2 2         #ndx ndy ndz (number of domains in each direction)
0 0 0         #ifperiod(3) (0:for wall,dirichlet 1:for periodic)
 0.01         #ts (Time step)
100           #ntime (number of time iterations)
3             #pt (projection type >> 1:strong settings, 2:weak settings)
2 1           #nnl term (FORM 1:convective, 2:skew-symetric) (Scheme 1:FFD 2:AB 3:RK)
2 2 1         #time order (du/dt[1,2,3], vdu/dx[0,1,2,3,4] and p[0,1,2,3])
3             #psm (0:nothing, 1:petsc nullspace, 2:dirichlet at one point)
6 6           #so(2) (scheme order for solver and derivatives)
1             #ifImplicit 1:Implict, 0:Explicit
0             #ifFilter (0:none, 1:u,v,w, 2:rhsPHI)
# Restart, inlet
0             #ifrestart (Read a restart file >> 0:nothing 1:yes)
0             #ifinlet (Read/Generate inlet planes >> 0:nothing 1:yes)
1 1 1 1 1 1 #bctuvw (1: Dirichlet 2: Neumann)
2 2 2 2 2 2 #bctp   (1: Dirichlet 2: Neumann)
# Forcing Parameters
0 0 0         #ifforce(3) (forcing in each directions >> 0:nothing 1:Schlatter2012)
###
## Grid options
####
0 0 0         #ifReadMesh X, Y, Z (0: generates 1: 1D Mesh 2: 2D Mesh 3: 3D Mesh)
 0.0 1.0 0.9 # (start and end, streching factor in x-dir)
 0.0 1.0 0.9 # (start and end, streching factor in y-dir)
 0.0 1.0 0.9 # (start and end, streching factor in z-dir)
0             #ifmap (mapping >> 0:nothing, 1:static, 2:dynamic)
#####
# Data Collection
#####
1             #ifsavefield (Save fields >> 0:no, 1:yes)
100           #incsavefield(Save every x iterations)
0             #ifsaveplane (Save plane >> 0:no, 1:yes)
500           #incsaveplane(Save every x iterations)
0             #ifsaverestart (Save plane >> 0:no, 1:yes)
10            #incsaverestart(Save every x iterations)
#####
### Exact Solver Options (various test, works only if simtype is 0)
######
0             #ifForceUStar    (Put exact values >> 0:no, 1:yes)
0             #ifForcePhi      (Put exact values >> 0:no, 1:yes)
0             #ifForceRhsUStar (Put exact values >> 0:no, 1:yes)
0             #ifForceRhsPhi   (Put exact values >> 0:no, 1:yes)
```

Bibliography

[1] A. Lozano-Durán, O. Flores, and J. Jiménez, “The three-dimensional structure of momentum transfer in turbulent channels,” J. Fluid Mech. **694**, 100–130 (2012).

[2] M. Hultmark, M. Vallikivi, S. C. C. Bailey, and A. J. Smits, “Turbulent pipe flow at extreme Reynolds numbers,” Phys. Rev. Lett. **108**, 094501 (2012).

[3] J. A. Sillero, J. Jiménez, and R. D. Moser, “Two-point statistics for turbulent boundary layers and channels at Reynolds numbers up to $\delta + \approx 2000$,” Phys. Fluids **26**, 105109 (2014).

[4] J.-P. Laval, M. Marquillie, and U. Ehrenstein, “On the relation between kinetic energy production in adverse-pressure gradient wall turbulence and streak instability,” J. Turbul. **13**, N21 (2012).

[5] S. Laizet and N. Li, “Incompact3d: A powerful tool to tackle turbulence problems with up to o(105) computational cores,” Int. J. Numer. Meth. Fluids **67**, 1735–1757 (2010).

[6] P. Schlatter and R. Örlü, “Turbulent boundary layers at moderate Reynolds numbers: Inflow length and tripping effects,” J. Fluid Mech. **710**, 5–34 (2012).

[7] P. Schlatter, Q. Li, G. Brethouwer, A. V. Johansson, and D. S. Henningson, “Simulations of spatially evolving turbulent boundary layers up to,” Int. J. Heat Fluid Flow **31**, 251–261 (2010),

sixth International Symposium on Turbulence and Shear Flow Phenomena.

[8] S. Deck, N. Renard, R. Laraufie, and P.-É. Weiss, "Large-scale contribution to mean wall shear stress in high-Reynolds-number flat-plate boundary layers up to 13650," J. Fluid Mech. **743**, 202–248 (2014).

[9] J. Jiménez, S. Hoyas, M. P. Simens, and Y. Mizuno, "Turbulent boundary layers and channels at moderate Reynolds numbers," J. Fluid Mech. **657**, 335–360 (2010).

[10] S. Srinath, J. C. Vassilicos, C. Cuvier, J.-P. Laval, M. Stanislas, and J.-M. Foucaut, "Attached flow structure and streamwise energy spectra in a turbulent boundary layer," Phys. Rev. E **97**, 053103 (2018).

[11] O. G. Ernst and M. J. Gander, "Why it is difficult to solve Helmholtz problems with classical iterative methods," in *Lecture Notes in Computational Science and Engineering* (Springer Berlin Heidelberg, 2011) pp. 325–363.

[12] G. Hagen, "Ueber die bewegung des wassers in engen cylindrischen röhren," Ann. Phys. Chem. **122**, 423–442 (1839).

[13] O. Reynolds, "An experimental investigation of the circumstances which determine whether the motion of water shall be direct or sinuous, and of the law of resistance in parallel channels." Proc. Roy. Soc. London **35**, 84–99 (1883).

[14] G. Eiffel, "Sur la résistance des sphères dans l'air en mouvement," Comptes Rendus **155**, 1597–1599 (1912).

[15] G. K. Batchelor, *The theory of homogeneous turbulence* (Cambridge university press, 1953).

[16] D. Young, *First Course In Turbulence* (University of Pittsburgh Press, 1999).

[17] S. B. Pope, *Turbulent Flows* (Cambridge University Press, 2000).

[18] G. T. Chapman and M. Tobak, "Observations, theoretical ideas, and modeling of turbulent flows—past, present, and future," in *Theoretical Approaches to Turbulence* (Springer New York, 1985) pp. 19–49.

[19] J. Hinze, "Turbulence, 2nd ed., 790," (1975).

[20] L. Prandtl, "Bericht uber Untersuchungen zur ausgebildeten Turbulenz," Zeitschrift fur angew. Math. u. Mechanik **5**, 136–139 (1925).

[21] L. Prandtl, "Zur turbulenten Strömung in Rohren und längs Platten," Ergebnisse der aerodynamischen versuchsanstalt zu göttingen **4**, 18–29 (1932).

[22] T. Kármán *et al.*, "Mechanische änlichkeit und turbulenz," Nachrichten von der Gesellschaft der Wissenschaften zu Göttingen, Mathematisch-Physikalische Klasse **1930**, 58–76 (1930).

[23] H. Schlichting and K. Gersten, *Boundary-Layer Theory*, Vol. 7 (Springer Berlin Heidelberg, 2017).

[24] A. K. M. F. Hussain, "Coherent structures—reality and myth," Phys. Fluids **26**, 2816 (1983).

[25] D. Schanz, S. Gesemann, and A. Schröder, "Shake-the-box: Lagrangian particle tracking at high particle image densities," Exp Fluids **57**, 70 (2016).

[26] J. Leray, "Sur le mouvement d'un liquide visqueux emplissant l'espace," Acta Math. **63**, 193–248 (1934).

[27] T. Ishihara, T. Gotoh, and Y. Kaneda, “Study of high–Reynolds number isotropic turbulence by direct numerical simulation,” Annu. Rev. Fluid Mech. **41**, 165–180 (2009).

[28] M. Lee and R. D. Moser, “Direct numerical simulation of turbulent channel flow up to,” J. Fluid Mech. **774**, 395–415 (2015).

[29] J. Kim, P. Moin, and R. Moser, “Turbulence statistics in fully developed channel flow at low Reynolds number,” J. Fluid Mech. **177**, 133 (1987).

[30] P. R. Spalart, “Direct simulation of a turbulent boundary layer up to r $\theta = 1410$,” J. Fluid Mech. **187**, 61 (1988).

[31] M. P. Simens, J. Jiménez, S. Hoyas, and Y. Mizuno, “A high-resolution code for turbulent boundary layers,” J. Comput. Phys. **228**, 4218–4231 (2009).

[32] M. Lee and R. D. Moser, “Spectral analysis on Reynolds stress transport equation in high Firewall-bounded turbulence,” (2015).

[33] Y. Mizuno, “Spectra of energy transport in turbulent channel flows for moderate Reynolds numbers,” J. Fluid Mech. **805**, 171–187 (2016).

[34] J. Sillero, J. Jiménez, R. D. Moser, and N. P. Malaya, “Direct simulation of a zero-pressure-gradient turbulent boundary layer up toReθ= 6650,” J. Phys.: Conf. Ser. **318**, 022023 (2011).

[35] P. Schlatter, R. Örlü, Q. Li, G. Brethouwer, J. H. M. Fransson, A. V. Johansson, P. H. Alfredsson, and D. S. Henningson, “Turbulent boundary layers up to reθ=2500 studied through simulation and experiment,” Phys. Fluids **21**, 051702 (2009).

[36] J. H. Lee and H. J. Sung, “Very-large-scale motions in a turbulent boundary layer,” J. Fluid Mech. **673**, 80–120 (2011).

[37] J. A. Sillero, J. Jiménez, and R. D. Moser, "One-point statistics for turbulent wall-bounded flows at Reynolds numbers up to $\delta+ \approx 2000$," Phys. Fluids **25**, 105102 (2013).

[38] I. Solak and J.-P. Laval, "Large-scale motions from a direct numerical simulation of a turbulent boundary layer," Accepted to Phys. Rev. E (2018).

[39] J.-P. Laval and M. Marquillie, "Direct Numerical Simulations of converging-diverging channel flow," in *Progress in wall turbulence : understanding and modelling*, ERCOFTAC Series, edited by M. Stanislas, J. Jiménez, and I. Marusic (Springer, Villeneuve d'Ascq, France, April 21-23, 2009) pp. 203–210.

[40] J.-H. Lee and H. J. Sung, "Effects of an adverse pressure gradient on a turbulent boundary layer," Int. J. Heat Fluid Flow **29**, 568–578 (2008).

[41] A. G. Gungor, Y. Maciel, M. P. Simens, and J. Soria, "Analysis of a turbulent boundary layer subjected to a strong adverse pressure gradient," J. Phys.: Conf. Ser. **506**, 012007 (2014).

[42] P. R. Spalart and J. H. Watmuff, "Experimental and numerical study of a turbulent boundary layer with pressure gradients," J. Fluid Mech. **249**, 337 (1993).

[43] M. Skote, D. Henningson, and R. Henkes, "Direct Numerical Simulation of Self-Similar Turbulent Boundary Layers in Adverse Pressure Gradients," Flow, Turbulence and Combustion **60**, 47–85 (1998).

[44] V. Kitsios, C. Atkinson, J. Sillero, G. Borrell, A. Gungor, J. Jiménez, and J. Soria, "Direct numerical simulation of a self-similar adverse pressure gradient turbulent boundary layer," Int. J. Heat Fluid Flow **61**, 129–136 (2016).

[45] V. Kitsios, A. Sekimoto, C. Atkinson, J. A. Sillero, G. Borrell, A. G. Gungor, J. Jiménez, and J. Soria, "Direct numerical simulation of a self-similar adverse pressure gradient turbulent boundary layer at the verge of separation," J. Fluid Mech. **829**, 392–419 (2017).

[46] J. H. Lee, "Large-scale motions in turbulent boundary layers subjected to adverse pressure gradients," J. Fluid Mech. **810**, 323–361 (2016).

[47] S. K. Robinson, "Coherent motions in the turbulent boundary layer," Annu. Rev. Fluid Mech. **23**, 601–639 (1991).

[48] J. Jiménez and A. Lozano-Durán, "Coherent structures in wall-bounded turbulence," in *Progress in Wall Turbulence 2* (Springer International Publishing, 2015) pp. 37–46.

[49] R. Dekou, J.-M. Foucaut, S. Roux, M. Stanislas, and J. Delville, "Large scale organization of a near wall turbulent boundary layer," Int. J. Heat Fluid Flow **61**, 12–20 (2016).

[50] A. Lozano-Durán and J. Jiménez, "Time-resolved evolution of coherent structures in turbulent channels: Characterization of eddies and cascades," J. Fluid Mech. **759**, 432–471 (2014).

[51] R. Mathis, N. Hutchins, and I. Marusic, "Large-scale amplitude modulation of the small-scale structures in turbulent boundary layers," J. Fluid Mech. **628**, 311 (2009).

[52] B. Ganapathisubramani, N. Hutchins, J. P. Monty, H. Ng, and I. Marusic, "Near-wall influence of large-scale motions in high Reynolds number turbulent boundary layers," in *TSFP DIGITAL LIBRARY ONLINE* (Begel House Inc., 2009).

[53] S. Hugues and A. Randriamampianina, "An improved projection scheme applied to pseudospectral methods for the incompressible

navier-stokes equations," Int. J. Numer. Meth. Fluids **28**, 501–521 (1998).

[54] S. Laizet and E. Lamballais, "High-order compact schemes for incompressible flows: A simple and efficient method with quasi-spectral accuracy," J. Comput. Phys. **228**, 5989–6015 (2009).

[55] J. Kim and P. Moin, "Application of a fractional-step method to incompressible navier-stokes equations," J. Comput. Phys. **59**, 308–323 (1985).

[56] S. K. Lele, "Compact finite difference schemes with spectral-like resolution," J. Comput. Phys. **103**, 16–42 (1992).

[57] G. Danabasoglu, S. Biringen, and C. Streett, "Application of the spectral multidomain method to the navier-stokes equations," J. Comput. Phys. **113**, 155–164 (1994).

[58] S. Balay, W. D. Gropp, L. C. McInnes, and B. F. Smith, "Efficient Management of Parallelism in Object Oriented Numerical Software Libraries," in *Modern Software Tools in Scientific Computing*, edited by E. Arge, A. M. Bruaset, and H. P. Langtangen (Birkhäuser Press, 1997) pp. 163–202.

[59] S. Balay, S. Abhyankar, M. F. Adams, J. Brown, P. Brune, K. Buschelman, L. Dalcin, V. Eijkhout, W. D. Gropp, D. Kaushik, M. G. Knepley, D. A. May, L. C. McInnes, R. T. Mills, T. Munson, K. Rupp, P. Sanan, B. F. Smith, S. Zampini, H. Zhang, and H. Zhang, *PETSc Users Manual*, Tech. Rep. ANL-95/11 - Revision 3.9 (Argonne National Laboratory, 2018).

[60] O. Reynolds, "On the dynamical theory of incompressible viscous fluids and the determination of the criterion," Philosophical Transactions of the Royal Society A: Mathematical, Physical and Engineering Sciences **186**, 123–164 (1895).

[61] A. K. M. F. Hussain and W. C. Reynolds, “The mechanics of an organized wave in turbulent shear flow,” J. Fluid Mech. **41**, 241 (1970).

[62] W. K. George, “Lectures in Turbulence for the 21st Century,” Chalmers University of Technology (2009).

[63] J. Boussinesq, *Théorie de l’écoulement tourbillonnant et tumultueux des liquides dans les lits rectilignes à grande section...*, Vol. 1 (Gauthier-Villars, 1897).

[64] J. Sillero, *High Reynolds number turbulent boundary layers*, Ph.D. thesis, PhD thesis, Universidad Politénica de Madrid (2014).

[65] W. K. George, “Recent advancements toward the understanding of turbulent boundary layers,” AIAA Journal **44**, 2435–2449 (2006).

[66] W. K. George, “Is there a universal log law for turbulent wall-bounded flows?” Philosophical Transactions of the Royal Society A: Mathematical, Physical and Engineering Sciences **365**, 789–806 (2007).

[67] C. B. Millikan, “A critical discussion of turbulent flow in channels and circular tubes,” in *Proc. 5th Int. Congress on Applied Mechanics (Cambridge, MA, 1938)* (Wiley, 1939) pp. 386–392.

[68] F. H. Clauser, “Turbulent boundary layers in adverse pressure gradients,” J. Aeronaut. Sci. **21**, 91–108 (1954).

[69] T. Theodorsen, “Mechanism of turbulence,” (1952).

[70] A. A. Townsend, *The structure of turbulent shear flow* (Cambridge university press, 1956).

[71] A. A. Townsend, “Equilibrium layers and wall turbulence,” J. Fluid Mech. **11**, 97 (1961).

[72] A. E. Perry, S. Henbest, and M. S. Chong, "A theoretical and experimental study of wall turbulence," J. Fluid Mech. **165**, 163 (1986).

[73] A. K. M. F. Hussain, "Coherent structures and turbulence," J. Fluid Mech. **173**, 303 (1986).

[74] M. Stanislas, J. Carlier, J.-M. Foucaut, and P. Dupont, "Double spatial correlations, a new experimental insight into wall turbulence," Comptes Rendus de l'Académie des Sciences - Series IIB - Mechanics-Physics-Astronomy **327**, 55–61 (1999).

[75] A. Lozano-Durán and J. Jiménez, "Effect of the computational domain on direct simulations of turbulent channels up to reτ = 4200," Phys. Fluids **26**, 011702 (2014).

[76] M. Stanislas, "Near wall turbulence: An experimental view," Phys. Rev. Fluids **2**, 100506 (2017).

[77] R. J. Adrian, C. D. Meinhart, and C. D. Tomkins, "Vortex organization in the outer region of the turbulent boundary layer," J. Fluid Mech. **422**, 1–54 (2000).

[78] J. Lin, *Etude détaillée des structures cohérentes de la zone tampon de la turbulence de paroi à l'aide de données de PIV stéréoscopique*, Ph.D. thesis, Ecole Centrale de Lille (2006).

[79] J. Lin, J. P. Laval, J. M. Foucaut, and M. Stanislas, "Quantitative characterization of coherent structures in the buffer layer of near-wall turbulence. part 1: Streaks," Exp Fluids **45**, 999–1013 (2008).

[80] A. E. Perry and M. S. Chong, "On the mechanism of wall turbulence," J. Fluid Mech. **119**, 173 (1982).

[81] J. C. del Álamo, J. Jiménez, P. Zandonade, and R. D. Moser, "Self-similar vortex clusters in the turbulent logarithmic region," J. Fluid Mech. **561**, 329 (2006).

[82] S. Robinson, S. J. Kline, and P. Spalart, “A review of quasi-coherent structures in a numerically simulated turbulent boundary layer,” NASA Ames Research Center; Moffett Field, CA, United States (United States, 1989).

[83] J. C. Hunt, A. A. Wray, and P. Moin, “Eddies, streams, and convergence zones in turbulent flows,” 2. Proceedings of the 1988 Summer Program (United States, 1988) pp. 193–208, studying Turbulence Using Numerical Simulation Databases,.

[84] J. Zhou, R. J. Adrian, S. Balachandar, and T. M. Kendall, “Mechanisms for generating coherent packets of hairpin vortices in channel flow,” J. Fluid Mech. **387**, 353–396 (1999).

[85] W. Schoppa and F. Hussain, “Coherent structure generation in near-wall turbulence,” J. Fluid Mech. **453**, 57–108 (2002).

[86] M. R. Head and P. Bandyopadhyay, “New aspects of turbulent boundary-layer structure,” J. Fluid Mech. **107**, 297 (1981).

[87] H. P. Bakewell, “Viscous sublayer and adjacent wall region in turbulent pipe flow,” Phys. Fluids **10**, 1880 (1967).

[88] B. Ganapathisubramani, E. K. Longmire, and I. Marusic, “Experimental investigation of vortex properties in a turbulent boundary layer,” Phys. Fluids **18**, 055105 (2006).

[89] J. Carlier and M. Stanislas, “Experimental study of eddy structures in a turbulent boundary layer using particle image velocimetry,” J. Fluid Mech. **535**, 143–188 (2005).

[90] S. J. Kline, W. C. Reynolds, F. A. Schraub, and P. W. Runstadler, “The structure of turbulent boundary layers,” J. Fluid Mech. **30**, 741 (1967).

[91] K. P. Nolan and T. A. Zaki, "Conditional sampling of transitional boundary layers in pressure gradients," J. Fluid Mech. **728**, 306–339 (2013).

[92] E. R. Corino and R. S. Brodkey, "A visual investigation of the wall region in turbulent flow," J. Fluid Mech. **37**, 1 (1969).

[93] J. M. Wallace, H. Eckelmann, and R. S. Brodkey, "The wall region in turbulent shear flow," J. Fluid Mech. **54**, 39 (1972).

[94] A. S. W. Thomas and M. K. Bull, "On the role of wall-pressure fluctuations in deterministic motions in the turbulent boundary layer," J. Fluid Mech. **128**, 283 (1983).

[95] W. W. Willmarth and S. S. Lu, "Structure of the Reynolds stress near the wall," J. Fluid Mech. **55**, 65 (1972).

[96] R. D. Moser, J. Kim, and N. N. Mansour, "Direct numerical simulation of turbulent channel flow up to reτ=590," Phys. Fluids **11**, 943–945 (1999).

[97] P. S. Bernard and R. A. Handler, "Reynolds stress and the physics of turbulent momentum transport," J. Fluid Mech. **220**, 99 (1990).

[98] P. S. Bernard, J. M. Thomas, and R. A. Handler, "Vortex dynamics and the production of Reynolds stress," J. Fluid Mech. **253**, 385 (1993).

[99] K. C. Kim and R. J. Adrian, "Very large-scale motion in the outer layer," Phys. Fluids **11**, 417–422 (1999).

[100] M. Guala, S. E. Hommema, and R. J. Adrian, "Large-scale and very-large-scale motions in turbulent pipe flow," J. Fluid Mech. **554**, 521 (2006).

[101] B. Balakumar and R. Adrian, "Large- and very-large-scale motions in channel and boundary-layer flows," Philosophical Trans-

actions of the Royal Society A: Mathematical, Physical and Engineering Sciences **365**, 665–681 (2007).

[102] N. Hutchins and I. Marusic, "Evidence of very long meandering features in the logarithmic region of turbulent boundary layers," J. Fluid Mech. **579**, 1 (2007).

[103] D. J. C. Dennis and T. B. Nickels, "Experimental measurement of large-scale three-dimensional structures in a turbulent boundary layer. part 2. long structures," J. Fluid Mech. **673**, 218–244 (2011).

[104] B. Ganapathisubramani, E. K. Longmire, and I. Marusic, "Characteristics of vortex packets in turbulent boundary layers," J. Fluid Mech. **478**, 35–46 (2003).

[105] J. Jiménez, J. C. Del Álamo, and O. Flores, "The large-scale dynamics of near-wall turbulence," J. Fluid Mech. **505**, 179–199 (2004).

[106] Y. Wu, "A study of energetic large-scale structures in turbulent boundary layer," Phys. Fluids **26**, 045113 (2014).

[107] J. Lee, J. H. Lee, J.-I. Choi, and H. J. Sung, "Spatial organization of large- and very-large-scale motions in a turbulent channel flow," J. Fluid Mech. **749**, 818–840 (2014).

[108] L. S. G. Kovasznay, V. Kibens, and R. F. Blackwelder, "Large-scale motion in the intermittent region of a turbulent boundary layer," J. Fluid Mech. **41**, 283 (1970).

[109] J. H. Lee and H. J. Sung, "Comparison of very-large-scale motions of turbulent pipe and boundary layer simulations," Phys. Fluids **25**, 045103 (2013).

[110] I. Marusic, K. M. Talluru, and N. Hutchins, "Controlling the large-scale motions in a turbulent boundary layer," in *Fluid-*

Structure-Sound Interactions and Control (Springer Berlin Heidelberg, 2013) pp. 17–26.

[111] M. Yoon, J. Hwang, J. Lee, H. J. Sung, and J. Kim, "Large-scale motions in a turbulent channel flow with the slip boundary condition," Int. J. Heat Fluid Flow **61**, 96–107 (2016), sI TSFP9 special issue.

[112] G. I. Taylor, "Statistical theory of turbulence," Proceedings of the Royal Society A: Mathematical, Physical and Engineering Sciences **151**, 421–444 (1935).

[113] H. L. Grant, "The large eddies of turbulent motion," J. Fluid Mech. **4**, 149 (1958).

[114] K. T. Christensen and R. J. Adrian, "Statistical evidence of hairpin vortex packets in wall turbulence," J. Fluid Mech. **431**, 433–443 (2001).

[115] M. Tutkun, W. K. George, J. Delville, M. Stanislas, P. B. Johansson, J.-M. Foucaut, and S. Coudert, "Two-point correlations in high Reynolds number flat plate turbulent boundary layers," J. Turbul. **10**, N21 (2009).

[116] A. Fage and H. C. H. Townend, "An examination of turbulent flow with an ultramicroscope," Proceedings of the Royal Society A: Mathematical, Physical and Engineering Sciences **135**, 656–677 (1932).

[117] R. E. Falco, "Coherent motions in the outer region of turbulent boundary layers," Phys. Fluids **20**, S124 (1977).

[118] G. L. Brown and A. S. W. Thomas, "Large structure in a turbulent boundary layer," Phys. Fluids **20**, S243 (1977).

[119] C. J. Kähler, “Investigation of the spatio-temporal flow structure in the buffer region of a turbulent boundary layer by means of multiplane stereo PIV,” Exp Fluids **36**, 114–130 (2003).

[120] K. T. Christensen and Y. Wu, “Characteristics of vortex organization in the outer layer of wall turbulence,” in *TSFP DIGITAL LIBRARY ONLINE* (Begel House Inc., 2005).

[121] J. C. del Álamo and J. Jiménez, “Spectra of the very large anisotropic scales in turbulent channels,” Phys. Fluids **15**, L41 (2003).

[122] J. C. Del ÁLamo, J. Jiménez, P. Zandonade, and R. D. Moser, “Scaling of the energy spectra of turbulent channels,” J. Fluid Mech. **500**, 135–144 (2004).

[123] J. Hwang, J. Lee, and H. J. Sung, “Influence of large-scale accelerating motions on turbulent pipe and channel flows,” J. Fluid Mech. **804**, 420–441 (2016).

[124] C. Diaz-Daniel, S. Laizet, and J. C. Vassilicos, “Wall shear stress fluctuations: Mixed scaling and their effects on velocity fluctuations in a turbulent boundary layer,” Phys. Fluids **29**, 055102 (2017).

[125] N. Renard and S. Deck, “On the scale-dependent turbulent convection velocity in a spatially developing flat plate turbulent boundary layer at Reynolds number,” J. Fluid Mech. **775**, 105–148 (2015).

[126] G. Eitel-Amor, R. Örlü, and P. Schlatter, “Simulation and validation of a spatially evolving turbulent boundary layer up to,” Int. J. Heat Fluid Flow **47**, 57–69 (2014).

[127] A. J. Smits, B. J. McKeon, and I. Marusic, “High–Reynolds number wall turbulence,” Annu. Rev. Fluid Mech. **43**, 353–375 (2011).

[128] W. J. Baars, N. Hutchins, and I. Marusic, "Self-similarity of wall-attached turbulence in boundary layers," J. Fluid Mech. **823**, RS:1–12 (2017).

[129] N. Hutchins and I. Marusic, "Large-scale influences in near-wall turbulence," Philosophical Transactions of the Royal Society A: Mathematical, Physical and Engineering Sciences **365**, 647–664 (2007).

[130] M. de Giovanetti, H. J. Sung, and Y. Hwang, "Streak instability as an initiating mechanism of the large-scale motions in a turbulent channel flow," in *APS Meeting Abstracts* (2016).

[131] J. C. Vassilicos, J.-P. Laval, J.-M. Foucaut, and M. Stanislas, "The streamwise turbulence intensity in the intermediate layer of turbulent pipe flow," J. Fluid Mech. **774**, 324–341 (2015).

[132] A. Gungor, Y. Maciel, M. Simens, and J. Soria, "Scaling and statistics of large-defect adverse pressure gradient turbulent boundary layers," Int. J. Heat Fluid Flow **59**, 109–124 (2016).

[133] J. R. Brinkerhoff and M. I. Yaras, "Numerical investigation of transition in a boundary layer subjected to favourable and adverse streamwise pressure gradients and elevated free stream turbulence," J. Fluid Mech. **781**, 52–86 (2015).

[134] S.-I. Shah, J.-P. Laval, and M. Stanislas, "A specific behaviour of adverse pressure gradient near wall flows," in *ERCOFTAC Series* (Springer Netherlands, 2011) pp. 257–265.

[135] J. Monty, Z. Harun, and I. Marusic, "A parametric study of adverse pressure gradient turbulent boundary layers," Int. J. Heat Fluid Flow **32**, 575–585 (2011), 8th International Symposium on Engineering Turbulence Modelling and Measurements, June 9 to 11, Marseille, France.

[136] Y. Maciel, A. G. Gungor, and M. Simens, "Structural differences between small and large momentum-defect turbulent boundary layers," Int. J. Heat Fluid Flow **67**, 95–110 (2017).

[137] M. Marquillie, U. Ehrenstein, and J.-P. Laval, "Instability of streaks in wall turbulence with adverse pressure gradient," J. Fluid Mech. **681**, 205–240 (2011).

[138] E. Lamballais, V. Fortuné, and S. Laizet, "Straightforward high-order numerical dissipation via the viscous term for direct and large eddy simulation," J. Comput. Phys. **230**, 3270–3275 (2011).

[139] R. Gautier, S. Laizet, and E. Lamballais, "A DNS study of jet control with microjets using an immersed boundary method," International Journal of Computational Fluid Dynamics **28**, 393–410 (2014).

[140] T. S. Lund, X. Wu, and K. D. Squires, "Generation of turbulent inflow data for spatially-developing boundary layer simulations," J. Comput. Phys. **140**, 233–258 (1998).

[141] G. Borrell, J. A. Sillero, and J. Jiménez, "A code for direct numerical simulation of turbulent boundary layers at high Reynolds numbers in BG/P supercomputers," Comput. Fluids **80**, 37–43 (2013), selected contributions of the 23rd International Conference on Parallel Fluid Dynamics ParCFD2011.

[142] X. Wu, "Inflow turbulence generation methods," Annu. Rev. Fluid Mech. **49**, 23–49 (2017).

[143] X. Wu and P. Moin, "Direct numerical simulation of turbulence in a nominally zero-pressure-gradient flat-plate boundary layer," J. Fluid Mech. **630**, 5 (2009).

[144] H. Choi and P. Moin, "Grid-point requirements for large eddy sim-

ulation: Chapman's estimates revisited," Phys. Fluids **24**, 011702 (2012).

[145] J. P. Monty and M. S. Chong, "Turbulent channel flow: Comparison of streamwise velocity data from experiments and direct numerical simulation," J. Fluid Mech. **633**, 461 (2009).

[146] J. C. Del Álamo and J. Jiménez, "Estimation of turbulent convection velocities and corrections to Taylor's approximation," J. Fluid Mech. **640**, 5 (2009).

[147] J. F. Morrison, B. J. McKEON, W. Jiang, and A. J. Smits, "Scaling of the streamwise velocity component in turbulent pipe flow," J. Fluid Mech. **508**, 99–131 (2004).

[148] T. A. Zaki, "From streaks to spots and on to turbulence: Exploring the dynamics of boundary layer transition," Flow Turbulence Combust **91**, 451–473 (2013).

[149] J. Hwang, J. Lee, H. J. Sung, and T. A. Zaki, "Inner–outer interactions of large-scale structures in turbulent channel flow," J. Fluid Mech. **790**, 128–157 (2016).

[150] B. Ganapathisubramani, N. Hutchins, W. T. Hambleton, E. K. Longmire, and I. Marusic, "Investigation of large-scale coherence in a turbulent boundary layer using two-point correlations," J. Fluid Mech. **524**, 57–80 (2005).

[151] M. Vallikivi, B. Ganapathisubramani, and A. J. Smits, "Spectral scaling in boundary layers and pipes at very high Reynolds numbers," J. Fluid Mech. **771**, 303–326 (2015).

[152] M. Hassouna and A. Farag, "Variational curve skeletons using gradient vector flow," IEEE Trans. Pattern Anal. Mach. Intell. **31**, 2257–2274 (2009).

[153] J. Soria, V. Kitsios, and C. Atkinson, “On the identification of intense Reynolds stress structures in wall-bounded flows using information-limited two-dimensional planar data,” Eur. J. Mech. B. Fluids **55**, 279–285 (2016).

[154] J. C. Vassilicos and J. C. R. Hunt, “Fractal dimensions and spectra of interfaces with application to turbulence,” in *Proceedings of the Royal Society of London A: Mathematical, Physical and Engineering Sciences*, Vol. 435 (The Royal Society, 1991) pp. 505–534.

[155] J. M. Wallace, “Quadrant analysis in turbulence research: History and evolution,” Annu. Rev. Fluid Mech. **48**, 131–158 (2016).

[156] S. Hoyas and J. Jiménez, “Scaling of the velocity fluctuations in turbulent channels up to reτ=2003,” Phys. Fluids **18**, 011702 (2006).

[157] I. Marusic, W. J. Baars, and N. Hutchins, “Scaling of the streamwise turbulence intensity in the context of inner-outer interactions in wall turbulence,” Phys. Rev. Fluids **2**, 100502 (2017).

[158] M. Marquillie, *Simulation numérique et étude de la stabilité d’un écoulement de couche limite décollé*, Ph.D. thesis (2003), universite de Nice-Sophia Antipolis.

[159] M. Marquillie and U. Ehrenstein, “On the onset of nonlinear oscillations in a separating boundary-layer flow,” J. Fluid Mech. **490**, 169–188 (2003).

[160] U. Ehrenstein, M. Marquillie, and C. Eloy, “Skin friction on a flapping plate in uniform flow,” Philosophical Transactions of the Royal Society A: Mathematical, Physical and Engineering Sciences **372**, 20130345–20130345 (2014).

[161] A. Žnidarčič, O. Coutier-Delgosha, M. Marquillie, and M. Dular, “An algorithm for fast DNS cavitating flows simulations using

homogeneous mixture approach," J. Phys.: Conf. Ser. **656**, 012143 (2015).

[162] A. Znidarcic, *Un nouvel algoritme pour la simulation DNS et LES des ecoulements cavitants*, Ph.D. thesis (2016), eNSAM.

[163] H. P. Langtangen, K.-A. Mardal, and R. Winther, "Numerical methods for incompressible viscous flow," Adv. Water Resour. **25**, 1125–1146 (2002).

[164] J. Guermond, P. Minev, and J. Shen, "An overview of projection methods for incompressible flows," Comput. Methods Appl. Mech. Eng. **195**, 6011–6045 (2006).

[165] R. Témam, "Sur l'approximation de la solution des équations de navier-stokes par la méthode des pas fractionnaires (I)," Arch. Rational Mech. Anal. **32**, 135–153 (1969).

[166] R. Témam, "Sur l'approximation de la solution des équations de navier-stokes par la méthode des pas fractionnaires (II)," Arch. Rational Mech. Anal. **33**, 377–385 (1969).

[167] D. L. Brown, R. Cortez, and M. L. Minion, "Accurate projection methods for the incompressible navier–stokes equations," J. Comput. Phys. **168**, 464–499 (2001).

[168] S. A. Orszag, M. Israeli, and M. O. Deville, "Boundary conditions for incompressible flows," J Sci Comput **1**, 75–111 (1986).

[169] G. E. Karniadakis, M. Israeli, and S. A. Orszag, "High-order splitting methods for the incompressible navier-stokes equations," J. Comput. Phys. **97**, 414–443 (1991).

[170] A. J. Chorin, "Numerical solution of the navier-stokes equations," Math. Comput. **22**, 745 (1968).

[171] G. Reis, I. Tasso, L. Souza, and J. Cuminato, "A compact finite differences exact projection method for the navier–stokes equations on a staggered grid with fourth-order spatial precision," Comput. Fluids **118**, 19–31 (2015).

[172] S. Abide and S. Viazzo, "A 2D compact fourth-order projection decomposition method," J. Comput. Phys. **206**, 252–276 (2005).

[173] W. Chen, J. C. Chen, and E. Y. Lo, "An interpolation based finite difference method on non-uniform grid for solving navier–stokes equations," Comput. Fluids **101**, 273–290 (2014).

[174] S. Abdallah, "Numerical solutions for the pressure Poisson equation with Neumann boundary conditions using a non-staggered grid, i," J. Comput. Phys. **70**, 182–192 (1987).

[175] S. Abdallah, "Numerical solutions for the incompressible navier-stokes equations in primitive variables using a non-staggered grid, II," J. Comput. Phys. **70**, 193–202 (1987).

[176] E. Dormy, "An accurate compact treatment of pressure for colocated variables," J. Comput. Phys. **151**, 676–683 (1999).

[177] R. K. Shukla and X. Zhong, "Derivation of high-order compact finite difference schemes for non-uniform grid using polynomial interpolation," J. Comput. Phys. **204**, 404–429 (2005).

[178] A. Poux, S. Glockner, E. Ahusborde, and M. Azaı¨ez, "Open boundary conditions for the velocity-correction scheme of the navier–stokes equations," Comput. Fluids **70**, 29–43 (2012).

[179] Y. Morinishi, T. Lund, O. Vasilyev, and P. Moin, "Fully conservative higher order finite difference schemes for incompressible flow," J. Comput. Phys. **143**, 90–124 (1998).

[180] Y. Morinishi, "Skew-symmetric form of convective terms and fully conservative finite difference schemes for variable density low-Mach number flows," J. Comput. Phys. **229**, 276–300 (2010).

[181] S. Abide, M. S. Binous, and B. Zeghmati, "An efficient parallel high-order compact scheme for the 3D incompressible navier–stokes equations," International Journal of Computational Fluid Dynamics **31**, 214–229 (2017).

[182] N. Li and S. Laizet, "2decomp & fft-a highly scalable 2d decomposition library and fft interface," in *Cray User Group 2010 conference* (2010) pp. 1–13.

[183] G. Sutmann, "Compact finite difference schemes of sixth order for the Helmholtz equation," J. Comput. Appl. Math. **203**, 15–31 (2007).

[184] Y. S. Wong and G. Li, "Exact finite difference schemes for solving Helmholtz equation at any wavenumber," International Journal of Numerical Analysis and Modeling, Series B **2**, 91–108 (2011).

[185] J. B. Bell, P. Colella, and H. M. Glaz, "A second-order projection method for the incompressible navier-stokes equations," J. Comput. Phys. **85**, 257–283 (1989).

[186] A. Quarteroni and A. Valli, *Domain decomposition methods for partial differential equations* (Oxford University Press, 1999).

[187] O. Daube, "Resolution of the 2D navier-stokes equations in velocity-vorticity form by means of an influence matrix technique," J. Comput. Phys. **103**, 402–414 (1992).

[188] M. O. Deville, P. F. Fischer, and E. H. Mund, *High-Order Methods for Incompressible Fluid Flow*, Vol. 9 (Cambridge University Press, 2002).

[189] G. H. Golub, L. C. Huang, H. Simon, and W.-P. Tang, "A fast Poisson solver for the finite difference solution of the incompressible navier–stokes equations," SIAM J. Sci. Comput. **19**, 1606–1624 (1998).

[190] M. Marquillie, J.-P. Laval, and R. Dolganov, "Direct numerical simulation of a separated channel flow with a smooth profile," J. Turbul. **9**, N1 (2008).

[191] S. Laizet, *Développement d'un code de calcul combinant des schémas de haute précision avec une méthode de frontières immergées pour la simulation des mouvements tourbillonnaires en aval d'un bord de fuite*, Ph.D. thesis, Poitiers (2005), universite de Poitiers.

[192] I. M. Babuška and S. A. Sauter, "Is the pollution effect of the FEM avoidable for the Helmholtz equation considering high wave numbers?" SIAM J. Numer. Anal. **34**, 2392–2423 (1997).

[193] K. Wang and Y. S. Wong, "Is pollution effect of finite difference schemes avoidable for multi-dimensional Helmholtz equations with high wave numbers?" *International Journal of Numerical Analysis and Modeling*, Commun. Comput. Phys. **21**, 490–514 (2017).

[194] C. R. Ethier and D. A. Steinman, "Exact fully 3D navier-stokes solutions for benchmarking," Int. J. Numer. Meth. Fluids **19**, 369–375 (1994).

[195] R. K. Shukla, M. Tatineni, and X. Zhong, "Very high-order compact finite difference schemes on non-uniform grids for incompressible navier–stokes equations," J. Comput. Phys. **224**, 1064–1094 (2007).

[196] J.-P. Laval, J. C. Vassilicos, J.-M. Foucaut, and M. Stanislas, "Comparison of turbulence profiles in high-Reynolds-number tur-

bulent boundary layers and validation of a predictive model," J. Fluid Mech. **814** (2017), 10.1017/jfm.2017.63.

[197] K. Wang and Y. S. Wong, "Is pollution effect of finite difference schemes avoidable for multi-dimensional Helmholtz equations with high wave numbers?" Commun. Comput. Phys. **21**, 490–514 (2017).

[198] U. Ehrenstein and R. Peyret, "A chebyshev collocation method for the navier-stokes equations with application to double-diffusive convection," Int. J. Numer. Meth. Fluids **9**, 427–452 (1989).